Dissertation zur Erlangung des Doktorgrades der Fakultät für Chemie und Pharmazie der Ludwig-Maximilians-Universität München

Structural analysis of ribosome associated GTPases and antibiotics

Maximiliane Julia Wieland

aus

Gräfelfing, Deutschland

2020

Erklärung

Diese Dissertation wurde im Sinne von § 7 der Promotionsordnung vom 28. November 2011 von Herrn Prof. Dr. Daniel Wilson betreut

Eidesstattliche Versicherung

Diese Dissertation wurde eigenständig und ohne unerlaubte Hilfe erarbeitet.

München, den 08.09.2020

_____

Maximiliane Wieland

Dissertation eingereicht am 09.09.2020

1. Gutachter: Herr Prof. Dr. Daniel N. Wilson
2. Gutachter: Herr Prof. Dr. Roland Beckmann

Mündliche Prüfung am 23.10.2020

Für meine Mutter

Quando una stella cade dal cielo, illumina il mare con con il suo bagliore unico.

Table of contents

Acknowledgements

First and foremost I want to thank Daniel for accepting this biologist into his group of structural biochemists. I got to learn many new biochemical techniques and discovered my passion for processing. I am very grateful for everything, most importantly for having patience along this lengthy journey to the finish line, for finding encouraging words and for always seeing something in results even when I was not convinced.

Of course I also want to thank Roland Beckmann and his group, who gave us a "second home" and were like one big family. I am especially glad to have met my friends Anne, Ting and Jen who were and still are available for support of any kind. Big thanks to Birgitta Beatrix, who kept an eye on the Wilsons and made sure everything was in order there, too; Heidi Sieber, Andrea Gilmozzi and Joanna Musial, who treated us like one of their own; as well as to the tech/cluster-team of Lukas Kater, André Heuer and Thomas Becker, who kept everything running smoothly. A special thanks to the world-class cryo-EM team of Otto Berninghausen, Susanne Rieder and Charlotte Ungewickell for prepping countless grids and shooting (in my case) many spirits and some titan data sets. Without you, we would all be pretty lost.

I also want to thank Jürgen Lassak and am happy that he can once again be part of my academic journey. He ignited and inspired my passion for scientific work during the bachelor thesis, and without him I would not be the scientist I am today.

Any past and present member of the Wilson group has been an important part of my PhD journey, and I want to thank them all: Stefan, Daniel Sohmen, Micha, Bertrand, Paul, Patrick, Tatjana, Meriem, Fabian, Timm, Caillan, and especially my girls, Katrin, Maha, Karo, Aga and Claudia. There has always been a lot of interaction, whether it was about processing, wet lab, sharing a quick laugh, cake or a beer, and I am sad to leave an exceptional atmosphere like this behind me. With the move to Hamburg a lot of new, awesome people were introduced, and I want to say a huge thanks to Danny, who took so much paperwork of our shoulders, and Katrin who helped us out in the lab (despite all her other obligations) and made our lives so much easier.

My friends Svenja, Irene, Simge, Nadja, and Christina, and family have also been a great help in this odyssey all across Germany, and I appreciate all they have done for me. And last but not least, my dear Johann, thank you for your continuous love, enthusiasm and support throughout this journey.

List of Publications

Publication 1

Pausch, P., Steinchen, W., **Wieland, M.**, Klaus, T., Freibert, S. A., Altegoer, F., Wilson, D. N. and Bange, G. (2018). Structural basis for (p)ppGpp-mediated inhibition of the GTPase RbgA. *J Biol Chem* 293: 19699-709

Publication 2

Steinchen, W., Majkini, M., **Wieland, M.**, Dornes, A., Giammarinaro, P.I., Lepak, A., Burnett, B.J., Blanchard, S.C., Wilson, D.N. and Bange, G. (Manuscript) Structural basis for the (p)ppGpp-dependent control of the translation elongation factor EF-Tu

Publication 3

Osterman, I. A.*, **Wieland, M.***, Maviza, T. P.*, Lashkevich, K. A., Lukianov, D. A., Komarova, E. S., Zakalyukina, Y. V., Buschauer, R., Shiriaev, D. I., Leyn, S. A., Zlamal, J. E., Biryukov, M. V., Skvortsov, D. A., Tashlitsky, V. N., Polshakov, V. I., Cheng, J., Polikanov, Y. S., Bogdanov, A. A., Osterman, A. L., Dmitriev, S. E., Beckmann, R., Dontsova, O. A., Wilson, D. N. and Sergiev, P. V. (2020). Tetracenomycin X inhibits translation by binding within the ribosomal exit tunnel. *Nat Chem Biol*

Publications not included in the thesis:

Publication 4

Limbrick, E.*, Graf, M.*, Derewacz, D. K., Nguyen, F., Spraggins, J. M., **Wieland, M.**, Ynigez-Gutierrez, A., Reisman, B. J., Zinshteyn, B., McCulloch, K. M., Iverson, T. M., Green, R., Wilson, D. N. and Bachmann, B. O. (2020). A bifunctional nitrone conjugated secondary metabolite targeting the ribosome. *J Am Chem Soc*

*) these authors contributed equally to the publication

Contribution report

This dissertation contains results obtained in the course of my PhD from Nov. 2015 to June 2020 under supervision of Prof. Dr. Daniel N. Wilson at both the Gene Center of Ludwig-Maximilians University in Munich and the University of Hamburg. Here mentioned publications were results of international collaborations with Roland Beckmann (LMU Munich, Germany), Scott C. Blanchard (Memphis, USA), Gert Bange (Philipps-University Marburg, Germany) as well as Ilya A. Osterman and Petr V. Sergiev (Skoltech Institute Moscow, Russia).

Publication 1 (Pausch et al., 2017)

In this publication we characterised the inhibition of ribosome biogenesis-associated protein RbgA by the alarmones (p)ppGpp, and showed that binding sterically obstructs formation of an active complex. I conducted binding assays to monitor interaction between a mature 50S and RbgA in the presence of different nucleotides, i.e. GTP, GDPNP and (p)ppGpp. From this I prepared samples for subsequent cryo-EM data collection, which I also processed. Moreover, I contributed the main figure 4 of the cryo-EM density and associated supplementary figures 5-8.

Publication 2 (Steinchen et al., unpublished)

This study examines the effect of (p)ppGpp on the elongation factor EF-Tu biochemically and structurally, and showed EF-Tu is capable of pppGpp hydrolysis. I conducted electrophoretic mobility shift assays to survey interactions between EF-Tu and aminoacylated tRNAs.

Publication 3: (Osterman et al., 2020)

This paper examines the mechanism of inhibition of the antibiotic tetracenomycin X through various biochemical assays as well as cryo-EM of the human and *E. coli* ribosome. I was involved in conducting *E. coli* based transcription-translation assays, as well as analysis of other biochemical data. Furthermore, I processed the bacterial cryo-EM dataset, modelled and validated the structure, interpreted interactions between drug and ribosomes, determined conservation of the binding site, and compared it to the related mechanisms of the antibiotics doxorubicin, tetracycline and elloramycins. I helped in manuscript preparation and prepared all graphs, as well as the main and extended data figures.

Abbreviations

30SIC	30S initiation complex
30SPIC	30S pre-initiation complex
70SIC	70S initiation complex
70SEC	70S elongation complex
A	adenine
aa	amino acid
aa-tRNA	aminoacyl-tRNA
argB	argyrin B
ATP	adenine triphosphate
ASL	anticodon stem loop
C	cytosine
CCW	counter clockwise
CP	central protuberance
CPK	central pseudoknot
CTD	C-terminal domain
CTF	Contrast transfer function
CW	clockwise
DC	decoding centre
Dox	doxorubicin
DMSO	dimethylsulfoxide
DNA	deoxyribonucleic acid
EF-G	elongation factor GTPase
EF-Ts	elongation factor thermo-stable
EF-Tu	elongation factor thermo-unstable
EMSA	electrophoretic mobility shift assay
Ery	erythromycin
EtOH	Ethanol
FA	fusidic acid
Fluc	Firefly luciferase
FSC	Fourier shell correlation
G-domain	GTPase domain
GAC	GTPase-associated centre
GDP	guanosine-5’-diphosphate

GMPPCP	β,γ-methylene guanosine -5'triphosphate
GDPNP	guanosine 5'-[β,γ-imido]-triphosphate
GEF	guanine exchange factor
GTP	guanosine-5'-triphosphate
h#	helix# of the small ribosomal subunit
H#	helix# of the large ribosomal subunit
IC_{50}	concentration at which 50% of reaction are inhibited
IF	initiation factor
kDa	kilodalton
LSU	large subunit (50S)
(f)Met	(formyl)methionine
MIC	minimal inhibitory concentration
mRNA	messenger RNA
MRSA	multidrug resistant *Staphylococcus aureus*
NPC	nascent peptide chain
NPET	nascent polypeptide exit tunnel
NRPS	non-ribosomal peptide synthetase
nt	nucleotide
NTD	N-terminal domain
nr70S	non-rotated state 70S ribosome
OD	optical density
ORF	open reading frame
PAGE	polyacrylamide gel electrophoresis
P_i	inorganic / orthophosphate
POST	post-translocation 70S state
PoTC	post-termination complex
PTC	peptidyl transferase center
RF	release factor
RNA	ribonucleic acid
RNAP	DNA-dependent RNA polymerase
(p)ppGpp	guanosine-3' -diphosphate- 5'-tri/diphosphate
tRNA	transfer RNA
RbgA	ribosome biogenesis factor A
RF	release factor

r-protein	ribosomal protein
rRNA	ribosomal RNA
RRF	ribosome recycling factor
RSH	RelA/ SpoT homologue
SAH	short alarmone hydrolase
SAS	short alarmone synthetase
SD	Shine-Dalgarno
SDS	sodium dodecyl sulphate
SRC	stalled ribosome complex
SRL	sarcin-ricin loop
SRP	signal recognition particle
SSU	small subunit (30S)
T	thymine
TcmX	tetracenomycin X
TGS	threonyl-tRNA synthetase, GTPase, and SpoT
U	uridine
u/bL#	universal/bacterial large subunit protein #
u/bS#	universal/bacterial small subunit protein #
v/v	volume per volume
VRE	vancomycin resistant *Enterococcus*
w/v	weight per volume
WT	wild type

Summary

The ribosome constitutes the scaffold for one of the most important processes within a living cell; jointly with tRNAs, mRNAs and a number of assisting factors, they comprise the macromolecular machinery responsible for decoding of mRNAs and translation of proteins. This makes ribosomes and translation an attractive point of action. Under stress conditions, bacterial cells induce a stringent response, mediated by the alarmones (p)ppGpp, to limit a waste of resources. With translation being an extremely energy consuming process, it is targeted as well. To understand this process, we studied the effect it has on two targeted GTPases, namely the ribosome biogenesis co-factor RbgA, and the elongation factor EF-Tu. We applied cryo-EM to solve the structure of RbgA interacting with its substrate, the 50S. Initially a low-resolved and flexible density was interpreted as RbgA associated with rRNA helices. However, further cryo-EM of 50S in the absence of RbgA revealed a similar density. X-ray crystal structure of RbgA bound to (p)ppGpp showed that the 3'-pyrophosphate moiety likely inhibits RbgA from adopting a conformation allowing binding to ribosomal particles, thus hindering it from producing mature and translation competent 50S. In the second study, an X-ray crystal structure analysis of EF-Tu in the presence of pppGpp revealed a similar mode of inhibition, as 3'-pyrophosphate would sterically clash with switch I in an ordered conformation. Accordingly, switch I adopts a disordered conformation, which we suggest will obstruct EF-Tu from binding aminoacylated tRNAs. We conducted EMSAs and could indeed show that in the presence of (p)ppGpp, complex formation of EF-Tu with tRNA was inhibited. Besides the stringent response, also a number of antibiotics target translation. In a third study, we revealed that the polyketide antibiotic tetracenomycin X (TcmX) inhibits translation. Through stacking interactions onto a conserved U1782-U2586 base-pair and coordination of two Mg^{2+} ions, TcmX binds inside the nascent peptide exit tunnel, blocking translation elongation. From toe-printing experiments with different templates we suggest it has a sequence-specific stalling mechanism, analogous to macrolides. In a fourth project we conducted biochemical experiments showing that the antibiotic argyrin B inhibits bacterial translation by trapping the elongation factor EF-G on the ribosome. A cryo-EM structure of EF-G on the 70S ribosome in the presence of argyrin B confirms a previously determined binding site between domain III and V, and shows that the drug inhibits conformational changes of EF-G necessary for subsequent dissociation.

1. Introduction

One of the most accepted theories on the origin of life is that it started with RNA molecules (Gilbert, 1986; Noller, 2012), which were able to serve both as molecules with enzymatic activity and as storage of genetic information. Formation of amino acids under pre-biotic conditions has been achieved (Miller, 1953), and a co-evolution of ribosomes and proteins is conceivable (Noller, 2012). As the ribose group poses an easy point of attack, RNA is less stable, and life mitigated to storing information in the more reliable form of DNA, and evolved to what we know today.

The essence of life is the reproduction on an organismal and cellular level. The latter is described in the central dogma of molecular biology (Crick, 1970): genetic information is stored in DNA, but it also serves as template for transcription of RNA. The RNA in return is employed in protein synthesis and translated into polypeptide chains consisting of amino acids. Translation itself is a highly complex process facilitated by a multitude of distinct RNAs: the transcribed messenger RNA (mRNA) contains a code, which is deciphered by transfer RNAs (tRNAs). tRNAs assume the role of adapters between RNA and proteins, as they recognise a three-nucleotide code in the mRNA and carry the corresponding amino acid. Macromolecular machineries termed ribosomes represent a scaffold for this decoding event between tRNA and mRNA. They promote a precise translation process, and act as ribozymes as they facilitate the peptide-bond formation between amino acids (Steitz & Moore, 2003).

The enzymatic core of the ribosome, the peptidyl transferase centre (PTC), has been suggested to be the primordial part of the ribosome (Fox, 2010). Ribosomes must have existed in the last universal common ancestor (LUCA), as ribosomes across all domains of life share a common core, whereas the exposed exterior domains become increasingly diverse (Melnikov et al., 2012). By comparing ribosomal structures of organisms, with increasing organism complexity, the ribosome has been suggested to evolve via several phases of accretion: ancestral expansion segments (AES), tRNA-like mini-helices, attach to existing helices and domains, thus expanding ribosome function (Petrov et al., 2015). From an initial simple helix-formation to protect against degradation, the non-specific ribozyme function of the PTC was formed. Further increases in RNA structure not only stabilised the active centre, but expansion of the tunnel guiding and sheltering the created peptides facilitate the formation of longer oligopeptides. The oligopeptides formed in this manner can bind to the RNA, providing further protection against degradation. Concrete decoding employing tRNA and mRNA evolved only in the later phases of ribosome evolution.

1.1. The bacterial translation machinery

Ribosomes comprise both RNA and proteins and consist of two subunits, termed the large and the small subunit (LSU and 30S, respectively; Fig 1A). In *Escherichia coli*, the large subunit, also termed 50S, consists of two ribosomal RNAs (rRNAs), namely the 5S and the 23S rRNA, and 33 ribosomal proteins (L1-L36). The small subunit (30S) consists of the 16S rRNA and 21 ribosomal proteins (S1-S21; Fig. 1B). While 34 ribosomal proteins are universally conserved across eukarya, archaea and bacteria, 21 are unique bacterial proteins. For translation itself, most ribosomal proteins are expendable. However, they play an important role during the biogenesis, ensuring correct folding of the rRNA (Wilson & Nierhaus, 2005).

In the process of translation, the tRNAs traverse the ribosome through three distinct binding sites (Fig. 1C) (Schmeing & Ramakrishnan, 2009; Opron & Burton, 2018). This process is referred to as elongation and is always coupled to mRNA movement.

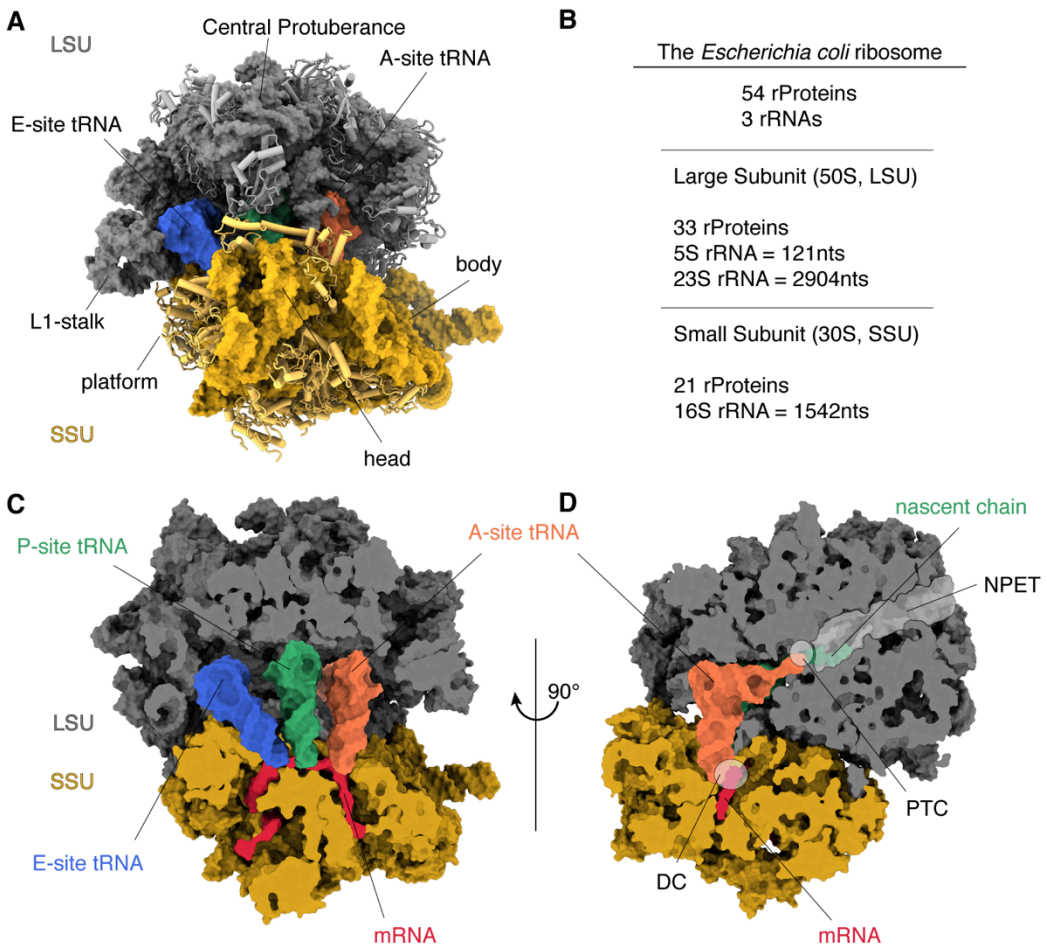

Figure 1: The bacterial ribosome. (A) Overview of the *Escherichia coli* ribosome: the large subunit (LSU) consists of 2 rRNA strands (grey surface) and 33 proteins (grey cartoon), whereas the small subunit (30S) has one rRNA strand (yellow surface) and 21 proteins (yellow cartoon). **(B)** Composition of the overall *E. coli* ribosome and the respective subunits. **(C)** Transverse section through the ribosome, exposing the three distinct tRNA binding sites of A-site (orange), P-site (green) and E-site (blue), as well as the mRNA **(D)** Transverse section through the ribosome showing the decoding centre (DC) between tRNA and mRNA at the A-site, the peptidyl transferase centre (PTC) and a short nascent polypeptide chain in the nascent peptide exit tunnel (NPET).

In the A-site, the mRNA nucleotide triplet determining the amino acid is decoded and an aminoacyl-tRNA with the respective amino acid can bind. The P-site holds the tRNA with the peptidyl-chain, and at the E-site deacetylated tRNAs exit the ribosome (Agrawal et al., 2000; Yusupov et al., 2001). While the decoding centre (DC) in situated in the small subunit (Fig. 1D), the enzymatic reaction is carried out in the PTC in the large subunit. Here, the polypeptide bound to the P-site tRNA is transferred to the A-site tRNA. The following translocation moves the A-site tRNA to the P-site, the now deacylated P-site tRNA to the E-site, and subsequently the E-site tRNA is ejected. Coupled movement of tRNA and mRNA leads to a new codon presenting itself in the A-site, and the cycle begins anew. The growing polypeptide is guided through the nascent peptide exit tunnel (NPET; Fig. 1D), which is approximately 100 Å in length (Nissen et al., 2000). Once the N-terminal end of the peptide reaches the exit, further processing proteins like chaperones or the signal recognition particle (SRP), facilitating membrane insertion, can interact with the nascent peptide (Deuerling et al., 2019). Elongation of the nascent peptide chain (NPC) continues until the ribosome encounters a stop-codon, which does not encode a respective tRNA. The peptide chain is released from the P-site tRNA to form a functional protein, and the ribosome can be recycled for a new round of translation.

1.2. Ribosome Biogenesis

Ribosomes exercise one of the core tasks within a living cell, and as such it is critical that accurate ribosome assembly is ensured. The subunits are assembled separately and only join for translation once they are matured. This complex process encompasses rRNA transcription, processing and modification of nucleotides, as well as r-protein translation, and finally joining of the rRNA and protein components. Some of these processes can take place simultaneously, and binding of r-proteins to the RNA proceeds in a hierarchical order. Furthermore, a multitude of biogenesis co-factors assist in the assembly and provide checkpoints during maturation.

Composition and expression of ribosomal RNA. *E. coli* possesses seven rRNA rrn operons (*rrnA, B, C, D, E, G, H*) encoding 16S, 23S and 5S rRNA (Ellwood & Nomura, 1982), as well as tRNAs encoded in the intergenic spacers (Fig 2A). The operons can be divided into two groups; group one type operons encode $tRNA^{Ala}$ and $tRNA^{Ile}$ between the 16S and 23S rRNA, whereas group two encodes $tRNA^{Glu}$ (Condon et al., 1995b). All seven operons are largely conserved in the rRNA, however, they differ mostly in their promoter regions and still show

around 2% variation within the rRNA sequence (Maeda et al., 2015). Divergence can be found outside the catalytic regions and at the solvent surface, which define protein interactions. Not all operons are equally transcribed under native conditions (Maeda et al., 2015). An upstream regulatory region (UP), containing two promoters, P1 and P2 (Young & Steitz, 1979)(Fig. 2A) is recognised by transcription activator Fis (Ross et al., 1990), and the global transcription repressor HN-S (Afflerbach et al., 1998). However, not all rRNA operons are regulated equivalently (Hillebrand et al., 2005). Possession of multiple rRNA operons is not only a means of backup in case of mutations, but has been proven to be crucial for adaptation to cold shock, starvation or other stress conditions (Condon et al., 1995a).

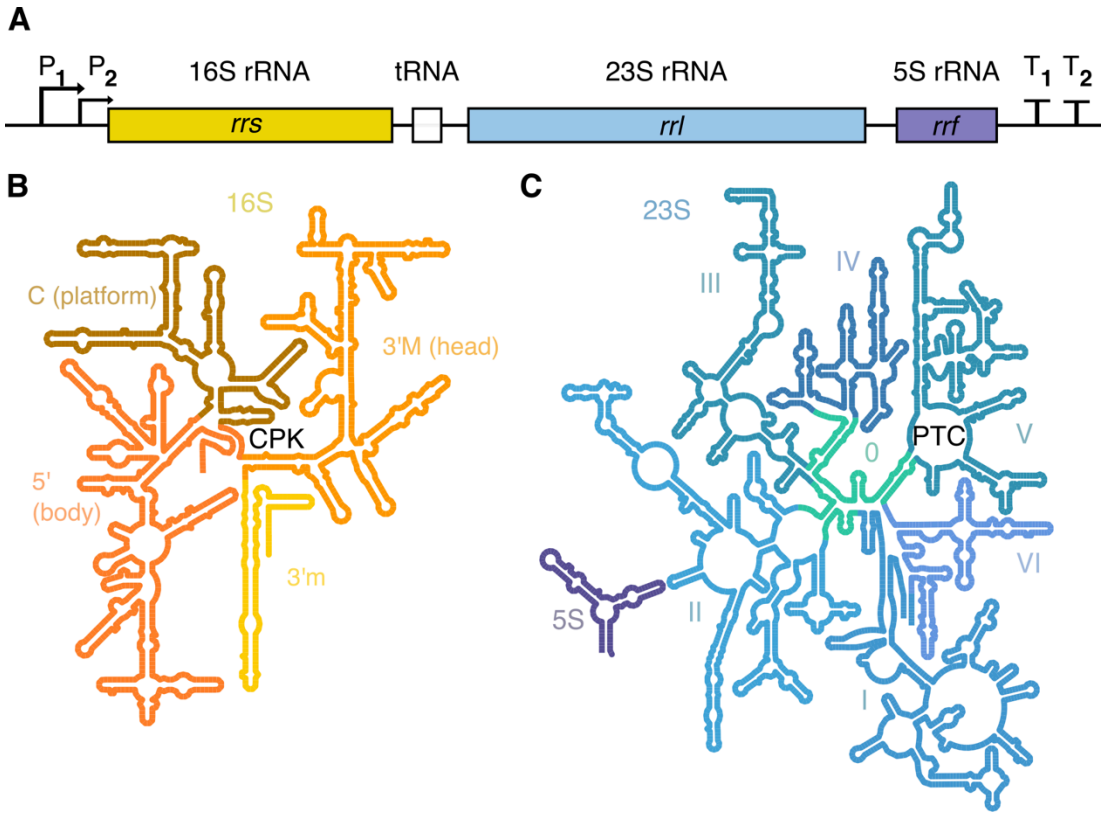

Figure 2: rRNA operon organisation and secondary structure. (A) A typical rRNA operon organisation, consisting of two preceding promoters (P_1, P_2), the gene coding for the 16S rRNA (*rrs*), one or two tRNA genes, followed by the 23S rRNA gene (*rrl*) and the 5S rRNA gene (*rrf*), and finally transcription two terminators (T_1, T_2). **(B)** The secondary structure of the 16S rRNA, with four distinct domains (5', central domain (C), 3' major (3'M) and the 3' minor (3'm)). The central pseudoknot (CPK) connects all domains. **(C)** The secondary structure of the 23S (blue) rRNA can be divided into 7 domains (0-IV), where domain 0 connects all domains. The peptidyl transferase centre (PTC) is located in domain V. 5S rRNA is depicted in purple. Secondary structure data as provided by (Petrov et al., 2013; Petrov et al., 2014).

Processing of rRNA. The operons are transcribed by the DNA dependent RNA polymerase (RNAP) as one transcript (Ginsburg & Steitz, 1975). A multitude of RNA polymerases are active on each operon, causing characteristic christmas-tree shaped Miller spreads due to different transcript lengths, as they proceed along the rDNA (French & Miller, 1989). With an

average transcription rate of 80-90nt/s (Dennis et al., 2009), transcription of one rRNA operon (~5 kbp) takes roughly one minute. *In vivo,* transcription by RNAP cannot be substituted by T7 polymerase at 37 °C, as it leads to translation-incompetent subunits (Lewicki et al., 1993). At lower temperatures, viability of T7 transcribed subunits is restored, further supporting the importance of transcription-coupled ribosome assembly (de Narvaez & Schaup, 1979). Although transcribed from one operon, the subunits are assembled separately. During on-going transcription is the primary transcript cleaved by RNase III, separating the 16S, 23S and 5S precursors with 3' and 5' overhangs (Dunn & Studier, 1973; Nikolaev et al., 1973; Szeberényi et al., 1984). Following, a multitude of RNases act together to mature the rRNA (Shajani et al., 2011; Sulthana & Deutscher, 2013; Bechhofer & Deutscher, 2019). RNase E further processes the 16S and 5S precursor from the 5' end (Szeberényi et al., 1984; Li et al., 1999b). In *E. coli,* 23S and 5S rRNA are cleaved at the 3' end by RNase T (Li & Deutscher, 1995; Li et al., 1999a). Finally, the remaining nucleotides at the 5' ends of these rRNA strands are removed exonucleolytically by RNase AM (Jain, 2020). In *Bacillus subtilis,* the RNase Mini-III recognises 23S dsRNA overhangs independent of prior RNase III cleavage, and substitutes RNase AM and T from *E. coli* (Redko & Condon, 2010). Additionally, processing of the 5S precursor in *B. subtilis* is carried out by a single enzyme, RNase M5, but is dispensable for functional 70S formation (Condon et al., 2001).

Modifications on the rRNA. Ribosomal RNA carries 36 modifications, mostly in the form of pseudouridylation, methylation at the 2'-OH of the ribose or methylation of the bases (Decatur & Fournier, 2002; Kaczanowska & Rydén-Aulin, 2007; Shajani et al., 2011). These modifications occur during ribosome assembly (Siibak & Remme, 2010), and possibly function as assembly checkpoints (Sergeeva et al., 2015). The majority of 16S modifications occur late in assembly, whereas the majority of 23S modifications are made early in assembly. 16S modifications are dispensable for an active 70S, albeit leading to less efficient translation (Krzyzosiak et al., 1987). *In vitro* reconstitution of functional 70S using T7 transcribed 16S rRNA without modifying enzymes present is possible (Shimojo et al., 2020). Seven modifications of the 23S have been proven vital (Green & Noller, 1996) and *in vitro* reconstitution still requires purification of matured 23S (Nikolay et al., 2018). Some modifications appear to be important for RNA integrity and assembly (Polikanov et al., 2015; Wang et al., 2020), like pseudouridylation of H69 in the 50S, which is important for peptide release by RF2 (Kipper et al., 2011). However, the exact functions of most modifications are still unknown (Sergeeva et al., 2015; Stojković et al., 2020) and strains deficient in methylation or pseudouridylation are still viable (O'Connor et al., 2018; Pletnev et al., 2020).

Some modifications are optional for normal function and can be used as a means of antibiotic resistance through steric hindrance of binding (Maravić, 2004; Kehrenberg et al., 2005).

Ribosomal proteins. The majority of ribosomal proteins are encoded in the *str-S10-spc-α* gene region (Jaskunas et al., 1977; Cerretti et al., 1983), which can be divided into four operons. The residual proteins are scattered across the genome in operons encoding at least one further protein, which are either other ribosomal proteins or other essential proteins like translation factors or the β-subunit of RNAP (Zengel & Lindahl, 1994). To avoid wasting resources on expression of unnecessary ribosomal proteins, expression should occur stoichiometrically to rRNA synthesis. This is achieved by negative autogenous regulation of r-protein operons: select unincorporated r-proteins can bind to their own mRNA, and in this way obstruct translation (Zengel & Lindahl, 1994; Aseev et al., 2016). Lack of r-proteins, which are important during early assembly points, causes accumulation of intermediates and an abundance of late binding proteins, subsequently leading to repression of tertiary binding proteins (Sykes et al., 2010).

Incorporation of r-proteins. Ribosome assembly occurs co-transcriptionally, i.e. r-proteins are recruited while transcription is still in process (de Narvaez & Schaup, 1979; Rodgers & Woodson, 2019). On one hand is the construction of a ribosomal subunit a hierarchical process, meaning binding of certain proteins relies on prior binding of early step binding proteins. Nonetheless, these hierarchical strings are only partially dependent on one another, and many roads lead to ribosome as parallel assembly pathways exist (Gupta & Culver, 2014; Davis & Williamson, 2017). The first assembly maps were postulated by Nomura (Mizushima & Nomura, 1970) and Nierhaus (Herold & Nierhaus, 1987) for the 30S and 50S, respectively, after *in vitro* reconstitution experiments: primary r-proteins are proteins binding to the rRNA early in assembly, thus initiating assembly, and give a platform for other proteins down the pathway (secondary/mid and tertiary/late proteins) (Shajani et al., 2011). For the 30S, uS7, uS15 and uS4 have been identified as initiator proteins for the 5', central and 3' domain, respectively. For the 50S, uL3, uL4, bL20 and uL24 are crucial for assembly initiation, out of which only uL3 binds in the 3' end and the others the 5' end of the 23S. The postulated original assembly maps still stand today, with few minor corrections; *in vitro* reconstitutions often lack the co-transcriptional assembly, and to overcome resulting kinetic traps of unusual secondary folding, non-physiological magnesium concentrations, long incubation times or heat activation are necessary (Nierhaus, 1991). *In vivo* observations, made possible by innovations and advancements such as in the cryo-EM field in recent years (Razi et al., 2017), led to revisions of the assembly maps. Intermediate assembly stages resulting from r-protein

deletions could be visualised and revealed that ribosome assembly is not strictly hierarchical but has parallel pathways (Mulder et al., 2010; Leong et al., 2013; Davis et al., 2016). In the absence of early assembly proteins, particles can get stuck in kinetic traps, which, however, can be overcome after addition of missing proteins, similar to *in vitro* reconstitutions. Additionally, it has been shown that some initiator proteins like uS4 and uS7 bind transiently to help initial binding of downstream proteins and only become stably incorporated at a later stage (Duss et al., 2019; Rodgers & Woodson, 2019).

Assembly of the 30S occurs in a transcription-coupled 5' – 3' direction (Duss et al., 2018). The body (Fig. 2B) is matured first (Dutca & Culver, 2008), then the platform, and the 3' domain, consisting of the head and h44, is formed last (Davis & Williamson, 2017). As a result, maturation of each domain is independent of the other domains, and if one domain cannot be matured, the remaining ones will still fold correctly (Razi et al., 2019). The central pseudo knot (CPK) connects all domains, and if correct maturation is disrupted here, translation becomes inhibited (Brink et al., 1993).

Maturation of the 50S, however, is more complex as a multitude of inter-domain interactions within the 23S occur, and maturation is dependent on these interactions. Depletion of bL17 provided further evidence of parallel assembly pathways present also in the 50S (Davis et al., 2016). While for 30S maturation, four building blocks have been identified, for the 50S six have been found (Davis & Williamson, 2017). The solvent face of the ribosome, consisting of domains I, IV and parts of domain II and III (Fig. 2C), is formed first. Many assembly intermediates present a lack of the central protuberance, yet it has been determined to mature in the second step already. In a third step, the subunit interface is advanced. Domain V, and the PTC within it, is matured only in the 4th building block, so rather late and in contrast to evolutionary development. Block five includes flexible structures, like the uL1 stalk and H68-H71. Block six comprises further subunit interface regions.

Ribosomal assembly co-factors. To aid in the complex process of biogenesis, a host of transiently interacting assembly co-factors come into play: DEAD-box proteins, chaperones and GTPases (Wilson & Nierhaus, 2007; Britton, 2009; Shajani et al., 2011). DEAD box proteins are RNA-dependent ATPases with helicase activity, and assist mostly in 50S assembly. Strains depleted in these proteins, like CsdA or SrmB, show either cold or heat sensitive phenotypes combined with disturbed ribosome profiles, but are generally dispensable for assembly at 37 °C (Shajani et al., 2011; Redder et al., 2015).

Deletion of RNA chaperones is not lethal, however, lack of some proteins like RimM leads to an accumulation of immature 30S subunits with an unprocessed h44 (Leong et al., 2013).

These particles can can mature into functional 30S after an increased incubation time (Thurlow et al., 2016). Similarly, RbfA (Ribosome binding factor A) is a coldshock protein, which acts late in 16S maturation. At 37 °C, Δ*rbfA* cells show only a mild inhibition of growth and an accumulation of immature 30S, however, at lower temperatures the phenotype becomes more severe (Dammel & Noller, 1995; Xia et al., 2003). The conserved RNA chaperone Hfq, which has been known as translational regulator by guiding sRNA to its counterpart mRNA, was also identified as a ribosome biogenesis factor (Andrade et al., 2018). By contrast, most ribosome assembly associated GTPases are essential and conserved across the domains (Britton, 2009). For instance, the GTPase Era (*E. coli* ras-like) is responsible for folding of h23 and h24 in the 30S platform (Razi et al., 2019). For 30S *in vitro* reconstitution addition of Era alone is sufficient to achieve assembly under physiological conditions (Tamaru et al., 2018). Another GTPase essential for 30S maturation is YqeH. In contrast to other assembly co-factors, no immature 30S particles accumulate in the absence YqeH since the 16S precursor becomes degraded (Loh et al., 2007). The exact function of this GTPase is yet to be discovered. In 50S assembly, a greater number of essential GTPases participate. Der (double Era like GTPase in *E. coli*; YphC in *B. subtilis*) is conserved in all eubacteria (Hwang & Inouye, 2006; Schaefer et al., 2006) and is essential for CP maturation (Ni et al., 2016). Similarly, deletion of the essential GTPases YsxC and RbgA (Ribosome Biogenesis GTPase A; formerly YlqF) in *B. subtilis* (but not *E. coli*) leads to accumulation of 50S precursor particles, sedimenting at 44.5S and 45S, respectively (Schaefer et al., 2006; Uicker et al., 2006). The three GTPases appear to function during late stage assembly (Matsuo et al., 2006; Schaefer et al., 2006), and precursor particles all lack uL16, bL28, bL35 and bL36, and to a lesser extent bL27 and bL33 (Uicker et al., 2006; Ni et al., 2016). Each of the GTPases can bind to the precursor particle of the other GTPases (Ni et al., 2016), but the order or whether they bind simultaneously remains to be determined.

RbgA is a widely conserved biogenesis co-factor, and its yeast homologue Lsg1 targets late assembly 60S precursors at the subunit interface (Ma et al., 2017; Malyutin et al., 2017). Likewise, the mitochondrial homologue Mtg1 aids in intersubunit bridge formation (Kim & Barrientos, 2018; Jaskolowski et al., 2020). RbgA belongs to the family of circular permutated GTPases (cpGTPases), meaning that the G-domain motives G1-G5 have changed order and are now in the G4-G5-G1-G2-G3 order (Anand et al., 2006), and requires potassium for GTPase activity (Achila et al., 2012). Solving the crystal structure of RbgA (Kim et al., 2008) allowed the identification of a structurally conserved ANTAR (AmiR–NasR Transcription Anti-termination Regulator) RNA interacting motif in the C-terminal domain

(Gulati et al., 2013). The N-terminal domain comprises the G-domain and, in addition to G1-G5, conserved regions CR1-3 (Gulati et al., 2013). G3 holds the switch II motif, which normally contains the catalytically active histidine residue. In RbgA, however, it is connected with the CR3 and forms a loop, linking the G- and ANTAR domain and possible conveying secondary structure rearrangements upon GTP hydrolysis. Furthermore, the catalytically active histidine His9 (His84 in EF-Tu; His92 in EF-G) is in fact found in CR1, explaining why deletion of ten N-terminal residues results in a loss of function (Matsuo et al., 2007). RbgA GTPase activity is stimulated by binding to the ribosome, and addition of GDPNP leads to stable interaction with the mature 50S (Matsuo et al., 2006; Achila et al., 2012). Mutations in uL6 at the H97 interaction site partially relieve the growth defect caused by absence of RbgA (Gulati et al., 2014). Together with cryo-EM studies of immature $45S_{RbgA}$ particles, which showed lack of the CP (Li et al., 2013; Jomaa et al., 2014), this gave a first indication of RbgA function: stabilisation of H97 to facilitate uL16 and further protein binding to stabilise the CP. A recent cryo-EM structure of $45S_{RbgA}$ bound to RbgA showed stabilisation of uL6, and also H91-93 in the A and P site (Seffouh et al., 2019). The ANTAR domain interacts with H62 and H4, while the G-domain occupies the space H69 and H71 would reside in in a mature 50S particle. The catalytic H9 is still 8 Å away from the γ-phosphate, indicating that GTP hydrolysis could not have been triggered in this conformation. Possibly, further conformational changes occur when the 50S is matured, ultimately permitting GTP hydrolysis and dissociation of RbgA.

1.3. The Prokaryotic Translation Cycle

After completing the maturation process, the ribosome is ready to continue to the translation cycle. It consists of four phases: initiation, elongation, termination and recycling (Fig. 3). Like for assembly, each phase of the translation cycle is guided by co-factors as well. For initiation of the bacterial translation cycle, three initiation factors IF1-3 are necessary. They recruit the initiator fMet-$tRNA^{fMet}$ to the P-site and ensure correct positioning of the start-codon and interaction between the two. In *E. coli*, AUG is the most abundant start codon with ~83%, followed by GUG (~14%) and UUG (~3%) (Rocha et al., 1999). These class I start codons are favoured by IF3, whereas class II codons (<1%) are discriminated against, and lead to poor expression levels of the downstream gene (Sussman et al., 1996). Notably, *infC*, the gene encoding for IF3, utilizes AUU, one of five class II start codons, and thus convey an autoregulatory mechanism of IF3.

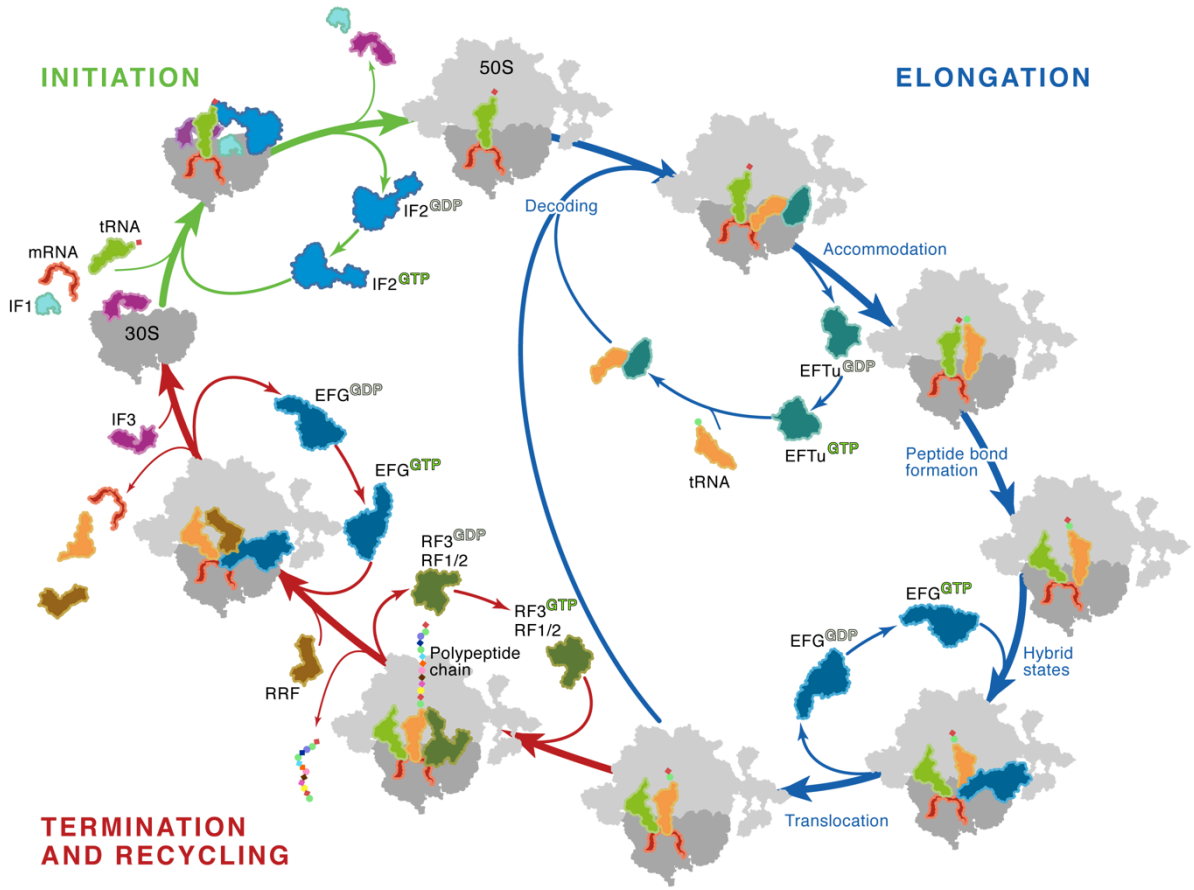

Figure 3: The bacterial translation cycle. A translation cycle starts with the initiation (left upper corner; green arrows), when mRNA and initiation factors associate with the 30S and recruit the initiator tRNA. After accommodation of the tRNA, the 50S can bind to the 30S to progress from an initiation to an elongation complex (right side; blue arrows). EF-Tu delivers charged tRNA to decode the codon presenting in the A-site. After peptide-bond formation, the tRNAs adopt a hybrid state, and translocation is facilitated by EF-G. The ribosome continues in the elongation cycle until a stop codon presents itself in the A-site, which entails termination (left bottom corner; red arrows). RF1 or RF2 bind the stop codon and release the produced peptide from the P-site tRNA. Subsequently, RRF and EF-G bind and disassemble the 70S into 30S and 50S. A new translation cycle can begin. Figure on the basis of (Sohmen et al., 2009).

Following the initiation, elongation factors (EF) Tu and G deliver the successive tRNAs to the ribosome and aid in the translocation of the tRNAs, respectively. Once a stop-codon presents itself in the A-site, the elongation cycle ends and the ribosome enters the process of translation termination. During regular translation termination, class I release factors (RF) recognise the stop-codon and subsequently mediate release of the finished polypeptide. There are three stop codons most commonly used in bacteria: UAA, UAG and UGA, also known as ochre, amber and opal, respectively. Conversely to the start codon, stop codon usage is correlated to the genomic GC content, with UAA being favoured by low-GC and UGA by high GC content bacteria (Rocha et al., 1999; Povolotskaya et al., 2012). Accordingly, in *E. coli* UAA makes up 63% of all stop codons, followed by UGA with 29%. UAG represents merely 8% of all stop codons and has, in a minority of archaea and bacteria, even been remodelled to code for a novel amino acid, pyrrolysine (Ambrogelly et al., 2007; Tharp et al.,

2018). As such, the amber stop codon has been alienated and exploited to encode non-standard or non-canonical amino acids in both bacteria and eukaryotes (Wang, 2017; Kato, 2019). This has opened the field to practical applications, such as fluorescent tagging of target proteins, stabilising proteins and interactions for subsequent structure analysis by native cross-linking, or improving recombinant expression of eukaryotic proteins in *E. coli* by encoding eukaryotic specific post-translational modifications (Liu & Schultz, 2010).

After translation termination, EF-G, in interplay with the ribosome recycling factor (RRF), split the 70S ribosome into its subunits, and IF3 disengages the remaining tRNA and mRNA from the 30S. A new translation cycle can then commence.

Like ribosome assembly, translation takes place co-transcriptionally in bacteria. This is partly facilitated by interaction between a ribosome and RNAP, either by direct 30S and RNAP interaction (Kohler et al., 2017) or indirect via uS10 and NusG, which binds to RNAP (Burmann et al., 2010). This complex of ribosome and RNAP has been named *expressome.* Analysis of cryo Electron Tomography (cryo-ET) of *Mycoplasma pneumoniae* cells estimates that 2.8% of all ribosomes reside within an expressome and shows NusA forming a bridge between RNAP and 30S (O'Reilly et al., 2020). It has been suggested that interaction between the ribosome and RNAP decreases drop-off rates of RNAP and ensures transcription of the entire reading frame (Conn et al., 2019). However, this interaction has been challenged to occur only stochastically (Chen & Fredrick, 2020), for instance when RNAP is transcribing slowly and the ribosomes reach the end of the transcript.

Translation speed in bacteria generally ranges from 4-20 amino acids per second (Sørensen & Pedersen, 1991; Proshkin et al., 2010; Zhu et al., 2016). Translation velocity is impacted by the encoded gene, either through rare codon usage or positively charged amino acids like arginine or lysine, which can interact with the ribosomal exit tunnel (Lu & Deutsch, 2008; Dimitrova et al., 2009; Requião et al., 2016). Occasionally the ribosome can encounter amino acid sequences, which form secondary structures within the tunnel and lead to ribosome stalling (Sohmen et al., 2015; Su et al., 2017). For the specific poly-proline staller sequence PPP, elongation factor P (EF-P) can rescue translation by stabilising the P-site tRNA to allow peptide bond formation and ribosomes to resume elongation (Ude et al., 2013; Huter et al., 2017a).

1.3.1. Initiation

Translation initiation describes the process of recruitment of mRNA and the fMet-tRNA^{fMet} to the 30S. It marks the assembly of a 30S initiation complex (30SIC), which progresses to a 70SIC and ultimately forms an elongation competent complex.

At a last maturation checkpoint, the ribosome biogenesis factor RbfA can be displaced from mature 30S subunits by IF3, predominantly in the stationary phase and under starvation conditions (Sharma & Woodson, 2020). Release does not take place from immature 30S particles, ensuring only functional particle proceed to the translation cycle. IF3 binds in the E–site of the 30S with its C-terminal domain (CTD), and upon initial binding probes the P-site for mRNA with its N-terminal domain (NTD) (Hussain et al., 2016) (Fig. 4A), to safeguard correct positioning of the start codon in the P-site (La Teana et al., 1995). Joining of the mRNA is independent of initiation factor or tRNA binding (Milon & Rodnina, 2012). A rotation and upward movement of the head opens the mRNA channel, possibly to facilitating mRNA binding and positioning (Hussain et al., 2016). Subsequent positioning of the start codon in the P-site is assisted by helix formation between the Shine-Dalgarno contained in the mRNA and anti-Shine-Dalgarno sequence in the 3' of the 16S rRNA (Shine & Dalgarno, 1974). Initiation can occur at correct sites in the absence of the anti-SD, albeit significantly less efficiently (Sussman et al., 1996; Saito et al., 2020).

IF2 is a GTPase and comprises a G-domain within its N-terminal domain (NTD) and recruits formlyated initiator fMet-tRNA^{fMet} to the P-site with domain IV in its CTD (Milon et al., 2010). fMet-tRNA^{fMet} is not only discernible by IF2 because of the formyl modification, but also due to an exceptionally GC-rich anticodon stem (Roy et al., 2018). *In vitro*, binding of IF3 and IF2 occur independently of one another and without hierarchical restrictions (Milon & Rodnina, 2012). The last and smallest factor, IF1, only joins after IF2 or IF3 binding. It binds in the A-site (Fig. 4B) and stabilises IF2 and increases initiation fidelity (Hartz et al., 1989; Antoun et al., 2006; Milon & Rodnina, 2012).

After fMet-tRNA^{fMet} recruitment, IF3 samples correct codon–anticodon interaction (Meinnel et al., 1999). It undergoes conformational changes throughout the initiation complex formation in order to fulfil multiple functions (Hussain et al., 2016) (Fig. 4A-C). The NTD moves upon tRNA binding to interact with the tRNA elbow (Fig. 4B). Once the codon-anticodon pairing is stable, the complex progresses from the 30SPIC (pre-initiation complex) to the 30SIC. Accommodation of the tRNA leads to conformational changes and displacement of the IF3 CTD (Fig. 4C), weakening IF3 binding to the 30S (Hussain et al., 2016).

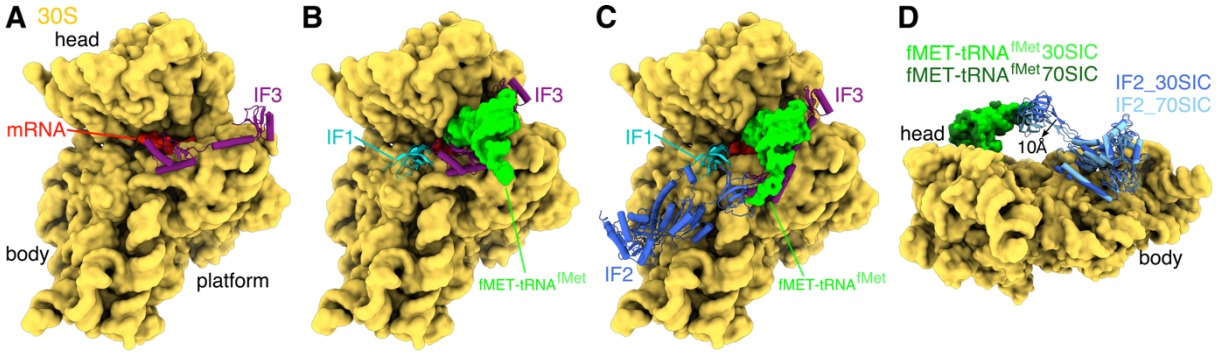

Figure 4: The translation initiation process in bacteria. (A-C) View onto the 30S (yellow) subunit interface. **(A)** The CTD of IF3 (purple) interacts with the mRNA (red) in the P-site and ensures correct positioning of the start codon. **(B)** IF1 (cyan) binds in the A-site. Upon tRNA (limegreen) binding, the NTD of IF3 moves substantially to interact with the elbow region of the tRNA. **(C)** IF2 (blue) binds on the body, close to the A-site and recognises the fMet with its CTD. Correct codon–anticodon interaction disengages the CTD of IF3. **(D)** Transitioning from the 30SIC to the 70SIC, domain IV of IF2 moves 10 Å (blue vs. light blue) and slight movement in the tRNA (green vs. dark green) can be observed. Figures (A-C) based on PDBs from Hussain et al., 2016, and (D) on Kaledhonkar et al., 2019.

Subsequent dissociation of IF3 allows 50S subunit joining for 70SIC formation. IF1 dissociates early during SU joining and allows formation of the critical B2a intersubunit bridge (Kaledhonkar et al., 2019). fMet-tRNA^{fMet} adopts different conformations throughout the initiation complex formation, and upon 50S binding, the elbow moves 11 Å to switch from interactions with uL1 to interactions with the CP (Sprink et al., 2016). The IF2 CTD moves 10 Å to enable accommodation of the 50S (Fig. 4D). Through subunit joining, IF2 comes in contact with the Sarcin-Ricin-Loop (SRL) in the 23S rRNA and the GTPase-associated centre (GAC) including bL12, which triggers GTP hydrolysis (Qin et al., 2009). Subsequent conformational changes and P_i release lead to IF2 dissociation and allow the initiator tRNA to accommodate from the P/I to the P/P state. The 70S elongation complex (70SEC) is thus formed (Kaledhonkar et al., 2019).

1.3.2. Elongation

After IF1 and IF2 release from the 70S initiation complex, the A-site becomes available for a new tRNA. Divergent to the initiator tRNA being recruited by already bound IF2 (Milon et al., 2010), during the elongation phase the aminoacylated tRNA is delivered to the ribosome in a tertiary complex with the EF-Tu (elongation factor thermo-unstable) and GTP, or in a quaternary complex including the EF-Tu guanine exchange factor (GEF) EF-Ts (Burnett et al., 2014). Recruitment of the EF-Tu–tRNA complex is facilitated by the bL12 stalk (Dey et al., 1995; Savelsbergh et al., 2000b; Kothe et al., 2004; Diaconu et al., 2005; Helgstrand et al., 2007). The majority of EF-Tu co-localizes with ribosomes as shown by single molecule fluorescent microscopy (Mustafi & Weisshaar, 2018). Upon binding of the ternary complex,

the A-site is sampled by the tRNA. The delivered tRNA anti-codon can either be cognate (all three bases match), near-cognate (one base does not match) or non-cognate (only one or no bases match). Incorporation of the amino acid corresponding to the codon is critical for correct protein composition. Accordingly, several checkpoints are applied during decoding: the first safety measure for a continuous elongation cycle is the discrimination against deacylated tRNA by EF-Tu. EF-Tu forms several hydrogen bonds with the 3'-aminoacyl bond through residues in its domain II, which accommodates the CCA-end (Nissen et al., 1996). Once EF-Tu delivers a charged tRNA to the ribosome two further checkpoints have to be passed, which are initial selection and proofreading (Ieong et al., 2016). The initial selection discriminates between non- and near-/cognate tRNAs, and non-cognate are quickly rejected (Rodnina et al., 2017; Kavaliauskas et al., 2018). Already in this step, the ratio of selection of a near-cognate versus a cognate tRNA is 1:6, and proofreading increases specificity again, permitting only one in 24 (Blanchard et al., 2004). After accommodation of the correct tRNA, the growing peptide chain is transferred from the P-site tRNA to the A-site tRNA and thus the nascent peptide chain elongated by one amino acid. Following peptide bond formation, EF-G binds to the ribosome to accelerate translocation of the tRNAs from the A- and P- to the P- and E-site, respectively (Ling & Ermolenko, 2016; Noller et al., 2017). While E-site tRNA dissociates, only the P-site tRNA remains and the A-site is unoccupied. It can be sampled for a new round of decoding.

Decoding. When EF-Tu delivers a tRNA to the A-site, the tRNA adopts an A/T-state; its anti-codon stem-loop (ASL) is placed in the A-site to interact with the mRNA, whereas the acceptor stem is tilted and interacting with EF-Tu. The decoding centre in the 16S rRNA, comprising G530, A1492 and A1493, monitors base-pairing between the anticodon of the tRNA and the codon in the mRNA (Ogle et al., 2001; Loveland et al., 2020). If no interactions develop, near- or non-cognate tRNAs are discarded in the initial screening and the ternary complex dissociates (Morse et al., 2020). This process repeats until a cognate tRNA is delivered, and base-pairing between mRNA and tRNA takes place. A1493 interacts with the minor groove of the codon-anticodon helix to screen base-pairing of the first nucleotide in the triplet (Loveland et al., 2017). G530 flips into an anti-position and first stabilises the backbone of the helix at the second nucleotide. This omits screening of the third base-pair, thus permitting wobble base-pairing. In case of cognate and near-cognate tRNAs, G530 shifts deeper into the tRNA-mRNA helix, A1492 flips out and establishes hydrogen bonds with G530. This brings the shoulder (G530) and body (A1492) into closer contact, and the 30S

accommodates a closed conformation (Ogle et al., 2002; Schmeing et al., 2009). This shift in the shoulder causes the GTPase domain of EF-Tu to dock onto the SRL, which triggers GTP hydrolysis (Loveland et al., 2017; Loveland et al., 2020). Docking to the SRL is essential for GTP hydrolysis, as mutation of the SRL has adverse effects on accommodation and EF-Tu release (Hausner et al., 1987; Bilgin & Ehrenberg, 1994; Blanchard et al., 2004; García-Ortega et al., 2010). Hydrolysis inducing domain closure occurs significantly faster for cognate than for near-cognate, and not at all for non-cognate tRNAs (Pape et al., 1999; Blanchard et al., 2004; Morse et al., 2020).

Upon GTP hydrolysis, switch I in domain I of EF-Tu undergoes substantial conformational changes. Switch I transforms from an α-helical structure to a β-sheet, guiding the CCA-end away from EF-Tu (Girodat et al., 2020). Consequently, switch I no longer interacts with the tRNA, and can adopt a conformation incompatible with tRNA interaction. Additionally, domain I rotates by 90° away from domain II, as shown by recent cryo-EM data (Loveland et al., 2020). Destabilisation of domain I leads to the release of the CCA-end of the tRNA from domain II, prompting accommodation of the A/T-tRNA. Domain III is the last to dissociate from the ribosome during the process of accommodation, indicating that an EF-Tu independent proof-reading step takes place (Loveland et al., 2020). This is consistent with smFRET data showing that EF-Tu dissociates before the tRNA is fully accommodated in the PTC (Morse et al., 2020). The A-site tRNA has to move through an accommodation corridor to position its CCA end in the PTC. However, the corridor does not allow free movement and is occluded by 23S rRNA (Whitford et al., 2010; Loveland et al., 2020). Therefore, to enable movement, the accommodation of the tRNA elbow takes place first, and in combination with minor rotation of the 30S allows the acceptor stem to bypass the obstacles (Loveland et al., 2020; Morse et al., 2020). Consequently, EF-Tu dissociation is delayed when accommodation of the elbow is obstructed (Morse et al., 2020). Interestingly, if accommodation into the PTC is blocked by antibiotics, or because a near-cognate tRNA fails the last steps of proofreading, EF-Tu can repeatedly bind and form a ternary complex on the ribosome to retrieve tRNAs (Morse et al., 2020).

EF-Tu dissociates in a GDP-conformation from the ribosome and relies on EF-Ts (Elongation factor thermo-stable) as a GEF to be recharged with GTP (Gromadski et al., 2002; Thirup et al., 2015). Accommodation of the A-site tRNA on the ribosome permits the next step: transfer of the P-site tRNA peptide chain to the A-site.

Peptide bond formation. Stable accommodation of the tRNAs is ensured via interactions with the 23S rRNA located at the PTC. G2251 in the P-loop and G2553 in the A-loop base-pairing with the C75 of the P- and A-site tRNAs, respectively (Samaha et al., 1995; Kim & Green, 1999). Once the new tRNA has fully accommodated in the A-site, and the aminoacylated CAA-end localises to the PTC, peptide bond formation can take place. The accommodation of A-site tRNA leads to conformational changes of the ribosomal RNA in the PTC. Nucleotides U2585 and A2505 move to an induced state, and position the P-site tRNA for the following peptide bond formation (Schmeing et al., 2005b). Failure to accommodate the A-site accurately leaves the nucleotides in an uninduced state, simultaneously preventing peptide bond formation and protecting the peptidyl tRNA from spontaneous hydrolysis.

The α-amine of the A-site amino acid catalyses a nucleophilic attack on the carbonyl carbon of the P-site amino acid (Fig. 5A), consequently breaking the ester bond between the amino acid and A76 of the P-site tRNA and attaching the carbonyl carbon to the α-amine of the A-site; therefore, the growing peptide chain is transferred to the A-site and leaves the P-site deacetylated (Fig. 5B). As the 3'-O of the P-site tRNA is too far away from the attacking α-amine, a direct proton transfer is not possible. The precise mechanism of proton transfer is yet to be determined; nevertheless, some important components have been identified (Fig. 5C). The 2'-OH of the P-site tRNA A76 is crucial for peptide bond formation, as substitution of the oxygen with hydrogen or fluorine substantially stunts the reaction (Weinger et al., 2004; Zaher et al., 2011). Structure analysis showed hydrogen bonding between the attacking α-amine and 2'-OH (Schmeing et al., 2005a; Polikanov et al., 2014). Additionally, the 2'-OH group of A2541 of it is crucial for peptide bond formation (Erlacher et al., 2006; Lang et al., 2008). Accordingly, mutation of the nucleobase at this position does not affect peptide bond formation, which long concealed the function of its contribution. During peptide bond formation, a concerted movement of protons takes place and a tetrahedral intermediate is formed (Fig. 5C). However, the exact process is still unknown, and two mechanisms have been proposed: the proton-wire and a proton-shuttle (Fig. 5D, E). The proton wire suggests that the proton movement starts at the N-terminal end of bL27, which is about 10 Å from the attacking α-amino group (Polikanov et al., 2014). Deprotonation of this N-terminus, in combination with the negative charge of the phosphate backbone of A76 in the A-site, exercises attraction on the protons of a water molecule (W1) in their proximity (Fig. 5D). This water forms a proton-wire with the 2'-OH of both the P-site A76 and A2451, inducing deprotonation of the attacking α-amine. While a second water molecule (W2) stabilises the temporarily negatively charged tetrahedral intermediate at the carbonyl oxygen, another water

molecule (W3) (Fig. 5D) assists in protonation of the 3'-O of the P-site tRNA, and finally facilitating transfer of the peptidyl chain onto the A-site tRNA. In the eight-membered proton-shuttle mechanism (Fig. 5E), on the other hand, only W3 contributes to the peptide bond formation (Schmeing et al., 2005a; Wallin & Aqvist, 2010). Calculation of activation energies, consistent with biochemical experiments, have suggested the proton shuttle could be supported by an additional magnesium (Świderek et al., 2015), or an additional water leading to a ten-membered proton shuttle (Kazemi et al., 2018).

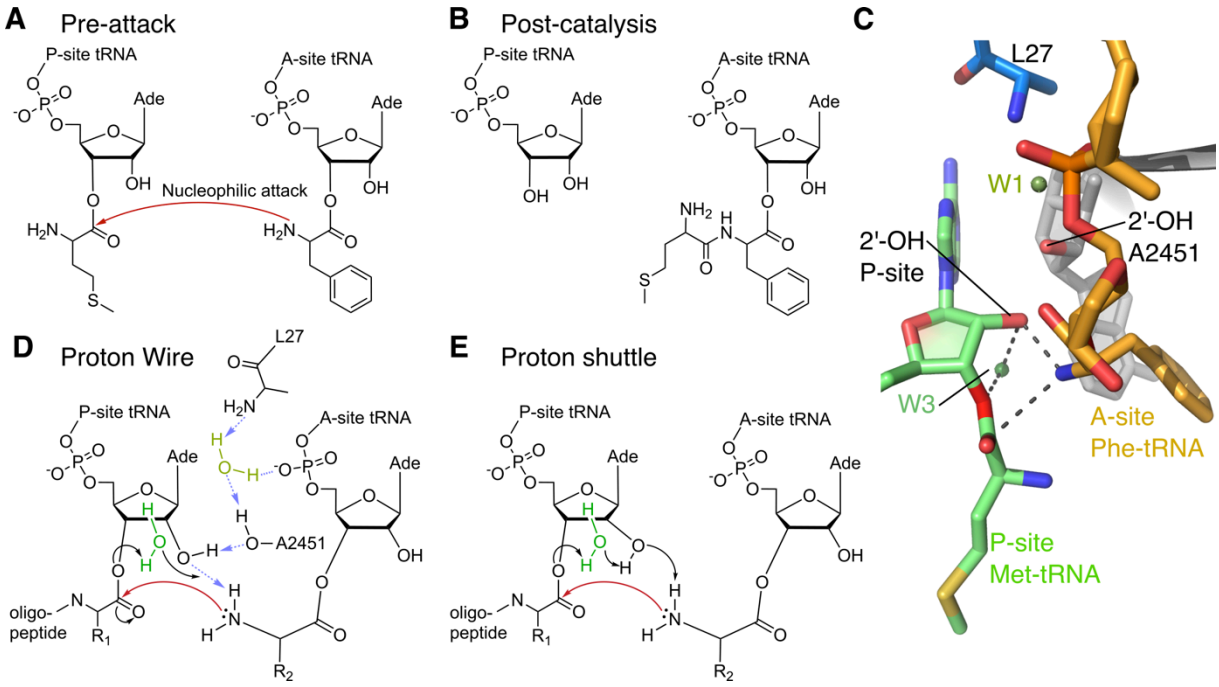

Figure 5: Structural analysis of peptide bond formation. (A, B, D, E) Chemical 2D structures of the peptide bond formation process **(A)** Peptide bond formation is initiated via a nucleophilic attack of the A-site tRNA α-amine on the P-site carbonyl carbon **(B)** After successful reaction, the methionine is transferred to the A-site, and the P-site tRNA is deacylated. **(C)** 3D crystal structure (based on PDB 1VYA from Polikanov et al., 2014) of a pre-attack complex: both proton shuttle and proton wire rely on a water molecule (W3) aiding in the proton transfer. A tetrahedral intermediate (presented by dashes) is formed during the attack of the A-site tRNA (orange) α-amine on the P-site (lime). **(C, D)** In the proton wire mechanism, another water molecule (W1, olive green) is coordinated by bL27 and the 2'OH of A2451. **(D)** The proton wire (blue arrows) suggests the N-terminus of bL27 and the phosphate backbone of A76 of the P-site tRNA promote a partially negatively charged water molecule W1 (olive). After nucleophilic attack, the proton is guided back via W3 (green) and 2'-OH to W1. **(E)** The proton shuttle suggests a similar path, however the proton is transferred back to the attacking amine.

The role of bL27 in the peptide bond formation is still controversial; some researchers have determined it dispensable for peptide bond formation, consistent with the proton shuttle mechanism (Maracci et al., 2015), while others found the absence of it to have an adverse effect, albeit a limited one (Wower et al., 1998; Maguire et al., 2005; Trobro & Aqvist, 2008; Voorhees et al., 2009).

Further research is required to determine if either one of these mechanisms is accurate, as neither one is fully consistent with the existing literature. Additionally, neither proposed

mechanism resolves the question of initial deprotonation of the A-site NH_3^+, which is necessary for the nucleophilic attack. Conceivably, the precise mechanism can only be elucidated if this crucial step is taken into account.

Translocation. After transfer of the peptidyl-moiety to the A-site tRNA, the deacetylated P-site tRNA enhances formation of tRNA hybrid states (Moazed & Noller, 1989; Julián et al., 2008). The deacetylated P-site tRNA adopts a P/E hybrid state, in which the ASL stays stably bound to the mRNA codon in the P-site, whereas the CCA-end on the large subunit tilts towards the E-site. The uL1 stalk adopts a closed conformation to interact with the P/E-tRNA and stabilises the hybrid state (Munro et al., 2007). Likewise, the A-site tRNA adopts an A/P hybrid state. The majority of this initial shift in the tRNAs is coupled (Munro et al., 2007), and leads to an unlocking of the 70S ribosome, meaning movement of the large and the small subunit are no longer coupled to one another (Valle et al., 2003). The 30S body and platform rotate 7° counter clockwise (CCW) relative to the 50S, from a classical non-rotated to a rotated hybrid state (Frank & Agrawal, 2000; Ratje et al., 2010). Like the tRNA hybrid state, subunit rotation is essential for translocation (Horan & Noller, 2007). This movement occurs spontaneously and is also described to be ratchet-like as the ribosome repeatedly rotates back and forth. This rotation facilitates binding of EF-G, which has a high affinity to the rotated state. Binding of EF-G both promotes and stabilises the small subunit in the rotated state (Spiegel et al., 2007; Cornish et al., 2008; Belardinelli et al., 2016). Translocation can occur in the absence of EF-G, however, it proceeds up to 100 times slower (Bergemann & Nierhaus, 1983; Katunin et al., 2002; Munro et al., 2010). EF-G is suggested to couple tRNA and mRNA movement (Zhou et al., 2019), as translocation in its absence is more prone to frame shifting (Peng et al., 2019). Additionally, EF-G can facilitate sliding along stretches of noncoding mRNA using multiple rounds of GTP-hydrolysis (Klimova et al., 2019). Aside from translocation, EF-G is also necessary for ribosome splitting at the end of the translation cycle.

EF-G establishes multiple interactions with the ribosome upon binding (Fig. 6A). Domain I (G-domain) contacts the GAC, involving bL12 as well as the SRL (Helgstrand et al., 2007; Pulk & Cate, 2013; Carlson et al., 2017). Both interactions are important for GTP-hydrolysis of EF-G (Savelsbergh et al., 2005; García-Ortega et al., 2010; Carlson et al., 2017). A2662 in the SRL positions the catalytically active H92 in switch II to coordinate the water for GTP hydrolysis. Domain II establishes stacking interactions with the 16S of the body, whereas domain III predominantly interacts with uS12 (Fig. 6A). Domain IV is flexible, and inserts

itself into the decoding centre on the small subunit, mimicking a tRNA in the A/T state and (Fig. 6) (Gao et al., 2009; Ratje et al., 2010; Pulk & Cate, 2013; Ramrath et al., 2013). Furthermore is domain IV crucial for translocation (Savelsbergh et al., 2000a; Holtkamp et al., 2014a; Liu et al., 2014b), and restricting its freedom of movement impairs translocation (Peske et al., 2000). Loop I and II in the tip of domain IV establish contacts with the decoding centre, as well as the A-site tRNA (Zhou et al., 2014; Zhou et al., 2019). Consequently, EF-G promotes a head swivel, a rotation 18° relative to the body, and stabilises this conformation (Ratje et al., 2010; Belardinelli et al., 2016).

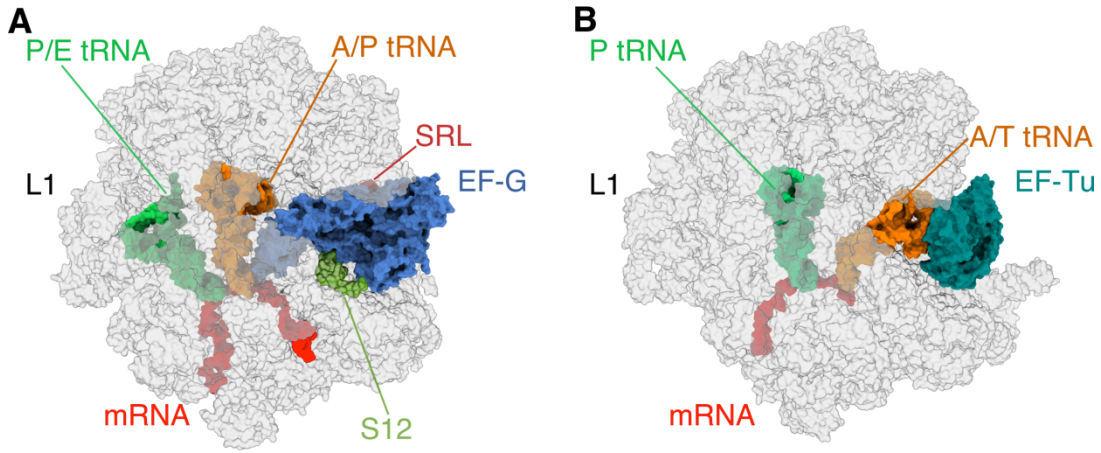

Figure 6: EF-G mimics the ternary complex of EF-Tu and tRNA. (A) During translocation, EF-G (blue) establishes contacts with the SRL in the 23S rRNA, uS12 ins the body (green, only soluble surface shown), as well as the DC and A/P tRNA (orange) with domain IV (Zhou et al., 2014). **(B)** EF-Tu (teal) delivers a tRNA (orange) to an elongating ribosome with a P-site tRNA (limegreen) for decoding (Loveland et al., 2020).

GTP-hydrolysis takes place shortly after EF-G binding. Conversely, P_i release from EF-G does not happen directly after hydrolysis (Savelsbergh et al., 2003). It does, however, induce major conformational changes in EF-G. Switch I locks the GTP in its binding pocket, and upon hydrolysis, switch I changes from an ordered to disordered conformation (Gao et al., 2009; Ticu et al., 2009). This leads to disruption of a hydrophobic pocket created by a multitude of interactions between switch I/II, domain II and III (Pulk & Cate, 2013). Domain II and III move apart and subsequently destabilise EF-G on the ribosome (Gao et al., 2009). Conformational changes in EF-G are coupled to the ribosome and cause a back-rotation of the body (Gao et al., 2009; Munro et al., 2010).

Translocation of the tRNAs is guided by interactions of the ASLs with the head and during translocation, intermediate chimeric hybrid states constituting ap/P- and pe/E-tRNA are formed (Ramrath et al., 2013; Zhou et al., 2013; Zhou et al., 2014). In particular, the ASLs form interactions with the head corresponding to the A- or P-site, and simultaneously interacts

with the P- or E-site on the body, as denoted by the first letter (a or p) and the second letter (p or e), respectively. These rigid interactions between ASL and 16S rRNA couple movement of the head to that of the tRNAs (Ramrath et al., 2013). The opposed head swivel and back-ratcheting of the body (Belardinelli et al., 2016) allow translocation of the mRNA by one codon and the tRNAs to adopt a classic E/E and P/P state. Only after translocation is completed will EF-G dissociate from the ribosome, concomitantly with further back rotation of head and body, and followed by dissociation of E-site tRNA (Spiegel et al., 2007; Belardinelli et al., 2016). Once off the ribosome, cytosolic EF-G exchanges GDP to GTP, and is ready for a new round of translocation. The 30S adopts a classic non-rotated POST-translocational state with only a peptidyl-tRNA in the P-site. A new codon presents itself in the A-site for a new cycle of elongation.

The exact mechanism by which translocation occurs is still debated. Early research suggested that EF-G breaks interactions of the DC and the codon-anticodon duplex (Ratje et al., 2010). Subsequently the latch formed by h34 in the head and the G530 region is opened, thus unlocking the movement of the 30S head and body and facilitating Brownian motion driven translocation uncoupled from the ribosome, while guiding the A-site tRNA by constant contact. Another proposed mechanism is that EF-G actively pushes the tRNA-mRNA complex through the ribosome. During GTP hydrolysis, a measurable mechanical force is released (Yao et al., 2013; Chen et al., 2016; Yin et al., 2019). This active movement has been termed a power-stroke and depends on the free movement of domain IV (Yin et al., 2019). This is consistent with X-ray structures showing EF-G in a compacted conformation, suggesting that domain IV moves by 100 Å and rotates 90° for performance (Lin et al., 2015; Zhou et al., 2020). However, these structures were achieved by linking EF-G to bL9 and thus during crystal formation was forced to bind to the neighbouring ribosome, thus raising the question as to whether this conformation occurs on the ribosome under more physiological conditions.

Likely, EF-G-facilitates translocation in a combination of Brownian movement and power stroke (Holtkamp et al., 2014b). Time resolved cryo-EM has become an increasingly more reliable method for differentiating the many individual states of each step in the translation, such as initiation (Kaledhonkar et al., 2019), decoding (Loveland et al., 2020) and recycling (Fu et al., 2019). Application of this method to translocation could give valuable insights and further understanding to the exact mechanism, which is utilized by EF–G to facilitate translocation.

1.3.3. Termination

When the ribosome has successfully translated a given mRNA, a stop codon in the A-site marks the end of the open reading frame (ORF). This codon is not recognised by tRNAs, but rather by the class I release factors RF1 and RF2. They differ in stop codon recognition, which makes both essential to a functioning translation cycle. UAA presents the most commonly used stop codon in *E. coli* (Rocha et al., 1999), and is accordingly recognised by both release factors, whereas UAG is only recognised by RF1 and UGA by RF2 (Scolnick et al., 1968). Remarkably, substituting all UAG codons in *E. coli* for UAA, has rendered RF1 dispensable for cell survival (Amiram et al., 2015). The codon discrimination between the two factors originates in conserved but divergent recognition sequences, PVT and SPF for RF1 and RF2, respectively (Ito et al., 2000; Zhou et al., 2012). Both factors interact with U1 of the stop codon via the adjacent backbone of the α5 helix in domain II, and interact with the third nucleotide via a threonine. The threonine in the RF1 PVT motif interacts with both U1 and A2, thus discriminating against G2 (Laurberg et al., 2008). Conversely, the serine in the SPF motif likely interacts solely with the nucleotide at the second position, allowing either A2 or G2. Additionally, a glutamine facilitating G3 binding in RF1 is substituted with a hydrophobic valine in RF2, which aids in active discrimination against G3 (Korostelev et al., 2008).

RF1/2 initially bind to the ribosome in a compacted conformation, and upon accommodation, i.e. stable interaction with the stop codon, domain III extends to the PTC (Petry et al., 2005). Domain III holds the conserved and for peptide release essential GGQ motif (Zavialov et al., 2002; Mora et al., 2003), and the conformational change accommodates the GGQ motif in the PTC. The two glycines are crucial for forming the loop inserting into the PTC, as a GAQ mutation slows the reaction by a few orders of magnitude (Zavialov et al., 2002). Furthermore, the glutamine residue carries a conserved methylation, which increases peptide release efficiency (Dincbas-Renqvist et al., 2000; Mora et al., 2007). Surprisingly, substitution of the glutamine side chain has a marginal effect on peptide release (Mora et al., 2003): the backbone amide, rather than the side chain amide, is in hydrogen bond distance with the 3' ester bond of the A76 and stabilises reaction intermediates. Similarly to peptide bond formation, a nucleophilic attack is carried out by a water molecule. Again, a tetrahedral intermediate is formed, in which the 2'OH of the A76 of the tRNA functions once more as a proton shuttle (Trobro & Aqvist, 2009; Jin et al., 2010; Kuhlenkoetter et al., 2011).

After peptide release has been completed by RF1/2, the class II release factor RF3 facilitates release of RF1/2 (Freistroffer et al., 1997; Koutmou et al., 2014). Recent findings suggest it does so by inducing a rotated state of the ribosome, which leads to RF1/2 release (Graf et al.,

2018). While the ribosome can adopt a rotated state spontaneously in the absence of RF3, 70S bound to RF2 are more likely to be rotated than those bound to RF1 (Adio et al., 2018). Albeit the difference and ratio of rotated to non-rotated is minimal, this leads to a decreased dependency of RF2 on RF3-mediated release.

Divergent to initial findings, does binding of RF3 to the ribosome not depend on a deacylated P-site tRNA (Peske et al., 2014), it was suggested that its GTPase activity is not necessary for RF release (Adio et al., 2018). Rather, GTP hydrolysis appears to be a mechanism to disengage RF3 from the ribosome. After the release factors dissociate, a deacylated P/E-site tRNA and the mRNA remain bound to the post termination complex (PoTC).

1.3.4. Recycling

The last phase in a translation cycle is the dissociation of ribosomal subunits and dislodging of the remaining tRNA and mRNA. This step is called recycling, as the ribosome can consequently be reused for a new round of translation. Recycling is carried out by three factors: EF-G, the ribosome recycling factor RRF, and IF3 (Karimi et al., 1999). Concerted action of EF-G and RRF split the ribosome into its subunits (Ito et al., 2002; Zavialov et al., 2005), whereas IF3 dissociates the remaining tRNA (Karimi et al., 1999; Prabhakar et al., 2017).

RRF plays an indispensable part in ribosome recycling. Depletion in the exponential phase shows a bacteriostatic effect, as it leads to re-initiation at downstream ORFs and consequently ribosomes are incapable of initiating at new mRNAs (Janosi et al., 1998). RRF consists of only two domains, a three-helix bundle and a small globular like domain, which are connected by extremely flexible hinges (Toyoda et al., 2000). Initial theories for the splitting mechanism suggested that RRF acts as a tRNA mimic and is translocated to the P-site, which in turn translocates the P/E-tRNA into the E-site, where it finally dissociates (Hirokawa et al., 2002). In contrast, X-ray crystallography and cryo-EM studies on the RRF-70S/50S complex showed that RRF does not act a tRNA mimic (Wilson et al., 2005; Gao et al., 2007; Fu et al., 2016). Rather, domain I extends toward the PTC and interacts with the 23S rRNA at the P-loop, whereas domain II interacts with uS12 and, together with the hinge region, with domain IV of EF-G. Furthermore, while GTP hydrolysis is necessary for splitting (Hirokawa et al., 2008; Savelsbergh et al., 2009; Prabhakar et al., 2017), EF-G mutants deficient in translocation were still functional in ribosome recycling (Fujiwara et al., 2004).

Binding of RRF to the PoTC at the A-site stabilises the ribosome in a rotated state (Prabhakar et al., 2017). Only binding of RRF prior to EF-G association can lead to successful

disassembly, as EF-G alone will simply dissociate after GTP-hydrolysis. Conversely, the disassembly is rate-limited by EF-G, as even high RRF concentrations cannot increase disassembly speed at low EF-G concentrations (Borg et al., 2016a; Prabhakar et al., 2017).
Currently, the proposed mechanism is that domain IV of EF-G induces a rotation of RRF domain II, which pushes it, like a wedge, between H69 and h44, disrupting the central B2a intersubunit bridge (Wilson et al., 2005; Pai et al., 2008; Fu et al., 2016; Zhou et al., 2020). Consequently, the interactions between the subunits are destabilised, ultimately leading to dissociation into 50S and a 30S-tRNA-mRNA complex and release of RRF and EF-G. Subsequently, IF3 binds to the 30S and dissociates the tRNA (Karimi et al., 1999; Prabhakar et al., 2017). Binding of IF3 is necessary for this last step in ribosome recycling, as in its absence, the ribosome will reassemble (Hirokawa et al., 2005; Prabhakar et al., 2017). Although the exact mechanism by which the mRNA disengages from the 30S remains to be elucidated, the mRNA dissociates only after the tRNA. Ultimately, the subunits are ready for a new round of translation.

1.4. The stringent response

In order to adapt to environmental changes, bacteria have developed the so-called stringent response (Cashel & Gallant, 1969; Hauryliuk et al., 2015; Irving & Corrigan, 2018). It is triggered by increased amounts of uncharged tRNAs and is promoted by two secondary metabolites, pppGpp and ppGpp (Haseltine & Block, 1973; Sprinzl & Richter, 1976). Also known as alarmones, these metabolites are produced by RSH (RelA/SpoT homologue) type proteins. They impact and modulate a multitude of processes within the cell, like transcription, translation and DNA replication. Furthermore, increasing evidence reveals that the stringent response is also involved for antibiotic resistance, for instance by inducing formation of so called persister cells (Maisonneuve & Gerdes, 2014).
Alarmone-producing proteins are conserved across all bacteria and also plants (Atkinson et al., 2011; Jimmy et al., 2020). Alarmones are generated by transfer of a pyrophosphate from ATP to the 3'-OH of either GTP or GDP. Notably, the 2'-OH of the accepting nucleotide plays a pivotal role during this process (Patil et al., 2020). Upon induced amino acid starvation, GTP and GDP concentrations drop from 755 µM and 306 µM to about half their concentrations under optimal conditions, whereas their alarmone counterparts rise to ~800 and 500 µM (Varik et al., 2017; Zborníková et al., 2019).

RSH-type proteins are ~70 kDa multi-domain proteins, comprising both a SYN (Synthetase) as well as a HD (Hydrolase) domain in the N-terminus. Additionally, the C-terminal domain interacts with the deacylated tRNA (Jain et al., 2006; Arenz et al., 2016). Most bacteria possess a bifunctional Rel, whereas β- and γ proteobacteria possess a monofunctional RelA, which lacks hydrolysis activity despite an existing HD domain. Instead, in these bacteria SpoT compensates this deficiency. Inversely to RelA, it possesses only weak synthetase activity (Xiao et al., 1991). RSH-type proteins act in an autoregulatory manner by adopting an open or closed conformation, which brings the HD and SYN domain into contact and induces steric obstruction (Hogg et al., 2004; Tamman et al., 2020).

Additionally to the long alarmone producing and degrading RSH-type proteins, in some bacteria also short variants exist (Atkinson et al., 2011; Jimmy et al., 2020). Depending if they consist of a hydrolase or a synthetase domain, they are called SAH or SAS (small alarmone hydrolase/synthetase), and they function in homo-multimer forms (Steinchen et al., 2015; Manav et al., 2018).

While the principle of the stringent response is conserved in all bacteria, not all targets are. RNAP is directly targeted in *E. coli* (Zuo et al., 2013), while in the majority of other bacteria, the respective binding site is not present (Krásný & Gourse, 2004; Hauryliuk et al., 2015). Instead, according to current theory, alarmones inhibit GTP-dependent processes by depletion of the GTP/GDP pool. Furthermore, in *Bacillus*, a heat shock is also responsible for triggering stringent response (Schäfer et al., 2020).

When nutrients and charged tRNAs become scarce, abundant protein production becomes counterproductive, and transcription is predominantly inhibited directly by restriction of RNAP activity (Sanchez-Vazquez et al., 2019). On the other hand, genes associated with biosynthesis, like amino acid or fatty acid, are upregulated. The stringent response further addresses protein synthesis by targeting various points in the translation cycle. First off, rRNA transcription from P1 is inhibited, although the different operons appear to be affected to varying degrees (Barker et al., 2001; Kolmsee et al., 2011). Simultaneously, ribosomal proteins are down-regulated, this however originates from the previously mentioned auto-regulation (Burgos et al., 2017). Next to rRNA transcription, ribosome assembly becomes inhibited by binding of (p)ppGpp to assembly GTPases, like Era, Obg(E) or RbgA (Buglino et al., 2002; Feng et al., 2014; Corrigan et al., 2016). Binding of alarmones to the active site of RbgA inhibits conformational rearrangement necessary for hydrolysis (Pausch et al., 2018). This likely prevents RbgA dissociation after 50S maturation and inhibits subunit joining during the initiation step, similarly to Obg (Feng et al., 2014). Moreover, translation itself is

also obstructed by (p)ppGpp, by inhibiting the translation associated GTPases, namely IF2, EF-Tu, EF-G and RF3 (Kanjee et al., 2012).

While alarmones are commonly addressed as (p)ppGpp, differentiating between the tetra- and penta-phosphate form is pivotal. pppGpp has been shown to still allow IF2 and EF-Tu to function in their respective purposes (Hamel & Cashel, 1974; Milon et al., 2006; Vinogradova et al., 2020), whereas ppGpp exhibits inhibitory effects similar to GDP (Rojas et al., 1984; Diez et al., 2020) and also inhibits RF3 function (Kihira et al., 2012). Conversely, EF-G function is inhibited by either the tetra- and penta-phosphate form (Hamel & Cashel, 1973). Importantly, select GTPases, like EF-Tu and IF2, are capable of hydrolysing pppGpp to ppGpp. Structural studies for these GTPases can give further insights into the mechanism by which alarmones inhibit one but not the other.

1.5. Antibiotics

While human-kind has made great advances in the medical field in the last century, antibiotic resistances and especially resistance against last resort antibiotics is becoming more prevalent each day. The need for new antimicrobial agents has not decreased since the discovery and introduction of penicillin 80 years ago. In 2017, the World Health Organisation (WHO) released a list of priority pathogens, primarily consisting of Gram-negative bacteria, with *A. baumanii*, *P. aeruginosa* and *Enterobacteriacea* classified as critical (WHO, 2017); due to their outer membrane, Gram-negative bacteria possess a naturally increased resistance against antibiotics. *M. tuberculosis* was given the highest priority, as it leads to 1.8 million deaths annually. It possesses an additional outer layer consisting of mycolic acid, which enhances antibiotic resistance even more. Special antibiotics like ethambutol, inhibiting mycobacteria-specific cell wall synthesis, are necessary for treatment (Schubert et al., 2017).

Researchers are using different methods to tackle the increasingly difficult problem of antibiotic resistance (Vila et al., 2019). The most straightforward approach is to modify previously approved antibiotics in order to counteract resistance mechanisms, e.g. make them resistant against inactivating chemical modifications by the pathogens (Marschall et al., 2019). About 40% of currently investigated antibiotics are modified β-lactam antibiotics, and two of the most recent FDA (US Food and Drug Administration) approved Gram-negative targeting antibiotics – omadacycline and eravacycline – are tetracycline-derivatives (WHO, 2019a).

Besides modification of known antibiotics, investigation of new compounds with novel and distinct targets to circumvent cross-resistance is a central aspect in combating antitbiotic resistance (Durand et al., 2019). Antimicrobial peptides (AMPs) are one class of such

compounds, that are being rediscovered and optimised. They originate from the innate immune and host defence system, and can be found mostly in higher eurkaryotic organisms, although they are in some form present in all domains (Ageitos et al., 2017). Currently, 27 AMPs are in the pre-clinical pipeline (WHO, 2019b). The most prevalent mechanism of AMPs is membrane permeabilisation (Epand & Vogel, 1999; Brogden, 2005), and therefore also exerts an undesireable cytotoxic effects on humans. However, in recent years, advances have been made in the field, proline-rich AMPs (PrAMPs) which target the translation machinery, have been characterised (Scocchi et al., 2011; Graf et al., 2017) and shown promising results as improved AMPs with less cytotoxicity (Mardirossian et al., 2019).

Moreover, many antimicrobial drugs have been originally discovered as secondary metabolites in bacteria, mainly the class of Gram-positive Actinobacteria, especially the order of Actinomycetales (Genilloud, 2017; Hutchings et al., 2019), and the order of Gram-negative Myxobacteria (Schaberle et al., 2014; Landwehr et al., 2016). As genome sequencing becomes more affordable and a standard approach, combined with bioinformatics tools and high-throughput screening assays to asses cytotoxicity or translation inhibition, a plethora of novel compounds are being discovered (Steele et al., 2019). Furthermore, assays screening for active molecules could in the future become less extensive, as algorithms are being trained to evaluate chemical properties and predict potential antimicrobial activity (Stokes et al., 2020).

Additional to modification and discovery of novel compounds, understanding bacterial resistance mechanisms can give valuable insight and further points of action. For instance, resistance against β-lactam antibiotics is facilitated through degradation by β-lactamases. Indeed, it has become common to administer β-lactamase inhibitors like clavulanic acid in combination with β-lactam antibiotics (Huttner et al., 2020).

1.5.1. Argyrins

The family of argyrins has first been isolated from an *Actinoplanes* strain as antibiotics A21459 A and B (Ferrari et al., 1996; Selva et al., 1996). A few years later they were rediscovered in myxobacteria, *Archangium gephyra* Ar8082 and *Cystobacter sp.* SBCb004 (Sasse et al., 2002; Vollbrecht et al., 2002). They were renamed argyrins A-H, where argyrin A and B correspond to antibiotics A21459 B and A, respectively, and represent the most dominant products (Pogorevc et al., 2019). The structures of argyrin A-H were solved by X-ray and NMR and revealed a cyclic octa-peptide antibiotic (Fig. 7), consisting of D-alanine, glycine, one modified and one unmodified tryptophan, 2-(1'- aminoethyl)-thiazole-4-carboxylic acid, sarcosine and dehydroalanine. In argyrin B, D and G the alanine is replaced

by D-α-aminobutyrate (Vollbrecht et al., 2002). The originally reported structure of argyrin A and B (Ferrari et al., 1996) had to be corrected as the methoxy modification in the second tryptophan moiety (R_4) resides at the C4 and not at the C5.

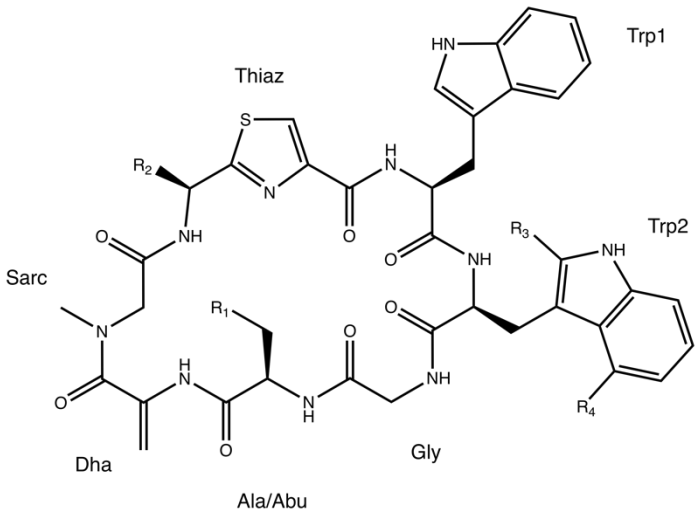

Argyrin	R_1	R_2	R_3	R_4
A	H	CH_3	H	OCH_3
B	CH_3	CH_3	H	OCH_3
C	H	CH_3	CH_3	OCH_3
D	CH_3	CH_3	CH_3	OCH_3
E	H	CH_3	H	H
F	H	CH_2OH	H	OCH_3
G	CH_3	CH_2OH	H	OCH_3
H	H	H	H	OCH_3

Figure 7: Chemical structure of the Argyrin family. The circular octapeptide antibiotics consist of one modified (Trp2) and one unmodified Tryptophane (Trp1), Aminoethyl-Thiazolecarboxylic acid (Thiaz), Sarcosine (Sarc), Dehydroalanine (Dha), and Alanine (Ala; R_1 = H; Argyrin A, C, E, F and H) or α-aminobutyrate (Abu; $R_2 = CH_3$; Argyrin B, D and G).

As the argyrins consist of non-proteinogenic amino acids like D-amino acids and a thiazole-ring, a non-ribosomal synthetic pathway had been presumed. While the chemical synthesis of several argyrins has been published (Ley et al., 2002; Bulow et al., 2010; Chen et al., 2014), the biosynthetic cluster from the producer strain was only discovered recently (Pogorevc et al., 2019). Through scanning of the *Cystobacter* genome for homologues of previously identified non-ribosomal peptide synthetase (NRPS) genes, the argyrin biosynthetic gene cluster (*arg* BGC) was determined with a size of 33kbp and consisting of five genes, *arg1-5*. Arg2 and Arg3 represent the octamodular NRPS subunits 1 and 2, respectively. Together they generate the circular octapeptide, Arg2 starts synthesis with either an alanine or α-aminobutyrate determining R_1, and Arg3 determines R_2 by incorporating either alanine or serine. Arg1, 4 and 5 have been identified as a SAM-dependent-methyltransferase, an *O*–methyltransferase and a tryptophan-dioxygenase, resulting in the methyl- (R_3) and methoxy-modifications (R_4) on the Trp2 moiety.

Intriguingly, the argyrins show a high antimicrobial activity against a number of Gram-negative bacteria (Selva et al., 1996; Sasse et al., 2002). Argyrin A and B showed high activity against *Clostridium, Proteus*, and an intermediate activity against *Staphylococcus aureus* as well as *Pseudomonas aeruginosa* and a hyperpermeable *Salmonella* strain (Selva et al., 1996). No activity could be detected against yeast. Specifically, argyrin A-E and H showed activity against *Staphyloccocus* and an *Escherichia coli* Δ*tolC* as well as

Pseudomonas with IC_{50} values ranging from 0.08-1.4 µM (Sasse et al., 2002). Argyrin F and G carry a hydroxymethylgroup at R_2 and have a substantially lower IC_{50} of 5 and 4 µM, respectively.

Initial investigations into the mode of action showed that *in vitro* neither RNA nor DNA synthesis were affected by the antibiotics, but rather that bacterial poly-Phe synthesis was inhibited (Selva et al., 1996). Additionally, argyrin B was found to be a strong inhibitor of the autoimmune response and displayed a cytotoxic effect (Sasse et al., 2002). Due to the cytotoxic effect the possibility to use the argyrins as anti-cancer drugs was pursued in further research. Argyrin A was identified as a strong proteasome inhibitor, leading to stabilisation of the tumor-suppressor protein $p27^{kip1}$ (Nickeleit et al., 2008). Further investigation showed that argyrin F is another potent candidate with anti-tumor activity, likewise inhibiting the proteasome (Bulow et al., 2010; Chen et al., 2017), as well as Argyrin B (Allardyce et al., 2019). Computational analysis showed, however, that the different compounds have different proteasome subunit-specificities due different modifications (Stauch et al., 2010; Loizidou & Zeinalipour-Yazdi, 2014; Allardyce et al., 2019).

Resistance mutation studies in *P. aeruginosa* lead to the identification of EF-G1 as the target for both argyrin A and B (Bielecki et al., 2012; Nyfeler et al., 2012). Resistance mutations identified a novel binding site in EF-G between domain III and V. Interacting residues are extremely conserved, and indeed also yeast and mammalian mitochondrial EF-G is targeted by argyrin B (Nyfeler et al., 2012). A crystal-structure of *P. aeruginosa* EF-G1 in complex with argyrin B showed that hydrogen bonds and van der Waals interactions are important for binding of the drug. EF-G adopts an elongated and previously not reported conformation, which is not compatible with binding to ribosomes. Concluding, it has been suggested that inhibition of binding of EF-G to the ribosome is the mechanism by which argyrins inhibit translation (Nyfeler et al., 2012).

1.5.2. Tetracenomycins

Similar to the argyrins, tetracenomycin C (TcmC) was first isolated 40 years ago from a strain belonging to the Actinomycetales, *Streptomyces glaucescens* GLA.0 (Weber et al., 1979). It showed activity mostly against other *Streptomyces* strains, as well as some other Actinobacteria like *Corynebacterium* and *Brevibacterium*. NMR analysis revealed a tetracyclic structure with two neighbouring benzene rings. The X-ray structure of TcmC was solved in 1992, giving the final stereochemistry of the A-ring (Fig. 8) (Egert et al., 1992).

The biosynthetic cluster was identified, involving 12 genes (Motamedi et al., 1986). Extensive studies were undertaken to identify the role of each gene. The Polyketide synthase (PKS) genes *tcmKLM* were the first to be characterised as two keto-synthases and an acyl-carrier protein, respectively (Bibb et al., 1989; Gramajo et al., 1991). TcmN belongs to the PKS as well and is a bifunctional protein with a cyclase and an aromatase domain (Summers et al., 1992). TcmI is the D-ring cyclase (Summers et al., 1993). TcmJ has a still unknown function, however in its absence there is drastic decrease in production of the PKS intermediate TcmF2 (Bao et al., 1998). Concluding, TcmIJKLMN generate the tetracyclic scaffold, and TcmGHOP are responsible for modifications. Both TcmO and TcmP are O-methyltransferases (Summers et al., 1992; Decker et al., 1993). TcmG hydroxylyses the scaffold at three positions (Shen & Hutchinson, 1994), and TcmH is a monooxygenase (Shen & Hutchinson, 1993). Expression of the *tcm* cluster occurs only in the stationary phase, likely to combat competing Streptomyces for scarce nutrients (Gramajo et al., 1991). *tcmGHJKLMNO* appears to be transcribed as polycistronic mRNA under control of the *tcmG* promoter, while *tcmP* is monocistronic and interestingly has the same start side for transcription and translation, meaning it is missing a RBS which might influence and regulate tetracenomycin production (Decker & Hutchinson, 1993).

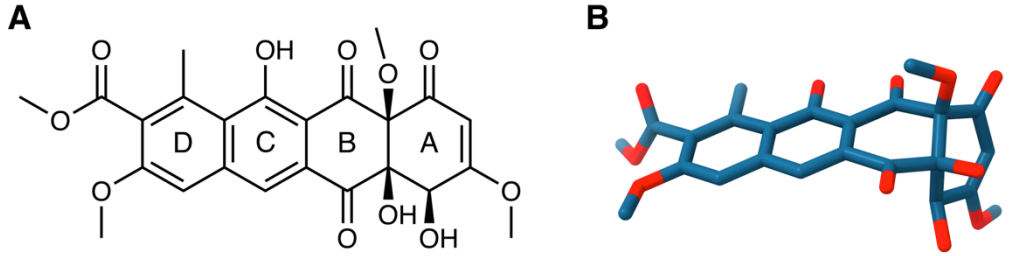

Figure 8: Structure of TcmX. (A) Chemical 2D structure of TcmX and rings labelled D-A from left to right. **(B)** 3D structure of TcmX in the same ring orientation as **(A)**

Tcm producer strains gain resistance through utilisation of an efflux pump, TcmA. TcmA expression is negatively regulated by the transcriptional repressor TcmR. In the absence of tetracenomycins, it is stably bound to an intergenic region between the neighbouring although oppositely oriented genes *tcmA* and *tcmR*. Binding of tetracenomycins to TcmR in the stationary phase leads to dissociation, subsequent transcription and expression of TcmA and TcmR. As a result, tetracenomycin is exported, leading to a decrease in intracellular concentration. Eventually, the concentration will become insufficient to inhibit TcmR sufficiently, and transcription will be repressed again (Guilfoile & Hutchinson, 1992a; Guilfoile & Hutchinson, 1992b). Leaky expression of TcmR from a second promotor downstream of the TcmR-binding site leads to sufficient repression during the exponential phase.

Despite similarity to tetracycline antibiotics, *in vitro* poly-Phe synthesis was not affected by tetracenomycin C (Weber et al., 1979). TcmC was screened for anti-herpes virus activity in HeLa cells, and showed protection with an IC_{50} of 32 µM, while the IC_{50} for cytotoxicity was at 212 µM (Alarcon et al., 1984). Interestingly, cytotoxicity was measured via inhibition of [^{35}S]-methionine incorporation.

TcmX, a 12a-*O*-methylether of TcmC, was later isolated from *Nocardia mediterranea*, also belonging to the order of Actinomycetales (Khoo, 1988; Anderson et al., 1989). It showed the same activity spectrum as tetracenomycins C. Together with the structurally related elloramycins, which carry a rhamnose moiety at the C-8, TcmX and TcmC were shown to be active against murine leukaemia cells with IC_{50}s of 3.3 µM, 1.2 µM and 0.6 µM, respectively (Lazar et al., 1981; Rohr & Zeeck, 1990). Intriguingly, a structural intermediate ($TcmD_3$), which is still missing methylation and hydroxylations, was found to have some activity against *B. subtilis*, however was not active against *Streptomyces* (Rohr et al., 1988) Recently, TcmX was isolated from the marine Actinomycete *Saccharothrix* sp. 10-10 (Liu et al., 2014a). Surprisingly, in this study TcmX showed activity against both methicillin resistant *S. aureus* (MRSA) and vancomycin resistant *Enterococcus* (VRE) with MIC values of 32-64µg/ml. Moreover, novel tetracenomycin-related metabolites, the Saccharothrixones and Seco-tetracenomycins, were identified from the same strain, however they were either inactive or only moderately active against both cancer cell lines and bacteria (Gan et al., 2015; Liu et al., 2018).

Due to structural similarity to the DNA intercalator doxorubicin, the planar structure given by the neighbouring aromatic rings, as well as preliminary results indicating binding to DNA and inhibition of uracil incorporation, intercalation with DNA has been suggested to be the inhibitory mechanism for the tetracenomycins (Hutchinson, 1997), however, no studies were undertaken to illuminate the actual mechanism of this antibiotic family. A recently published study suggests TcmX leads to cell cycle arrest exclusively in lung cancer cells by down regulating Cyclin D1 and does not affect healthy cells (Qiao et al., 2019). The study, however, shows inconsistencies in the data and lacks appropriate negative controls. Indeed it has been determined that TcmX inhibits protein synthesis by binding in the ribosomal nascent peptide exit tunnel (Osterman et al., 2020). Structural comparison with doxorubicin suggests that tetracenomycins universally cannot intercalate with dsDNA, nor bind to the tetracycline binding site on the 30S, due to the stereochemistry of the characteristic A-ring. The binding site in the NPET is conserved between *E. coli* and human ribosomes, making tetracenomycins also an attractive agent for cancer treatment.

2. Objectives

Stringent response (Publication 1 and 2)

During the stringent response, the secondary messengers (p)ppGpp target a multitude of processes and proteins within the bacterial cell. However, the exact mechanism by which some targets, especially ribosome-associated GTPases, are inhibited by the alarmones is still not well understood. Inhibition had been reported but not explored further of ribosome-biogenesis co-factor RbgA and EF-Tu (Rojas et al., 1984; Corrigan et al., 2016). Moreover, while interactions between RbgA and the 45S or 50S had been analysed biochemically (Achila et al., 2012), no structure of the complex was available. To address this, we employed cryo-EM to solve a structure of the RbgA-50S complex, as well as aimed to obtain a structure of (p)ppGpp stalled EF-Tu on the translating ribosome. Both studies were accompanied by affinity measurements, hydrolysis activity and X-ray analysis of the GTPases in complex with the alarmone.

Tetracenomycin X (Publication 3)

With antibiotic resistance on the rise, investigation of novel compounds with distinct target binding sites is indispensable. One such novel compound is the antibiotic tetracenomycin X (TcmX) (Weber et al., 1979; Anderson et al., 1989). TcmX had been suggested to be a DNA intercalator (Hutchinson, 1997), and was recently reported to be active against MRSA and VRE (Liu et al., 2014a). Conversely our data indicated that ribosomes are targeted. We aimed to gain insight into the mechanism of this antibiotic by monitoring translation in the presence of the antibiotic, obtaining a cryo-EM structure as well as toe-printing to examine which phase of translation is inhibited.

Argyrin B (unpublished results)

The argyrin family of circular peptide antibiotics were first reported to inhibit bacterial translation (Sasse et al., 2002) and resistance mutations identified EF-G as the target (Bielecki et al., 2012; Nyfeler et al., 2012). A crystal structure of EF-G bound to argyrin B suggested it induces conformational changes incompatible with ribosome binding. To verify this hypothesis, we applied binding-assays, monitored GTPase activity and obtained a cryo-EM of a 70S ribosome with EF-G in the presence of argyrin B.

3. Cumulative Thesis: Summary of publications

3.1. Paper 1 - Structural basis for (p)ppGpp-mediated ribosomal large subunit arrest by RbgA

Patrick Pausch, Maximiliane Wieland, Thomas Klaus, Sven-Andreas Freibert, Wieland Steinchen, Daniel N. Wilson and Gert Bange

J Biol Chem 293: 19699-709 (2018)

Under unfavourable conditions, a stringent response is provoked in bacteria (Cashel & Gallant, 1969). Production of the secondary messengers (p)ppGpp, also termed alarmones, is induced. These molecules lead to a decrease in multiple essential cellular processes, like DNA replication and protein synthesis, in order to conserve resources and partially divert them to for survival necessary processes. One of the targeted processes within the bacterial cell is ribosome biogenesis. Besides rRNA transcription, several assembly co-factors are also inhibited by ppGpp (Corrigan et al., 2016). One of these targeted proteins is RbgA, a factor conserved across all domains of life. RbgA assists in the late-stage assembly of the 50S and associates with an immature 45S particle. While presumably the majority of the targets of alarmones have been identified at this point, the mechanism of action is not well explained for most of them.

To characterise the mode of inhibition of RbgA by alarmones, we analysed biochemical and structural data. K_d measurements revealed that (p)ppGpp affinity to RbgA was similar to that of GDP/GTP, with values between 5.04 µM (GTP) and 3.26 µM (ppGpp). High-resolution X-ray crystallography of *S. aureus* RbgA revealed that binding of alarmones, when compared to GDP/GMPPNP, does not induce major conformational changes off the ribosome, which would hinder association with a 45S particle. However, positioning of the δ- and ε-phosphates likely prevents RbgA from adopting a hydrolysis competent state: both the G2 (switch I) and G3 (switch II) motif are displaced and incapable of coordination of for hydrolysis essential Mg^{2+} or K^{+}. This is further supported by GTPase assays showing RbgA is not able to hydrolyse (p)ppGpp, neither in the absence nor in the presence of ribosomes. We set out to obtain a RbgA-50S-GMPPNP complex by cryo-EM, as no structural data on a native RbgA-45S or RbgA-50S complex had been published at this point. Reconstruction of the *B. subtilis* complex revealed a class (34%) of 50S with missing densities for H68-H71. This conformation was termed $50S_{Int}$. Low-pass filtering disclosed an undefined density in proximity to where the helices are in the mature particle. No defined density for RbgA could

be discovered, and we concluded, since its binding site is at the displaced helices, it was likely part of the undefined density.

3.2. Paper 2 - Structural basis for the (p)ppGpp-dependent control of the translation elongation factor EF-Tu

Wieland Steinchen, Mohamad Majkini, Maximiliane Wieland, Anita Dornes, Pietro I. Giammarinaro, Alex Lepak, Benjamin Burnett, Scott C. Blanchard, Daniel N. Wilson and Gert Bange

unpublished

Late in the bacterial life cycle, when nutrients become scarce and uncharged tRNAs become abundant, the stringent response is triggered. Uncharged tRNAs binding to an elongating ribosome stall translation. This complex is recognised by RSH-type proteins, which become activated and produce the secondary messengers (p)ppGpp. These molecules are also known as alarmones have multiple targets within the cell, and besides RNAP, also inhibit GTPases associated with translation. Due to a lack of charged tRNAs, translation is impaired, and thus a waste of GTP resources can be prevented. One of the targeted GTPases is EF-Tu (Hamel & Cashel, 1974).

To examine the impact of the tetra- and penta-phosphate guanosine, we determined the structure of an EF-Tu–pppGpp complex at 2 Å employing X-ray crystallography. Surprisingly, the structure revealed an electron density for ppGpp and an Mg^{2+}, not pppGpp. Positioning of the 3'-phosphates is not only incompatible with rearrangement of the switch I motif of EF-Tu, but also consequently with interactions with aa-tRNA. To underline the structural analysis, we performed electrophoretic mobility shift assays (EMSA) as well as fluorescence spectroscopy to monitor ternary complex formation. Indeed, (p)ppGpp was able to out-compete GTP once ratios of alarmone to GTP were >1, and inhibit ternary complex formation. As the structure showed density for ppGpp instead of the originally added pppGpp, we investigated whether this was due to active hydrolysis by EF-Tu or possible cross-contamination with ppGpp. Our results indicate that EF-Tu indeed is able to hydrolyse pppGpp. Moreover, we show that EF-Ts, the guanosine exchange factor of EF-Tu, can displace (p)ppGpp from EF-Tu, facilitating translation recovery after resolution of the SR.

3.3. Paper 3 - Tetracenomycin X inhibits translation by binding within the ribosomal exit tunnel

Ilya A. Osterman, Maximiliane Wieland, Tinashe P. Maviza, Kseniya A. Lashkevich, Dmitrii A. Lukianov, Ekaterina S. Komarov, Yuliya V. Zakalyukina, Robert Buschauer, Dmitrii I. Shiriaev, Semen A. Leyn, Jaime E. Zlamal, Mikhail V. Biryukov, Dmitry A. Skvortsov, Vadim N. Tashlitsky, Vladimir I. Polshakov, Jingdong Cheng, Yury S. Polikanov, Alexey A. Bogdanov, Andrei L. Osterman, Sergey E. Dmitriev, Roland Beckmann, Olga A. Dontsova, Daniel N. Wilson and Petr V. Sergiev

Nat Chem Biol (2020)

The tetracenomycins are molecules belonging to the group of the aromatic polyketides first identified in 1979 (Weber et al., 1979). They are planar tetracyclic naphthacenequinone derivatives, with structural similarities to the DNA intercalating compound doxorubicin (Dox) and the translation inhibiting compound tetracycline (Tet). They were first identified in actinomycetales, and as such have been found to be mostly active against other actinomycetales, but also against multiple cancer cell lines (Lazar et al., 1981; Rohr & Zeeck, 1990). However, no activity against bacteria could be detected. Recently, they were rediscovered in a marine actinomycete, *Saccharothrix* sp. 10-10, and showed activity against multi-resistant bacteria (Liu et al., 2014a). Due to initial experiments showing no inhibition of *in vitro* Poly-Phe synthesis and structural similarity to Doxorubicin, it has been assumed to function as a DNA intercalator as well.

Conversely, we found its mechanism of action is inhibition of translation. We identified Tetracenomycin X (TcmX) from *Amycolatopsis* sp. 23, and through extensive biochemical analysis and comparison with Dox and Tet, we could show that *in vitro* TcmX inhibits incorporation of valine, and not that of thymidine, and translation of a Fluc reporter construct with an IC_{50} of 1.5 μM. Analysis of resistance mutations revealed mutations in the 23S rRNA, but not in the 16S, where Tet binds. Cryo-EM analysis of *E. coli* 70S ribosomes confirmed the TcmX binding site within the nascent peptide exit tunnel, close to the PTC. The drug stacks onto the non-canonical base-pair of U1782-U2586 and coordinates two Mg^{2+} for further interactions. Strikingly, the non-canonical base-pair is conserved in the eukaryotic ribosome. Consequently, cryo-EM analysis of a human 80S ribosome revealed the same binding site, stacking upon the corresponding U3644-U4352 base-pair. Further experiments on HEK293T cells showed that the cytotoxicity concentration at which TcmX permits only 50% cell survival (CC_{50}) was at 2.5 μM. The IC_{50} for *in vivo* translation inhibition of a Fluc reporter coincided with 2.5 μM. Intriguingly, translation of a Fluc reporter in a whole cell

extract showed an increased IC_{50} of 10 μM. This suggests additional targets in human cells besides translation.

The binding site of TcmX lies at the beginning of the NPET, opposing to the macrolide erythromycin (Ery) binding site. To prove a similar mode of action, i.e. inhibition of translation elongation, we conducted toe-printing assays. The use of two different templates, TrpL-2Ala and ErmBL, established that neither initiation nor termination was inhibited, but translation elongation. Comparison to Ery showed a similar amino acid preference for stalling for the TrpL-2Ala template, but not for ErmBL. Therefore, the mechanism by which TcmX inhibits elongation occurs in a sequence-specific manner.

4. Unpublished results

The argyrins represent a family of circular octa-peptides, with modifications present at multiple residues (Ferrari et al., 1996; Sasse et al., 2002; Vollbrecht et al., 2002) (Fig. 9A). They exhibited activity in translation inhibition as well as cytotoxicity (Sasse et al., 2002). Because of their cytotoxic effect the argyrins were further investigated as anti-cancer drugs (Nickeleit et al., 2008; Bülow et al., 2010; Chen et al., 2017); argyrin A, B and F were shown to target the proteasome, however, all with differing subunit specificities (Bülow et al., 2010; Allardyce et al., 2019).

Argyrins inhibit bacterial translation

In bacteria, the target of argyrin A and B has been identified as the prokaryotic elongation-factor G (Nyfeler et al., 2012; Bielecki et al., 2012). Structural determination of EF-G complexed with argyrin B led to the hypothesis that argyrin arrests EF-G in a conformation incompatible with ribosome binding. Poly-Phe synthesis was indeed inhibited (Sasse et al., 2002). To confirm this under more physiological conditions, coupled transcription-translation assays employing Firefly Luciferase (Fluc) were carried out (Fig. 9B). All tested argyrins A-D inhibited translation, with IC_{50} values of 2-3 µM, with the exception of argyrin C, which showed delayed inhibition with an IC_{50} of 10.5 µM.

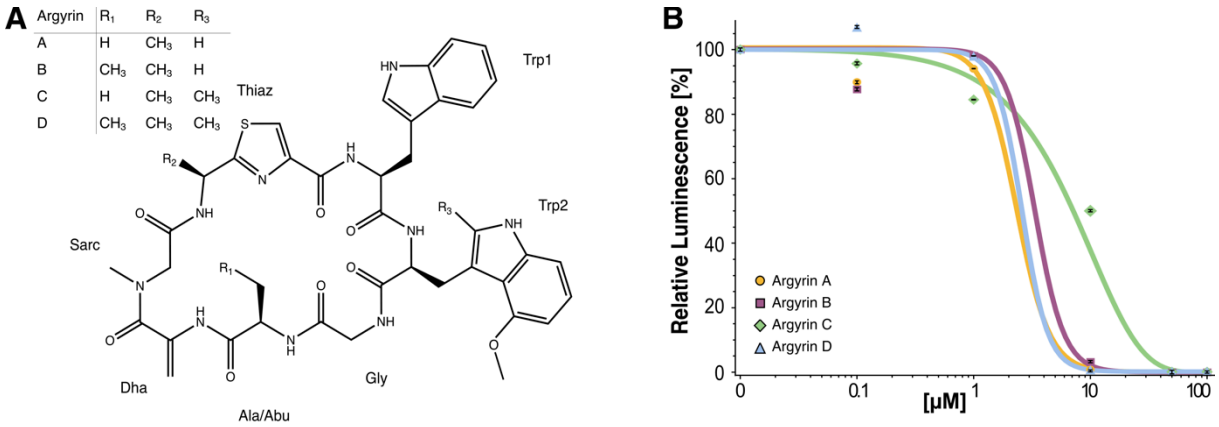

Figure 9: Argyrins inhibit translation (A) Chemical structure of Argyrins A-D showing the circular nature and differences in R1-R3 **(B)** *In vitro* Firefly luciferase assay were performed in the presence of varying concentrations of argyrins.

Argyrins inhibit the ribosome-dependent GTPase activity of EF-G

EF-G is targeted by another antibiotic, fusidic acid (FA), which inhibits its function (Tanaka et al., 1968), but allows for one round of hydrolysis (Bodley et al., 1970). To test whether argyrins function similarly, GTP-hydrolysis activity of EF-G in the presence of argyrins was evaluated. For this purpose malachite green assays were conducted. In the process of GTP

hydrolysis, EF-G releases an inorganic phosphate (P_i). Malachite green in combination with molybdate will form a complex with P_i, which can be measured spectrophotometrically. EF-G activity is stimulated by interactions with the ribosome, thus the assays were performed in the presence of purified *E. coli* 70S ribosomes. A time course of EF-G in the absence of any inhibitors showed that within a 90 min window EF-G hydrolysed the added GTP (20 µM) almost entirely (Fig. 10A). In the absence of ribosomes GTP hydrolysis after 90 min showed only marginal activity (1.4 µM P_i). Plotting time against GTP hydrolysed per ribosome revealed the majority of hydrolysis occurred within the first 30 min. Between 60 and 90 min the slope declined drastically and plateaued around 530 GTP/ribosome at 90 min (Fig. 10B). Thus, for the following assays an incubation time of 60 min was chosen. The impact of argyrins on GTP-hydrolysis was examined in the presence of varying concentrations (0, 0.1, 1, 10, 50, and 100 µM). Figure 10C shows one representative experiment. At 1 µM, all argyrins displayed 40-50% inhibition. Argyrin B and D were most active at 50 µM (20%), whereas argyrin A and C had reduced activity at concentrations higher than 10 µM. P_i release in the presence of fusidic acid (FA) was monitored as a positive control and showed a slightly higher IC_{50} of ~3 µM. However, FA also displayed a greater degree of inhibition than any argyrin with only 10% residual activity at 100 µM.

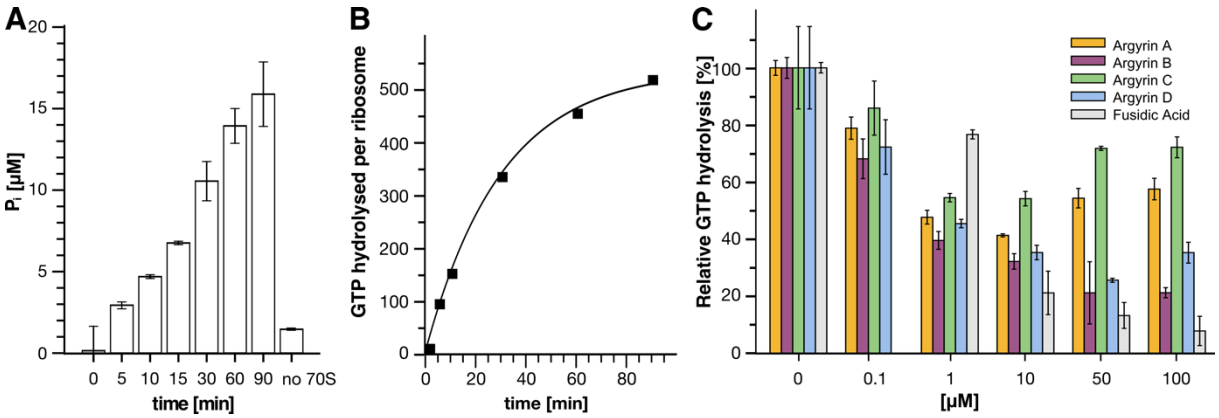

Figure 10: Phosphatase assays of EF-G. (A) Time course of EF-G (60 nM), ribosomes (30 nM) and GTP (20 µM) up to 90 minutes of incubation at room temperature. **(B)** Time course data plotted against GTP hydrolysed per ribosome fits a logarithmic curve. The steep slope begins to flatten after 30 minutes and appears to plateau after 90 minutes. **(C)** GTP-Hydrolysis inhibition of EF-G in the presence of argyrins A-D and Fusidic acid as a control. Mean values and standard deviations are calculated from two independent experiments.

Argyrin B stabilizes EF-G on the ribosome

Some translation-targeting antibiotics lock their target protein on the ribosome, preventing access to the following factor. FA indeed traps EF-G on the ribosome (Bodley et al., 1969), as kirromycin does with EF-Tu (Vogeley et al., 2001). To test if argyrin bound EF-G is indeed incapable of ribosome-interaction as proposed (Nyfeler et al., 2012), or rather functions

similarly and traps EF-G on the ribosome, co-sedimentation assays of EF-G and 70S ribosomal particles were performed (Fig. 11). The comparison of free protein in the sucrose-cushion supernatant (SN) to the pellet (P), which consists of ribosomes and any protein bound to it, indicates whether the protein is stably bound to the ribosome or not. In the reaction with only GTP, EF-G can be found in the pellet only at sub-stoichiometric concentrations, and mostly in the supernatant. Conversely, in both the reaction with ArgB and the positive control of FA, it is stably bound to the ribosome at stoichiometric concentrations. As EF-G was added in 3-fold excess over ribosomes, it can still be found in the supernatant of all three reactions. In the absence of ribosomes EF-G does not pellet, confirming that pelleting is ribosome-dependent.

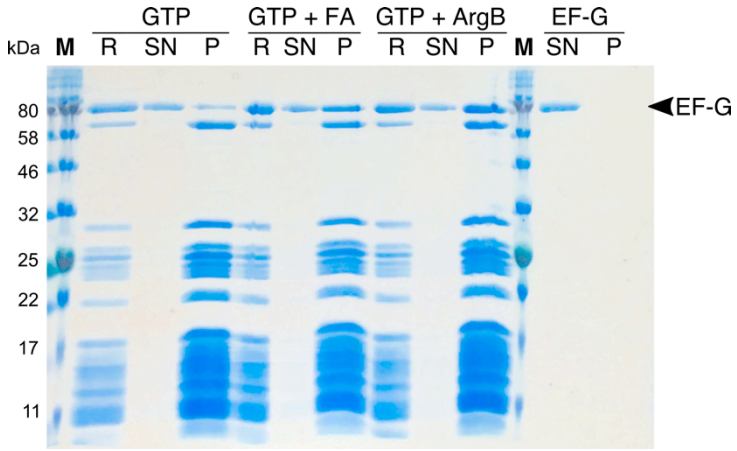

Figure 11: Argyrins traps EF-G on the ribosome. Co-Sedimentation assay of EF-G with 70S particles in the presence of FA or argyrin B; comparison of whole reaction (R) before subjecting it to a sucrose gradient, the remaining particles in the sucrose supernatant after centrifugation (SN) and in the pellet (P).

Cryo-EM structure of a 70S–EF-G–Argyrin B complex

In order to understand how argyrin B traps EF-G on the ribosome, 4.5 OD/mL of the 70S–EF-G–GTP–ArgB from the co-sedimentation assay reaction were applied to grids and the structure was determined by cryo-EM.

Processing of the high-resolution complex. The dataset was initially processed with RELION2. However, this yielded mediocre resolution of the argyrin binding site. Therefore, the dataset was reprocessed with RELION3, which holds novel polishing and multibody-refinement tools to increase resolution. 7,891 micrographs were subjected to a resolution cut-off of 3.5 Å and a defocus cut-off of 30,000. Residual 3,629 micrographs were manually inspected for thon-rings and ice quality. From the remaining 3,466 micrographs 610,946 particles were picked using GAUTOMATCH. After 2D-classification, focus-sorting was performed on 557,434 particles with a soft mask around EF-G, using four classes (Fig. 12A). All but class IV (~20%) showed extra density for EF-G, as well as argyrin B.

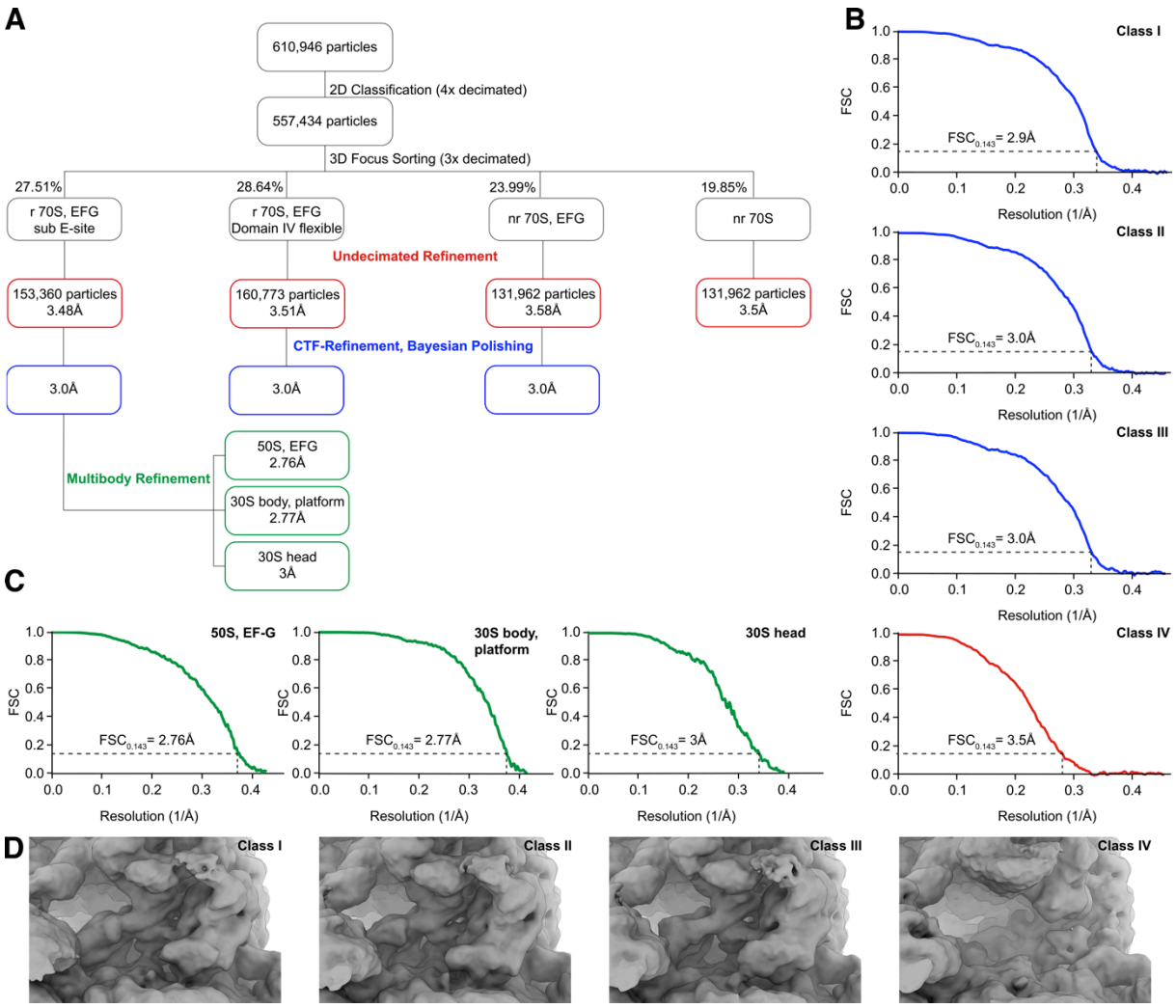

Figure 12: Processing of the *E. coli* 70S – EF-G Argyrin B complex. (A) From 610,946 2D classified particles, 557,434 were used for initial reconstruction. Subsequently, a focus mask of EF-G was applied for sorting into four classes. ClassI-III contained EF-G, whereas Class IV (19.85%) was an empty 70S. Following undecimated refinement were classes containing EF-G subjected to two rounds of CTF-refinement and Bayesian polishing. Multibody refinement of class I using masks for 50S+EF-G, 30S body+ platform, and 30S head significantly improved final resolution. **(B)** FSC curves of refined classes I-IV: EF-G containing classes CTF-refined and subjected to Bayesian polishing (blue curves), whereas the empty 70S class was only subjected to undecimated refinement (red curve) **(C)** FSC curves for multibody refined bodies of class I (green curves). **(D)** Decimated EF-G density in the A-site of class I-III and lack thereof in class IV.

Closer analysis of class I of the EF-G–Argyrin–70S complex showed a ribosome in the rotated state. Likewise, class II contained rotated ribosomes, however a slightly different rotation, and domain IV adopted an unreported conformation with lacking density for α_1 (Fig. 12D). Contrary to class I and II, class III contained non-rotated ribosomes. Domain II of EF-G formed varying interactions with the 30S in all classes. Class IV contained only empty ribosomes and was not further pursued after reconstruction of the undecimated volume. The final gold standard $FSC_{0.143}$ value for class IV indicated a resolution of 3.5 Å (Fig. 12B).

Class I-III were further CTF-refined and polished, and showed $FSC_{0.143}$ value of 3.0 Å (Fig. 12B). All classes were subjected to multi-body refinement for a better resolution. Several approaches were tried for the best outcome. First trials of multibody-refinement with four soft masks (EF-G, 50S, 30S body/platform and 30S head) resulted in a significantly

decreased resolution of EF-G. Since EF-G has multiple contacts with the ribosome, both attaching it to the 30S body and platform mask, as well as splitting and refining it with the respective interaction partners (30S head with domain IV, 30S body and platform with domain II-III, and 50S with domain I and V) was attempted. However, the only approach, which resulted in a better resolution, was applying three masks, for 50S with EF-G, the 30S head, and the 30S body and platform in class I (Fig. 12C). It was not possible to visualise the missing helix in class II, and class III did not represent a native state; hence class I was selected for further evaluation.

Resolution. Resolution estimation and locally filtered maps of post-processed polished and multibody volumes were calculated using SPHIRE1.3, as the built-in RELION resolution estimation did not seem accurate. Prior to multibody-refinement overall complex resolution was at 3 Å, yet resolution of the 30S was at 4-7 Å (Fig. 13A). After multibody-refinement a resolution of 2.8 Å for 50S and 30S body and platform, and 3 Å for the head was achieved (Fig. 13C). Resolution of EF-G could not be improved during multibody-refinement, and ranged between 3-4.5 Å after polishing (Fig. 13D).

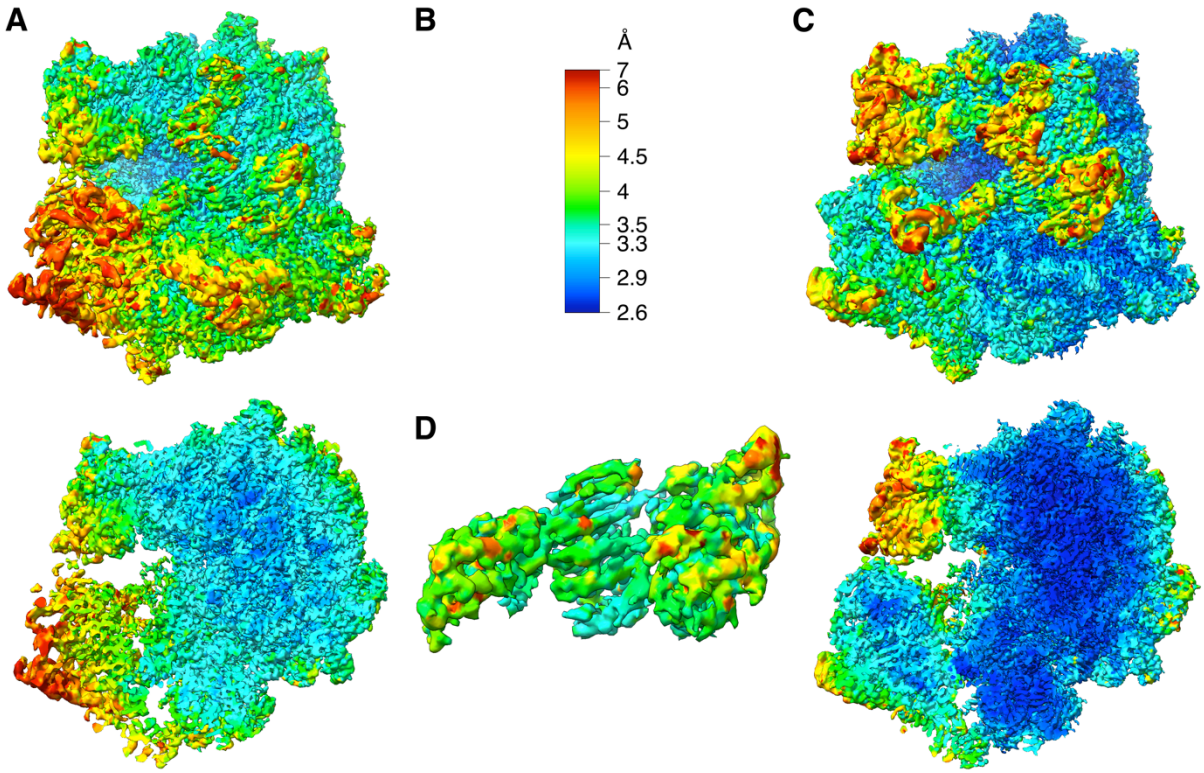

Figure 13: Resolution of the *E. coli* 70S – EF-G Argyrin B Class I (A) local resolution of locally filtered refined class 1 **(B)** resolution colour key for all resolution maps **(C)** local resolution of locally filtered multibody refined maps **(D)** local resolution of EF-G from polished class I.

Overall complex conformation. Class I comprises a rotated 70S with substoichiometric density for E-site tRNA, and EF-G in the A-site (Fig. 14A). As previously observed (Nyfeler et al., 2012), a density for Argyrin B was detected between domain III and V of EF-G (Fig. 14B). The resolution of EF-G was sufficient to see side-chain densities in parts of the protein. The density for Argyrin B is well resolved and covered all residues (Fig. 14C). bS1 was present in co-sedimentation assays, however, in the final reconstruction only helix 1 at the interface with uS2 was visible (Beckert et al., 2018).

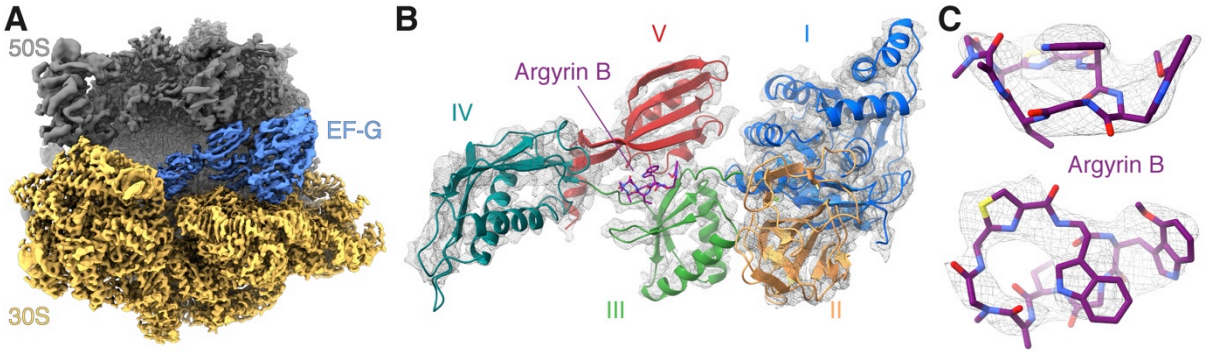

Figure 14: Cryo-EM structure of class I: *E. coli* 70S in complex with EF-G and Argyrin B. (A) Cryo-EM map of the 70S ribosome (30S, yellow; 50S, grey) and EF-G (blue). **(B)** Atomic model of EF-G and Argyrin fit into the cryo-EM density map. **(C)** Zoom in of Argyrin B density between domains III and V of EF-G.

The complex was formed with GTP, yet the density in the binding complies with GDP and a coordinated Mg^{2+}-ion, which is coordinated with T24 (Fig. 15A). Apart from switch I (aa 38-64), domain I was well resolved, displaying side chain densities (Fig. 15A). Alignment with an EF-G complexed with the non-hydrolysable GTP analogue GMPPCP (Fig. 15B) showed that density for the γ-phosphate was missing. A comparison of the binding site to other GDP-bound EF-Gs further confirms GDP (Fig. 15C, D), whereas in a hydrolysis-deficient EF-G, GTP extends further (Fig. 15E).

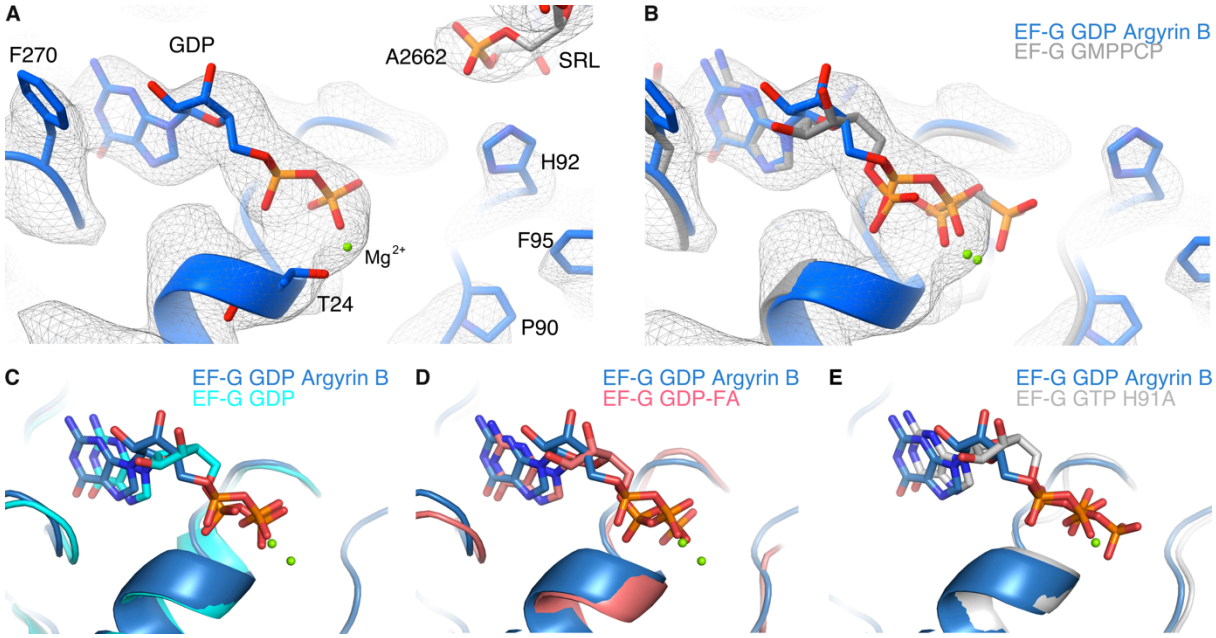

Figure 15: The GDP binding site and comparison to other GTP-analogues and conformations. (A) Cryo-EM density for GDP shown in mesh in the argyrin B bound EF-G complex. Comparison of conformations to **(B)** EF-G bound to non-hydrolysable GMPPCP (silver, PDB 4v9p), showing GTP does not fit the density **(C)** GDP-bound *T. thermophilus* EFG (cyan; PDB 2bm0) **(D)** fusidic acid bound *T. thermophilus* (PDB 4v5f) **(E)** hydrolysis-deficient H91A *E. coli* EF-G (PDB 3ja1).

Interactions between argyrin B and EF-G

A single density for argyrin B was found between domains III and V, forming interactions with both. The unmodified W1 moiety of argyrin B formed van der Waals interactions with the backbone of M682 in domain V as well as M617 and Y684 (Fig. 16A, C), and toward W448 in domain III. The modified W2 moiety of argyrin B was found to interact with P414 (Fig. 16A, B). A hydrogen bond was formed between the drug and the backbone of A489 and further van der Waals interactions were formed with the backbone in the linker between domain III and IV (Fig 16B, D). S417 was in hydrogen-bonding distance the backbone oxygen between W1 and the thiazole ring of argyrin B, and at a lower threshold connecting density could be observed (not shown). Furthermore, density suggests that the W2 forms van der Waals interactions with P414 and that the methoxy group of W2 in argyrin B forms a hydrogen-bond with the backbone of P414.

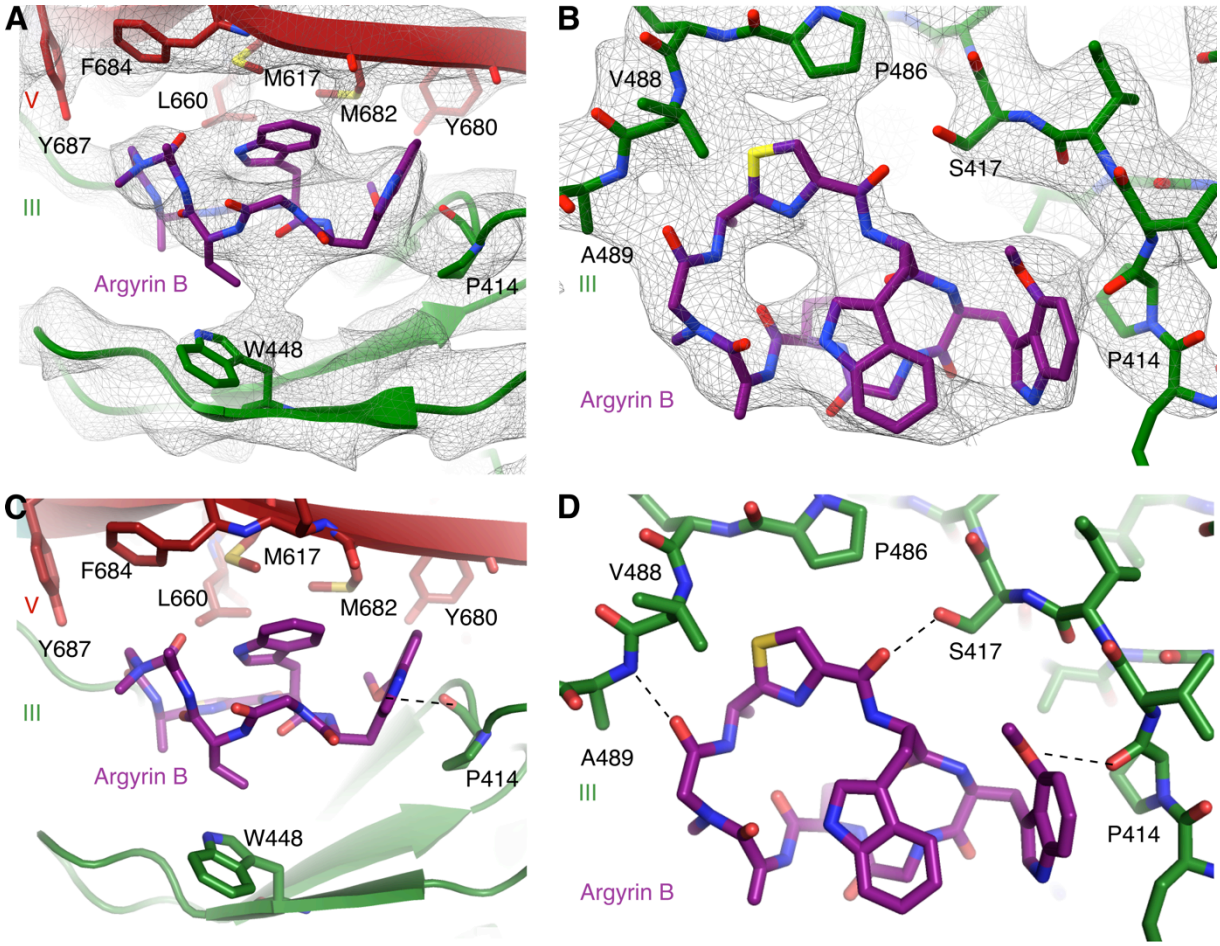

Figure 16: Interactions between Argyrin B and *E. coli* EF-G. (A, B) Cryo-EM densities displayed in mesh for the argyrin B (purple) binding site in EF-G between domain III (green) and V (red). For less noise, a Gauss filter of 0.8 was applied to the post-processed map. **(C)** Interactions or Argyrin with domain III (green) and V (red) are formed with Y687, M617 and M682 and weakly with L660. Y680 mutations can confer resistance in *pae*, but no interactions could be detected. **(D)** Hydrogen bonding with A489 and van der Waals interactions with V488, Q487, P486 occur but no density can be detected for interactions with S417.

EF-G trapped on the ribosome by Argyrin represents a GTP-like state

The complex was formed with GTP, but missing density for switch I (aa 38-64) and density matching to GDP indicated that GTP-hydrolysis and P_i release had occurred. Interestingly, alignment with an EF-G bound to a non-hydrolysable GMPPCP (Pulk & Cate, 2013) showed a remarkable similarity with a R.M.S.D of 0.8 (Fig. 17A), and alignment with a FA-bound state (Gao et al., 2009) had a R.M.S.D of 1.6 (Fig. 17B). Comparison of the EF-G–Argyrin complex to the GMPPCP and FA structure displayed only marginal differences. Although domain IV is generally flexible, it is similar in these three structures. Comparison to an EF-G-GDP complex in the absence of the ribosome showed a drastic movement in domains III-V (Fig. 17C). Furthermore, the *Pseudomonas aeruginosa* EF-G in complex with argyrin B

exhibited an elongated conformation (Fig. 17D), which had led to the assumption it was incompatible with ribosome binding.

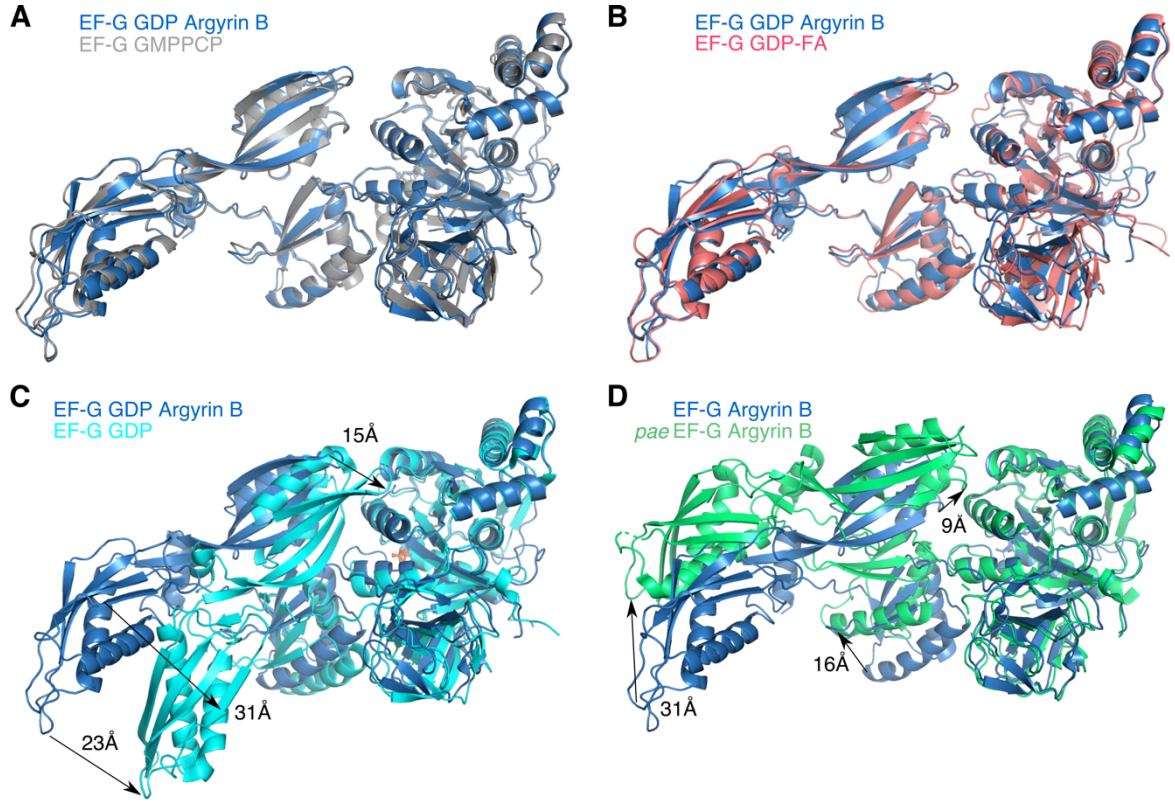

Figure 17: Alignment of EF-G structure on domain I to (A) *E.coli* EF-G bound to non-hydrolysable GMPPCP (silver, PDB 4v9p) R.M.S.D.: 0.8 **(B)** fusidic acid bound *T. thermophilus* (pink; PDB 4v5f) R.M.S.D.: 1.6 **(C)** GDP-bound *T. thermophilus* EFG in the absence of ribosomes (cyan; PDB 2bm0) R.M.S.D.: 5.7 **(D)** *P. aeruginosa* EF-G bound to Argyrin B (limegreen; PDB 4fn5)

Not only switch I beomes disordered upon P_i release, also switch II exhibits minor conformation changes. This movement became only apparent in an EF-G structure off the ribosome (Fig. 18A, cyan), whereas compared to EF-G–FA trapped on the ribosome or EF-G–GMPPCP, no changes were observed (Fig. 18A, pink, silver).

The major divergence between these structures can be found in domains II and III (Fig. 18B-D). Disordering of switch I leads to a loss of intramolecular interactions with switsch II and domain III. As a result, domain II and III move apart by 7 Å (Pulk & Cate, 2013; Gao et al., 2009), ultimately leading to the release of EF-G. In the argyrin B trapped EF-G, no distancing of domain II and III could be observed.

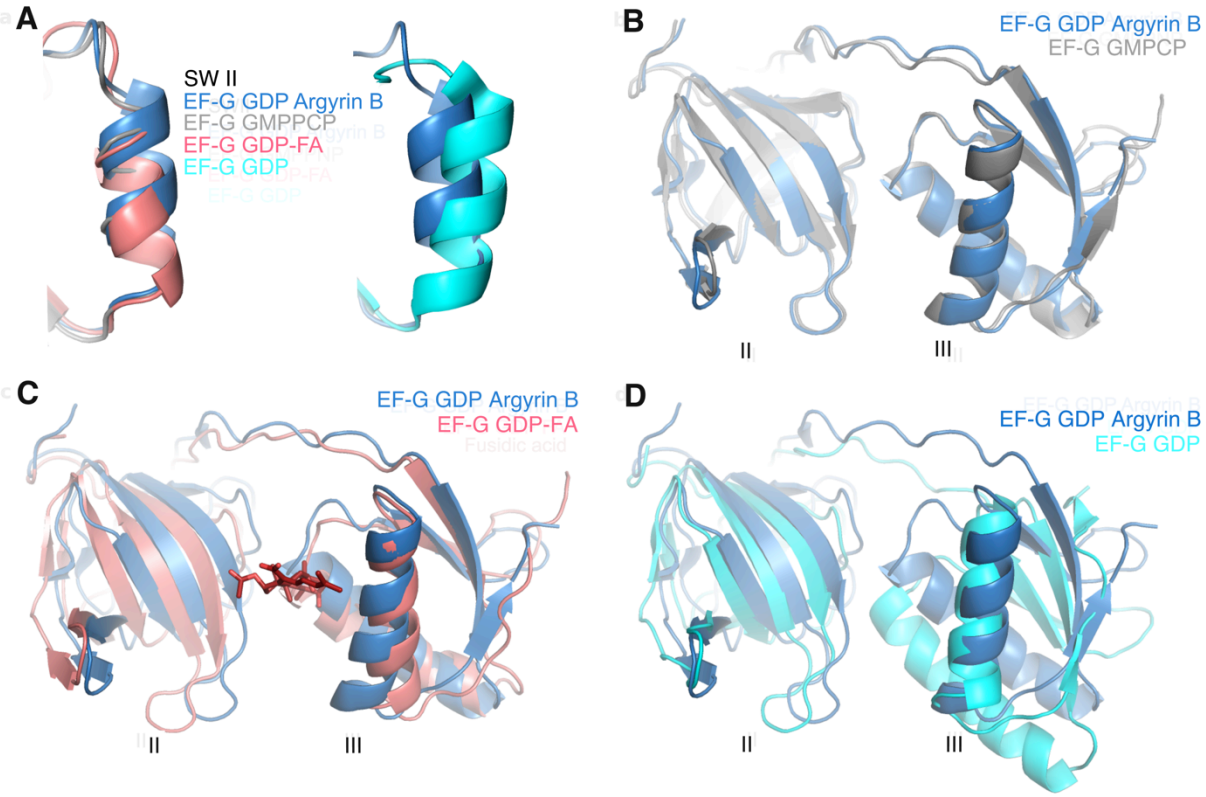

Figure 18: Comparison of switch II, as well as domain II and III conformations across the translocation cycle (A) Switch II remains stable in compared structures bound to fusidic acid (pink; PDB 4v5f) or non-hydrolysable GMPPCP (silver; PDB 4v9p), but moves in the GDP-bound EF-G (cyan; PDB 2bm0). Comparison of domain II and III conformations to **(B)** EF-G bound to non-hydrolysable GMPPCP (silver, PDB 4v9p) **(C)** fusidic acid bound *T. thermophilus* (pink; PDB 4v5f**)** and **(D)** *T. thermophilus* EF-G without ribosome binding (cyan; PDB 2bm0).

Interactions with the ribosome

EF-G displayed numerous contacts with the ribosome (Fig. 19). Domain II contacted the 16S rRNA by stacking interactions between F329 and A55 in h5 and R362 and U368 in h15 (Fig. 19A). H76 in S12 inserted between the β-sheets and α1 in domain III and formed a hydrogen bond with Q428 (Fig. 19B). Domain IV contacted the backbone of C1209-1210 in the head region of the 16S rRNA (Fig. 19C). Densities for the two loops in domain IV reaching towards the A-site were not well resolved and hence contacts with h44 could not be determined. In the large subunit, domain V contacted the 23S rRNA with interactions between the backbone of L642 and A1067 and hydrogen bonds between R637 and U2473 (Fig. 19D). An interaction of H92 with the phosphate of A2662 in the SRL was detected at a higher threshold than depicted in Fig. 15A, as well as other interactions of the backbone of domain V with A2660.

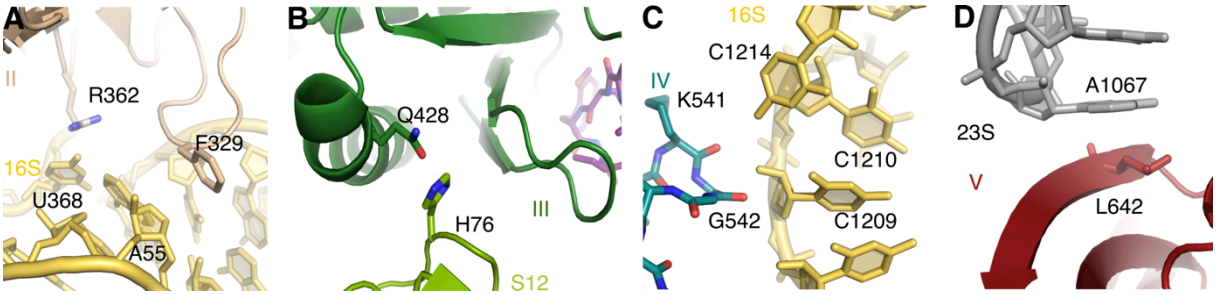

Figure 19: Interactions of the Argyrin B inhibited EF-G with the 70S Ribosome (A) Domain II contacts the 16S rRNA by stacking interactions between R362 and U368 in h15 and F329 and A55 in h5 **(B)** H76 in S12 forms a hydrogen bond with Q428 in domain III. **(C)** Domain IV contacts the 16S rRNA at the head, by G542 interacting with the phosphate backbone of C1209 and C1210 in h34 **(D)** Domain V interacts with the 23S rRNA at A1067 and U2437.

Intramolecular interactions

While the conformation was similar to the GMPPCP-bound EF-G, switch I was disordered and interactions between it and domain III could no longer be established. Other interactions within the molecule were still present. As in the GMPPCP reference structure, K323 contacted the backbone of A66, while amino acids in switch II, namely R101 and I97, established contacts with domain III, E441 and P443, respectively (Fig. 20A). Stacking interactions between residues R491 and P570 from domain IV with Y687 in domain V could lead to stabilisation of domain IV (Fig. 20B). Contrary to the GMPPCP bound EF-G, no interaction between R639 and E614 could be detected. Rather, R639 established contacts with P659 ad P691 (Fig. 20C).

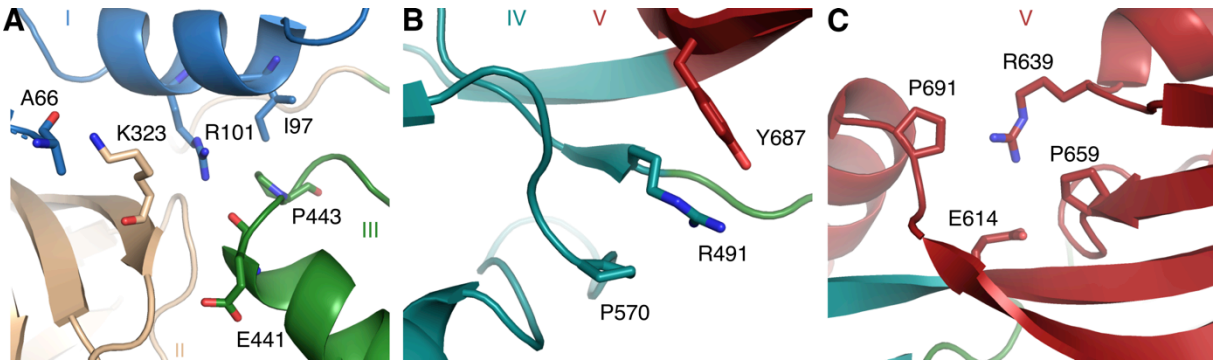

Figure 20: Intramolecular interactions of EF-G (A) interactions between domain I (blue), II (sand) and III (green) **(B)** stacking interactions between domain IV (teal) and V (red) could lead to stabilisation of domain IV. Y687 is also contacted by argyrin B. **(C)** interactions within domain V (red).

Argyrin binding obstructs hydrolysis induced domain movement of EF-G

Comparison with the GDP-bound EF-G off the ribosome and alignment on the G-domain showed large movements within domain III-V (Fig. 17C). To detect possible movement of domain III in relation to domain V, and vice versa, the structures were aligned on either domain III (Fig. 21A, C) or domain V (Fig. 21B, D). Alignment on domain III showed some

residual similarities in domains I and II. Domain V, however, showed a movement by about 20 Å towards domain I. Conversely, alignment on domain V only showed similarities in domain IV. A closer look at the argyrin-binding site of the domain III aligned structures (Fig. 21C) again displayed the movement of domain V away from the binding site. Conversely, in the domain V aligned structures, domain III moved towards the binding site.

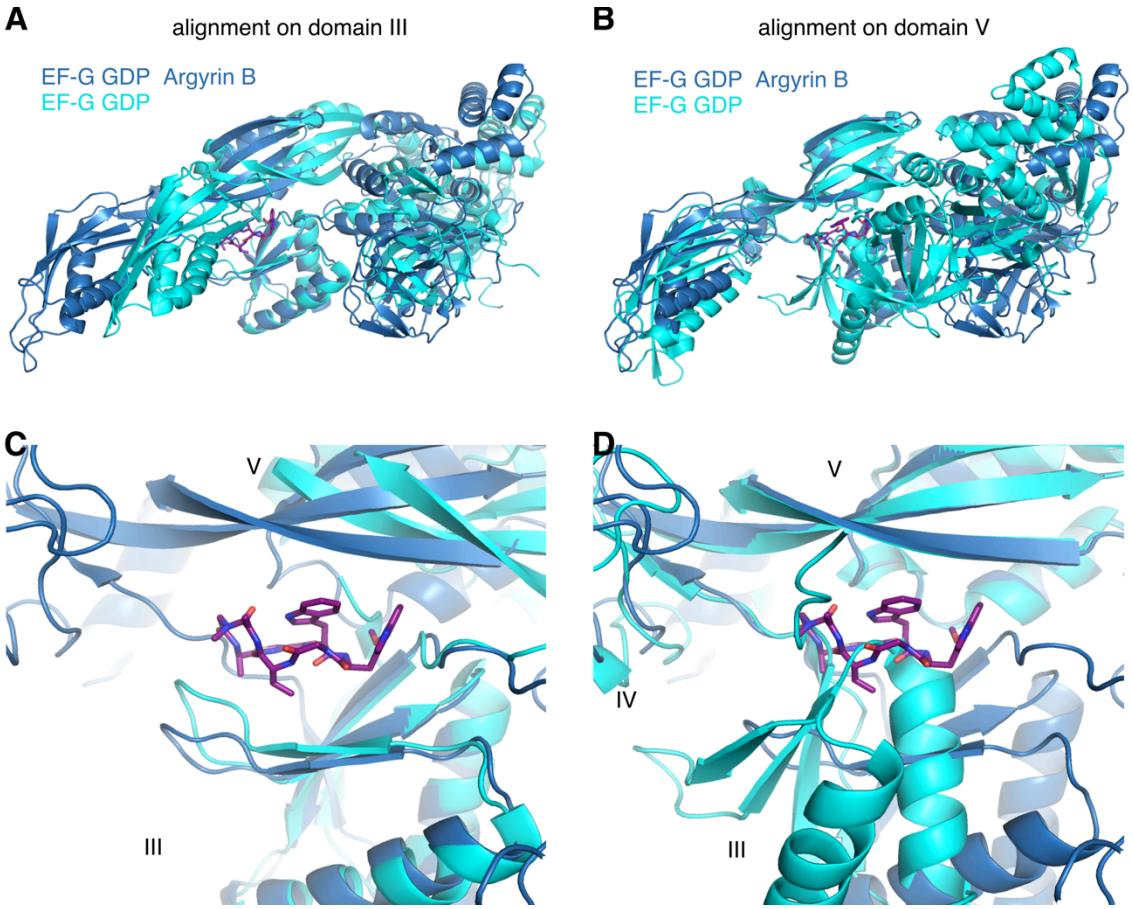

Figure 21: Comparison to the off-ribosome EF-G–GDP state. Overview of the complete EF-G, aligned on **(A)** domain III or **(B)** domain V. Zoom in on the argyrin binding site of **(C)** alignment on domain III shows the movement of domain V away from the binding site (domain I, II and IV not displayed for clarity), whereas **(D)** the domain V aligned structure shows the drastic movement of domain III into the binding site (domain I and II not displayed for clarity).

5. Discussion

5.1. Exploration of the alarmone mediated stringent response effect on ribosome-associated GTPases

For survival under stressful conditions like nutrient deprivation, bacteria deploy the stringent response. Secondary messengers are produced by RSH-type proteins (Atkinson et al., 2011), which utilise ATP to transfer a pyrophosphate moiety onto the 3'-OH of either GDP or GTP, resulting in (p)ppGpp. One of the main targets of these so-called alarmones is RNAP, leading to transcription inhibition, while simultaneously allowing selective transcription of vital genes. Naturally, it stands to reason that these GDP/GTP derivatives can bind to and inhibit GTPases as well. Indeed, a number of studies have shown that GTPases associated with ribosome assembly and translation are targeted by the stringent response (Bennison et al., 2019). A number of structures for (p)ppGpp targets exist to elucidate the respective mechanism of inhibition (Steinchen & Bange, 2016), however, there are only a few regarding GTPases, like assembly co-factor ObgE (Buglino et al., 2002), RF3 (Kihira et al., 2012) or the ribosome-associated GTPase BipA (Fan et al., 2015; Kumar et al., 2015). Nevertheless, neither the mechanism of action is well explained for most of them, nor why some are able to hydrolyse pppGpp, whereas others are not. We set out to further characterise and structurally analyse the mode of inhibition of alarmones for RbgA and EF-Tu.

5.1.1. RbgA

For cryo-EM reconstruction of a RbgA-50S complex, 0.4 µM *B. subtilis* 50S were incubated with 1 µM *B. subtilis* RbgA and 500 µM of GMPPNP. Although RbgA functions on immature 45S particles, its GTP hydrolysis is stimulated only by mature 50S (Achila et al., 2012). Consequently, GMPPNP stabilises it on the 50S, and co-sedimentation assays showed stable binding of RbgA to the ribosomal particle following centrifugation. Cryo-EM reconstruction of this complex using FREALIGN resulted in 4 distinct classes, two of which were of low resolution and showed bias, owing to the natural predisposition of 50S particles to be positioned flat on the subunit interspace. Two higher resolved classes constituting a mature 50S and a 50S with missing densities for H68-H71 were resolved to 3.58 Å and 3.65 Å, respectively. The lack of H68-H71 resembled immature $45S_{RbgA}$ particles (Li et al., 2013). Higher threshold and low-pass filtering of the map visualised H71 to be only slightly distorted and an extra density was present in its proximity. As it coincided partially with the RbgA binding site, we speculated that binding of RbgA lead to a destabilisation of this region, and

that the additional density contained both RbgA and H67-H69 in a highly flexible state. Reconstruction utilizing Relion2.0 did not result in improved maps. Reviewer requested negative controls for the cryo-EM with *B. subtilis* 50S revealed that H67-H71 are unstable in both reconstructions, independent of RbgA binding (Fig. 22A). This indicated that RbgA likely dissociated during grid making. To counteract dissociation and get a functional 50S-RbgA complex, we cross-linked the components prior to grid making. However, electron densities were poorly resolved and did not yield any detectable 50S-RbgA complex.

Recently, the structure of a *B. subtilis* $45S_{RbgA}$-RbgA complex was solved (Seffouh et al., 2019) (Fig 22B, C). $45S_{RbgA}$ were purified from a Δ*rbgA* background and mixed with heterologously expressed RbgA at a ratio of 1:40 (0.5 µm 45S to 20 µM RbgA) under the addition of 2 mM of the non hydrolysable GTP analogue GMPPNP. This is in stark contrast to our ratio of 1:2.5, and could indicate that for successful reconstitution higher concentrations of RbgA and nucleotide are necessary.

Comparing our observed affinity to GTP and (p)ppGpp to previous findings (Corrigan et al., 2016), indicated that they are similar for GTP (5.56 ± 1.88 µM vs. 5.04 µM), and comparable for pppGpp (2.65 ± 0.45 µM vs. 4.31 µM). For ppGpp, however, there is a difference of one order of magnitude (0.49 ± 0.06 µM vs. 3.26 µM). The experimental setup was different, as in our case we varied the nucleotide concentration from 10 nM to 100 µM, and kept RbgA concentration stable at 200 nM. Corrigan and colleagues, however, applied 2.78 nM of α-^{32}-ppGpp and added 100 µM of competing nucleotide and varied the RbgA concentration from 10 nM to 100 µM. Possibly this setup is more suitable for measurement of high affinities.

Where Corrigan and colleagues saw a drop in GTP hydrolysis activity in the presence of 70S and 1 mM (p)ppGpp to 20% residual activity, we observed maximum inhibition at a ratio of GTP:(p)ppGpp of 1:4 (0.25 mM and 1 mM), and then only to around 50%. This two-fold difference likely originates in contrasting experimental setups. Firstly, incubation time in our setup was 30 min at 37 °C, thus only half of what Corrigan et al. used. More importantly, they mixed 10 µM of RbgA with only 118 nM 70S and 2.78 nM of α-^{32}-P-GTP, whereas we used equimolar concentrations of RbgA and 70S at 1 µM.

We set out to solve crystal structures of *Staphylococcus aureus* RbgA in complex with GDP, GMPPNP as well as (p)ppGpp. None of the structures could show an ordered G2 domain, indicative of an inactive conformation of RbgA, likely because the δ-phosphate would clash with the G2 domain (Fig. 22D). However, a structural rearrangement of G2 to coordinate a Mg^{2+} is necessary for GTPase activation. Comparison of our structure with the ribosome-bound RbgA indicates that the ε-phosphate would also clash with the phosphate backbone of

G1779 (Bsu numbering; Eco: G1770) (Fig. 22D). This is in agreement with our preliminary co-sedimentation assays of 50S and RbgA, which showed an increase in unbound fraction upon addition of (p)ppGpp, albeit minimal. However, the 3'-OH added pyrophosphate could adopt a different conformation on the ribosome as the GTP-binding pocket faces toward the C-terminal RNA interacting domain, which is 8 Å away and cannot constrict the movement of the pyrophosphate.

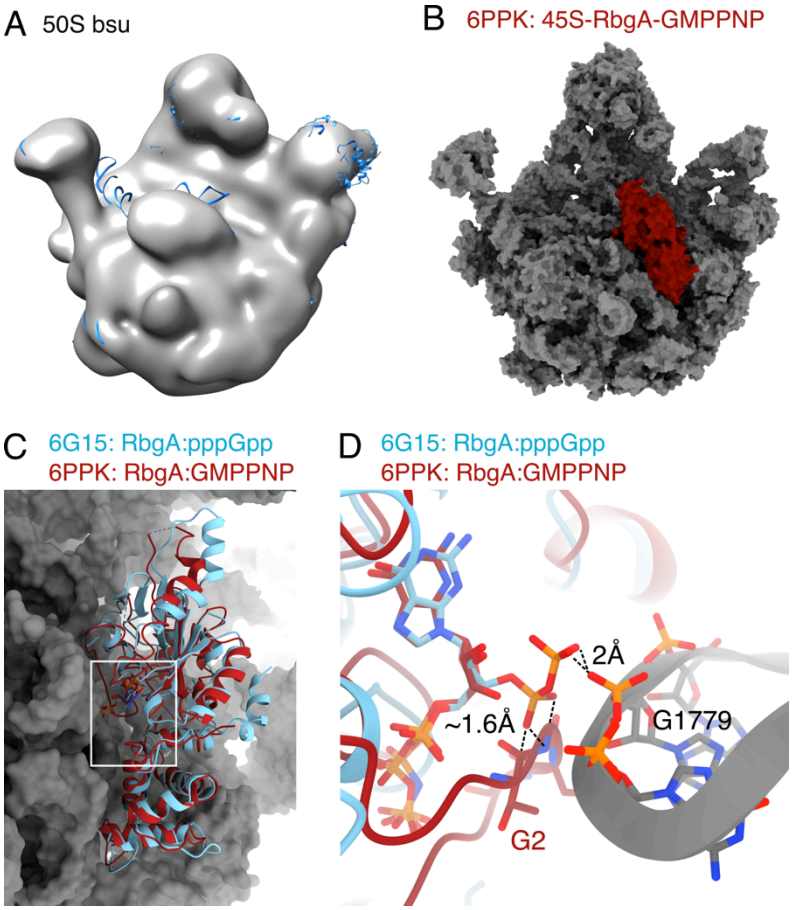

Figure 22: RbgA on the large subunit. **(A)** Spirit reconstruction of a *B. subtilis* 50S in the absence of any ligands. Fitting of the 3J9W 50S shows missing H68-H71, like the reconstruction of our 50S-RbgA-GMPPNP complex. **(B)** Cryo-EM density of a *B. subtilis* 45S (grey) complexed with RbgA-GMPPNP (red) **(C)** Alignment of our *S. aureus* RbgA-pppGpp structure (blue) to the RbgA-45S complex. The GTP binding pocket (white box) is localised in the middle of the protein on the side facing the ribosome. **(D)** Zoom in to the GTP-binding site of RbgA in proximity to H64. The switch I containing G2 motif becomes ordered upon binding to the ribosome. The 3'-OH added pyrophosphate of alarmones would likely clash with G2 and H64.

Although the structure of the *B. subtilis* $45S_{RbgA}$-RbgA complex was solved, and G2 adopts a structured conformation upon binding to the ribosomal particle, the exact mechanism of how hydrolysis is induced in RbgA still cannot be explained entirely. Its GTPase activity is stimulated primarily by matured 50S particles. In contrast to most other ribosome-associated GTPases, RbgA is not dependent on the SRL to position the catalytically active Histidine for hydrolysis. In the $45S_{RbgA}$-RbgA complex, His9 is with a distance of 8 Å not positioned close enough to induce hydrolysis. It stands to reason that maturation of the 23S rRNA is accompanied by a restructuring of H92, followed by the rearrangement of CR1 to position His9. Comparison to a *B. subtilis* 70S structure (Sohmen et al., 2015) (PDB 3jw9) indeed shows a difference of 2-4 Å upon accommodation of the neighbouring H71, however away

from CR1. Conceivably, this will lead to the re-structuring of CR1 and positioning of His9 for hydrolysis.

Recently, the mitochondrial homolog Mtg1 has been solved in complex with mtEngA on a mitochondrial ribosome biogenesis intermediate (Jaskolowski et al., 2020). A comparison of the complexes to gain further insight into the possible GTPase mechanism is not possible, as the deposited structures have not been published yet. Similarly to Mtg1, the yeast homologue of RbgA, Lsg1, was not observed in the absence of the co-factor Nmd3 (Malyutin et al., 2017). Hence, a similar approach might be necessary for a bacterial complex to assess the exact GTPase mechanism: RbgA-GMPPNP mixed with purified $45S_{RbgA}$, assembly co-factors like YphC and YsxC, which operate on the same intermediate (Ni et al., 2016), and r-proteins to give an authentic 50S-RbgA complex.

Concluding, contradicting data about whether (p)ppGpp will allow RbgA binding to the 45S exists. Contrary to EF-Tu (Wieland et al., 2020, unpublished)(Hamel & Cashel, 1974), RbgA cannot hydrolyse pppGpp. This is in agreement with our structural analysis, which shows that binding of (p)ppGpp prevents G2 from adopting a conformation permitting Mg^{2+} coordination and correspondingly GTP hydrolysis. Although binding of (p)ppGpp could obstruct interaction with the 50S subunit, it has been shown that pppGpp can lead to stabilisation of RbgA on the 50S (Achila et al., 2012). Screening for complex formation with similar concentrations as used for the $45S_{RbgA}$-RbgA (Seffouh et al., 2019) could be conducted, i.e. 20 µM RbgA, 2 mM (p)ppGpp and 0.5 µM 45S or 50S. Consequently the complete mechanism of RbgA inhibition by alarmones still remains unsolved and further studies need to be conducted.

5.1.2. EF-Tu

All translation-associated GTPases (IF2, EF-Tu, EF-G, RF3, BipA) have been implicated to be targeted by (p)ppGpp (Bennison et al., 2019). To ascertain inhibition of translation by (p)ppGpp, we used a transcription-translation coupled system overexpressing GFP with concentrations of 0, 10, 100, and 1000 µM. We saw an inverse correlation between expression and increasing alarmone concentration, with only 30% and 40% of residual expression levels at 1000 µM. Although transcription is also targeted by (p)ppGpp, an effect in this coupled system is unlikely. For *E. coli* and other α-, β-, γ-, δ-proteobacteria a conserved MAR sequence at the RNAP N-terminus has been determined to be the target for (p)ppGpp (Ross et al., 2013; Hauryliuk et al., 2015). Like the *T. thermophilus* or *B. subtilis* RNAPs, T7 does not possess this sequence, and for these bacteria it has been suggested that alarmones inhibit

transcription by depleting the GTP pool rather than by direct binding. Consequently, a transcription-translation coupled system deploying T7 for transcription is likely not inhibited by (p)ppGpp at the level of transcription, so that the inhibition we observed is indeed inhibition of translation. Our translation inhibition levels are also in accordance with early translation assays showing ~65% inhibition of translation from pre-transcribed mRNAs (Legault et al., 1972). However, since (p)ppGpp inhibits other translation-associated GTPases, a direct correlation of translation inhibition to EF-Tu inhibition cannot be deduced.

Early data indicates that EF-Tu can form a ternary complex in the presence of pppGpp and deliver tRNA to the ribosome (Hamel & Cashel, 1974; Pingoud et al., 1983). Thus, we initially attempted to form a native 70S–EF-Tu–tRNA–(p)ppGpp complex. To this end we employed the ErmBL construct, which stalls translation in the presence of erythromycin, due to an interaction of Val9 and Asp10 with the PTC (Arenz et al., 2014b). The stalled complex still allows binding of the downstream encoded Lys11 in the A-site tRNA, which could trap EF-Tu on the ribosome. Transcription-translation in the presence of Ery was allowed to go on for 25 min before alarmones were added to the reaction to trap EF-Tu during delivery to the stalled ribosome. Sucrose gradients were fractioned to analyse the ribosome profile, and addition of Ery compared to the negative control showed a prominent disome peak, indicating that stalling was successful. One reaction was carried out in the absence of Ery but in the presence of pppGpp, and did not show an increased disome peak. Sucrose gradient fractions were precipitated and analysed by Western Blotting to confirm the presence of EF-Tu on stalled 70S ribosomes. However, EF-Tu could only be detected in the cytosolic fraction in all samples. We concluded that after allowing the reaction for 25 min all complexes were already stalled with an accommodated tRNA occupying the A-site, making trapping of EF-Tu on the stalled complex impossible. The experiments could be repeated with the addition of alarmones from the beginning for higher chances of trapping EF-Tu on the stalled ribosome. Alternatively, the ErmBL-SRC could be purified and mixed with EF-Tu, Lys-tRNA^{Lys} and alarmones for complex formation.

In order to get structural insights, we analysed a crystal structure of EF-Tu complexed with pppGpp. The overall structure was comparable to an inactive GDP-bound state. Additionally, switch I could not be modelled due to adopting an unstructured conformation. Interaction of alarmones with the same binding site as GTP/GDP had been shown by a low-resolution crystal structure (Suck & Kabsch, 1981), and concordantly we identified a density in the GTP domain. Surprisingly, despite the complex being formed with pppGpp, the density matched a ppGpp and Mg^{2+} density. Ribosome-independent pppGpp hydrolysis to ppGpp had been

described before (Hamel & Cashel, 1974) and we verified that hydrolysis was indeed EF-Tu dependent; in the absence of EF-Tu no hydrolysis was observed, and hydrolysis showed a strong correlation with EF-Tu concentration. As EF-Tu depends on EF-Ts as a GEF *in vivo*, we examined whether it also has the capacity to exchange alarmones. In our fluorescent screen, we found that the exchange of GTP for ppGpp or GDP is accelerated by EF-Ts, as has been reported previously (Arai et al., 1972). Furthermore, we show that EF-Ts able to displace any bound alarmone from EF-Tu, in concordance with earlier studies (Miller et al., 1973).

For ternary complex formation of EF-Tu–GTP–tRNA, switch I and II adopt a specific conformation to allow aa-tRNA binding. Upon further examination of the crystal structure and comparing it to both the inactive GDP and the active GTP (GMPPNP) bound state, we found that the 3'-OH pyrophosphate moiety would sterically hinder switch I from adopting either the α-helical (GTP) or the β-sheet (GDP) ordered conformation. This would render EF-Tu incapable to accommodate and interact with tRNA. This prompted us to carry out electrophoretic mobility shift assays (EMSAs) to monitor native ternary complex formation. In the presence of GTP, a ternary complex could be formed with EF-Tu and Lys-tRNA^{Lys}. At equimolar concentrations of GTP and (p)ppGpp, the guanosine-tetraphosphate already showed near-complete inhibition of ternary complex formation, and the pentaphosphate had only a minor effect. At a four-fold excess of (p)ppGpp, ternary complex formation was completely abolished. Moreover, we screened ternary complex formation via fluorescent spectroscopy with Cy5Q labelled EF-Tu and Cy3B Phe-tRNA^{Phe}. In this combination, Cy3B functions as a donor and Cy5Q as a quencher, so that upon ternary complex formation the fluorescent signal is low, and is increased upon complex dissociation. Correspondingly, only very low levels of fluorescence could be measured in the presence of only GTP, EF-Tu, and tRNA. Upon addition of ppGpp, an increase in fluorescence of 50% could be observed, and additional supplementation of GDP lead to a recovery of 80% of the fluorescent signal. Notably, the ratio of GTP to ppGpp/GDP in the fluorescent assay was 1:10. Displacement of GTP by ppGpp is in agreement with the EMSA, which also showed inhibition of ternary complex formation and our affinity assays, which show that both ppGpp and GDP can disengage GTP from EF-Tu. Hence, we concluded that (p)ppGpp inhibits EF-Tu by obstructing ternary complex-formation.

However, this study of alarmone mediated inhibition of EF-Tu shows multiple disparities and contradictions to earlier studies (Hamel & Cashel, 1973; Miller et al., 1973; Hamel & Cashel, 1974; Pingoud & Block, 1981).

Our affinity measurements of alarmones to EF-Tu and dissociation constants differ vastly from other studies. For reference we calculated a Mant-GTP K_d of 1.6 ± 0.4 µM. This is in stark contrast to the previously reported Mant-GTP K_d of 60 nM (Gromadski et al., 2002). Likewise, our K_d for GDP (0.4 ± 1.3 µM) differed considerably from previously reported values. Indeed the K_d for GDP has been indicated to be in the single-digit nanomolar range multiple times (Arai et al., 1974; Maracci & Rodnina, 2016), which results in a difference of two orders of magnitude. EF-Tu has a substantially lower affinity for GTP, reported to be in the 60-500 nM range (Arai et al., 1974; Fasano et al., 1978; Maracci & Rodnina, 2016). This is somewhat closer to our calculated values of 1.4 ± 1.1 µM, but still shows a discrepancy. Similarly, the K_d value for ppGpp was previously reported to be at 8 nM (Miller et al., 1973), whereas our calculated value lies at 0.5 ± 1.2 µM. Since ppGpp has been reported to be able to displace even GDP from EF-Tu both in the presence as well as in the absence of EF-Ts (Arai et al., 1972; Miller et al., 1973), it must have a higher affinity than GDP, which our values do not comply with. Nevertheless, it should be mentioned that in an earlier study a K_I value of 600 nM has been calculated for ppGpp, which is comparable to our value (Rojas et al., 1984); however, this was tested in a competition assay of ppGpp and GDP, rather than ppGpp and GTP, and their K_d for GDP was 60 nM. As our reference value for Mant-GTP is already higher than past research documented, it could indicate that the majority of purified EF-Tu is not present in a nucleotide binding compatible conformation. Another explanation is that the setup, like for RbgA-(p)ppGpp affinity measurements, is unsuitable to detect low-molecular affinities.

Similarly, the validity of the EMSA is unclear, as only a minority of tRNA displayed a shift. A variety of factors could account for this. For one is the EF-Tu substrate for ternary complex formation aminoacylated tRNA, so applied tRNA could have been insufficiently charged. Furthermore, considering the aforementioned discrepancy in affinity measurements, a fraction of purified protein could be misfolded or after purification slightly denatured EF-Tu incapable of nucleotide and/or tRNA interaction.

In contrast to RbgA, EF-Tu, along with other GTPases like IF2, has been reported to be capable of using pppGpp as a substrate to carry out tRNA delivery (Hamel & Cashel, 1973; Hamel & Cashel, 1974; Milon et al., 2006). ppGpp on the other hand inhibits function by preventing ternary complex formation (Legault et al., 1972; Miller et al., 1973; Pingoud & Block, 1981). This is in contrast to our EMSA results. Observed inhibition could be due to ppGpp contamination of the pppGpp preparation. If one quarter of the prepared compound was indeed ppGpp, at 1 mM supposed pppGpp, the ppGpp would be equimolar to added GTP,

hence leading to disassembly of the ternary complex as seen for the ppGpp containing reaction.

In our structure of ppGpp–EF-Tu–Mg^{2+} we observed switch I in a disordered conformation. We reason that this is the result of steric clash with the 3'-OH pyrophosphate. However, we cannot make any statements about structural arrangements prior to hydrolysis. Recent time-resolved cryo-EM shows that after hydrolysis and P_i release, switch I temporarily becomes disordered before it adopts the GDP-associated β-sheet conformation (Loveland et al., 2020). Structural analysis of RbgA also lead to the assumption that the 3'-OH pyrophosphate would inhibit G2 ordering. G2 becomes ordered upon interaction with the 50S or immature 50S particles (Seffouh et al., 2019). Conversely, biochemical data suggests pppGpp traps RbgA on the 50S (Achila et al., 2012), which indicates that in RbgA, there is no steric clash caused by alarmones. In EF-Tu, like in RbgA, the pyrophosphates are not coordinated by any protein residues, and could likewise adopt a different conformation to allow switch I ordering. Taken together, it seems likely that we caught an EF-Tu intermediate as otherwise it remains enigmatic how EF-Tu can hydrolyse pppGpp if it were incompatible with switch I ordering. To elucidate this concern, complex formation with hydrolysis deficient EF-Tu (e.g. His84Ala (Daviter et al., 2003)) could be undertaken.

Lastly, the physiological relevance of (p)ppGpp mediated inhibition of EF-Tu *in vivo* has always been disputed (Miller et al., 1973; Pingoud et al., 1983; Rojas et al., 1984). In Poly-Phe assays a ratio of 1:5 showed a reduction of 78% (Miller et al., 1973). Under stringent response inducing amino acid starvation conditions the ratio of GTP to ppGpp is close to 1:3 (280:800 µM) (Zborníková et al., 2019). From this we can infer that only about 40% of translation would be inhibited *in vivo* – that is if all present (p)ppGpp interacts only with the translational GTPases. Additionally, EF-Ts can readily displace (p)ppGpp and exchange it for GTP, and *in vivo* concentrations of EF-Ts are greater than used in the cited assay. GTP-bound EF-Tu then forms a ternary complex, which is directly transported to the ribosome. To verify physiological relevance of translation inhibition, one could induce (p)ppGpp over production of a cloned SAS protein, while simultaneously expressing a fluorescent reporter like GFP or β-galactosidase for subsequent assays. Prerequisite for such an assay would be that transcription of both loci is under the control of an alarmone-independent RNAP, possibly T7, which should be confirmed beforehand by measuring transcript levels in the presence of alarmones.

5.2. Investigation of novel translation inhibiting antibiotics

A steady increase of antibiotic resistant microbes has boosted the search for novel antibiotics. A group with a concerning resistance profile are classified together as the *ESKAPE* organisms, where each letter stands for the initial of the species. Only two of these organisms (*Enteroccocus faecium* and *Staphylococcus aureus*) are Gram-positive. The others (*Klebsiella pneumonia*, *Acinetobacter baumanii*, *Pseudomonas aeruginosa* and *Enterobacter* spp.) are Gram-negative bacteria and thus possess an additional outer layer, which gives an advantage toward antimicrobial compounds targeting and crossing the cell wall.

To contribute to the fight against antibiotic resistance, we routinely investigate novel compounds for antibacterial activity and check for translation inhibition. Additionally, we identify targets and resistance mutations and attempt to describe the mechanism through which the compound exerts its function. Part of our investigations were the drugs Tetracenomycin X and the family of argyrins.

5.2.1. TcmX

Gram-positive bacteria have been an invaluable source for the identification of novel antibiotics. The tetracenomycin family has first been described in 1979 as a metabolite purified from *Streptomyces glaucescens* (Weber et al., 1979). Crystal structure analysis revealed a tetracyclic aromatic polyketide containing a naphthacenequinone chromophore. A structural resemblance to the DNA intercalator doxorubicin and preliminary, yet never published data, suggested that tetracenomycins exert their activity by disrupting DNA replication (Hutchinson, 1997). Growth inhibition assays showed activity against *Streptomyces* and other *Actinomycetes*, however, none against other Gram−positive or −negative bacteria, so only against strains similar to the producer. Additionally, TcmC and TcmX showed a strong inhibition of murine leukaemia cells (Rohr & Zeeck, 1990). Like other compounds from that time, this family of antibiotics was not further pursued and re-discovered multiple times in other organsims, including by us. Continuous testing for new antimicrobial compounds in a collaborating lab first revealed that TcmX indeed inhibits translation, rather than DNA replication (Osterman et al., 2020). This was unexpected as TcmC had previously not shown any inhibition of Poly-Phe synthesis (Weber et al., 1979). Resistance mutation analysis revealed a binding site on the 50S, rather than on the 30S, where another similar compound, tetracycline, binds in the decoding centre, obstructing A-site tRNA binding. More specifically, we found resistance mutations found at the beginning of the nascent peptide exit tunnel, in proximity to the PTC.

While mutation analysis can indicate the binding site, the exact position was determined by cryo-EM. Processing of a 70S-TcmX complex with RELION3 revealed one viable class of 70S particles with 29% (161,195 particles). The class was resolved to a resolution of 2.9 Å. The search for additional densities confirmed the binding site to be at the beginning of the NPET, close to the PTC, consistent with resistance mutations. The drug stacks upon the non-canonical U1782-U2586 base-pair with its naphthalene rings C and D. Additionally, two magnesium ions are coordinated by oxygens on the B- and C, and the A-ring, respectively. One magnesium is in hydrogen-bonding distance to the phosphate backbone of U2441. The second magnesium is in hydrogen-bonding distance to N3 of A2587. Besides stacking onto the U1782-U2586 base-pair, the C4-hydroxy group in ring A of TcmX forms a strong interaction with O4 of the uracil base of U1782. A2062 is in proximity to the TcmX binding site and has been shown to play an important role in macrolide mediated stalling by protruding into the peptide exit tunnel (Hansen et al., 2002; Vazquez-Laslop et al., 2008). In the presence of TcmX, A2062 is not well resolved, however it appears to adopt an outward conformation, perpendicular to TcmX, effectively narrowing the path of the nascent chain by several angstrom. The C9-carbomethoxy moiety is in proximity to U2585 (3.3 Å to the U2585 2'-OH), which adopts an activated, induced conformation for peptide-bond formation. Density for the base is badly resolved, which makes an exact determination of the conformation impossible. The complex was formed with a non-translating 70S ribosome, so it remains undetermined if during translation in the presence of TcmX U2585 could become stuck in an un-induced conformation, as is the case for the ErmBL staller in the presence of erythromycin (Arenz et al., 2014b).

Moreover, we employed toe-print experiments to confirm whether the drug inhibits translation at the initiation, elongation or termination phase. As the TcmX binding site is situated a mere 8 Å (2-3 amino acids) from the C76 of the P-site tRNA, we speculated elongation could be inhibited after a few cycles of elongation. Toe-printing of a tryptophan staller template revealed stalling after seven amino acids at the IFVL sequence, with valine in the P-site. This sequence is reminiscent of the ErmCL-staller (IFVI), and accordingly, erythromycin (Ery) induced stalling at the same site. On the ErmBL template, TcmX lead to stalling only at the penultimate (16th) codon (STIL, with isoleucine in the P-site), behaving differently than Ery, which stalled at VDK (7th codon), with aspartate in the P-site. This hints at a sequence-specific stalling mechanism of the drug rather than inhibition of translation altogether, and explains why initial attempts to screen for translation inhibition with Poly-Phe were unsuccessful. Intriguingly, the binding site of tetracenomycin X is on the opposite side

of the tunnel wall to erythromycin, thus not sharing identical interaction partners or resistance mutations. Binding of both antibiotics simultaneously leaves a distance of only 4.5-5 Å at the narrowest point between both antibiotics. Combination therapy using both antibiotics could inhibit translation by obstructing the tunnel completely, simultaneously decreasing the probability of viable resistance mutations. Unexpectedly, an attempt of disome formation with a di-cistronic construct using the TrpL-2Ala staller sequence did not show disome formation, in the presence of neither Ery, nor TcmX. An ErmCL_S10K template (Arenz et al., 2014a) showed disome formation in the presence of Ery, but not of TcmX. One possible explanation is that TcmX induced stalling on these sequences is not strong enough to persist centrifugation after the translation reaction. Considering the likelihood of sequence-specific translation inhibition, screening of translation of randomised amino acid sequences could be conducted. Stalling could be visualised using toe-print assays. Subsequently, cryo-EM analysis of identified stalled complexes can elucidate interactions between amino acids, TcmX and the tunnel. Due to unsuccessful disome experiments, sucrose gradient mediated purification of stalled complexes should be omitted, and saturation of stalled complexes reinforced by substoichiometric concentrations of ribosomes compared to the drug.

Commonly, Gram-negative bacteria possess an efflux pump in the outer membrane (TolC), which facilitates the export of detrimental compounds (Zgurskaya et al., 2011), leading to increased resistance and tolerance against antibiotics. Notably, an *E. coli* wild-type strain was not inhibited by TcmX. Only upon deletion of TolC did cells become sensitive. Comparing resistance mutations to the binding site showed, that the greatest increase in MIC (from 1 µM to 16 µM) occurred when the non-canonical base-pair U1782-U2586 was disrupted. Notably, only mutations at U2586 to G or A were observed upon natural selection, but not that of U1782. Possibly, a mutation in this region perturbs the 23S rRNA and results in a growth-deficient phenotype. However, artificially introduced U1782C was a viable mutation and displayed the same MIC. Mutation of both U1782 and U2586 to cytosine allows the formation of another non-canonical base-pair and indeed showed only a minor increase of the MIC to 4 µM. This illustrates that the maintenance of a base-pair in the TcmX binding site is crucial for activity.

Strikingly, the U1782-U2586 base-pair is conserved across the eukaryotic domain. A cryo-EM reconstruction of a *H. sapiens* 60S-TcmX complex confirmed the same binding site, and we postulated the mechanism of action to be translation inhibition in eukaryotic cell lines, as well. Accordingly, TcmX inhibited translation of a Fluc-reporter construct both in a HEK293T cell-extract and on intact cells. However, there is a 4-fold increase of IC_{50} between

the *in vitro* (2.5 µM) and *in vivo* experiments (10 µM), which indicates that TcmX might have additional targets within the cell or exerts its function mainly via disruption of the cell membrane.

The cytotoxicity of tetracenomycins (CC_{50} of 2.5 µM) and related compounds makes them unfitting for internal application against bacterial infection in humans, however, topical applications could be investigated. Nevertheless, modifications are necessary to decrease cytotoxicity. Due to a high degree of conservation of the binding-site, attempting to increase bacteria-specificity could prove difficult. Rather, the apoptotic effect could be reduced and uptake increased by conjugation with nanoparticles, as done for doxorubicin, for cancer treatment (Ahn et al., 2013). Another possibility is decreasing the hydrophobicity. A tetracenomycin related group of antibiotics are the elloramycins, in which the C8 of the tetracenomycin backbone is rhamnosylated. Thus, it can be inferred that they employ the same mechanism and binding site. In elloramycin A, the rhamnose is permethylated and exhibits a 5-fold higher reported IC_{50} of 3.3 µM against leukemia cells, compared to TcmX (Rohr & Zeeck, 1990). Elloarmycin B on the other hand shows moderate activity against *B. brevis*, *M. luteus* and an increased activity against *S. aureus*, with MICs of 30 and 10 µg/ml, respectively (Fiedler et al., 1986). Notably, it lacks one methyl-group on the rhamnose and additionally there is a 12a-*O*-methylation in TcmX. Similarly, the tetracenomycin synthesis intermediate $TcmD_3$ shows minimal activity against *B. subtilis*, contrary to TcmX. It holds hydroxyl-side chains, which only later in the synthesis become methylated (Rohr et al., 1988). Taken together, a decrease in hydrophobicity could alleviate the cytotoxic effect of TcmX on eukaryotic cells increase solubility and increase bacterial-specificity, making it an attractive target for future studies.

5.2.2. Argyrins

Argyrins displayed great expression inhibition of a Fluc-reporter with an IC_{50} of 2 µM, and near-complete inhibition at 10 µM, exception for argyrin C, which showed an IC_{50} of 10 µM and complete inhibition only at 100 µM. This is in agreement with early translation inhibition assays employing [^{3}H]-Phenylalanine, which showed complete inhibition at 60 µM (Selva et al., 1996). In the GTPase assay, argyrins showed a lower IC_{50} than FA, and argyrin B and D were as effective as FA (20% residual activity). For FA, the IC_{50} regarding tripeptide formation has been reported to be at 1 µM (Borg et al., 2015), and a GTPase assay on *P. aeruginosa* EF-G showed a similar curve to our results (Palmer et al., 2013). Interestingly, argyrin A and C showed a decrease in inhibition at concentrations higher than 50 µM. This

could be due to different affinities for EF-G and increased argyrin-dimer formation or aggregation, as in the reported crystal structure interaction of the NH in the W2 moiety to a neighbouring argyrin have been mentioned (Vollbrecht et al., 2002).

The inhibition mechanism of argyrin on EF-G had been suggested to induce an elongated conformation incompatible with ribosome binding, based on a crystal structure of *P. aeruginosa* EF-G1 (Nyfeler et al., 2012). For verification we performed co-sedimentation assays to monitor binding of EF-G to 70S ribosomes in the presence of argyrin B and found that EF-G gets trapped on the 70S in the presence of argyrin B. The previously reported structure was prepared in the absence of ribosomes, so we analysed the cryo-EM structure of our EF-G–Argyrin–70S complex to elucidate whether this reported elongated conformation was present in our sample. Reconstruction with RELION3.0 showed three classes containing EF-G and argyrin densities, whereas one class (19.85%) comprised empty ribosomes. Thus, argyrin traps EF-G on the ribosome, forming a stable complex. Class III presented non-rotated particles and worse density for EF-G, thus it was not pursued further. Class II contained ribosomes in a rotated state; however domain IV showed hitherto unreported flexibility, which resulted in the loss of the α-helix in domain IV. Class I comprised ribosomes in a rotated state, i.e. the substrate for EF-G, with all domains of EF-G showing good density. Only domain II showed in all classes significantly lower resolution compared to the other domains. Class I was subjected to multibody refinement and resulted in an average resolution of 2.85 Å across the complex, and EF-G ranging from 3 to 5 Å. Domain II and IV both were rather flexible and did not show good resolution. While the L7/12 stalk showed a low resolved density, modelling of bL12 and interactions with EF-G was not possible.

The 30S rotation in class I was similar to that of a translocation intermediate of EF-G–FA with ap/P- and pe/E-tRNA, which showed an extensive head swivel of 18° and a rotation of the body by 2.5° (Ramrath et al., 2013). Moreover, EF-G conformation did seem comparable (R.M.S.D = 1), however, at an average resolution of 6.8 Å, it did not allow for accurate comparison. A multitude of EF-G–70S complexes exist, and for analysis of EF-G the structure in the presence of the non-hydrolysable GMPPCP with an average resolution of 2.9 Å (Pulk & Cate, 2013) was chosen as it was extremely similar to the argyrin B bound EF-G presented here. This demonstrates that argyrin B bound EF-G does not adopt an elongated conformation on the ribosome, as seen by Nyfeler and colleagues. Additionally, despite an unambiguous density for GDP, the complex solved here displays a GTP-like conformation rather than GDP-like. Whether P_i was released actively from EF-G or diffused during complex formation or grid-making cannot be established from this complex. His92 in FA-

GDP complexes has been reported to flip 90-140° after GTP hydrolysis. This flip cannot be observed in our structure, suggesting passive diffusion. Furthermore, the malachite green assay indicated that P_i release is indeed hindered. This assay is not suitable for a time sensitive analysis, as colour development occurs over a time window of 15-30 minutes. Real-time and highly sensitive kinetic analysis of single-round P_i release by monitoring fluorescently MDCC-labelled phosphate binding protein (MDCC-PBP) as previously reported (Savelsbergh et al., 2005; Koripella et al., 2015) can further expand and verify results from malachite green assays.

Further examination of the complex revealed that the interactions with the ribosome and those within EF-G itself resembled that of the GMPPCP-stalled EF-G, with exceptions. Naturally, interactions between domain III and switch I can no longer be formed. However, interactions between domain II, III and switch II are still in place, suggesting this network of salt bridges does not become unstable when switch I no longer provides a shield, but are only broken upon movement of domain II and III. Notable was the interaction between S12 and domain III, as it was different from the GMPPCP structure; it did not interact through residues from the domain III β-sheets, but with Q428 in the domain III α-helix. This distinction is likely due to different rotation degrees of the 30S. A structure of EF–G trapped by GDPNP (PDB 4v9j) (Zhou et al., 2013) shows a more comparable rotation and indeed the interaction is similar to the one in our structure. Analogous to our structure, the backbone of C1209 and C1210 in h34 contacts the conserved Gly531 loop II in domain IV, as seen in the GDPNP-II and Ramrath complex, whereas the GMPPCP complex does not show any interactions, due to different rotations of the head. Overall, this shows that binding of argyrin likely traps EF-G in a translocation intermediate comparable to the Ramrath EF-G–FA structure and GDPNP-II. Rotation of the head as seen in our structure likely allows for translocation of tRNAs. Conversely, contacts with A1067 as observed here were also reported for cross-linked EF-G, which was deficient in translocation (Peske et al., 2000). smFRET or translocation assays similar to toe-prints, but allowing only for translocation of one amino acid, need to be conducted in order to determine whether argyrin inhibits translocation.

The eukaryotic homologue of EF-G, eEF2, is targeted by the antibiotic Sordarin, leading to inhibition of translocation (Domínguez et al., 1999). Sordarins bind similarly to argyrins between domain III and V and its mechanism is suggested to be two-fold: it induces conformational changes in the for eukaryotic translocation crucial diphtamide-modified histidine in the tip of domain IV, thus preventing translocation; additionally, it blocks movement of domain III to and thus hinders the release of eEF2 (Pellegrino et al., 2018).

Although bacteria do not possess such a modified residue, a similar mechanism of hindering release is conceivable for argyrins. Sordarin binding to eEF2 is increased in the presence of ribosomes (Domínguez & Martín, 1998), and a same effect could be applicable to argyrin B. While a structure of EF-G and argyrin B in the absence of ribosomes (and nucleotide) has been described (Nyfeler et al., 2012), comparison to a GDP-bound EF-G off the ribosome reveals it is generally not compatible with argyrin binding (Fig. 21). By forming strong interactions with domain III, its movement away from domain II, as seen to a certain extent in the FA-stalled complex, is likely inhibited.

An additional interest for future research is the question whether argyrins effect both translocation and recycling. FA has been reported to have different effects on both processes, however, with conflicting results (Savelsbergh et al., 2009; Borg et al., 2016b). Contrary to translocation, recycling is dependent on GTP hydrolysis and subsequent conformation changes. Logically, recycling should be affected to a greater extent than translocation, which can also occur in the absence of EF-G. Nevertheless, trapping of EF-G on the ribosome will inhibit elongation regardless, whereas recycling is an event that takes place significantly less often than translocation. Easily executed pelleting assays, which will pellet only 50S or70S but not 30S, or sucrose gradients can be conducted to check for splitting activity. Alternatively, stop-flow light scattering approaches as for FA could be conducted to monitor recycling in the presence of argyrins.

Examination of the *Pae* EF-G1 interactions with argyrin B (Fig. 23A, B) reveal analogous interactions compared to our structure; more specifically, van der Waals interactions with residues the β-sheet of domain V (M620, M685, F687) as well as contacting the backbone of A489. Furthermore, structure alignment shows that relation of domain III and V to one another are comparable (Fig. 23C). Curiously, despite the binding site similarities *Pseudomonas* is more susceptible to argyrins (Sasse et al., 2002; Jones et al., 2017), whereas *E. coli* is resistant. Both bacteria are Gram-negative, so the discrepancy cannot be explained solely based on membrane composition. WT *P. aeruginosa* was more sensitive to argyrin B than A, and shows an MIC of 16 and 8 µg/ml, respectively (Jones et al., 2017). Deletion of efflux pumps in *P. aeruginosa* halves the MIC values to 8 and 4 µg/ml, respectively. Conversely, *E. coli* becomes only upon deletion of TolC sensitive, but regardless shows a higher MIC of 16 µg/ml (Jones et al., 2017). As deletion of TolC and other efflux pumps drastically increased susceptibility (Jones et al., 2017), it can be assumed that argyrins are indeed capable of passing membranes without difficulty, however, they are neutralised by efflux pumps. As this is a common obstacle found in Gram-negative bacteria, researchers

have started investigations into TolC inhibiting compounds (Green et al., 2020). A combination therapy of both drugs to promote antibiotic efficacy even against Gram-negative bacteria could alleviate this problem.

A protein sequence alignment of EF-G1 of *S. aureus*, *P. aeruginosa* and *E. coli* shows that the interaction site is extremely conserved between these bacteria, the latter two are even almost entirely identical (Fig. 23D). Additionally amino acids, which displayed resistance mutations in *P. aeruginosa*, are conserved in these bacteria, too. The most striking divergence is located in the domain III β-sheet beneath the argyrin, as the *Pae* Lys448 (Fig. 23A) is not conserved. In *E. coli* this residue is Trp448 (Fig. 9A), whereas in *S. aureus*, it is His440. Argyrins are still able to bind to all these EF-Gs, however affinities might differ.

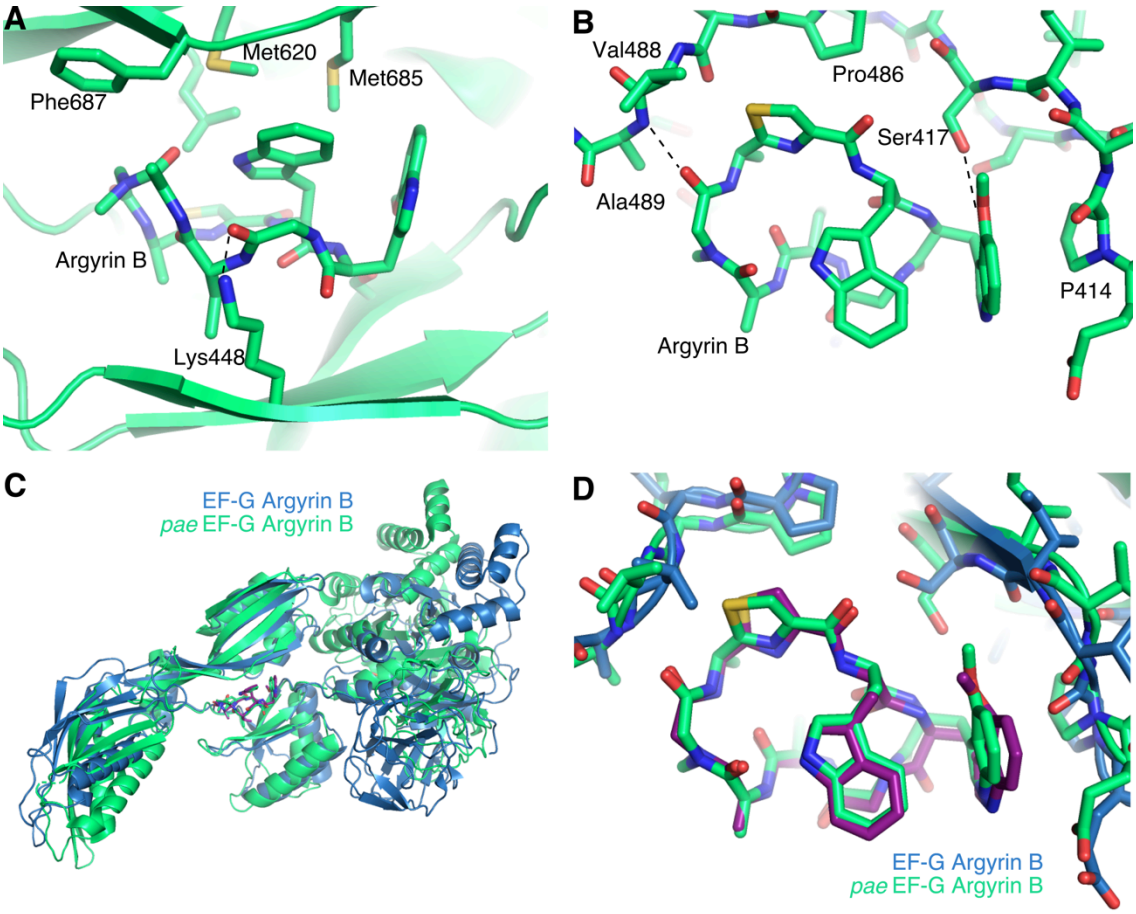

Figure 23: Interactions between Argyrin B and EF-G and comparison to *P. aeruginosa* EF-G (A) In complex with *P. aeruginosa* EF-G argyrin B forms hydrogen bonds with the backbone of Ala489 (*pae* numbering), and van der Waals interactions with the backbone of Gln487 and Val488 in the linker domain between domain III and IV **(B)** hydrogen bonds are formed with Lys488 and Ser417 in Domain III and several van der Waals interactions occur with Phe687, Met685 and Met 620 in domain V. **(C, D)** Alignment of argyrin B of both models structures. **(C)** Overall EF-G conformation shows the interaction site is similar, but leads to major discrepancy in the G-domain **(D)** the interactions site in domain III is conserved in both *P. aeruginosa* and *E. coli* EF-G

While only minor differences can be found between argyrin A-D (Fig. 24), they still seem to impact the efficiency of EF-G binding. Argyrin A has been proven to target EF-G (Bielecki et al., 2012). Argyrin A and C have an alanine at R1and not an α-aminobutyrate residue like argyrin B (Fig. 24 B, C). This appears to be important for stable binding to EF-G, as indicated by decreased activity in the GTP-hydrolysis assays. Methylation of R3 in Trp2 in ArgC and ArgD (Fig. 17C, D) does not face towards EF-G, and does not seem to have any impact on interactions, as ArgD does not show less inhibition of hydrolase activity than ArgB. In combination with the Ala instead of Abu at R1, however, it seems to have a negative impact. Argyrin E, which lacks the methoxy-group on W2, has been shown to have a slightly increased IC_{50} compared to argyrin A-D (Sasse et al., 2002), which stresses the importance of hydrogen bonding capacity of this moiety. Argyrin G and H show a hydroxyl-group added to the methyl-group next to the thiazole ring, and simultaneous drastically decreased activity against *P. aeruginosa*. It is feasible that the extension towards the beta-sheet in domain III could lead to minor clashes and thus reduce affinity to EF-G.

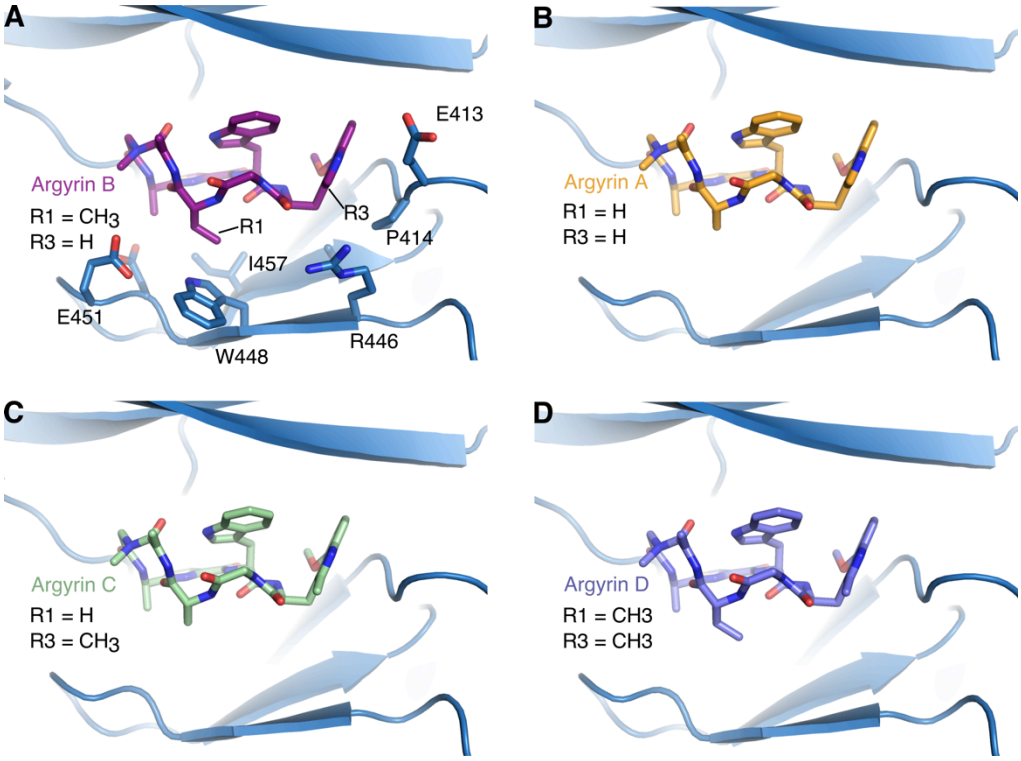

Figure 24: Fitting of other Argyrins in the binding site. (A) Argyrin B in the binding site of EF-G between domain III and V. R1 is extending towards the β-sheets in domain III and forms interactions (compare S.fig3). **(B)** Argyrin A is lacking the extra methyl-group at R1 **(C)** Argyrin C is lacking the methyl-group at R1, however is methylated in the Trp2 moiety at R3. **(D)** Argyrin D possesses both the methyl-group at R1 as well as the R3 methylation in Trp2.

Notably, eEF2 has been reported not to be targeted by argyrins (Nyfeler et al., 2012). Yeast cells were resistant against argyrin B and only became sensitive when the medium was supplemented with ethanol/glycerol. The authors concluded that metabolising of these carbon sources was mitochondrion-dependent and showed mEF-G1 to be the target for argyrins in these cells. Furthermore, they reported that under hypoxic conditions, metabolism becomes independent of mitochondrial oxidation and sensitive cancer cell lines became resistant again. Due to rapid cell growth, most tumors experience hypoxic conditions, stimulating the growth of nearby blood vessels for increased oxygen supply. This is in agreement with only 18 of 512 tested cancer cell lines sensitive to argyrin B with an $IC_{50} < 1$ μM (Nyfeler et al., 2012). Nevertheless, it is also possible that the addition of ethanol facilitated argyrin uptake and target-interaction, and sensitive cell lines were more permissive for uptake. Although mEF−G1 mutations gave some resistance against argyrin B, other, more plausible cellular targets are conceivable. In fact, numerous publications demonstrated that argyrins target the proteasome (Bulow et al., 2010; Allardyce et al., 2019). New research shows that argyrin B selectively binds to the immunoproteasome, which is present only in unhealthy cells (Allardyce et al., 2019). This would make argyrin B an ideal compound for antibiotic development, as it can target pathogenic bacteria and under normal conditions, it will likely not affect healthy cells.

6. Methods

6.1. Buffers and solutions

Buffer/Solution	Composition
Buffer A	25mM HEPES-KOH, pH 7.4 20 mM MgOAc 100mM KOAc store at 4 °C
SDS-PAGE (volumes for two small gels)	
4% stacking gel	6.1 mL H_2O 1.3 mL Bis-Acrylamid (30 %; 37.5:1) 2.5 mL Tris-HCl (0.5 M, pH 6.8) 100 µL SDS (10 %) 10 µL TEMED 100 µL APS (10 %)
18% separating gel	1.95 mL H_2O 9 mL Bis-Acrylamid (30 %; 37.5:1) 3.9 mL Tris-HCl (1.5 M, pH 8.8) 150 µL SDS (10 %) 15 µL TEMED 150 µL APS (10 %)
10X SDS-PAGE running buffer	250 mM Tris-HCl 1.92 M Glycin 1 % (w/v) SDS *ad* 1L with H_2O
4X SDS sample buffer	200 mM Tris-HCl, pH 6.8 8 % (w/v) SDS 0.4 % (w/v) bromphenolblue 40 % (v/v) glycerol 200 mM DTT

6.2. Ribosome Purification

6.2.1. Crude Ribosomal pelleting

Ribosomes were purified as previously described (Nierhaus, 1990). A 4L LB culture of *E. coli* BL21 was incubated at 37 °C and harvested in the exponential phase at an $OD_{600} \approx 1.5$, by centrifugation at 5,000g and 4 °C for 25 min. Pelleted cells were flash frozen in liquid nitrogen and stored at -80 ° C, or directly processed further. After resuspension in 20 mL of Buffer A, disrupted utilising a microfluidizer. The crude cell lysate was centrifuged at 21,000 g for 20 min at 4 °C in a JLA-25.5 rotor. Membrane debris was discarded and the cleared lysate was layered on a high salt (800 mM KCl) 25% sucrose cushion in buffer A and

centrifuged for 17.5 h at 39,000 rpm and 4 °C in a Ti45 rotor. The obtained transparent ribosome pellet was resuspended in 4 mL buffer A and A_{260} was measured.

6.2.2. Sucrose gradient centrifugation

For separation of ribosomal particles, a 10-40% sucrose density gradient in buffer A was carried out. A total of 120 OD of the purified ribosomes was layered onto the gradient and centrifuged for 3.5 h at 30,000 rpm and 4 °C in a SW32 rotor. Ribosome profiles were measured at a wavelength of 254 nm using a gradient machine. The 70S peaks were collected and subsequently pelleted for 14.5h at 43,000 rpm and 4 °C using a Ti45 rotor. The pellets obtained were resuspended in 300 µL buffer A and A_{260} was measured to determine 70S concentration (OD/mL).

6.3. Biochemical Methods

6.3.1. *In vitro* transcription-translation

For coupled transcription-translation assays, the rapid translation system (RTS *E. coli* HY; biotechrabbit) expressing firefly luciferase (Fluc) from a pIVEX2.3 plasmid was employed and prepared according to manufacturer protocol. From a mastermix 4.5 µL reactions were aliquoted and mixed with 0.5 µL argyrin in varying concentrations, dissolved in DMSO. Final DMSO concentrations were more than 1% of whole reaction volume. Negative control was carried out in the presence of DMSO instead of water. The reactions were incubated for 30 min at 30 °C at 400 rpm in a Thermomixer (Eppendorf) and stopped by adding 5 µL of Kanamycin (50 mg/mL) to each reaction. 5 µL of the stopped reaction were transferred to a black 96-well microtiter plate and mixed with 40 µL of Fluc substrate (Promega). Fluorescence emitted by Fluc oxidised luciferin was measured using a TECAN infinite 200Pro plate reader.

6.3.2. Malachite Green Phosphatase Assay

To assess GTPase activity of EF-G in the presence of argyrins, a Malachite Green Phosphatase Assay Kit (BioAssay Systems) was employed. Standard curves were created using the kit-supplied phosphate. Where applicable, a white 96-well microtiter plate with transparent bottoms was pre-loaded with 0.8 µL of antibiotic in the respective concentration and mixed with 72 µL of mastermix, containing 30 nM 70S and 60 nM EF-G in buffer A. Reactions were started by addition of 8 µL 200 µM GTP (final concentration 20 µM) and

except for the time curve incubated for 60 minutes at room temperature. All reactions were carried out in independent duplicates. For colour development, the working reagent was prepared using room temperature reagents, 100 volumes of reagent A and 1 volume of reagent B. GTPase reactions were quenched by addition of 20 µL working reagent. After 15 minutes of colour development, the absorbance measured at a wavelength of 620 nm using a TECAN infinite 200Pro plate reader. Contrary to manufacturer recommendation of 30-minute colour development, 15 minutes were chosen as precipitations formed during longer incubation periods, which altered and falsified exact readings.

6.3.3. Co-sedimentation assays

To monitor stable interactions between EF-G and the 70S ribosome, co-sedimentation (binding) assays were preformed. 0.4 µM of purified *E. coli* 70S were mixed with 1 µM EF-G, 500 µM of nucleotide (GTP) and 50 µM of either argyrin B or fusidic acid. Buffer A was added to final 150 µL and incubated at 37 °C for 15 minutes. 120 µl of reaction was subsequently loaded on 75 µL of a 10% (w/v) sucrose cushion in buffer A and centrifuged for 35 minutes at 70,000 rpm in a TLA100 rotor at 4 °C. Supernatant was quickly transferred to a new tube and the pellet was resuspended by rinsing 20 µL buffer A thrice over it without air bubble formation. 1 µL pellet was diluted in 99 µL MilliQ-H_2O and A_{260} was measured to determine 70S concentration (OD/mL x 0.024 = µM). 10 pmol of pellet (P), 10 µL of pre-centrifugation reaction (R) and supernatant (S) were mixed with 4X SB and boiled at 95 °C for 10 minutes before being loaded on a 18% SDS-PAGE.

6.3.4. SDS-PAGE

For general protein analysis via SDS-PAGE after Laemmli (Laemmli, 1970), a 18% separating gel with 4% stacking gel were prepared and run in 1X SDS-running buffer. Samples were mixed according to volume with 4X SB-buffer. As a standard Color Prestained Protein Standard, broad range (11-230kDa) (NEB) was loaded. The gel was run at 220V until the running front reached the end of the gel.

For protein detection, gels were subsequently stained with Instant Blue (Expedeon) over night and washed with water before image scanning.

6.4. Cryo-EM

6.4.1. Data collection and single particle reconstruction

For grid formation, 4.5 A_{260}/ml of argyrin B–EF-G–70S complex from the co-sedimentation assays were used. 3.5 µl of the complex was applied to 2 nm precoated Quantifoil R3/3 holey carbon supported grids and vitrified using a Vitrobot Mark IV (FEI company). Data collection was performed using a FEI Titan Krios transmission electron microscope equipped with a Falcon II direct electron detector at 300 kV with a dose of 2.5 e-/Å^2 per frame, using a pixel size of 1.084 Å and a defocus range of -0.5 to -3.5 µm, resulting in 7891 micrographs. The first ten frames (28e-/Å^2 in total) were aligned using MotionCor2 (Zheng et al., 2017). Power spectra, defocus values, astigmatism and estimation of micrograph resolution were determined by CTFFIND4 software (Rohou & Grigorieff, 2015). A resolution cut-off of 3.5 Å and defocus cut-off of 30,000 were applied. Following further visual inspection of micrographs for thon-rings and ice quality, 3466 micrographs were used for automated particle picking by GAUTOMATCH (http://www.mrc-lmb.cam.ac.uk/kzhang). 610,946 particles were extracted using RELION3 (Zivanov et al., 2018) and subjected to 2D-classficiation using 130 classes. 557,434 particles were focus-sorted with a soft-mask around EF-G into four classes for 300 rounds. Class I to III showed EF-G density, whereas class IV constituted an empty 70S and was not further pursued. Contrast transfer function (CTF) and beam tilt refinement with subsequent Bayesian polishing was performed on class I to III. Using the gold standard criterion (Fourier shell correlation of 0.143), post-processed maps showed an improved resolution by roughly 0.5 Å, resulting in average resolution of 3 Å for class I to III. Class I was subjected multi-body refinement with three masks, consisting of 50S with EF-G, 30S body and platform, and 30S head. Resolutions were improved to 2.76 Å, 2.77 Å and 3 Å, respectively, reaching 2.6 Å in the 50S core. The refined maps were sharpened by applying an automatically determined *B* factor using RELION 3.0 (Zivanov et al., 2018). Local resolution and maps filtered according to local resolution were computed using SPHIRE 1.3 (Moriya et al., 2017).

6.4.2. Modelling

The molecular model for the ribosome was based on a previous cryo-EM structure of the *E. coli* 70S ribosome (PDB 5mgp) (Huter et al., 2017b), where the 30S was divided into head and body/platform models. For EF-G, a GMPPCP trapped complex (PDB 4v9p) (Pulk & Cate, 2013) was used as a start model. Ribosomal structures were rigid-body fit in the respective

locally filtered maps, using UCSF Chimera (Pettersen et al., 2004). An atomic model for argyrin B was generated *de novo* from the chemical 2D structure (PubChem CID 9940787) using the in Chemdraw integrated Chem3D software. Restraints for argyrin B were generated using PHENIX eLBOW (Moriarty et al., 2009). The molecular models were manually adjusted and refined using Coot (Emsley & Cowtan, 2004). The atomic models were combined and refined using realspace-refined with secondary structure restraints calculated by PHENIX 1.14 (Adams et al., 2010).

7. References

Achila, D., Gulati, M., Jain, N., Britton, R. A. (2012). Biochemical characterization of ribosome assembly GTPase RbgA in Bacillus subtilis. *J Biol Chem* 287: 8417-23

Adams, P. D., Afonine, P. V., Bunkóczi, G., Chen, V. B., Davis, I. W., Echols, N., Headd, J. J., Hung, L. W., Kapral, G. J., Grosse-Kunstleve, R. W., McCoy, A. J., Moriarty, N. W., Oeffner, R., Read, R. J., Richardson, D. C., Richardson, J. S., Terwilliger, T. C., Zwart, P. H. (2010). PHENIX: a comprehensive Python-based system for macromolecular structure solution. *Acta Crystallogr D Biol Crystallogr* 66: 213-21

Adio, S., Sharma, H., Senyushkina, T., Karki, P., Maracci, C., Wohlgemuth, I., Holtkamp, W., Peske, F., Rodnina, M. V. (2018). Dynamics of ribosomes and release factors during translation termination in E. coli. *Elife* 7

Afflerbach, H., Schröder, O., Wagner, R. (1998). Effects of the Escherichia coli DNA-binding protein H-NS on rRNA synthesis in vivo. *Mol Microbiol* 28: 641-53

Ageitos, J. M., Sanchez-Perez, A., Calo-Mata, P., Villa, T. G. (2017). Antimicrobial peptides (AMPs): Ancient compounds that represent novel weapons in the fight against bacteria. *Biochem Pharmacol* 133: 117-38

Agrawal, R. K., Spahn, C. M., Penczek, P., Grassucci, R. A., Nierhaus, K. H., Frank, J. (2000). Visualization of tRNA movements on the Escherichia coli 70S ribosome during the elongation cycle. *J Cell Biol* 150: 447-60

Ahn, S., Seo, E., Kim, K., Lee, S. J. (2013). Controlled cellular uptake and drug efficacy of nanotherapeutics. *Scientific Reports* 3: 1997

Alarcon, B., Lacal, J. C., Fernandez-Sousa, J. M., Carrasco, L. (1984). Screening for new compounds with antiherpes activity. *Antiviral Res* 4: 231-44

Allardyce, D. J., Bell, C. M., Loizidou, E. Z. (2019). Argyrin B, a non-competitive inhibitor of the human immunoproteasome exhibiting preference for beta1i. *Chem Biol Drug Des* 94: 1556-67

Ambrogelly, A., Palioura, S., Söll, D. (2007). Natural expansion of the genetic code. *Nat Chem Biol* 3: 29-35

Amiram, M., Haimovich, A. D., Fan, C., Wang, Y. S., Aerni, H. R., Ntai, I., Moonan, D. W., Ma, N. J., Rovner, A. J., Hong, S. H., Kelleher, N. L., Goodman, A. L., Jewett, M. C., Söll, D., Rinehart, J., Isaacs, F. J. (2015). Evolution of translation machinery in recoded bacteria enables multi-site incorporation of nonstandard amino acids. *Nat Biotechnol* 33: 1272-79

Anand, B., Verma, S. K., Prakash, B. (2006). Structural stabilization of GTP-binding domains in circularly permuted GTPases: implications for RNA binding. *Nucleic Acids Res* 34: 2196-205

Anderson, M. G., Khoo, C. L., Rickards, R. W. (1989). Oxidation processes in the biosynthesis of the tetracenomycin and elloramycin antibiotics. *J Antibiot (Tokyo)* 42: 640-3

Andrade, J. M., Dos Santos, R. F., Chelysheva, I., Ignatova, Z., Arraiano, C. M. (2018). The RNA-binding protein Hfq is important for ribosome biogenesis and affects translation fidelity. *Embo j* 37

Antoun, A., Pavlov, M. Y., Lovmar, M., Ehrenberg, M. (2006). How initiation factors maximize the accuracy of tRNA selection in initiation of bacterial protein synthesis. *Mol Cell* 23: 183-93

Arai, K., Arai, N., Kawakita, M., Kaziro, Y. (1972). Interaction of guanosine 5'-diphosphate, 2'-(or 3'-) diphosphate(ppGpp) with elongation factors from E. coli. *Biochem Biophys Res Commun* 48: 191-6

Arai, K., Kawakita, M., Kaziro, Y. (1974). Studies on the polypeptide elongation factors from E. coli. V. Properties of various complexes containing EF-Tu and EF-Ts. *J Biochem* 76: 293-306

Arenz, S., Abdelshahid, M., Sohmen, D., Payoe, R., Starosta, A. L., Berninghausen, O., Hauryliuk, V., Beckmann, R., Wilson, D. N. (2016). The stringent factor RelA adopts an open conformation on the ribosome to stimulate ppGpp synthesis. *Nucleic Acids Res* 44: 6471-81

Arenz, S., Meydan, S., Starosta, A. L., Berninghausen, O., Beckmann, R., Vázquez-Laslop, N., Wilson, D. N. (2014a). Drug sensing by the ribosome induces translational arrest via active site perturbation. *Mol Cell* 56: 446-52

Arenz, S., Ramu, H., Gupta, P., Berninghausen, O., Beckmann, R., Vazquez-Laslop, N., Mankin, A. S., Wilson, D. N. (2014b). Molecular basis for erythromycin-dependent ribosome stalling during translation of the ErmBL leader peptide. *Nat Commun* 5: 3501

Aseev, L. V., Koledinskaya, L. S., Boni, I. V. (2016). Regulation of Ribosomal Protein Operons rplM-rpsI, rpmB-rpmG, and rplU-rpmA at the Transcriptional and Translational Levels. *J Bacteriol* 198: 2494-502

Atkinson, G. C., Tenson, T., Hauryliuk, V. (2011). The RelA/SpoT homolog (RSH) superfamily: distribution and functional evolution of ppGpp synthetases and hydrolases across the tree of life. *PLoS One* 6: e23479

Bao, W., Wendt-Pienkowski, E., Hutchinson, C. R. (1998). Reconstitution of the iterative type II polyketide synthase for tetracenomycin F2 biosynthesis. *Biochemistry* 37: 8132-8

Barker, M. M., Gaal, T., Josaitis, C. A., Gourse, R. L. (2001). Mechanism of regulation of transcription initiation by ppGpp. I. Effects of ppGpp on transcription initiation in vivo and in vitro. *J Mol Biol* 305: 673-88

Bechhofer, D. H., Deutscher, M. P. (2019). Bacterial ribonucleases and their roles in RNA metabolism. *Crit Rev Biochem Mol Biol* 54: 242-300

Beckert, B., Turk, M., Czech, A., Berninghausen, O., Beckmann, R., Ignatova, Z., Plitzko, J. M., Wilson, D. N. (2018). Structure of a hibernating 100S ribosome reveals an inactive conformation of the ribosomal protein S1. *Nat Microbiol* 3: 1115-21

Belardinelli, R., Sharma, H., Caliskan, N., Cunha, C. E., Peske, F., Wintermeyer, W., Rodnina, M. V. (2016). Choreography of molecular movements during ribosome progression along mRNA. *Nat Struct Mol Biol* 23: 342-8

Bennison, D. J., Irving, S. E., Corrigan, R. M. (2019). The Impact of the Stringent Response on TRAFAC GTPases and Prokaryotic Ribosome Assembly. *Cells* 8

Bergemann, K., Nierhaus, K. H. (1983). Spontaneous, elongation factor G independent translocation of Escherichia coli ribosomes. *J Biol Chem* 258: 15105-13

Bibb, M. J., Biro, S., Motamedi, H., Collins, J. F., Hutchinson, C. R. (1989). Analysis of the nucleotide sequence of the Streptomyces glaucescens tcmI genes provides key information about the enzymology of polyketide antibiotic biosynthesis. *EMBO J* 8: 2727-36

Bielecki, P., Lukat, P., Husecken, K., Dotsch, A., Steinmetz, H., Hartmann, R. W., Muller, R., Haussler, S. (2012). Mutation in elongation factor G confers resistance to the antibiotic argyrin in the opportunistic pathogen Pseudomonas aeruginosa. *Chembiochem* 13: 2339-45

Bilgin, N., Ehrenberg, M. (1994). Mutations in 23 S ribosomal RNA perturb transfer RNA selection and can lead to streptomycin dependence. *J Mol Biol* 235: 813-24

Blanchard, S. C., Gonzalez, R. L., Kim, H. D., Chu, S., Puglisi, J. D. (2004). tRNA selection and kinetic proofreading in translation. *Nat Struct Mol Biol* 11: 1008-14

Bodley, J. W., Zieve, F. J., Lin, L. (1970). Studies on translocation. IV. The hydrolysis of a single round of guanosine triphosphate in the presence of fusidic acid. *J Biol Chem* 245: 5662-7

Bodley, J. W., Zieve, F. J., Lin, L., Zieve, S. T. (1969). Formation of the ribosome-G factor-GDP complex in the presence of fusidic acid. *Biochem Biophys Res Commun* 37: 437-43

Borg, A., Holm, M., Shiroyama, I., Hauryliuk, V., Pavlov, M., Sanyal, S., Ehrenberg, M. (2015). Fusidic acid targets elongation factor G in several stages of translocation on the bacterial ribosome. *J Biol Chem* 290: 3440-54

Borg, A., Pavlov, M., Ehrenberg, M. (2016a). Complete kinetic mechanism for recycling of the bacterial ribosome. *Rna* 22: 10-21

Borg, A., Pavlov, M., Ehrenberg, M. (2016b). Mechanism of fusidic acid inhibition of RRF- and EF-G-dependent splitting of the bacterial post-termination ribosome. *Nucleic Acids Res* 44: 3264-75

Brink, M. F., Verbeet, M. P., de Boer, H. A. (1993). Formation of the central pseudoknot in 16S rRNA is essential for initiation of translation. *Embo j* 12: 3987-96

Britton, R. A. (2009). Role of GTPases in bacterial ribosome assembly. *Annu Rev Microbiol* 63: 155-76

Brogden, K. A. (2005). Antimicrobial peptides: pore formers or metabolic inhibitors in bacteria? *Nat Rev Microbiol* 3: 238-50

Buglino, J., Shen, V., Hakimian, P., Lima, C. D. (2002). Structural and biochemical analysis of the Obg GTP binding protein. *Structure* 10: 1581-92

Bulow, L., Nickeleit, I., Girbig, A. K., Brodmann, T., Rentsch, A., Eggert, U., Sasse, F., Steinmetz, H., Frank, R., Carlomagno, T., Malek, N. P., Kalesse, M. (2010). Synthesis and biological characterization of argyrin F. *ChemMedChem* 5: 832-6

Burgos, H. L., O'Connor, K., Sanchez-Vazquez, P., Gourse, R. L. (2017). Roles of Transcriptional and Translational Control Mechanisms in Regulation of Ribosomal Protein Synthesis in Escherichia coli. *J Bacteriol* 199

Burmann, B. M., Schweimer, K., Luo, X., Wahl, M. C., Stitt, B. L., Gottesman, M. E., Rösch, P. (2010). A NusE:NusG complex links transcription and translation. *Science* 328: 501-4

Burnett, B. J., Altman, R. B., Ferguson, A., Wasserman, M. R., Zhou, Z., Blanchard, S. C. (2014). Direct evidence of an elongation factor-Tu/Ts·GTP·Aminoacyl-tRNA quaternary complex. *J Biol Chem* 289: 23917-27

Carlson, M. A., Haddad, B. G., Weis, A. J., Blackwood, C. S., Shelton, C. D., Wuerth, M. E., Walter, J. D., Spiegel, P. C., Jr. (2017). Ribosomal protein L7/L12 is required for GTPase translation factors EF-G, RF3, and IF2 to bind in their GTP state to 70S ribosomes. *Febs j* 284: 1631-43

Cashel, M., Gallant, J. (1969). Two Compounds implicated in the Function of the RC Gene of Escherichia coli. *Nature* 221: 838-41

Cerretti, D. P., Dean, D., Davis, G. R., Bedwell, D. M., Nomura, M. (1983). The spc ribosomal protein operon of Escherichia coli: sequence and cotranscription of the ribosomal protein genes and a protein export gene. *Nucleic Acids Res* 11: 2599-616

Chen, C., Cui, X., Beausang, J. F., Zhang, H., Farrell, I., Cooperman, B. S., Goldman, Y. E. (2016). Elongation factor G initiates translocation through a power stroke. *Proc Natl Acad Sci U S A* 113: 7515-20

Chen, C. H., Genapathy, S., Fischer, P. M., Chan, W. C. (2014). A facile approach to tryptophan derivatives for the total synthesis of argyrin analogues. *Org Biomol Chem* 12: 9764-8

Chen, M., Fredrick, K. (2020). RNA Polymerase's Relationship with the Ribosome: Not So Physical, Most of the Time. *J Mol Biol*

Chen, X., Bui, K. C., Barat, S., Thi Nguyen, M. L., Bozko, P., Sipos, B., Kalesse, M., Malek, N. P., Plentz, R. R. (2017). Therapeutic effects of Argyrin F in pancreatic adenocarcinoma. *Cancer Lett* 399: 20-28

Condon, C., Brechemier-Baey, D., Beltchev, B., Grunberg-Manago, M., Putzer, H. (2001). Identification of the gene encoding the 5S ribosomal RNA maturase in Bacillus subtilis: mature 5S rRNA is dispensable for ribosome function. *Rna* 7: 242-53

Condon, C., Liveris, D., Squires, C., Schwartz, I., Squires, C. L. (1995a). rRNA operon multiplicity in Escherichia coli and the physiological implications of rrn inactivation. *J Bacteriol* 177: 4152-6

Condon, C., Squires, C., Squires, C. L. (1995b). Control of rRNA transcription in Escherichia coli. *Microbiol Rev* 59: 623-45

Conn, A. B., Diggs, S., Tam, T. K., Blaha, G. M. (2019). Two Old Dogs, One New Trick: A Review of RNA Polymerase and Ribosome Interactions during Transcription-Translation Coupling. *Int J Mol Sci* 20

Cornish, P. V., Ermolenko, D. N., Noller, H. F., Ha, T. (2008). Spontaneous intersubunit rotation in single ribosomes. *Mol Cell* 30: 578-88

Corrigan, R. M., Bellows, L. E., Wood, A., Gründling, A. (2016). ppGpp negatively impacts ribosome assembly affecting growth and antimicrobial tolerance in Gram-positive bacteria. *Proc Natl Acad Sci U S A* 113: E1710-9

Crick, F. (1970). Central dogma of molecular biology. *Nature* 227: 561-3

Dammel, C. S., Noller, H. F. (1995). Suppression of a cold-sensitive mutation in 16S rRNA by overexpression of a novel ribosome-binding factor, RbfA. *Genes Dev* 9: 626-37

Davis, J. H., Tan, Y. Z., Carragher, B., Potter, C. S., Lyumkis, D., Williamson, J. R. (2016). Modular Assembly of the Bacterial Large Ribosomal Subunit. *Cell* 167: 1610-22 e15

Davis, J. H., Williamson, J. R. (2017). Structure and dynamics of bacterial ribosome biogenesis. *Philos Trans R Soc Lond B Biol Sci* 372

Daviter, T., Wieden, H. J., Rodnina, M. V. (2003). Essential role of histidine 84 in elongation factor Tu for the chemical step of GTP hydrolysis on the ribosome. *J Mol Biol* 332: 689-99

de Narvaez, C. C., Schaup, H. W. (1979). In vivo transcriptionally coupled assembly of Escherichia coli ribosomal subunits. *J Mol Biol* 134: 1-22

Decatur, W. A., Fournier, M. J. (2002). rRNA modifications and ribosome function. *Trends Biochem Sci* 27: 344-51

Decker, H., Hutchinson, C. R. (1993). Transcriptional analysis of the Streptomyces glaucescens tetracenomycin C biosynthesis gene cluster. *J Bacteriol* 175: 3887-92

Decker, H., Motamedi, H., Hutchinson, C. R. (1993). Nucleotide sequences and heterologous expression of tcmG and tcmP, biosynthetic genes for tetracenomycin C in Streptomyces glaucescens. *J Bacteriol* 175: 3876-86

Dennis, P. P., Ehrenberg, M., Fange, D., Bremer, H. (2009). Varying rate of RNA chain elongation during rrn transcription in Escherichia coli. *J Bacteriol* 191: 3740-6

Deuerling, E., Gamerdinger, M., Kreft, S. G. (2019). Chaperone Interactions at the Ribosome. *Cold Spring Harb Perspect Biol* 11

Dey, D., Oleinikov, A. V., Traut, R. R. (1995). The hinge region of Escherichia coli ribosomal protein L7/L12 is required for factor binding and GTP hydrolysis. *Biochimie* 77: 925-30

Diaconu, M., Kothe, U., Schlunzen, F., Fischer, N., Harms, J. M., Tonevitsky, A. G., Stark, H., Rodnina, M. V., Wahl, M. C. (2005). Structural basis for the function of the ribosomal L7/12 stalk in factor binding and GTPase activation. *Cell* 121: 991-1004

Diez, S., Ryu, J., Caban, K., Gonzalez, R. L., Jr., Dworkin, J. (2020). The alarmones (p)ppGpp directly regulate translation initiation during entry into quiescence. *Proc Natl Acad Sci U S A* 117: 15565-72

Dimitrova, L. N., Kuroha, K., Tatematsu, T., Inada, T. (2009). Nascent peptide-dependent translation arrest leads to Not4p-mediated protein degradation by the proteasome. *J Biol Chem* 284: 10343-52

Dincbas-Renqvist, V., Engstrom, A., Mora, L., Heurgue-Hamard, V., Buckingham, R., Ehrenberg, M. (2000). A post-translational modification in the GGQ motif of RF2 from Escherichia coli stimulates termination of translation. *EMBO J* 19: 6900-7

Domínguez, J. M., Gómez-Lorenzo, M. G., Martín, J. J. (1999). Sordarin inhibits fungal protein synthesis by blocking translocation differently to fusidic acid. *J Biol Chem* 274: 22423-7

Domínguez, J. M., Martín, J. J. (1998). Identification of elongation factor 2 as the essential protein targeted by sordarins in Candida albicans. *Antimicrob Agents Chemother* 42: 2279-83

Dunn, J. J., Studier, F. W. (1973). T7 early RNAs and Escherichia coli ribosomal RNAs are cut from large precursor RNAs in vivo by ribonuclease 3. *Proc Natl Acad Sci U S A* 70: 3296-300

Durand, G. A., Raoult, D., Dubourg, G. (2019). Antibiotic discovery: history, methods and perspectives. *Int J Antimicrob Agents* 53: 371-82

Duss, O., Stepanyuk, G. A., Grot, A., O'Leary, S. E., Puglisi, J. D., Williamson, J. R. (2018). Real-time assembly of ribonucleoprotein complexes on nascent RNA transcripts. *Nat Commun* 9: 5087

Duss, O., Stepanyuk, G. A., Puglisi, J. D., Williamson, J. R. (2019). Transient Protein-RNA Interactions Guide Nascent Ribosomal RNA Folding. *Cell* 179: 1357-69 e16

Dutca, L. M., Culver, G. M. (2008). Assembly of the 5' and 3' minor domains of 16S ribosomal RNA as monitored by tethered probing from ribosomal protein S20. *J Mol Biol* 376: 92-108

Egert, E., Noltemeyer, M., Siebers, J., Rohr, J., Zeeck, A. (1992). The structure of tetracenomycin C. *J Antibiot (Tokyo)* 45: 1190-2

Ellwood, M., Nomura, M. (1982). Chromosomal locations of the genes for rRNA in Escherichia coli K-12. *J Bacteriol* 149: 458-68

Emsley, P., Cowtan, K. (2004). Coot: model-building tools for molecular graphics. *Acta Crystallogr D Biol Crystallogr* 60: 2126-32

Epand, R. M., Vogel, H. J. (1999). Diversity of antimicrobial peptides and their mechanisms of action. *Biochim Biophys Acta* 1462: 11-28

Erlacher, M. D., Lang, K., Wotzel, B., Rieder, R., Micura, R., Polacek, N. (2006). Efficient ribosomal peptidyl transfer critically relies on the presence of the ribose 2'-OH at A2451 of 23S rRNA. *J Am Chem Soc* 128: 4453-9

Fan, H., Hahm, J., Diggs, S., Perry, J. J., Blaha, G. (2015). Structural and Functional Analysis of BipA, a Regulator of Virulence in Enteropathogenic Escherichia coli. *J Biol Chem* 290: 20856-64

Fasano, O., Bruns, W., Crechet, J. B., Sander, G., Parmeggiani, A. (1978). Modification of elongation-factor-Tu . guanine-nucleotide interaction by kirromycin. A comparison with the effect of aminoacyl-tRNA and elongation factor Ts. *Eur J Biochem* 89: 557-65

Feng, B., Mandava, C. S., Guo, Q., Wang, J., Cao, W., Li, N., Zhang, Y., Zhang, Y., Wang, Z., Wu, J., Sanyal, S., Lei, J., Gao, N. (2014). Structural and functional insights into the mode of action of a universally conserved Obg GTPase. *PLoS Biol* 12: e1001866

Ferrari, P., Vekey, K., Galimberti, M., Gallo, G. G., Selva, E., Zerilli, L. F. (1996). Antibiotics A21459 A and B, new inhibitors of bacterial protein synthesis. II. Structure elucidation. *J Antibiot (Tokyo)* 49: 150-4

Fiedler, H. P., Rohr, J., Zeeck, A. (1986). Elloramycins B, C, D, E and F: minor congeners of the elloramycin producer Streptomyces olivaceus. *J Antibiot (Tokyo)* 39: 856-9

Frank, J., Agrawal, R. K. (2000). A ratchet-like inter-subunit reorganization of the ribosome during translocation. *Nature* 406: 318-22

Freistroffer, D. V., Pavlov, M. Y., MacDougall, J., Buckingham, R. H., Ehrenberg, M. (1997). Release factor RF3 in E.coli accelerates the dissociation of release factors RF1 and RF2 from the ribosome in a GTP-dependent manner. *Embo j* 16: 4126-33

French, S. L., Miller, O. L., Jr. (1989). Transcription mapping of the Escherichia coli chromosome by electron microscopy. *J Bacteriol* 171: 4207-16

Fu, Z., Indrisiunaite, G., Kaledhonkar, S., Shah, B., Sun, M., Chen, B., Grassucci, R. A., Ehrenberg, M., Frank, J. (2019). The structural basis for release-factor activation during translation termination revealed by time-resolved cryogenic electron microscopy. *Nat Commun* 10: 2579

Fu, Z., Kaledhonkar, S., Borg, A., Sun, M., Chen, B., Grassucci, R. A., Ehrenberg, M., Frank, J. (2016). Key Intermediates in Ribosome Recycling Visualized by Time-Resolved Cryoelectron Microscopy. *Structure* 24: 2092-101

Fujiwara, T., Ito, K., Yamami, T., Nakamura, Y. (2004). Ribosome recycling factor disassembles the post-termination ribosomal complex independent of the ribosomal translocase activity of elongation factor G. *Mol Microbiol* 53: 517-28

Gan, M., Liu, B., Tan, Y., Wang, Q., Zhou, H., He, H., Ping, Y., Yang, Z., Wang, Y., Xiao, C. (2015). Saccharothrixones A-D, Tetracenomycin-Type Polyketides from the Marine-Derived Actinomycete Saccharothrix sp. 10-10. *J Nat Prod* 78: 2260-5

Gao, N., Zavialov, A. V., Ehrenberg, M., Frank, J. (2007). Specific interaction between EF-G and RRF and its implication for GTP-dependent ribosome splitting into subunits. *J Mol Biol* 374: 1345-58

Gao, Y. G., Selmer, M., Dunham, C. M., Weixlbaumer, A., Kelley, A. C., Ramakrishnan, V. (2009). The structure of the ribosome with elongation factor G trapped in the posttranslocational state. *Science* 326: 694-9

García-Ortega, L., Alvarez-García, E., Gavilanes, J. G., Martínez-del-Pozo, A., Joseph, S. (2010). Cleavage of the sarcin-ricin loop of 23S rRNA differentially affects EF-G and EF-Tu binding. *Nucleic Acids Res* 38: 4108-19

Genilloud, O. (2017). Actinomycetes: still a source of novel antibiotics. *Nat Prod Rep* 34: 1203-32

Gilbert, W. (1986). Origin of Life: The RNA World. *Nature* 319: 618

Ginsburg, D., Steitz, J. A. (1975). The 30 S ribosomal precursor RNA from Escherichia coli. A primary transcript containing 23 S, 16 S, and 5 S sequences. *J Biol Chem* 250: 5647-54

Girodat, D., Blanchard, S. C., Wieden, H. J., Sanbonmatsu, K. Y. (2020). Elongation Factor Tu Switch I Element is a Gate for Aminoacyl-tRNA Selection. *J Mol Biol* 432: 3064-77

Graf, M., Huter, P., Maracci, C., Peterek, M., Rodnina, M. V., Wilson, D. N. (2018). Visualization of translation termination intermediates trapped by the Apidaecin 137 peptide during RF3-mediated recycling of RF1. *Nat Commun* 9: 3053

Graf, M., Mardirossian, M., Nguyen, F., Seefeldt, A. C., Guichard, G., Scocchi, M., Innis, C. A., Wilson, D. N. (2017). Proline-rich antimicrobial peptides targeting protein synthesis. *Nat Prod Rep* 34: 702-11

Gramajo, H. C., White, J., Hutchinson, C. R., Bibb, M. J. (1991). Overproduction and localization of components of the polyketide synthase of Streptomyces glaucescens involved in the production of the antibiotic tetracenomycin C. *J Bacteriol* 173: 6475-83

Green, A. T., Moniruzzaman, M., Cooper, C. J., Walker, J. K., Smith, J. C., Parks, J. M., Zgurskaya, H. I. (2020). Discovery of multidrug efflux pump inhibitors with a novel chemical scaffold. *Biochim Biophys Acta Gen Subj* 1864: 129546

Green, R., Noller, H. F. (1996). In vitro complementation analysis localizes 23S rRNA posttranscriptional modifications that are required for Escherichia coli 50S ribosomal subunit assembly and function. *Rna* 2: 1011-21

Gromadski, K. B., Wieden, H. J., Rodnina, M. V. (2002). Kinetic mechanism of elongation factor Ts-catalyzed nucleotide exchange in elongation factor Tu. *Biochemistry* 41: 162-9

Guilfoile, P. G., Hutchinson, C. R. (1992a). Sequence and transcriptional analysis of the Streptomyces glaucescens tcmAR tetracenomycin C resistance and repressor gene loci. *J Bacteriol* 174: 3651-8

Guilfoile, P. G., Hutchinson, C. R. (1992b). The Streptomyces glaucescens TcmR protein represses transcription of the divergently oriented tcmR and tcmA genes by binding to an intergenic operator region. *J Bacteriol* 174: 3659-66

Gulati, M., Jain, N., Anand, B., Prakash, B., Britton, R. A. (2013). Mutational analysis of the ribosome assembly GTPase RbgA provides insight into ribosome interaction and ribosome-stimulated GTPase activation. *Nucleic Acids Res* 41: 3217-27

Gulati, M., Jain, N., Davis, J. H., Williamson, J. R., Britton, R. A. (2014). Functional interaction between ribosomal protein L6 and RbgA during ribosome assembly. *PLoS Genet* 10: e1004694

Gupta, N., Culver, G. M. (2014). Multiple in vivo pathways for Escherichia coli small ribosomal subunit assembly occur on one pre-rRNA. *Nat Struct Mol Biol* 21: 937-43

Hamel, E., Cashel, M. (1973). Role of guanine nucleotides in protein synthesis. Elongation factor G and guanosine 5'-triphosphate,3'-diphosphate. *Proc Natl Acad Sci U S A* 70: 3250-4

Hamel, E., Cashel, M. (1974). Guanine nucleotides in protein synthesis. Utilization of pppGpp and dGTP by initiation factor 2 and elongation factor Tu. *Arch Biochem Biophys* 162: 293-300

Hansen, J. L., Ippolito, J. A., Ban, N., Nissen, P., Moore, P. B., Steitz, T. A. (2002). The structures of four macrolide antibiotics bound to the large ribosomal subunit. *Mol Cell* 10: 117-28

Hartz, D., McPheeters, D. S., Gold, L. (1989). Selection of the initiator tRNA by Escherichia coli initiation factors. *Genes Dev* 3: 1899-912

Haseltine, W. A., Block, R. (1973). Synthesis of guanosine tetra- and pentaphosphate requires the presence of a codon-specific, uncharged transfer ribonucleic acid in the acceptor site of ribosomes. *Proc Natl Acad Sci U S A* 70: 1564-8

Hauryliuk, V., Atkinson, G. C., Murakami, K. S., Tenson, T., Gerdes, K. (2015). Recent functional insights into the role of (p)ppGpp in bacterial physiology. *Nat Rev Microbiol* 13: 298-309

Hausner, T. P., Atmadja, J., Nierhaus, K. H. (1987). Evidence that the G2661 region of 23S rRNA is located at the ribosomal binding sites of both elongation factors. *Biochimie* 69: 911-23

Helgstrand, M., Mandava, C. S., Mulder, F. A., Liljas, A., Sanyal, S., Akke, M. (2007). The ribosomal stalk binds to translation factors IF2, EF-Tu, EF-G and RF3 via a conserved region of the L12 C-terminal domain. *J Mol Biol* 365: 468-79

Herold, M., Nierhaus, K. H. (1987). Incorporation of six additional proteins to complete the assembly map of the 50 S subunit from Escherichia coli ribosomes. *J Biol Chem* 262: 8826-33

Hillebrand, A., Wurm, R., Menzel, A., Wagner, R. (2005). The seven E. coli ribosomal RNA operon upstream regulatory regions differ in structure and transcription factor binding efficiencies. *Biol Chem* 386: 523-34

Hirokawa, G., Iwakura, N., Kaji, A., Kaji, H. (2008). The role of GTP in transient splitting of 70S ribosomes by RRF (ribosome recycling factor) and EF-G (elongation factor G). *Nucleic Acids Res* 36: 6676-87

Hirokawa, G., Kiel, M. C., Muto, A., Selmer, M., Raj, V. S., Liljas, A., Igarashi, K., Kaji, H., Kaji, A. (2002). Post-termination complex disassembly by ribosome recycling factor, a functional tRNA mimic. *Embo j* 21: 2272-81

Hirokawa, G., Nijman, R. M., Raj, V. S., Kaji, H., Igarashi, K., Kaji, A. (2005). The role of ribosome recycling factor in dissociation of 70S ribosomes into subunits. *Rna* 11: 1317-28

Hogg, T., Mechold, U., Malke, H., Cashel, M., Hilgenfeld, R. (2004). Conformational antagonism between opposing active sites in a bifunctional RelA/SpoT homolog modulates (p)ppGpp metabolism during the stringent response [corrected]. *Cell* 117: 57-68

Holtkamp, W., Cunha, C. E., Peske, F., Konevega, A. L., Wintermeyer, W., Rodnina, M. V. (2014a). GTP hydrolysis by EF-G synchronizes tRNA movement on small and large ribosomal subunits. *Embo j* 33: 1073-85

Holtkamp, W., Wintermeyer, W., Rodnina, M. V. (2014b). Synchronous tRNA movements during translocation on the ribosome are orchestrated by elongation factor G and GTP hydrolysis. *Bioessays* 36: 908-18

Horan, L. H., Noller, H. F. (2007). Intersubunit movement is required for ribosomal translocation. *Proc Natl Acad Sci U S A* 104: 4881-5

Hussain, T., Llacer, J. L., Wimberly, B. T., Kieft, J. S., Ramakrishnan, V. (2016). Large-Scale Movements of IF3 and tRNA during Bacterial Translation Initiation. *Cell* 167: 133-44 e13

Hutchings, M. I., Truman, A. W., Wilkinson, B. (2019). Antibiotics: past, present and future. *Curr Opin Microbiol* 51: 72-80

Hutchinson, C. R. (1997). Biosynthetic Studies of Daunorubicin and Tetracenomycin C. *Chem Rev* 97: 2525-36

Huter, P., Arenz, S., Bock, L. V., Graf, M., Frister, J. O., Heuer, A., Peil, L., Starosta, A. L., Wohlgemuth, I., Peske, F., Novacek, J., Berninghausen, O., Grubmuller, H., Tenson, T., Beckmann, R., Rodnina, M. V., Vaiana, A. C., Wilson, D. N. (2017a). Structural Basis for Polyproline-Mediated Ribosome Stalling and Rescue by the Translation Elongation Factor EF-P. *Mol Cell* 68: 515-27 e6

Huter, P., Müller, C., Beckert, B., Arenz, S., Berninghausen, O., Beckmann, R., Wilson, D. N. (2017b). Structural basis for ArfA-RF2-mediated translation termination on mRNAs lacking stop codons. *Nature* 541: 546-49

Huttner, A., Bielicki, J., Clements, M. N., Frimodt-Møller, N., Muller, A. E., Paccaud, J. P., Mouton, J. W. (2020). Oral amoxicillin and amoxicillin-clavulanic acid: properties, indications and usage. *Clin Microbiol Infect* 26: 871-79

Hwang, J., Inouye, M. (2006). The tandem GTPase, Der, is essential for the biogenesis of 50S ribosomal subunits in Escherichia coli. *Mol Microbiol* 61: 1660-72

Ieong, K. W., Uzun, Ü., Selmer, M., Ehrenberg, M. (2016). Two proofreading steps amplify the accuracy of genetic code translation. *Proc Natl Acad Sci U S A* 113: 13744-49

Irving, S. E., Corrigan, R. M. (2018). Triggering the stringent response: signals responsible for activating (p)ppGpp synthesis in bacteria. *Microbiology* 164: 268-76

Ito, K., Fujiwara, T., Toyoda, T., Nakamura, Y. (2002). Elongation factor G participates in ribosome disassembly by interacting with ribosome recycling factor at their tRNA-mimicry domains. *Mol Cell* 9: 1263-72

Ito, K., Uno, M., Nakamura, Y. (2000). A tripeptide 'anticodon' deciphers stop codons in messenger RNA. *Nature* 403: 680-4

Jain, C. (2020). RNase AM, a 5' to 3' exonuclease, matures the 5' end of all three ribosomal RNAs in E. coli. *Nucleic Acids Res* 48: 5616-23

Jain, V., Saleem-Batcha, R., China, A., Chatterji, D. (2006). Molecular dissection of the mycobacterial stringent response protein Rel. *Protein Sci* 15: 1449-64

Janosi, L., Mottagui-Tabar, S., Isaksson, L. A., Sekine, Y., Ohtsubo, E., Zhang, S., Goon, S., Nelken, S., Shuda, M., Kaji, A. (1998). Evidence for in vivo ribosome recycling, the fourth step in protein biosynthesis. *Embo j* 17: 1141-51

Jaskolowski, M., Ramrath, D. J. F., Bieri, P., Niemann, M., Mattei, S., Calderaro, S., Leibundgut, M., Horn, E. K., Boehringer, D., Schneider, A., Ban, N. (2020). Structural Insights into the Mechanism of Mitoribosomal Large Subunit Biogenesis. *Mol Cell*

Jaskunas, S. R., Fallon, A. M., Nomura, M. (1977). Identification and organization of ribosomal protein genes of Escherichia coli carried by lambdafus2 transducing phage. *J Biol Chem* 252: 7323-36

Jimmy, S., Saha, C. K., Kurata, T., Stavropoulos, C., Oliveira, S. R. A., Koh, A., Cepauskas, A., Takada, H., Rejman, D., Tenson, T., Strahl, H., Garcia-Pino, A., Hauryliuk, V., Atkinson, G. C. (2020). A widespread toxin-antitoxin system exploiting growth control via alarmone signaling. *Proc Natl Acad Sci U S A* 117: 10500-10

Jin, H., Kelley, A. C., Loakes, D., Ramakrishnan, V. (2010). Structure of the 70S ribosome bound to release factor 2 and a substrate analog provides insights into catalysis of peptide release. *Proc Natl Acad Sci U S A* 107: 8593-8

Jomaa, A., Jain, N., Davis, J. H., Williamson, J. R., Britton, R. A., Ortega, J. (2014). Functional domains of the 50S subunit mature late in the assembly process. *Nucleic Acids Res* 42: 3419-35

Jones, A. K., Woods, A. L., Takeoka, K. T., Shen, X., Wei, J. R., Caughlan, R. E., Dean, C. R. (2017). Determinants of Antibacterial Spectrum and Resistance Potential of the Elongation Factor G Inhibitor Argyrin B in Key Gram-Negative Pathogens. *Antimicrob Agents Chemother* 61

Julián, P., Konevega, A. L., Scheres, S. H., Lázaro, M., Gil, D., Wintermeyer, W., Rodnina, M. V., Valle, M. (2008). Structure of ratcheted ribosomes with tRNAs in hybrid states. *Proc Natl Acad Sci U S A* 105: 16924-7

Kaczanowska, M., Rydén-Aulin, M. (2007). Ribosome biogenesis and the translation process in Escherichia coli. *Microbiol Mol Biol Rev* 71: 477-94

Kaledhonkar, S., Fu, Z., Caban, K., Li, W., Chen, B., Sun, M., Gonzalez, R. L., Jr., Frank, J. (2019). Late steps in bacterial translation initiation visualized using time-resolved cryo-EM. *Nature* 570: 400-04

Kanjee, U., Ogata, K., Houry, W. A. (2012). Direct binding targets of the stringent response alarmone (p)ppGpp. *Mol Microbiol* 85: 1029-43

Karimi, R., Pavlov, M. Y., Buckingham, R. H., Ehrenberg, M. (1999). Novel roles for classical factors at the interface between translation termination and initiation. *Mol Cell* 3: 601-9

Kato, Y. (2019). Translational Control using an Expanded Genetic Code. *Int J Mol Sci* 20

Katunin, V. I., Savelsbergh, A., Rodnina, M. V., Wintermeyer, W. (2002). Coupling of GTP hydrolysis by elongation factor G to translocation and factor recycling on the ribosome. *Biochemistry* 41: 12806-12

Kavaliauskas, D., Chen, C., Liu, W., Cooperman, B. S., Goldman, Y. E., Knudsen, C. R. (2018). Structural dynamics of translation elongation factor Tu during aa-tRNA delivery to the ribosome. *Nucleic Acids Res* 46: 8651-61

Kazemi, M., Socan, J., Himo, F., Åqvist, J. (2018). Mechanistic alternatives for peptide bond formation on the ribosome. *Nucleic Acids Res* 46: 5345-54

Kehrenberg, C., Schwarz, S., Jacobsen, L., Hansen, L. H., Vester, B. (2005). A new mechanism for chloramphenicol, florfenicol and clindamycin resistance: methylation of 23S ribosomal RNA at A2503. *Mol Microbiol* 57: 1064-73

Khoo, C. L. Y. (1988). Structural and biosynthetic studies of the antibiotics tetracenomycin X and streptonigrin.

Kihira, K., Shimizu, Y., Shomura, Y., Shibata, N., Kitamura, M., Nakagawa, A., Ueda, T., Ochi, K., Higuchi, Y. (2012). Crystal structure analysis of the translation factor RF3 (release factor 3). *FEBS Lett* 586: 3705-9

Kim, D. F., Green, R. (1999). Base-pairing between 23S rRNA and tRNA in the ribosomal A site. *Mol Cell* 4: 859-64

Kim, D. J., Jang, J. Y., Yoon, H. J., Suh, S. W. (2008). Crystal structure of YlqF, a circularly permuted GTPase: implications for its GTPase activation in 50 S ribosomal subunit assembly. *Proteins* 72: 1363-70

Kim, H. J., Barrientos, A. (2018). MTG1 couples mitoribosome large subunit assembly with intersubunit bridge formation. *Nucleic Acids Res* 46: 8435-53

Kipper, K., Sild, S., Hetényi, C., Remme, J., Liiv, A. (2011). Pseudouridylation of 23S rRNA helix 69 promotes peptide release by release factor RF2 but not by release factor RF1. *Biochimie* 93: 834-44

Klimova, M., Senyushkina, T., Samatova, E., Peng, B. Z., Pearson, M., Peske, F., Rodnina, M. V. (2019). EF-G-induced ribosome sliding along the noncoding mRNA. *Sci Adv* 5: eaaw9049

Kohler, R., Mooney, R. A., Mills, D. J., Landick, R., Cramer, P. (2017). Architecture of a transcribing-translating expressome. *Science* 356: 194-97

Kolmsee, T., Delic, D., Agyenim, T., Calles, C., Wagner, R. (2011). Differential stringent control of Escherichia coli rRNA promoters: effects of ppGpp, DksA and the initiating nucleotides. *Microbiology* 157: 2871-79

Koripella, R. K., Holm, M., Dourado, D., Mandava, C. S., Flores, S., Sanyal, S. (2015). A conserved histidine in switch-II of EF-G moderates release of inorganic phosphate. *Sci Rep* 5: 12970

Korostelev, A., Asahara, H., Lancaster, L., Laurberg, M., Hirschi, A., Zhu, J., Trakhanov, S., Scott, W. G., Noller, H. F. (2008). Crystal structure of a translation termination complex formed with release factor RF2. *Proc Natl Acad Sci U S A* 105: 19684-9

Kothe, U., Wieden, H. J., Mohr, D., Rodnina, M. V. (2004). Interaction of helix D of elongation factor Tu with helices 4 and 5 of protein L7/12 on the ribosome. *J Mol Biol* 336: 1011-21

Koutmou, K. S., McDonald, M. E., Brunelle, J. L., Green, R. (2014). RF3:GTP promotes rapid dissociation of the class 1 termination factor. *Rna* 20: 609-20

Krásný, L., Gourse, R. L. (2004). An alternative strategy for bacterial ribosome synthesis: Bacillus subtilis rRNA transcription regulation. *Embo j* 23: 4473-83

Krzyzosiak, W., Denman, R., Nurse, K., Hellmann, W., Boublik, M., Gehrke, C. W., Agris, P. F., Ofengand, J. (1987). In vitro synthesis of 16S ribosomal RNA containing single base changes and assembly into a functional 30S ribosome. *Biochemistry* 26: 2353-64

Kuhlenkoetter, S., Wintermeyer, W., Rodnina, M. V. (2011). Different substrate-dependent transition states in the active site of the ribosome. *Nature* 476: 351-4

Kumar, V., Chen, Y., Ero, R., Ahmed, T., Tan, J., Li, Z., Wong, A. S., Bhushan, S., Gao, Y. G. (2015). Structure of BipA in GTP form bound to the ratcheted ribosome. *Proc Natl Acad Sci U S A* 112: 10944-9

La Teana, A., Gualerzi, C. O., Brimacombe, R. (1995). From stand-by to decoding site. Adjustment of the mRNA on the 30S ribosomal subunit under the influence of the initiation factors. *Rna* 1: 772-82

Laemmli, U. K. (1970). Cleavage of structural proteins during the assembly of the head of bacteriophage T4. *Nature* 227: 680-5

Landwehr, W., Wolf, C., Wink, J. (2016). Actinobacteria and Myxobacteria-Two of the Most Important Bacterial Resources for Novel Antibiotics. *Curr Top Microbiol Immunol* 398: 273-302

Lang, K., Erlacher, M., Wilson, D. N., Micura, R., Polacek, N. (2008). The role of 23S ribosomal RNA residue A2451 in peptide bond synthesis revealed by atomic mutagenesis. *Chem Biol* 15: 485-92

Laurberg, M., Asahara, H., Korostelev, A., Zhu, J., Trakhanov, S., Noller, H. F. (2008). Structural basis for translation termination on the 70S ribosome. *Nature* 454: 852-7

Lazar, G., Zahner, H., Breiding, S., Damberg, M., Zeeck, A. (1981). 3-Demethoxy-3-ethoxy-tetracenomycin C. *J Antibiot (Tokyo)* 34: 1067-8

Legault, L., Jeantet, C., Gros, F. (1972). Inhibition of in vitro protein synthesis by ppGpp. *FEBS Lett* 27: 71-75

Leong, V., Kent, M., Jomaa, A., Ortega, J. (2013). Escherichia coli rimM and yjeQ null strains accumulate immature 30S subunits of similar structure and protein complement. *Rna* 19: 789-802

Lewicki, B. T., Margus, T., Remme, J., Nierhaus, K. H. (1993). Coupling of rRNA transcription and ribosomal assembly in vivo. Formation of active ribosomal subunits in Escherichia coli requires transcription of rRNA genes by host RNA polymerase which cannot be replaced by bacteriophage T7 RNA polymerase. *J Mol Biol* 231: 581-93

Ley, S. V., Priour, A., Heusser, C. (2002). Total synthesis of the cyclic heptapeptide Argyrin B: a new potent inhibitor of T-cell independent antibody formation. *Org Lett* 4: 711-4

Li, N., Chen, Y., Guo, Q., Zhang, Y., Yuan, Y., Ma, C., Deng, H., Lei, J., Gao, N. (2013). Cryo-EM structures of the late-stage assembly intermediates of the bacterial 50S ribosomal subunit. *Nucleic Acids Res* 41: 7073-83

Li, Z., Deutscher, M. P. (1995). The tRNA processing enzyme RNase T is essential for maturation of 5S RNA. *Proc Natl Acad Sci U S A* 92: 6883-6

Li, Z., Pandit, S., Deutscher, M. P. (1999a). Maturation of 23S ribosomal RNA requires the exoribonuclease RNase T. *Rna* 5: 139-46

Li, Z., Pandit, S., Deutscher, M. P. (1999b). RNase G (CafA protein) and RNase E are both required for the 5' maturation of 16S ribosomal RNA. *Embo j* 18: 2878-85

Lin, J., Gagnon, M. G., Bulkley, D., Steitz, T. A. (2015). Conformational changes of elongation factor G on the ribosome during tRNA translocation. *Cell* 160: 219-27

Ling, C., Ermolenko, D. N. (2016). Structural insights into ribosome translocation. *Wiley Interdiscip Rev RNA* 7: 620-36

Liu, B., Li, J., Chen, M., Hao, X., Cao, F., Tan, Y., Ping, Y., Wang, Y., Xiao, C., Gan, M. (2018). Seco-Tetracenomycins from the Marine-Derived Actinomycete Saccharothrix sp. 10-10. *Mar Drugs* 16

Liu, B., Tan, Y., Gan, M. L., Zhou, H. X., Wang, Y. G., Ping, Y. H., Li, B., Yang, Z. Y., Xiao, C. L. (2014a). [Identification of tetracenomycin X from a marine-derived Saccharothrix sp. guided by genes sequence analysis]. *Yao Xue Xue Bao* 49: 230-6

Liu, C. C., Schultz, P. G. (2010). Adding new chemistries to the genetic code. *Annu Rev Biochem* 79: 413-44

Liu, G., Song, G., Zhang, D., Zhang, D., Li, Z., Lyu, Z., Dong, J., Achenbach, J., Gong, W., Zhao, X. S., Nierhaus, K. H., Qin, Y. (2014b). EF-G catalyzes tRNA translocation by disrupting interactions between decoding center and codon-anticodon duplex. *Nat Struct Mol Biol* 21: 817-24

Loh, P. C., Morimoto, T., Matsuo, Y., Oshima, T., Ogasawara, N. (2007). The GTP-binding protein YqeH participates in biogenesis of the 30S ribosome subunit in Bacillus subtilis. *Genes Genet Syst* 82: 281-9

Loizidou, E. Z., Zeinalipour-Yazdi, C. D. (2014). Computational inhibition studies of the human proteasome by argyrin-based analogues with subunit specificity. *Chem Biol Drug Des* 84: 99-107

Loveland, A. B., Demo, G., Grigorieff, N., Korostelev, A. A. (2017). Ensemble cryo-EM elucidates the mechanism of translation fidelity. *Nature* 546: 113-17

Loveland, A. B., Demo, G., Korostelev, A. A. (2020). Cryo-EM of elongating ribosome with EF-Tu•GTP elucidates tRNA proofreading. *Nature*

Lu, J., Deutsch, C. (2008). Electrostatics in the ribosomal tunnel modulate chain elongation rates. *J Mol Biol* 384: 73-86

Ma, C., Wu, S., Li, N., Chen, Y., Yan, K., Li, Z., Zheng, L., Lei, J., Woolford, J. L., Jr., Gao, N. (2017). Structural snapshot of cytoplasmic pre-60S ribosomal particles bound by Nmd3, Lsg1, Tif6 and Reh1. *Nat Struct Mol Biol* 24: 214-20

Maeda, M., Shimada, T., Ishihama, A. (2015). Strength and Regulation of Seven rRNA Promoters in Escherichia coli. *PLoS One* 10: e0144697

Maguire, B. A., Beniaminov, A. D., Ramu, H., Mankin, A. S., Zimmermann, R. A. (2005). A protein component at the heart of an RNA machine: the importance of protein l27 for the function of the bacterial ribosome. *Mol Cell* 20: 427-35

Maisonneuve, E., Gerdes, K. (2014). Molecular mechanisms underlying bacterial persisters. *Cell* 157: 539-48

Malyutin, A. G., Musalgaonkar, S., Patchett, S., Frank, J., Johnson, A. W. (2017). Nmd3 is a structural mimic of eIF5A, and activates the cpGTPase Lsg1 during 60S ribosome biogenesis. *EMBO J* 36: 854-68

Manav, M. C., Beljantseva, J., Bojer, M. S., Tenson, T., Ingmer, H., Hauryliuk, V., Brodersen, D. E. (2018). Structural basis for (p)ppGpp synthesis by the Staphylococcus aureus small alarmone synthetase RelP. *J Biol Chem* 293: 3254-64

Maracci, C., Rodnina, M. V. (2016). Review: Translational GTPases. *Biopolymers* 105: 463-75

Maracci, C., Wohlgemuth, I., Rodnina, M. V. (2015). Activities of the peptidyl transferase center of ribosomes lacking protein L27. *Rna* 21: 2047-52

Maravić, G. (2004). Macrolide resistance based on the Erm-mediated rRNA methylation. *Curr Drug Targets Infect Disord* 4: 193-202

Mardirossian, M., Sola, R., Beckert, B., Collis, D. W. P., Di Stasi, A., Armas, F., Hilpert, K., Wilson, D. N., Scocchi, M. (2019). Proline-Rich Peptides with Improved Antimicrobial Activity against E. coli, K. pneumoniae, and A. baumannii. *ChemMedChem* 14: 2025-33

Marschall, E., Cryle, M. J., Tailhades, J. (2019). Biological, chemical, and biochemical strategies for modifying glycopeptide antibiotics. *J Biol Chem* 294: 18769-83

Matsuo, Y., Morimoto, T., Kuwano, M., Loh, P. C., Oshima, T., Ogasawara, N. (2006). The GTP-binding protein YlqF participates in the late step of 50 S ribosomal subunit assembly in Bacillus subtilis. *J Biol Chem* 281: 8110-7

Matsuo, Y., Oshima, T., Loh, P. C., Morimoto, T., Ogasawara, N. (2007). Isolation and characterization of a dominant negative mutant of Bacillus subtilis GTP-binding protein, YlqF, essential for biogenesis and maintenance of the 50 S ribosomal subunit. *J Biol Chem* 282: 25270-7

Meinnel, T., Sacerdot, C., Graffe, M., Blanquet, S., Springer, M. (1999). Discrimination by Escherichia coli initiation factor IF3 against initiation on non-canonical codons relies on complementarity rules. *J Mol Biol* 290: 825-37

Melnikov, S., Ben-Shem, A., Garreau de Loubresse, N., Jenner, L., Yusupova, G., Yusupov, M. (2012). One core, two shells: bacterial and eukaryotic ribosomes. *Nat Struct Mol Biol* 19: 560-7

Miller, D. L., Cashel, M., Weissbach, H. (1973). The interaction of guanosine 5'-diphosphate, 2' (3')-diphosphate with the bacterial elongation factor Tu. *Arch Biochem Biophys* 154: 675-82

Miller, S. L. (1953). A production of amino acids under possible primitive earth conditions. *Science* 117: 528-9

Milon, P., Carotti, M., Konevega, A. L., Wintermeyer, W., Rodnina, M. V., Gualerzi, C. O. (2010). The ribosome-bound initiation factor 2 recruits initiator tRNA to the 30S initiation complex. *EMBO Rep* 11: 312-6

Milon, P., Rodnina, M. V. (2012). Kinetic control of translation initiation in bacteria. *Critical Reviews in Biochemistry and Molecular Biology* 47: 334-48

Milon, P., Tischenko, E., Tomšic, J., Caserta, E., Folkers, G., La Teana, A., Rodnina, M. V., Pon, C. L., Boelens, R., Gualerzi, C. O. (2006). The nucleotide-binding site of bacterial translation initiation factor 2 (IF2) as a metabolic sensor. *Proceedings of the National Academy of Sciences* 103: 13962

Mizushima, S., Nomura, M. (1970). Assembly mapping of 30S ribosomal proteins from E. coli. *Nature* 226: 1214

Moazed, D., Noller, H. F. (1989). Intermediate states in the movement of transfer RNA in the ribosome. *Nature* 342: 142-8

Mora, L., Heurgué-Hamard, V., Champ, S., Ehrenberg, M., Kisselev, L. L., Buckingham, R. H. (2003). The essential role of the invariant GGQ motif in the function and stability in vivo of bacterial release factors RF1 and RF2. *Mol Microbiol* 47: 267-75

Mora, L., Heurgué-Hamard, V., de Zamaroczy, M., Kervestin, S., Buckingham, R. H. (2007). Methylation of bacterial release factors RF1 and RF2 is required for normal translation termination in vivo. *J Biol Chem* 282: 35638-45

Moriarty, N. W., Grosse-Kunstleve, R. W., Adams, P. D. (2009). electronic Ligand Builder and Optimization Workbench (eLBOW): a tool for ligand coordinate and restraint generation. *Acta Crystallogr D Biol Crystallogr* 65: 1074-80

Moriya, T., Saur, M., Stabrin, M., Merino, F., Voicu, H., Huang, Z., Penczek, P. A., Raunser, S., Gatsogiannis, C. (2017). High-resolution Single Particle Analysis from Electron Cryo-microscopy Images Using SPHIRE. *J Vis Exp*

Morse, J. C., Girodat, D., Burnett, B. J., Holm, M., Altman, R. B., Sanbonmatsu, K. Y., Wieden, H. J., Blanchard, S. C. (2020). Elongation factor-Tu can repetitively engage aminoacyl-tRNA within the ribosome during the proofreading stage of tRNA selection. *Proc Natl Acad Sci U S A* 117: 3610-20

Motamedi, H., Wendt-Pienkowski, E., Hutchinson, C. R. (1986). Isolation of Tetracenomycin C-nonproducing Streptomyces Glaucescens Mutants *J Bacteriol* 167: 575-80

Mulder, A. M., Yoshioka, C., Beck, A. H., Bunner, A. E., Milligan, R. A., Potter, C. S., Carragher, B., Williamson, J. R. (2010). Visualizing ribosome biogenesis: parallel assembly pathways for the 30S subunit. *Science* 330: 673-7

Munro, J. B., Altman, R. B., O'Connor, N., Blanchard, S. C. (2007). Identification of two distinct hybrid state intermediates on the ribosome. *Mol Cell* 25: 505-17

Munro, J. B., Wasserman, M. R., Altman, R. B., Wang, L., Blanchard, S. C. (2010). Correlated conformational events in EF-G and the ribosome regulate translocation. *Nature Structural & Molecular Biology* 17: 1470-77

Mustafi, M., Weisshaar, J. C. (2018). Simultaneous Binding of Multiple EF-Tu Copies to Translating Ribosomes in Live Escherichia coli. *mBio* 9

Ni, X., Davis, J. H., Jain, N., Razi, A., Benlekbir, S., McArthur, A. G., Rubinstein, J. L., Britton, R. A., Williamson, J. R., Ortega, J. (2016). YphC and YsxC GTPases assist the maturation of the central protuberance, GTPase associated region and functional core of the 50S ribosomal subunit. *Nucleic Acids Res* 44: 8442-55

Nickeleit, I., Zender, S., Sasse, F., Geffers, R., Brandes, G., Sorensen, I., Steinmetz, H., Kubicka, S., Carlomagno, T., Menche, D., Gutgemann, I., Buer, J., Gossler, A., Manns, M. P., Kalesse, M., Frank, R., Malek, N. P. (2008). Argyrin a reveals a critical role for the tumor suppressor protein p27(kip1) in mediating antitumor activities in response to proteasome inhibition. *Cancer Cell* 14: 23-35

Nierhaus, K. 1990. Reconstitution of ribosomes, pp. 161-89

Nierhaus, K. H. (1991). The assembly of prokaryotic ribosomes. *Biochimie* 73: 739-55

Nikolaev, N., Silengo, L., Schlessinger, D. (1973). A role for ribonuclease 3 in processing of ribosomal ribonucleic acid and messenger ribonucleic acid precursors in Escherichia coli. *J Biol Chem* 248: 7967-9

Nikolay, R., Hilal, T., Qin, B., Mielke, T., Bürger, J., Loerke, J., Textoris-Taube, K., Nierhaus, K. H., Spahn, C. M. T. (2018). Structural Visualization of the Formation and Activation of the 50S Ribosomal Subunit during In Vitro Reconstitution. *Mol Cell* 70: 881-93.e3

Nissen, P., Hansen, J., Ban, N., Moore, P. B., Steitz, T. A. (2000). The structural basis of ribosome activity in peptide bond synthesis. *Science* 289: 920-30

Nissen, P., Kjeldgaard, M., Thirup, S., Clark, B. F., Nyborg, J. (1996). The ternary complex of aminoacylated tRNA and EF-Tu-GTP. Recognition of a bond and a fold. *Biochimie* 78: 921-33

Noller, H. F. (2012). Evolution of protein synthesis from an RNA world. *Cold Spring Harb Perspect Biol* 4: a003681

Noller, H. F., Lancaster, L., Zhou, J., Mohan, S. (2017). The ribosome moves: RNA mechanics and translocation. *Nat Struct Mol Biol* 24: 1021-27

Nyfeler, B., Hoepfner, D., Palestrant, D., Kirby, C. A., Whitehead, L., Yu, R., Deng, G., Caughlan, R. E., Woods, A. L., Jones, A. K., Barnes, S. W., Walker, J. R., Gaulis, S., Hauy, E., Brachmann, S. M., Krastel, P., Studer, C., Riedl, R., Estoppey, D., Aust, T., Movva, N. R., Wang, Z., Salcius, M., Michaud, G. A., McAllister, G., Murphy, L. O., Tallarico, J. A., Wilson, C. J., Dean, C. R. (2012). Identification of elongation factor G as the conserved cellular target of argyrin B. *PLoS One* 7: e42657

O'Connor, M., Leppik, M., Remme, J. (2018). Pseudouridine-Free Escherichia coli Ribosomes. *J Bacteriol* 200

O'Reilly, F. J., Xue, L., Graziadei, A., Sinn, L., Lenz, S., Tegunov, D., Blötz, C., Singh, N., Hagen, W. J. H., Cramer, P., Stülke, J., Mahamid, J., Rappsilber, J. (2020). In-cell architecture of an actively transcribing-translating expressome. *Science* 369: 554-57

Ogle, J. M., Brodersen, D. E., Clemons, W. M., Jr., Tarry, M. J., Carter, A. P., Ramakrishnan, V. (2001). Recognition of cognate transfer RNA by the 30S ribosomal subunit. *Science* 292: 897-902

Ogle, J. M., Murphy, F. V., Tarry, M. J., Ramakrishnan, V. (2002). Selection of tRNA by the ribosome requires a transition from an open to a closed form. *Cell* 111: 721-32

Opron, K., Burton, Z. F. (2018). Ribosome Structure, Function, and Early Evolution. *Int J Mol Sci* 20

Osterman, I. A., Wieland, M., Maviza, T. P., Lashkevich, K. A., Lukianov, D. A., Komarova, E. S., Zakalyukina, Y. V., Buschauer, R., Shiriaev, D. I., Leyn, S. A., Zlamal, J. E., Biryukov, M. V., Skvortsov, D. A., Tashlitsky, V. N., Polshakov, V. I., Cheng, J., Polikanov, Y. S., Bogdanov, A. A., Osterman, A. L., Dmitriev, S. E., Beckmann, R., Dontsova, O. A., Wilson, D. N., Sergiev, P. V. (2020). Tetracenomycin X inhibits translation by binding within the ribosomal exit tunnel. *Nat Chem Biol*

Pai, R. D., Zhang, W., Schuwirth, B. S., Hirokawa, G., Kaji, H., Kaji, A., Cate, J. H. (2008). Structural Insights into ribosome recycling factor interactions with the 70S ribosome. *J Mol Biol* 376: 1334-47

Palmer, S. O., Rangel, E. Y., Hu, Y., Tran, A. T., Bullard, J. M. (2013). Two homologous EF-G proteins from Pseudomonas aeruginosa exhibit distinct functions. *PLoS One* 8: e80252

Pape, T., Wintermeyer, W., Rodnina, M. (1999). Induced fit in initial selection and proofreading of aminoacyl-tRNA on the ribosome. *EMBO J* 18: 3800-7

Patil, P. R., Vithani, N., Singh, V., Kumar, A., Prakash, B. (2020). A revised mechanism for (p)ppGpp synthesis by Rel proteins: The critical role of the 2'-OH of GTP. *J Biol Chem*

Pausch, P., Steinchen, W., Wieland, M., Klaus, T., Freibert, S. A., Altegoer, F., Wilson, D. N., Bange, G. (2018). Structural basis for (p)ppGpp-mediated inhibition of the GTPase RbgA. *J Biol Chem* 293: 19699-709

Pellegrino, S., Demeshkina, N., Mancera-Martinez, E., Melnikov, S., Simonetti, A., Myasnikov, A., Yusupov, M., Yusupova, G., Hashem, Y. (2018). Structural Insights into the Role of Diphthamide on Elongation Factor 2 in mRNA Reading-Frame Maintenance. *J Mol Biol* 430: 2677-87

Peng, B. Z., Bock, L. V., Belardinelli, R., Peske, F., Grubmüller, H., Rodnina, M. V. (2019). Active role of elongation factor G in maintaining the mRNA reading frame during translation. *Sci Adv* 5: eaax8030

Peske, F., Kuhlenkoetter, S., Rodnina, M. V., Wintermeyer, W. (2014). Timing of GTP binding and hydrolysis by translation termination factor RF3. *Nucleic Acids Res* 42: 1812-20

Peske, F., Matassova, N. B., Savelsbergh, A., Rodnina, M. V., Wintermeyer, W. (2000). Conformationally restricted elongation factor G retains GTPase activity but is inactive in translocation on the ribosome. *Mol Cell* 6: 501-5

Petrov, A. S., Bernier, C. R., Gulen, B., Waterbury, C. C., Hershkovits, E., Hsiao, C., Harvey, S. C., Hud, N. V., Fox, G. E., Wartell, R. M., Williams, L. D. (2014). Secondary structures of rRNAs from all three domains of life. *PLoS One* 9: e88222

Petrov, A. S., Bernier, C. R., Hershkovits, E., Xue, Y., Waterbury, C. C., Hsiao, C., Stepanov, V. G., Gaucher, E. A., Grover, M. A., Harvey, S. C., Hud, N. V., Wartell, R. M., Fox, G. E., Williams, L. D. (2013). Secondary structure and domain architecture of the 23S and 5S rRNAs. *Nucleic Acids Res* 41: 7522-35

Petrov, A. S., Gulen, B., Norris, A. M., Kovacs, N. A., Bernier, C. R., Lanier, K. A., Fox, G. E., Harvey, S. C., Wartell, R. M., Hud, N. V., Williams, L. D. (2015). History of the ribosome and the origin of translation. *Proc Natl Acad Sci U S A* 112: 15396-401

Petry, S., Brodersen, D. E., Murphy, F. V. t., Dunham, C. M., Selmer, M., Tarry, M. J., Kelley, A. C., Ramakrishnan, V. (2005). Crystal structures of the ribosome in complex with release factors RF1 and RF2 bound to a cognate stop codon. *Cell* 123: 1255-66

Pettersen, E. F., Goddard, T. D., Huang, C. C., Couch, G. S., Greenblatt, D. M., Meng, E. C., Ferrin, T. E. (2004). UCSF Chimera--a visualization system for exploratory research and analysis. *J Comput Chem* 25: 1605-12

Pingoud, A., Block, W. (1981). The elongation factor Tu . guanosine tetraphosphate complex. *Eur J Biochem* 116: 631-4

Pingoud, A., Gast, F. U., Block, W., Peters, F. (1983). The elongation factor Tu from Escherichia coli, aminoacyl-tRNA, and guanosine tetraphosphate form a ternary complex which is bound by programmed ribosomes. *J Biol Chem* 258: 14200-5

Pletnev, P., Guseva, E., Zanina, A., Evfratov, S., Dzama, M., Treshin, V., Pogorel'skaya, A., Osterman, I., Golovina, A., Rubtsova, M., Serebryakova, M., Pobeguts, O. V., Govorun, V. M., Bogdanov, A. A., Dontsova, O. A., Sergiev, P. V. (2020). Comprehensive Functional Analysis of Escherichia coli Ribosomal RNA Methyltransferases. *Front Genet* 11: 97

Pogorevc, D., Tang, Y., Hoffmann, M., Zipf, G., Bernauer, H. S., Popoff, A., Steinmetz, H., Wenzel, S. C. (2019). Biosynthesis and Heterologous Production of Argyrins. *ACS Synth Biol* 8: 1121-33

Polikanov, Y. S., Melnikov, S. V., Söll, D., Steitz, T. A. (2015). Structural insights into the role of rRNA modifications in protein synthesis and ribosome assembly. *Nat Struct Mol Biol* 22: 342-44

Polikanov, Y. S., Steitz, T. A., Innis, C. A. (2014). A proton wire to couple aminoacyl-tRNA accommodation and peptide-bond formation on the ribosome. *Nat Struct Mol Biol* 21: 787-93

Povolotskaya, I. S., Kondrashov, F. A., Ledda, A., Vlasov, P. K. (2012). Stop codons in bacteria are not selectively equivalent. *Biol Direct* 7: 30

Prabhakar, A., Capece, M. C., Petrov, A., Choi, J., Puglisi, J. D. (2017). Post-termination Ribosome Intermediate Acts as the Gateway to Ribosome Recycling. *Cell Rep* 20: 161-72

Proshkin, S., Rahmouni, A. R., Mironov, A., Nudler, E. (2010). Cooperation Between Translating Ribosomes and RNA Polymerase in Transcription Elongation. *Science* 328: 504

Pulk, A., Cate, J. H. (2013). Control of ribosomal subunit rotation by elongation factor G. *Science* 340: 1235970

Qiao, X., Gan, M., Wang, C., Liu, B., Shang, Y., Li, Y., Chen, S. (2019). Tetracenomycin X Exerts Antitumour Activity in Lung Cancer Cells through the Downregulation of Cyclin D1. *Mar Drugs* 17

Qin, H., Grigoriadou, C., Cooperman, B. S. (2009). Interaction of IF2 with the ribosomal GTPase-associated center during 70S initiation complex formation. *Biochemistry* 48: 4699-706

Ramrath, D. J., Lancaster, L., Sprink, T., Mielke, T., Loerke, J., Noller, H. F., Spahn, C. M. (2013). Visualization of two transfer RNAs trapped in transit during elongation factor G-mediated translocation. *Proc Natl Acad Sci U S A* 110: 20964-9

Ratje, A. H., Loerke, J., Mikolajka, A., Brünner, M., Hildebrand, P. W., Starosta, A. L., Dönhöfer, A., Connell, S. R., Fucini, P., Mielke, T., Whitford, P. C., Onuchic, J. N., Yu, Y., Sanbonmatsu, K. Y., Hartmann, R. K., Penczek, P. A., Wilson, D. N., Spahn, C. M. (2010). Head swivel on the ribosome facilitates translocation by means of intra-subunit tRNA hybrid sites. *Nature* 468: 713-6

Razi, A., Britton, R. A., Ortega, J. (2017). The impact of recent improvements in cryo-electron microscopy technology on the understanding of bacterial ribosome assembly. *Nucleic Acids Res* 45: 1027-40

Razi, A., Davis, J. H., Hao, Y., Jahagirdar, D., Thurlow, B., Basu, K., Jain, N., Gomez-Blanco, J., Britton, R. A., Vargas, J., Guarne, A., Woodson, S. A., Williamson, J. R., Ortega, J. (2019). Role of Era in assembly and homeostasis of the ribosomal small subunit. *Nucleic Acids Res* 47: 8301-17

Redder, P., Hausmann, S., Khemici, V., Yasrebi, H., Linder, P. (2015). Bacterial versatility requires DEAD-box RNA helicases. *FEMS Microbiol Rev* 39: 392-412

Redko, Y., Condon, C. (2010). Maturation of 23S rRNA in Bacillus subtilis in the absence of Mini-III. *J Bacteriol* 192: 356-9

Requião, R. D., de Souza, H. J., Rossetto, S., Domitrovic, T., Palhano, F. L. (2016). Increased ribosome density associated to positively charged residues is evident in ribosome profiling experiments performed in the absence of translation inhibitors. *RNA Biol* 13: 561-8

Rocha, E. P., Danchin, A., Viari, A. (1999). Translation in Bacillus subtilis: roles and trends of initiation and termination, insights from a genome analysis. *Nucleic Acids Res* 27: 3567-76

Rodgers, M. L., Woodson, S. A. (2019). Transcription Increases the Cooperativity of Ribonucleoprotein Assembly. *Cell* 179: 1370-81 e12

Rodnina, M. V., Fischer, N., Maracci, C., Stark, H. (2017). Ribosome dynamics during decoding. *Philos Trans R Soc Lond B Biol Sci* 372

Rohou, A., Grigorieff, N. (2015). CTFFIND4: Fast and accurate defocus estimation from electron micrographs. *J Struct Biol* 192: 216-21

Rohr, J., Eick, S., Zeeck, A., Reuschenbach, P., Zahner, H., Fiedler, H. P. (1988). Metabolic products of microorganisms. 249. Tetracenomycins B3 and D3, key intermediates of the elloramycin and tetracenomycin C biosynthesis. *J Antibiot (Tokyo)* 41: 1066-73

Rohr, J., Zeeck, A. (1990). Structure-activity relationships of elloramycin and tetracenomycin C. *J Antibiot (Tokyo)* 43: 1169-78

Rojas, A. M., Ehrenberg, M., Andersson, S. G., Kurland, C. G. (1984). ppGpp inhibition of elongation factors Tu, G and Ts during polypeptide synthesis. *Mol Gen Genet* 197: 36-45

Ross, W., Thompson, J. F., Newlands, J. T., Gourse, R. L. (1990). E.coli Fis protein activates ribosomal RNA transcription in vitro and in vivo. *Embo j* 9: 3733-42

Ross, W., Vrentas, C. E., Sanchez-Vazquez, P., Gaal, T., Gourse, R. L. (2013). The magic spot: a ppGpp binding site on E. coli RNA polymerase responsible for regulation of transcription initiation. *Mol Cell* 50: 420-9

Roy, B., Liu, Q., Shoji, S., Fredrick, K. (2018). IF2 and unique features of initiator tRNA(fMet) help establish the translational reading frame. *RNA Biol* 15: 604-13

Saito, K., Green, R., Buskirk, A. R. (2020). Translational initiation in E. coli occurs at the correct sites genome-wide in the absence of mRNA-rRNA base-pairing. *Elife* 9

Samaha, R. R., Green, R., Noller, H. F. (1995). A base pair between tRNA and 23S rRNA in the peptidyl transferase centre of the ribosome. *Nature* 377: 309-14

Sanchez-Vazquez, P., Dewey, C. N., Kitten, N., Ross, W., Gourse, R. L. (2019). Genome-wide effects on Escherichia coli transcription from ppGpp binding to its two sites on RNA polymerase. *Proc Natl Acad Sci U S A* 116: 8310-19

Sasse, F., Steinmetz, H., Schupp, T., Petersen, F., Memmert, K., Hofmann, H., Heusser, C., Brinkmann, V., von Matt, P., Hofle, G., Reichenbach, H. (2002). Argyrins, immunosuppressive cyclic peptides from myxobacteria. I. Production, isolation, physico-chemical and biological properties. *J Antibiot (Tokyo)* 55: 543-51

Savelsbergh, A., Katunin, V. I., Mohr, D., Peske, F., Rodnina, M. V., Wintermeyer, W. (2003). An Elongation Factor G-Induced Ribosome Rearrangement Precedes tRNA-mRNA Translocation. *Molecular Cell* 11: 1517-23

Savelsbergh, A., Matassova, N. B., Rodnina, M. V., Wintermeyer, W. (2000a). Role of domains 4 and 5 in elongation factor G functions on the ribosome. *J Mol Biol* 300: 951-61

Savelsbergh, A., Mohr, D., Kothe, U., Wintermeyer, W., Rodnina, M. V. (2005). Control of phosphate release from elongation factor G by ribosomal protein L7/12. *EMBO J* 24: 4316-23

Savelsbergh, A., Mohr, D., Wilden, B., Wintermeyer, W., Rodnina, M. V. (2000b). Stimulation of the GTPase activity of translation elongation factor G by ribosomal protein L7/12. *J Biol Chem* 275: 890-4

Savelsbergh, A., Rodnina, M. V., Wintermeyer, W. (2009). Distinct functions of elongation factor G in ribosome recycling and translocation. *Rna* 15: 772-80

Schaberle, T. F., Lohr, F., Schmitz, A., Konig, G. M. (2014). Antibiotics from myxobacteria. *Nat Prod Rep* 31: 953-72

Schaefer, L., Uicker, W. C., Wicker-Planquart, C., Foucher, A. E., Jault, J. M., Britton, R. A. (2006). Multiple GTPases participate in the assembly of the large ribosomal subunit in Bacillus subtilis. *J Bacteriol* 188: 8252-8

Schäfer, H., Beckert, B., Frese, C. K., Steinchen, W., Nuss, A. M., Beckstette, M., Hantke, I., Driller, K., Sudzinová, P., Krásný, L., Kaever, V., Dersch, P., Bange, G., Wilson, D. N., Turgay, K. (2020). The alarmones (p)ppGpp are part of the heat shock response of Bacillus subtilis. *PLoS Genet* 16: e1008275

Schmeing, T. M., Huang, K. S., Kitchen, D. E., Strobel, S. A., Steitz, T. A. (2005a). Structural insights into the roles of water and the 2' hydroxyl of the P site tRNA in the peptidyl transferase reaction. *Mol Cell* 20: 437-48

Schmeing, T. M., Huang, K. S., Strobel, S. A., Steitz, T. A. (2005b). An induced-fit mechanism to promote peptide bond formation and exclude hydrolysis of peptidyl-tRNA. *Nature* 438: 520-4

Schmeing, T. M., Ramakrishnan, V. (2009). What recent ribosome structures have revealed about the mechanism of translation. *Nature* 461: 1234-42

Schmeing, T. M., Voorhees, R. M., Kelley, A. C., Gao, Y. G., Murphy, F. V. t., Weir, J. R., Ramakrishnan, V. (2009). The crystal structure of the ribosome bound to EF-Tu and aminoacyl-tRNA. *Science* 326: 688-94

Schubert, K., Sieger, B., Meyer, F., Giacomelli, G., Böhm, K., Rieblinger, A., Lindenthal, L., Sachs, N., Wanner, G., Bramkamp, M. (2017). The Antituberculosis Drug Ethambutol Selectively Blocks Apical Growth in CMN Group Bacteria. *mBio* 8

Scocchi, M., Tossi, A., Gennaro, R. (2011). Proline-rich antimicrobial peptides: converging to a non-lytic mechanism of action. *Cell Mol Life Sci* 68: 2317-30

Scolnick, E., Tompkins, R., Caskey, T., Nirenberg, M. (1968). Release factors differing in specificity for terminator codons. *Proc Natl Acad Sci U S A* 61: 768-74

Seffouh, A., Jain, N., Jahagirdar, D., Basu, K., Razi, A., Ni, X., Guarné, A., Britton, R. A., Ortega, J. (2019). Structural consequences of the interaction of RbgA with a 50S ribosomal subunit assembly intermediate. *Nucleic Acids Res* 47: 10414-25

Selva, E., Gastaldo, L., Saddler, G. S., Toppo, G., Ferrari, P., Carniti, G., Goldstein, B. P. (1996). Antibiotics A21459 A and B, new inhibitors of bacterial protein synthesis. I. Taxonomy, isolation and characterization. *J Antibiot (Tokyo)* 49: 145-9

Sergeeva, O. V., Bogdanov, A. A., Sergiev, P. V. (2015). What do we know about ribosomal RNA methylation in Escherichia coli? *Biochimie* 117: 110-8

Shajani, Z., Sykes, M. T., Williamson, J. R. (2011). Assembly of bacterial ribosomes. *Annu Rev Biochem* 80: 501-26

Sharma, I. M., Woodson, S. A. (2020). RbfA and IF3 couple ribosome biogenesis and translation initiation to increase stress tolerance. *Nucleic Acids Res* 48: 359-72

Shen, B., Hutchinson, C. R. (1993). Tetracenomycin F1 monooxygenase: oxidation of a naphthacenone to a naphthacenequinone in the biosynthesis of tetracenomycin C in Streptomyces glaucescens. *Biochemistry* 32: 6656-63

Shen, B., Hutchinson, C. R. (1994). Triple hydroxylation of tetracenomycin A2 to tetracenomycin C in Streptomyces glaucescens. Overexpression of the tcmG gene in Streptomyces lividans and characterization of the tetracenomycin A2 oxygenase. *J Biol Chem* 269: 30726-33

Shimojo, M., Amikura, K., Masuda, K., Kanamori, T., Ueda, T., Shimizu, Y. (2020). In vitro reconstitution of functional small ribosomal subunit assembly for comprehensive analysis of ribosomal elements in E. coli. *Commun Biol* 3: 142

Shine, J., Dalgarno, L. (1974). The 3'-terminal sequence of Escherichia coli 16S ribosomal RNA: complementarity to nonsense triplets and ribosome binding sites. *Proc Natl Acad Sci U S A* 71: 1342-6

Siibak, T., Remme, J. (2010). Subribosomal particle analysis reveals the stages of bacterial ribosome assembly at which rRNA nucleotides are modified. *Rna* 16: 2023-32

Sohmen, D., Chiba, S., Shimokawa-Chiba, N., Innis, C. A., Berninghausen, O., Beckmann, R., Ito, K., Wilson, D. N. (2015). Structure of the Bacillus subtilis 70S ribosome reveals the basis for species-specific stalling. *Nat Commun* 6: 6941

Sohmen, D., Harms, J. M., Schlunzen, F., Wilson, D. N. (2009). Enhanced SnapShot: Antibiotic inhibition of protein synthesis II. *Cell* 139: 212-12 e1

Sørensen, M. A., Pedersen, S. (1991). Absolute in vivo translation rates of individual codons in Escherichia coli: The two glutamic acid codons GAA and GAG are translated with a threefold difference in rate. *Journal of Molecular Biology* 222: 265-80

Spiegel, P. C., Ermolenko, D. N., Noller, H. F. (2007). Elongation factor G stabilizes the hybrid-state conformation of the 70S ribosome. *RNA* 13: 1473-82

Sprink, T., Ramrath, D. J. F., Yamamoto, H., Yamamoto, K., Loerke, J., Ismer, J., Hildebrand, P. W., Scheerer, P., Bürger, J., Mielke, T., Spahn, C. M. T. (2016). Structures of ribosome-bound initiation factor 2 reveal the mechanism of subunit association. *Science Advances* 2: e1501502

Sprinzl, M., Richter, D. (1976). Free 3'-OH group of the terminal adenosine of the tRNA molecule is essential for the synthesis in vitro of guanosine tetraphosphate and pentaphosphate in a ribosomal system from Escherichia coli. *Eur J Biochem* 71: 171-6

Stauch, B., Simon, B., Basile, T., Schneider, G., Malek, N. P., Kalesse, M., Carlomagno, T. (2010). Elucidation of the structure and intermolecular interactions of a reversible cyclic-peptide inhibitor of the proteasome by NMR spectroscopy and molecular modeling. *Angew Chem Int Ed Engl* 49: 3934-8

Steele, A. D., Teijaro, C. N., Yang, D., Shen, B. (2019). Leveraging a large microbial strain collection for natural product discovery. *J Biol Chem* 294: 16567-76

Steinchen, W., Bange, G. (2016). The magic dance of the alarmones (p)ppGpp. *Mol Microbiol* 101: 531-44

Steinchen, W., Schuhmacher, J. S., Altegoer, F., Fage, C. D., Srinivasan, V., Linne, U., Marahiel, M. A., Bange, G. (2015). Catalytic mechanism and allosteric regulation of an oligomeric (p)ppGpp synthetase by an alarmone. *Proc Natl Acad Sci U S A* 112: 13348-53

Steitz, T. A., Moore, P. B. (2003). RNA, the first macromolecular catalyst: the ribosome is a ribozyme. *Trends Biochem Sci* 28: 411-8

Stojković, V., Myasnikov, A. G., Young, I. D., Frost, A., Fraser, J. S., Fujimori, D. G. (2020). Assessment of the nucleotide modifications in the high-resolution cryo-electron microscopy structure of the Escherichia coli 50S subunit. *Nucleic Acids Res* 48: 2723-32

Stokes, J. M., Yang, K., Swanson, K., Jin, W., Cubillos-Ruiz, A., Donghia, N. M., MacNair, C. R., French, S., Carfrae, L. A., Bloom-Ackerman, Z., Tran, V. M., Chiappino-Pepe, A., Badran, A. H., Andrews, I. W., Chory, E. J., Church, G. M., Brown, E. D., Jaakkola, T. S., Barzilay, R., Collins, J. J. (2020). A Deep Learning Approach to Antibiotic Discovery. *Cell* 180: 688-702 e13

Su, T., Cheng, J., Sohmen, D., Hedman, R., Berninghausen, O., von Heijne, G., Wilson, D. N., Beckmann, R. (2017). The force-sensing peptide VemP employs extreme compaction and secondary structure formation to induce ribosomal stalling. *Elife* 6

Suck, D., Kabsch, W. (1981). X-ray determination of the GDP-binding site of Escherichia coli elongation factor Tu by substitution with ppGpp. *FEBS Lett* 126: 120-2

Sulthana, S., Deutscher, M. P. (2013). Multiple exoribonucleases catalyze maturation of the 3' terminus of 16S ribosomal RNA (rRNA). *J Biol Chem* 288: 12574-9

Summers, R. G., Wendt-Pienkowski, E., Motamedi, H., Hutchinson, C. R. (1992). Nucleotide sequence of the tcmII-tcmIV region of the tetracenomycin C biosynthetic gene cluster of Streptomyces glaucescens and evidence that the tcmN gene encodes a multifunctional cyclase-dehydratase-O-methyl transferase. *J Bacteriol* 174: 1810-20

Summers, R. G., Wendt-Pienkowski, E., Motamedi, H., Hutchinson, C. R. (1993). The tcmVI region of the tetracenomycin C biosynthetic gene cluster of Streptomyces glaucescens encodes the tetracenomycin F1 monooxygenase, tetracenomycin F2 cyclase, and, most likely, a second cyclase. *J Bacteriol* 175: 7571-80

Sussman, J. K., Simons, E. L., Simons, R. W. (1996). Escherichia coli translation initiation factor 3 discriminates the initiation codon in vivo. *Mol Microbiol* 21: 347-60

Świderek, K., Marti, S., Tuñón, I., Moliner, V., Bertran, J. (2015). Peptide Bond Formation Mechanism Catalyzed by Ribosome. *J Am Chem Soc* 137: 12024-34

Sykes, M. T., Sperling, E., Chen, S. S., Williamson, J. R. (2010). Quantitation of the ribosomal protein autoregulatory network using mass spectrometry. *Anal Chem* 82: 5038-45

Szeberényi, J., Roy, M. K., Vaidya, H. C., Apirion, D. (1984). 7S RNA, containing 5S ribosomal RNA and the termination stem, is a specific substrate for the two RNA processing enzymes RNase III and RNase E. *Biochemistry* 23: 2952-7

Tamaru, D., Amikura, K., Shimizu, Y., Nierhaus, K. H., Ueda, T. (2018). Reconstitution of 30S ribosomal subunits in vitro using ribosome biogenesis factors. *Rna* 24: 1512-19

Tamman, H., Van Nerom, K., Takada, H., Vandenberk, N., Scholl, D., Polikanov, Y., Hofkens, J., Talavera, A., Hauryliuk, V., Hendrix, J., Garcia-Pino, A. (2020). A nucleotide-switch mechanism mediates opposing catalytic activities of Rel enzymes. *Nat Chem Biol*

Tanaka, N., Kinoshita, T., Masukawa, H. (1968). Mechanism of protein synthesis inhibition by fusidic acid and related antibiotics. *Biochem Biophys Res Commun* 30: 278-83

Tharp, J. M., Ehnbom, A., Liu, W. R. (2018). tRNA(Pyl): Structure, function, and applications. *RNA Biol* 15: 441-52

Thirup, S. S., Van, L. B., Nielsen, T. K., Knudsen, C. R. (2015). Structural outline of the detailed mechanism for elongation factor Ts-mediated guanine nucleotide exchange on elongation factor Tu. *J Struct Biol* 191: 10-21

Thurlow, B., Davis, J. H., Leong, V., Moraes, T. F., Williamson, J. R., Ortega, J. (2016). Binding properties of YjeQ (RsgA), RbfA, RimM and Era to assembly intermediates of the 30S subunit. *Nucleic Acids Res* 44: 9918-32

Ticu, C., Nechifor, R., Nguyen, B., Desrosiers, M., Wilson, K. S. (2009). Conformational changes in switch I of EF-G drive its directional cycling on and off the ribosome. *Embo j* 28: 2053-65

Toyoda, T., Tin, O. F., Ito, K., Fujiwara, T., Kumasaka, T., Yamamoto, M., Garber, M. B., Nakamura, Y. (2000). Crystal structure combined with genetic analysis of the Thermus thermophilus ribosome recycling factor shows that a flexible hinge may act as a functional switch. *Rna* 6: 1432-44

Trobro, S., Aqvist, J. (2008). Role of ribosomal protein L27 in peptidyl transfer. *Biochemistry* 47: 4898-906

Trobro, S., Aqvist, J. (2009). Mechanism of the translation termination reaction on the ribosome. *Biochemistry* 48: 11296-303

Ude, S., Lassak, J., Starosta, A. L., Kraxenberger, T., Wilson, D. N., Jung, K. (2013). Translation elongation factor EF-P alleviates ribosome stalling at polyproline stretches. *Science* 339: 82-5

Uicker, W. C., Schaefer, L., Britton, R. A. (2006). The essential GTPase RbgA (YlqF) is required for 50S ribosome assembly in Bacillus subtilis. *Mol Microbiol* 59: 528-40

Valle, M., Zavialov, A., Sengupta, J., Rawat, U., Ehrenberg, M., Frank, J. (2003). Locking and unlocking of ribosomal motions. *Cell* 114: 123-34

Varik, V., Oliveira, S. R. A., Hauryliuk, V., Tenson, T. (2017). HPLC-based quantification of bacterial housekeeping nucleotides and alarmone messengers ppGpp and pppGpp. *Sci Rep* 7: 11022

Vazquez-Laslop, N., Thum, C., Mankin, A. S. (2008). Molecular mechanism of drug-dependent ribosome stalling. *Mol Cell* 30: 190-202

Vila, J., Moreno-Morales, J., Balleste-Delpierre, C. (2019). Current landscape in the discovery of novel antibacterial agents. *Clin Microbiol Infect*

Vinogradova, D. S., Zegarra, V., Maksimova, E., Nakamoto, J. A., Kasatsky, P., Paleskava, A., Konevega, A. L., Milón, P. (2020). How the initiating ribosome copes with ppGpp to translate mRNAs. *PLoS Biol* 18: e3000593

Vogeley, L., Palm, G. J., Mesters, J. R., Hilgenfeld, R. (2001). Conformational change of elongation factor Tu (EF-Tu) induced by antibiotic binding. Crystal structure of the complex between EF-Tu.GDP and aurodox. *J Biol Chem* 276: 17149-55

Vollbrecht, L., Steinmetz, H., Hofle, G., Oberer, L., Rihs, G., Bovermann, G., von Matt, P. (2002). Argyrins, immunosuppressive cyclic peptides from myxobacteria. II. Structure elucidation and stereochemistry. *J Antibiot (Tokyo)* 55: 715-21

Voorhees, R. M., Weixlbaumer, A., Loakes, D., Kelley, A. C., Ramakrishnan, V. (2009). Insights into substrate stabilization from snapshots of the peptidyl transferase center of the intact 70S ribosome. *Nat Struct Mol Biol* 16: 528-33

Wallin, G., Aqvist, J. (2010). The transition state for peptide bond formation reveals the ribosome as a water trap. *Proc Natl Acad Sci U S A* 107: 1888-93

Wang, L. (2017). Engineering the Genetic Code in Cells and Animals: Biological Considerations and Impacts. *Acc Chem Res* 50: 2767-75

Wang, W., Li, W., Ge, X., Yan, K., Mandava, C. S., Sanyal, S., Gao, N. (2020). Loss of a single methylation in 23S rRNA delays 50S assembly at multiple late stages and impairs translation initiation and elongation. *Proc Natl Acad Sci U S A* 117: 15609-19

Weber, W., Zahner, H., Siebers, J., Schroder, K., Zeeck, A. (1979). [Metabolic products of microorganisms. 175. Tetracenomycin C (author's transl)]. *Arch Microbiol* 121: 111-6

Weinger, J. S., Parnell, K. M., Dorner, S., Green, R., Strobel, S. A. (2004). Substrate-assisted catalysis of peptide bond formation by the ribosome. *Nat Struct Mol Biol* 11: 1101-6

Whitford, P. C., Geggier, P., Altman, R. B., Blanchard, S. C., Onuchic, J. N., Sanbonmatsu, K. Y. (2010). Accommodation of aminoacyl-tRNA into the ribosome involves reversible excursions along multiple pathways. *Rna* 16: 1196-204

WHO. (2017). Prioritization of pathogens to guide discovery, research and development of new antibiotics for drug-resistant bacterial infections, including tuberculosis. *Geneva: World Health Organisation*

WHO. (2019a). Antibacterial agents in clinical development: an analysis of the antibacterial clinical development pipeline. *Geneva: World Health Organisation*

WHO. (2019b). Antibacterial agents in preclinical development: an open access database. *Geneva: World Health Organisation*

Wilson, D. N., Nierhaus, K. H. (2005). Ribosomal proteins in the spotlight. *Crit Rev Biochem Mol Biol* 40: 243-67

Wilson, D. N., Nierhaus, K. H. (2007). The weird and wonderful world of bacterial ribosome regulation. *Crit Rev Biochem Mol Biol* 42: 187-219

Wilson, D. N., Schluenzen, F., Harms, J. M., Yoshida, T., Ohkubo, T., Albrecht, R., Buerger, J., Kobayashi, Y., Fucini, P. (2005). X-ray crystallography study on ribosome recycling: the mechanism of binding and action of RRF on the 50S ribosomal subunit. *EMBO J* 24: 251-60

Wower, I. K., Wower, J., Zimmermann, R. A. (1998). Ribosomal protein L27 participates in both 50 S subunit assembly and the peptidyl transferase reaction. *J Biol Chem* 273: 19847-52

Xia, B., Ke, H., Shinde, U., Inouye, M. (2003). The role of RbfA in 16S rRNA processing and cell growth at low temperature in Escherichia coli. *J Mol Biol* 332: 575-84

Xiao, H., Kalman, M., Ikehara, K., Zemel, S., Glaser, G., Cashel, M. (1991). Residual guanosine 3',5'-bispyrophosphate synthetic activity of relA null mutants can be eliminated by spoT null mutations. *J Biol Chem* 266: 5980-90

Yao, L., Li, Y., Tsai, T. W., Xu, S., Wang, Y. (2013). Noninvasive measurement of the mechanical force generated by motor protein EF-G during ribosome translocation. *Angew Chem Int Ed Engl* 52: 14041-4

Yin, H., Gavriliuc, M., Lin, R., Xu, S., Wang, Y. (2019). Modulation and Visualization of EF-G Power Stroke During Ribosomal Translocation. *Chembiochem* 20: 2927-35

Young, R. A., Steitz, J. A. (1979). Tandem promoters direct E. coli ribosomal RNA synthesis. *Cell* 17: 225-34

Yusupov, M. M., Yusupova, G. Z., Baucom, A., Lieberman, K., Earnest, T. N., Cate, J. H., Noller, H. F. (2001). Crystal structure of the ribosome at 5.5 A resolution. *Science* 292: 883-96

Zaher, H. S., Shaw, J. J., Strobel, S. A., Green, R. (2011). The 2'-OH group of the peptidyl-tRNA stabilizes an active conformation of the ribosomal PTC. *Embo j* 30: 2445-53

Zavialov, A. V., Hauryliuk, V. V., Ehrenberg, M. (2005). Splitting of the posttermination ribosome into subunits by the concerted action of RRF and EF-G. *Mol Cell* 18: 675-86

Zavialov, A. V., Mora, L., Buckingham, R. H., Ehrenberg, M. (2002). Release of peptide promoted by the GGQ motif of class 1 release factors regulates the GTPase activity of RF3. *Mol Cell* 10: 789-98

Zborníková, E., Knejzlík, Z., Hauryliuk, V., Krásný, L., Rejman, D. (2019). Analysis of nucleotide pools in bacteria using HPLC-MS in HILIC mode. *Talanta* 205: 120161

Zengel, J. M., Lindahl, L. (1994). Diverse Mechanisms for Regulating Ribosomal Protein Synthesis in Escherichia coli. 47: 331-70

Zgurskaya, H., Krishnamoorthy, G., Ntreh, A., Lu, S. (2011). Mechanism and Function of the Outer Membrane Channel TolC in Multidrug Resistance and Physiology of Enterobacteria. *Frontiers in Microbiology* 2

Zheng, S. Q., Palovcak, E., Armache, J. P., Verba, K. A., Cheng, Y., Agard, D. A. (2017). MotionCor2: anisotropic correction of beam-induced motion for improved cryo-electron microscopy. *Nat Methods* 14: 331-32

Zhou, D., Tanzawa, T., Lin, J., Gagnon, M. G. (2020). Structural basis for ribosome recycling by RRF and tRNA. *Nat Struct Mol Biol* 27: 25-32

Zhou, J., Korostelev, A., Lancaster, L., Noller, H. F. (2012). Crystal structures of 70S ribosomes bound to release factors RF1, RF2 and RF3. *Curr Opin Struct Biol* 22: 733-42

Zhou, J., Lancaster, L., Donohue, J. P., Noller, H. F. (2013). Crystal structures of EF-G-ribosome complexes trapped in intermediate states of translocation. *Science* 340: 1236086

Zhou, J., Lancaster, L., Donohue, J. P., Noller, H. F. (2014). How the ribosome hands the A-site tRNA to the P site during EF-G-catalyzed translocation. *Science* 345: 1188-91

Zhou, J., Lancaster, L., Donohue, J. P., Noller, H. F. (2019). Spontaneous ribosomal translocation of mRNA and tRNAs into a chimeric hybrid state. *Proc Natl Acad Sci U S A* 116: 7813-18

Zhu, M., Dai, X., Wang, Y. P. (2016). Real time determination of bacterial in vivo ribosome translation elongation speed based on LacZα complementation system. *Nucleic Acids Res* 44: e155

Zivanov, J., Nakane, T., Forsberg, B. O., Kimanius, D., Hagen, W. J., Lindahl, E., Scheres, S. H. (2018). New tools for automated high-resolution cryo-EM structure determination in RELION-3. *Elife* 7

Zuo, Y., Wang, Y., Steitz, T. A. (2013). The mechanism of E. coli RNA polymerase regulation by ppGpp is suggested by the structure of their complex. *Mol Cell* 50: 430-6

8. Publications

2018

Pausch, P., Steinchen, W., **Wieland, M.**, Klaus, T., Freibert, S. A., Altegoer, F., Wilson, D. N. and Bange, G. (2018). Structural basis for (p)ppGpp-mediated inhibition of the GTPase RbgA.
J Biol Chem 293: 19699-709

2020

Steinchen, W., Majkini, M., **Wieland, M.**, Dornes, A., Giammarinaro, P.I., Lepak, A., Burnett, B.J., Blanchard, S.C., Wilson, D.N. and Bange, G. Structural basis for the (p)ppGpp-dependent control of the translation elongation factor EF-Tu
Manuscript ready for publication

Osterman, I. A.*, **Wieland, M.***, Maviza, T. P.*, Lashkevich, K. A., Lukianov, D. A., Komarova, E. S., Zakalyukina, Y. V., Buschauer, R., Shiriaev, D. I., Leyn, S. A., Zlamal, J. E., Biryukov, M. V., Skvortsov, D. A., Tashlitsky, V. N., Polshakov, V. I., Cheng, J., Polikanov, Y. S., Bogdanov, A. A., Osterman, A. L., Dmitriev, S. E., Beckmann, R., Dontsova, O. A., Wilson, D. N. and Sergiev, P. V. (2020). Tetracenomycin X inhibits translation by binding within the ribosomal exit tunnel.
Nat Chem Biol

*) these authors contributed equally to the publication

Structural basis for (p)ppGpp-mediated ribosomal large subunit arrest by RbgA

Patrick Pausch[1,2,*], Maximiliane Wieland[3], Thomas Klaus[1,2], Sven-Andreas Freibert[2,4], Wieland Steinchen[1,2], Daniel N. Wilson[3,*] and Gert Bange[1,2,*]

[1]Department of Chemistry, Philipps-University Marburg, Hans-Meerwein-Strasse, C07, 35043 Marburg, Germany;
[2]Synmikro Center for synthetic Microbiology, Hans-Meerwein-Strasse, 35043 Marburg, Germany;
[3]Institute for Biochemistry and Molecular Biology, University of Hamburg, Hamburg, Germany;
[4]Institute für Cytobiology und Cytopathology, Philipps-University Marburg, Robert-Koch-Strasse 6, 35043 Marburg, Germany

*To whom correspondence should be addressed: Patrick.Pausch@synmikro.uni-marburg.de, Gert.Bange@synmikro.uni-marburg.de, Daniel.Wilson@chemie.uni-hamburg.de

Keywords: RbgA, GTPase, (p)ppGpp, stringent response, ribosome assembly, cryo-electron microscopy, X-ray crystallography

Abstract

Efficient adaptation to environmental changes is pivotal to all bacterial cells. Almost all bacterial species depend on the conserved stringent response system to prompt timely transcriptional and metabolic readjustments according to stress and nutrient depletion. The stringent response relies on the stress dependent synthesis of the second messenger nucleotide (p)ppGpp that pleiotropically targets and reprograms processes that consume cellular resources, such as the biogenesis of ribosomes. Here we show how (p)ppGpp acts on the ribosome biogenesis GTPase A (RbgA). We demonstrate by X-ray crystallography and *in vitro* activity assays that (p)ppGpp prevents the GTPase active conformation of *Staphylococcus aureus* RbgA by sterically blocking the association of the G2 motif via the 3'-pyrophosphate moieties. We furthermore show by cryo-EM that RbgA induces structural destabilization at H67-71 of the large subunit, suggesting that H67-71 represents the interface for RbgA on the large subunit. Taken together, our structural and biochemical characterization of RbgA in context of the stringent response alarmone reveals how (p)ppGpp affects the function of RbgA and reprograms the GTPase to act as a ribosomal large subunit arresting factor.

Introduction

Rapidly reproducing bacterial cells depend on an effective translational machinery to maintain their fast growth rate. At the heart of this machinery, ribosomes translate mRNA into proteins. However, functional ribosomes have to be assembled in an efficient manner to meet the high demand on the translational capacity during cell proliferation. In *Escherichia coli*, ribosome assembly is estimated to take approximately two minutes with a corresponding assembly rate of 100,000 ribosomes per hour [1]. Bacterial ribosome biogenesis involves the initial transcription of a ~5 kb primary ribosomal RNA (rRNA) transcript that is co-transcriptionally cleaved and modified to yield three mature rRNAs (23S, 16S and 5S) that provide a platform for assembly of large (50S) and small (30S) subunits. Folding of the rRNA occurs co-transcriptionally and is accompanied by the hierarchically variable and blockwise incorporation of ~50 ribosomal proteins (r-proteins) [2]. The assembly process involves a set of approximately 100 ribosome biogenesis factors to facilitate cleaving, modification and chaperoning of the intermediates in both, the 50S and 30S biogenesis pathways [3]. Therefore, ribosome biogenesis imposes a high metabolic load on bacterial cells and has to be precisely regulated during nutrient starvation to preserve cellular resources. In many bacterial species ribosome biogenesis is regulated by the stringent response system that senses stress stimuli and signals the stress level via the pleiotropically acting nucleotide messenger alarmones (p)ppGpp [4,5]. Upon stress, such as restricted nutrient availability, RSH (RelA/SpoT Homologue)-type proteins produce (p)ppGpp by transfer of pyrophosphate from ATP onto the 3′-OH moiety of GTP or GDP. Eventually, when environmental conditions ameliorate, (p)ppGpp is hydrolyzed by RSH-type hydrolases to retrieve GTP/GDP and consequently stress signaling declines. Alarmone-mediated regulation of ribosome biogenesis not only includes the repression of rRNA and r-protein gene transcription to shut down production of ribosomal components, but may also involve the inhibition of ribosome biogenesis factors to block the assembly of ribosomal subunits [4,6]. In particular, the *Staphylococcus aureus* ribosome biogenesis associated GTPases RbgA, HflX, Era, RsgA and ObgE have been recently shown to be directly targeted by (p)ppGpp to suppress GTPase activity [6]. It has been hypothesized that the (p)ppGpp mediated GTPase activity suppression prevents the final ribosome subunit maturation step and might therefore arrest subunits before they engage as matured subunits in 70S formation and translation [6].

The 50S subunit ribosome biogenesis GTPase RbgA (Ribosome biogenesis GTPase A, also: Ylqf) has been shown to be essential for growth in *Bacillus subtilis* [7]. Depletion of RbgA leads to a reduction of 70S ribosomes resulting from an arrest of large subunit biogenesis at pre-mature 45S particles that lack the ribosomal proteins L16, L27, L28, L33, L36 and L37 and might be incompetent in 70S formation [8–12]. RbgA homologues (YRG family – Ylqf-Related GTPase) are evolutionary widely distributed and can be found in all three kingdoms of life [13,14]. In *Saccharomyces cerevisiae*, the eukaryotic RbgA homologue Lsg1 acts late during the final ribosomal large subunit maturation and was shown to be involved in the GTPase-dependent release of the nuclear export adapter Nmd3 upon 60S subunit completion [15–17]. RbgA belongs to the TRAFAC (translation factor) GTPase family and comprises a N-terminal Rossmann fold GTP binding domain (G domain) and a C-terminal alpha helical domain [18]. The HAS-type G domain features a K-loop for K^+ ion cofactor binding and is characterized by a circularly permuted GTPase fold (cpGTPase) in which the conserved G1-G2-G3-G4-G5 motif is rearranged to G4-G5-G1-G2-G3 in the protein sequence [18–21]. It has been hypothesized that the cpGTPase fold might allow a nucleotide ligand-dependent movement of the C-terminal domain, which has also been suggested to be involved in rRNA contacts and might participate in rRNA remodeling [21]. Crystal structures of the RbgA homologues of *Thermotoga maritima* and *Bacillus subtilis* are available and reveal the N-terminal GTPase fold preceded by a alpha helical C-terminal putative RNA binding domain (PDB-IDs 3CNN, 3CNO, 3CNL and 1PUJ). However, the molecular details of ribosome interaction and the mechanism of GTPase activation for 50S maturation have remained enigmatic. Furthermore, the mechanism by which the stringent response alarmone (p)ppGpp blocks the GTPase activation of RbgA to arrest the maturation of large ribosomal subunits is also unknown.

Here we present high-resolution X-ray crystal structures of *S. aureus* RbgA in presence of GDP, GMPPNP, ppGpp and pppGpp suggesting that the nucleotides do not change RbgA's configuration in the ribosome-free state. We furthermore show by cryo electron microscopy (cryo-EM) of *B. subtilis* RbgA associated to 50S ribosomal subunits, that RbgA remodels the large ribosomal subunit in proximity to the A- and P-site at the 23S rRNA helices H67-H71. Comparison of ribosome-free RbgA with the ribosome associated GTPase active state of the eukaryotic RbgA homologue Lsg1 suggests how RbgA GTPase activation is triggered at the large subunit and

inhibited by (p)ppGpp. Taken together, our structural and biochemical analyses of RbgA for the first time reveal how the GTPase active conformation is suppressed by (p)ppGpp to arrest large ribosomal subunits during the stringent response.

Results

Structures of *S. aureus* RbgA bound to GDP and GMPPNP

Typically, GTPases undergo conformational rearrangements upon hydrolysis of GTP to GDP and the subsequent release of inorganic phosphate. To delineate nucleotide dependent conformational changes of *S. aureus* RbgA, we determined its crystal structures bound to GDP and the non-hydrolysable GTP analogue guanosine-5'-[(β,γ)-imido]triphosphate (GMPPNP) at 2.15 Å and 1.93 Å resolution, respectively (**Table 1**). Both structures revealed the two-domain architecture of RbgA consisting of the N-terminal G-domain followed by the C-terminal α-helical putative rRNA interaction domain (**Fig. 1A-E**). Both, GDP and GMPPNP, could be unambiguously identified in the unbiased electron density map within the GTPase active site of RbgA (**Fig. S1A-B**). The guanine base is accommodated by stacking interactions of lysine 88 and lysine 59 and identified by hydrogen bonding interactions of aspartate 86 and 61, and asparagine 58 of the G5 and G4 GTPase motifs, respectively (**Fig. 1D-E**). Amino acids 129 to 134 of the G1 motif contribute to coordination of the α-, β- and γ-phosphate moieties via hydrogen bonding and salt bridge interactions (**Fig. 1D-E**). The γ-phosphate of GMPPNP is furthermore surrounded by the non-polar sidechains of proline 129 and isoleucine 175 of the G1 and G3 motif and is less well defined in the electron density map than the α- and β-phosphate moieties (**Fig. S1B**). Thus, RbgA coordinates its GDP and GTP nucleotides in an identical fashion to other homologous GTPases. Despite the different nucleotide content, no significant structural differences between the GDP and GMPPNP-bound state could be observed. The root mean square deviations (r.m.s.d.) between both structures and the individual monomers in the unit cell were below 0.2 Å (**Table S1; Fig. S2A-E**). This observation is substantiated by the fact that both states of RgbA crystallized in the same space group with identical cell dimensions (**Table 1**). Therefore, we conclude that the conformational state of RgbA is not necessarily affected by the

nature of the nucleotide bound within its active site. However, it is important to note that crystal packing might impact the configuration in our structures.

Structures of ppGpp- and pppGpp-bound RbgA

The alarmones (p)ppGpp inhibit the GTPase activity of RbgA, yet the underlying molecular mechanism has remained unknown [6]. To address this question, we determined the crystal structures of RbgA bound to ppGpp and pppGpp at 1.8 Å and 1.65 Å resolution, respectively (**Fig. 2A-B, Table 1**). We unambiguously identified the alarmones ppGpp and pppGpp in the unbiased electron density map within the active site of the RbgA G-domain (**Fig. S1C-D**). The GDP and GTP moieties of ppGpp and pppGpp, respectively, associate to the active site in an identical fashion as their native nucleotide counterparts. The 3'-pyrophosphate moieties of both alarmones point away from the active site towards the solvent and seem to be stabilized only by the e-amino group of lysine 88 of the G5 motif (**Fig. 2A-B**). However, lysine 88 is not conserved among RbgA homologues arguing against a substantial role of this residue for the coordination of (p)ppGpp to RgbA (**Fig. S3**). This is further supported by comparable binding constants of RbgA for GDP, GTP, ppGpp and pppGpp as determined by MicroScale thermophoresis (**Figs. 2C and S4A-D**). Structural comparison of the alarmone-bound states of RbgA with its GDP/GMPPNP-bound states revealed no significant structural differences as indicated by the low r.m.s.d. (< 0.3 Å) (**Table S1; Fig. S2A-E**). These findings show that the alarmones do not alter the conformation of ribosome free RbgA.

RbgA binds nucleotides in the absence of magnesium

Our inspection of the electron density maps of the presented structures did not show electron density for magnesium, although magnesium was present in the final size exclusion buffer at a concentration of 20 mM. The absence of magnesium is also true for the crystal structures observed for the *T. maritima* RbgA in complex with GDP, GTP and GMPPNP (PDB IDs: 3CNN, 3CNO and 3CNL [18]). Since the Mg^{2+} ion cofactor is essential for catalysis, we reason that our structures and the previously reported structure of the *T. maritima* homologue do not represent the GTPase active conformation of RbgA. In canonical GTPases, binding of Mg^{2+} in a tetragonal bipyramidal coordination sphere is facilitated by the G1, G2 and G3 motifs. Serine/threonine of the G1 motif GxxxxGKS/T (P-loop) forms a direct contact while

aspartate of the G3 motif DxxG forms a water-mediated contact to the Mg^{2+}, which is required for tight binding of the cofactor [22]. The coordination sphere is completed by a contact via the conserved threonine of the G2 motif. However, our crystal structures revealed that although the G1 motif is in a position capable of interacting with a properly placed Mg^{2+} ion, the G2 (switch I) and G3 (switch II) motifs are positioned in a manner apparently not allowing interaction with the Mg^{2+} ion (**Fig. 3A**). Comparison of our structure and the *T. maritima* RbgA structure with the GTP-bound *B. subtilis* RbgA revealed that G3 rearrangement might coincide with GTP and Mg^{2+} cofactor binding (**Fig. 3B-C**). Noteworthy, the G3 motif is directly connected to the putative C-terminal RNA binding domain via a linker and rearrangement of the C-terminal domain upon contact with the large subunit might allow proper positioning of the G3 motif and GTP and Mg^{2+} cofactor binding, or *vice versa*. Mutation of the conserved phenylalanine at position 180 in the G3 linker region has been shown to be lethal for *B. subtilis* RbgA underlining the importance of this region [21]. In summary, displacement of the G2 and G3 motifs in absence of the proper RNA contact site might result in cofactor release and GTPase suppression.

Cryo-EM structure of an RbgA-50S complex

To analyze the interaction of RbgA with the large ribosomal subunit, we formed complexes of RbgA with 50S subunits in the presence of GMPPNP (**Fig. S5**). Since RbgA appears to be involved in a late step in large subunit biogenesis we formed complexes with mature 50S subunits, as it has been successfully performed previously for other bacterial ribosome biogenesis complexes (e.g. Era [23], RbfA [24] and RsgA [25,26] on the 30S subunit and EngA [27] and ObgE [28] on the 50S subunit). Moreover, mature large subunits have been shown to stimulate the GTPase activity of RbgA [19], and Lsg1 was trapped with GMPPNP on mature 60S subunits in the presence of Nmd3[17]. Therefore, the RbgA-50S-GMPPNP complex was applied to cryo-grids and cryo-EM data was collected on a Titan Krios (FEI) transmission electron microscope with a Falcon II direct electron detector. 3D classification using FREALIGN [29] revealed two major subpopulations of 50S particles, mature 50S particles (34%) and 50S-like particles (34%) that appeared to lack density for specific 23S rRNA helices, which we termed intermediate 50S ($50S_{Int}$) particles (**Fig. S6**). Both subpopulations were refined to yield cryo-EM maps of the mature 50S and $50S_{Int}$ particles (**Fig 4A-B**), with average resolutions of 3.6 Å and 3.7 Å, respectively

(**Fig. S7**). Fitting of molecular models for the 50S subunit immediately revealed that while strong density for 23S rRNA helices H67-H71 was present in the mature 50S subunit, this density was absent in the $50S_{Int}$ (**Figs. 4A-D**). This suggested that binding of RbgA to the mature 50S subunit leads to a destabilization of rRNA helices H67-H71, comparable to the cryo-EM structures of RbgA-depleted 45S particles [11,12] and also YphC-depleted 45S particles[30] (**Fig. S8A-D**). Surprisingly, no clear density for RbgA was observed in the cryo-EM maps of the $50S_{Int}$, suggesting that it was not stably bound to the particle and/or highly flexible. Filtering of the cryo-EM map to lower resolutions indeed revealed a large region of density located at the intersubunit surface within the region of H69 (**Fig. 4E**). Unfortunately, the density is poorly defined and may therefore represent the delocalized 23S rRNA helices alone or together with RbgA. We noted that the yeast homology of RbgA, Lsg1, was not observed in the absence of Nmd3 [17] and was poorly resolved in the structure of the pre-60S particle [31]. The use of 0.5% glutaraldehyde crosslinking in the 60S-Nmd3-Lsg1 localized the binding site of directly adjacent to H69 [17], where we observe the large delocalized electron density (**Fig. 4F**). Therefore, we conclude that if RbgA is present in the $50S_{Int}$ complex, being highly flexible due to its likely interaction with the destabilized helices H69-H71.

RbgA GTPase inhibition by (p)ppGpp

Comparison of the crystal structure of alarmone bound *S. aureus* RbgA, *B. subtilis* RbgA and *S. cerevisiae* Lsg1 revealed that the δ- and ε-phosphates are placed in a position that would allow proper positioning of the G3 motif, but may also prohibit full association of the G2 motif and should therefore impede Mg^{2+} and K^{+} coordination for hydrolase activation (**Fig. 5A**). Hence, RbgA should not be capable of pppGpp hydrolysis. To test this hypothesis, we assayed RbgA GTPase for the ability to hydrolyze (p)ppGpp (**Fig. 5B-E**). Strikingly, RbgA did not hydrolyze (p)ppGpp, showing that the additional phosphate moieties prohibit the catalytically active conformation likely by blocking association of the G2 motif (**Fig. 5B**). We additionally assayed the GTPase activity of RbgA in presence 70S ribosomes and (p)ppGpp (**Fig. 5**). As expected from a previous study [6], the presence of 70S ribosomes stimulated the GTPase activity of RbgA. Incubation of RbgA alone and in presence of 70S ribosomes with varying ratios of GTP:(p)ppGpp (1:1, 0.5:1 and 0.25:1) revealed that the GTP hydrolysis activity of RbgA is repressed only if the concentration of

(p)ppGpp exceeds that of GTP, arguing for a competitive inhibition (**Fig. 5C-E**). Summed up, the δ- and ε-phosphate moieties prohibit GTPase activation and might therefore sequester RbgA at large ribosomal subunits under stringent response conditions.

Discussion

(p)ppGpp blocks the GTPase active conformation of RbgA

In this study, we revealed how the stringent response alarmone (p)ppGpp suppresses the GTPase activity of the evolutionary widely conserved and essential large ribosomal subunit biogenesis cpGTPase RbgA. Our crystal structures of *S. aureus* RbgA suggest that ribosome-free RbgA exists in a conformation not compatible with hydrolysis of GTP, characterized by the displaced G2 and G3 motifs (switch I + II) that leads to a deficiency of the active site coordination of Mg^{2+} and K^{+}. We furthermore demonstrate by our biochemical analysis that RbgA is incapable of hydrolyzing (p)ppGpp, suggesting that the δ- and ε-phosphate moieties prohibit the active conformation by precluding full association of the G2 motif. Association of the G2 motif to the active site, however, has previously been noted in a biochemical analysis of RbgA from *B. subtilis* [19] to be crucial for efficient Mg^{2+}/K^{+} cofactor coordination and hence for formation of the active configuration. From our data and based on a model of the RbgA switch loop (K-loop), which was derived from a homology modeling according to the transition state structure of the GTPase MnmE we also conclude, that correct association of the loop structure is required to activate the GTPase. We moreover provide evidence for the alarmones (p)ppGpp acting in a GTP competitive manner to reduce the GTPase activity of RbgA. This suggests that (p)ppGpp likely sequesters RbgA 45S and 50S particles due to GTPase suppression, which is supported by the observation that pppGpp increases the affinity of RbgA for mature 50S subunits [19]. This, in turn, might withdraw mature 50S subunits from the formation of translationally active 70S ribosomes and consequently shuts down not only ribosome maturation but also protein production to economize cellular resources during starvation [6,19]. Taken together, our crystal structures and biochemical analyses of RbgA suggest that the alarmone (p)ppGpp prohibits formation of the

GTPase active configuration by sterically precluding association of the G2 motif via the δ- and ε-phosphate moieties in a GTP competitive manner.

Implications for final 50S ribosome subunit maturation

Final maturation of the large subunit is to some extend conserved between prokaryotic and eukaryotic ribosomes and incorporation of uL16 coincides with Lsg1/RbgA GTPase activation and release [12,17]. However, the process appears unequally more intricate in eukaryotes than in prokaryotes. In brief, delivery and incorporation of uL16 has been shown in *S. cerevisiae* to require the dedicated chaperone Sqt1 that shields uL16's N-terminal domain before incorporation at the central protuberance close to the P-site [32]. Incorporation of uL16 into mature the large subunit appears to be concerted with the release of Sqt1, the activation and dissociation of the GTPase Lsg1, and the release of large subunit export adapter Nmd3 [15–17,32]. However, it is not precisely understood if the GTPase activity of Lsg1 is required to assemble uL16 or if assembly of uL16 leads to activation of Lsg1 and Nmd3 release to signal for subunit maturation. A similar but less complex scenario has been observed in the prokaryotic 50S maturation. RbgA-depleted cells enrich uL16 deficient pre-45S particles and presence of uL16 is required for stimulation of the GTPase activity and release of RbgA [12]. Cryo-EM of pre-45S particles from RbgA depleted cells revealed that four 45S subunit regions have a particular high degree of conformational flexibility: the central protuberance, helix 38 (A-site finger), helices 89-93 of the PTC and helices 67-71 which are required for ribosomal intersubunit contacts [11,12]. Interestingly, our cryo-EM analyses of RbgA-50S particles show that densities for helices 76-71 are absent in the $50S_{Int}$ structure. Filtering of the cryo-EM map to lower resolution, however, revealed a large region of density within the region of H69. Since the binding interface of Lsg1 is located in the same region of the LSU and the ribosome maturation function is conserved between the homologues, we speculate that the RbgA binding interface on the 23S rRNA is analogously located on helices 67-71. Noteworthy, the distance between the putative binding site of RbgA as identified by cryo-EM and the incorporation site of uL16 in between helix 38 and 89 of the 23S rRNA are approximately 40 Å apart. Hence, RbgA might not be activated by a direct contact with uL16. It seems more conceivable that incorporation of uL16 induces structural rearrangement in the 23S rRNA, which propagates towards H68-71 of the large subunit. The mature 50S arrangement of H69-71 might then allow

RbgA to assume the GTPase active configuration by positioning its flexibly linked N-terminal G-domain and C-terminal putative RNA binding domain to rearrange the G-motifs capable of hydrolyzing GTP for RbgA release as suggested by the structural homology to the G-domain and RNA binding domain of Lsg1 (**Fig. 6**). In conclusion, our observation combined with the available structural data on 45S particles from RbgA-depleted cells suggests that RbgA associates to H68-71 of 45S particles, which in turn allows proper positioning of the surrounding PTC helices 89-93, helix 38 (A-site finger) and the adjacent CP compatible with recruitment of the final r-proteins. Incorporation of the final r-protein set may then establish the mature configuration of the CP and PTC, which leads to the mature configuration of H68-71 and eventually the GTPase activation and release of RbgA to signal for 50S completion.

Experimental procedures

Cloning of expression constructs. *S. aureus rbgA* was amplified by PCR from *S. aureus* USA300 genomic DNA (gDNA) using a forward primer that contained a NcoI restriction site and the coding sequence for a hexa-histidine tag and a reverse primer, which contained a BamHI restriction site. The fragment was digested with NcoI and BamHI and cloned into pET24d (Novagen). The *B. subtilis rbgA* homologue was amplified from *B. subtilis* 168 gDNA and cloned into pET24d via the same strategy.

Production and purification of RbgA. Constructs were transformed in *E. coli* BL21(DE3) (Novagen) for overexpression. Cells (Novagen) were inoculated into two liters of LB medium, supplemented with 25 g lactose and kanamycin (50 mg/l). Cells were incubated at 30 °C over night under rigorous shaking (180 revolutions per minute (rpm)). Cells were harvested by centrifugation (3,500 x g, 20 min, 4 °C) and resuspended in 20 ml buffer A (20 mM HEPES-Na, pH 8.0, 250 mM NaCl, 20 mM KCl, 20 mM $MgCl_2$, 40 mM imidazole) before lysis in a M-110L Microfluidizer (Microfluidics). The lysate was cleared at 47,850 x g for 20 min at 4 °C and the supernatant was applied onto two 1 ml HisTrap FF columns (GE Healthcare) for Ni-NTA affinity chromatography. After a wash step with 15 column volumes (CV) of buffer A, proteins were eluted with three CV of buffer B (20 mM HEPES-Na, pH 8.0,

250 mM NaCl, 20 mM KCl, 20 mM $MgCl_2$, 500 mM imidazole). Proteins were concentrated to 1 ml and further purified by size exclusion chromatography (SEC) using a HiLoad 26/600 Superdex 75 column (GE Healthcare) equilibrated in buffer C (20 mM HEPES-Na, pH 7.5, 200 mM NaCl). The main peak fractions were concentrated to 1.5 ml and dialyzed over night at 4 °C against 200 ml buffer C containing 10 g HCl-activated charcoal and 1 mM EDTA to remove Mg^{2+} and co-purified nucleotides. RbgA was subsequently subjected to a second SEC step using a HiLoad 26/600 Superdex 75 column (GE Healthcare) equilibrated in buffer D (20 mM HEPES-Na, pH 7.5, 20 mM KCl, 20 mM $MgCl_2$, 200 mM NaCl). The main peak fractions were concentrated and concentrations were determined using a NanoDrop Lite Spectrophotometer.

Preparation of (p)ppGpp. ppGpp and pppGpp were prepared as previously described [33].

Crystallization. Purified *S. aureus* RbgA was concentrated to 20 mg/ml. Nucleotides (GDP, GMPPNP, ppGpp or pppGpp) were added at a final concentration of 5 mM and RbgA was subsequently subjected to crystallization by sitting drop vapor-diffusion at 20 °C. Block shaped crystals grew within two days in drops containing: 1 µl RbgA-GDP and 1 µl crystallization buffer (0.2 M Lithium sulfate, 0.1 M MES pH 6.0, 35% (v/v) MPD); 1 µl RbgA-GMPPNP and 1 µl crystallization buffer (0.2 M Potassium fluoride, 0.1 M MES pH 6.0, 20% PEG 3350); 1 µl RbgA-ppGpp and 1 µl crystallization buffer (0.2 M Potassium sulfate, 20% PEG 3350); 1 µl RbgA-pppGpp and 1 µl crystallization buffer (0.2 M Potassium fluoride, 0.1 M MES pH 6.0, 20% PEG 3350). Crystals were transferred into crystallization buffer containing 20% (v/v) glycerol as cryo-protectant, subsequently flash frozen and stored in liquid nitrogen. No cryo-protectant was added to the crystals of RbgA-GDP due to the presence of 35% MPD in the crystallization buffer.

Data collection and structure determination. Diffraction data were collected at beamlines ID-30B, ID29 and ID23-1 of the European Synchrotron Radiation Facility (ESRF), Grenoble, France [34]. Data were processed with the XDS program package for data reduction [35], merging and scaling was performed using the AIMLESS program as implemented in the CCP4 package [36]. The RbgA-GDP dataset was

solved by molecular replacement using the crystal structure of *B. subtilis* RbgA (PDB-ID: 1PUJ) via the CCP4 implemented program Phaser [37]. Coot [38] in combination with Refmac5 (CCP4 package) and phenix.refine (PHENIX package[39]) was used for iterative model building and refinement. The GMPPNP, ppGpp and pppGpp RbgA state datasets were subsequently solved by molecular replacement using the GDP cleared *S. aureus* RbgA crystal structure (this study) via the CCP4 implemented program Phaser and refined using the phenix.refine software. Figures were prepared in Pymol (www.pymol.org).

Affinity measurements using Microscale Thermophoresis (MST). MST was performed on a Monolith NT.115 (NanoTemper Technologies GmbH, Munich, Germany) at 21°C (red LED power was set to 70% and infrared laser power to 25%) [40]. RbgA (50 µM) was labeled with the dye NT 647 according to the supplier's protocol (NanoTemper Technologies). 200 nM RbgA was titrated with GTP, GDP, ppGpp or pppGpp starting from a concentration of 0.5 mM in Buffer C (20 mM HEPES-Na, pH 7.5, 200 mM NaCl). To each measurement Tween20 (Sigma) was added to a final concentration of 0.05 mM. At least nine independent MST experiments were recorded at 680 nm and processed by NanoTemper Analysis 1.2.009. For fitting of the experimental data and K_d determination Origin8G was used.

Co-sedimentation assays. 50S subunits were isolated from the *B. subtilis* strain 168 as previously described [41]. Binding assays were carried out as previously described [42], with modifications. 0.4µM *B. subtilis* 50S were incubated with 1µM *B. subtilis* RbgA and 500µM of GMPPNP at 37 °C for 20 minutes in Binding Buffer (25mM HEPES-KOH, pH 7.4, 20 mM MgOAc, 100mM KOAc). The reaction was subsequently loaded on a 10% (w/v) sucrose cushion in Buffer A and centrifuged for 35 minutes at 80,000 rcf in a TLA100 rotor at 4 °C. For each condition, aliquots of the initial reaction (R), supernatant (S) and pellet (P) after centrifugation were analyzed via SDS-PAGE and stained with Instant BlueTM (Expedeon).

Cryo-grid preparation for the 50S-RbgA-GMPPNP complex. All following steps were performed in Binding Buffer (25mM HEPES-KOH, pH 7.4, 20 mM MgOAc, 100mM KOAc). For grid preparation, 4.5 OD A260/ml of the initial reaction of co-sedimentation assays was used. All samples were applied to 2 nm precoated

Quantifoil R3/3 holey carbon supported grids and vitrified using a Vitrobot Mark IV (FEI company).

Cryo-electron microscopy and single-particle reconstructions. Data collection was performed using an FEI Titan Krios transmission electron microscope equipped with a Falcon II direct electron detector at 300 kV using a pixel size of 1.084 Å and a defocus range of 0.5 to 3.5µm, initially resulting in 3995 microgaphs. Ten frames (dose per frame of 2.5 e-/Å2) were aligned using MotionCor2 [43]. Power spectra, defocus values, astigmatism and estimation of micrograph resolution were determined CTFFIND4 software [44]. Micrographs showing Thon rings beyond 3.5Å resolution were further inspected for good power spectra, resulting in 1629 micrographs. Particles were automatically picked by Gautomatch (http://www.mrc-lmb.cam.ac.uk/kzhang/) and single particles were extracted using RELION 1.4 [45]. Initial alignment was performed with 224,022 particles using FREALIGN [29], using the 50S from a *B. subtilis* 70S ribosome [46] as a reference structure. Afterwards a 3D classification using the same reference was performed resulting in two major classes, representing the 50S and RbgA-GMPPNP-50S-complex (Figure S6). These classes were further refined to a final average resolution of 3.58 Å and 3.64 Å (FSC0.143) for (Figure S7). 3D classification and initial alignment was performed using three times decimated data. The local resolution of the final maps was computed using ResMap [47] (Figure S7). The final maps were sharpened by dividing the maps by the modulation transfer function of the detector and by applying an automatically determined negative B factor to the maps using RELION 1.4. Resolution was estimated using the ‘‘gold standard’’ criterion (FSC = 0.143). Maps filtered according to local Resolution were computed using RELION 2.1 [48].

Ribosome preparation for RbgA GTPase assay. *B. subtilis* 168 was inoculated into 250 ml LB medium at an OD_{600} = 0.05 and incubated at 37 °C to an OD_{600} = 0.6 under rigorous shaking (180 rpm). Cells were subsequently cooled down by incubation on ice for 20 min and harvested by centrifugation (3,500 x g, 20 min, 4 °C). The cell pellet was resuspended in 20 ml buffer R_I (20 mM Tris/HCl pH 7.6, 15 mM $MgOAc_2$, 100 mM KOAc, 0.1 mM DTT) before lysis in a M-110L Microfluidizer (Microfluidics). Cell debris were removed by centrifugation at 47,850 x g for 20 min at 4 °C. The supernatant was transferred to a 35.5 ml polypropylene tube (Beckman

Coulter) and combined with 15 ml cushion buffer $S_{17.5}$ (20 mM Tris/HCl pH 7.6, 15 mM $MgOAc_2$, 100 mM KOAc, 0.1 mM DTT, 17.5% (w/v) sucrose). Ribosomes were pelleted by centrifugation at 200,000 x g for 2 h at 4 °C and resuspended in 400 µL R_I buffer.

GTPase activity of RbgA. GTPase activity of RbgA was monitored by high-performance liquid chromatography (HPLC). 1 µM RbgA was incubated together with GTP in absence or presence of ppGpp and pppGpp as indicated in figures and text in 20 mM HEPES-Na, pH 7.5, 20 mM $MgCl_2$, 1 mM KCl and 200 mM NaCl. Ribosomes were added at a final concentration of 1 µM where indicated. After 30 minutes at 37 °C, the reactions were stopped as described previously [49]. HPLC analysis was carried out on an Agilent 1100 Series system (Agilent Technologies) equipped with a C18 column (EC 250/4.6 Nucleodur HTec 3 µM; Macherey-Nagel). Nucleotides were eluted from the column with a buffer containing 50 mM KH_2PO_4, 50 mM K_2HPO_4, 10 mM tetrapentylammonium bromide and 20% (v/v) acetonitrile and detected at 260 nm in agreement with standards.

Acknowledgements

We acknowledge the Core facility “protein biochemistry and protein spectroscopy”, Marburg, for providing access to the MicroScale Thermophoresis instrument. Crystallographic data and models were deposited at the PDB (www.rcsb.org) under accessions 6G0Z (RbgA-GDP), 6G12 (RbgA-GMPPNP), 6G14 (RbgA-ppGpp) and 6G15 (RbgA-pppGpp).

Conflict of interest

The authors declare that they have no conflicts of interest with the contents of this article.

Author contributions

Conceptualization, P.P., D.N.W. and G.B.; Methodology, P.P., M.W., S.-A.F. and W.S.; Investigation, P.P., M.W., T.K., S.-A.F. and W.S.; Writing – Original Draft, P.P.,

M.W., D.N.W. and G.B.; Visualization, P.P. and M.W.; Supervision, P.P., D.N.W. and G.B.; Project Administration, D.N.W. and G.B.; Data curation, P.P. and M.W.; Funding Acquisition, G.B. and D.N.W.

References

1. Chen, S. S., Sperling, E., Silverman, J. M., Davis, H. & Williamson, J. R. Molecular BioSystems Measuring the dynamics of E . coli ribosome biogenesis using pulse-labeling and quantitative mass spectrometry. *Mol. Biosyst.* **8,** 3325–3334 (2012).
2. Davis, J. H. *et al.* Modular Assembly of the Bacterial Large Ribosomal Subunit. *Cell* **167,** 1610–1622.e15 (2016).
3. Shajani, Z., Sykes, M. T. & Williamson, J. R. Assembly of Bacterial Ribosomes. *Annu. Rev. Biochem.* **80,** 501–526 (2011).
4. Hauryliuk, V., Atkinson, G. C., Murakami, K. S., Tenson, T. & Gerdes, K. Recent functional insights into the role of (p)ppGpp in bacterial physiology. *Nat. Rev. Microbiol.* **13,** 298–309 (2015).
5. Steinchen, W. & Bange, G. The magic dance of the alarmones (p)ppGpp. *Mol. Microbiol.* **101,** 531–544 (2016).
6. Corrigan, R. M., Bellows, L. E., Wood, A. & Gründling, A. ppGpp negatively impacts ribosome assembly affecting growth and antimicrobial tolerance in Gram-positive bacteria. *Proc. Natl. Acad. Sci.* **113,** 201522179 (2016).
7. Morimoto, T. *et al.* Six GTP-binding proteins of the Era/Obg family are essential for cell growth in *Bacillus subtilis*. *Microbiology* **148,** 3539–3552 (2002).
8. Uicker, W. C., Schaefer, L. & Britton, R. A. The essential GTPase RbgA (YlqF) is required for 50S ribosome assembly in Bacillus subtilis. *Mol. Microbiol.* **59,** 528–540 (2006).
9. Matsuo, Y., Oshima, T., Loh, P. C., Morimoto, T. & Ogasawara, N. Isolation and Characterization of a Dominant Negative Mutant of Bacillus subtilis GTP-binding Protein , YlqF , Essential for Biogenesis and Maintenance of the 50 S Ribosomal Subunit *. *JBC* **282,** 25270–25277 (2007).
10. Matsuo, Y. *et al.* The GTP-binding Protein YlqF Participates in the Late Step of 50 S Ribosomal Subunit Assembly in Bacillus subtilis *. *JBC* **281,** 8110–8117

(2006).

11. Li, N. *et al.* Cryo-EM structures of the late-stage assembly intermediates of the bacterial 50S ribosomal subunit. *Nucleic Acids Res.* **41,** 7073–7083 (2013).
12. Jomaa, A. *et al.* Functional domains of the 50S subunit mature late in the assembly process. *Nucleic Acids Res.* **42,** 3419–3435 (2014).
13. Mier, P., Perez-Pulido, A. J., Reynaud, E. G. & Andrade-Navarro, M. A. Reading the Evolution of Compartmentalization in the Ribosome Assembly Toolbox□: The YRG Protein Family. *PLoS One* **12,** 1–11 (2017).
14. Britton, R. A. Role of GTPases in Bacterial Ribosome Assembly. *Annu. Rev. Microbiol.* 155–76 (2009). doi:10.1146/annurev.micro.091208.073225
15. Hedges, J., West, M. & Johnson, A. W. Release of the export adapter , Nmd3p , from and the cytoplasmic GTPase Lsg1p. *EMBO J.* **24,** 567–579 (2005).
16. West, M., Hedges, J. B., Chen, A. & Johnson, A. W. Defining the Order in Which Nmd3p and Rpl10p Load onto Nascent 60S Ribosomal Subunits. *Mol. Cell. Biol.* **25,** 3802–3813 (2005).
17. Malyutin, A. G., Musalgaonkar, S., Patchett, S., Frank, J. & Johnson, A. W. Nmd 3 is a structural mimic of eIF 5 A , and activates the cpGTPase Lsg 1 during 60 S ribosome biogenesis. *EMBO J.* **36,** 854–868 (2017).
18. Kim, D. J., Jang, J. Y., Yoon, H. & Suh, S. W. Do Jin Kim, Jun Young Jang, Hye-Jin Yoon, and Se Won Suh*. *Proteins* 1363–1370 (2008). doi:10.1002/prot.22112
19. Achila, D., Gulati, M., Jain, N. & Britton, R. A. Biochemical characterization of ribosome assembly gtpase RbgA in Bacillus subtilis. *J. Biol. Chem.* **287,** 8417–8423 (2012).
20. Anand, B., Verma, S. K. & Prakash, B. Structural stabilization of GTP-binding domains in circularly permuted GTPases□: Implications for RNA binding. *Nucleic Acids Res.* **34,** 2196–2205 (2006).
21. Gulati, M., Jain, N., Anand, B., Prakash, B. & Britton, R. A. Mutational analysis of the ribosome assembly GTPase RbgA provides insight into ribosome interaction and ribosome-stimulated GTPase activation. *Nucleic Acids Res.* **41,** 3217–3227 (2013).
22. Wittinghofer, A. & Vetter, I. R. Structure-Function Relationships of the G Domain , a Canonical Switch Motif. *Annu. Rev. Biochem.* 943–71 (2011). doi:10.1146/annurev-biochem-062708-134043

23. Sharma, M. R. *et al.* Interaction of Era with the 30S Ribosomal Subunit : Implications for 30S Subunit Assembly. *Mol. Cell* **18,** 319–329 (2005).
24. Datta, P. P. *et al.* Article Structural Aspects of RbfA Action during Small Ribosomal Subunit Assembly. *Mol. Cell* **28,** 434–445 (2007).
25. Razi, A., Guarné, A. & Ortega, J. The cryo-EM structure of YjeQ bound to the 30S subunit suggests a fidelity checkpoint function for this protein in ribosome assembly. *PNAS* **114,** E3396–E3403 (2017).
26. Lopez, J. P. *et al.* RsgA couples the maturation state of the 30S ribosomal decoding center to activation of its GTPase. *Nucleic Acids Res.* **45,** 6945–6959 (2017).
27. Zhang, X. *et al.* Structural insights into the function of a unique tandem GTPase EngA in bacterial ribosome assembly. *Nucleic Acids Res.* **42,** 13430–13439 (2014).
28. Feng, B. *et al.* Structural and Functional Insights into the Mode of Action of a Universally Conserved Obg GTPase. *PLoS Biol.* **12,** (2014).
29. Lyumkis, D., Brilot, A. F., Theobald, D. L. & Grigorieff, N. Likelihood-based classification of cryo-EM images using FREALIGN. *J. Struct. Biol.* **183,** 377–388 (2013).
30. Ni, X. *et al.* YphC and YsxC GTPases assist the maturation of the central protuberance , GTPase associated region and functional core of the 50S ribosomal subunit. *Nucleic Acids Res.* **44,** 8442–8455 (2016).
31. Ma, C. *et al.* Structural snapshot of cytoplasmic pre-60S ribosomal particles bound by Nmd3 , Lsg1 , Tif6 and Reh1. *Nat. Publ. Gr.* **24,** 214–220 (2017).
32. Pausch, P. *et al.* Co-translational capturing of nascent ribosomal proteins by their dedicated chaperones. *Nat. Commun.* **6,** 1–15 (2015).
33. Steinchen, W. *et al.* Catalytic mechanism and allosteric regulation of an oligomeric (p) ppGpp synthetase by an alarmone. *PNAS* **112,** 1–6 (2015).
34. Gabadinho, J. *et al.* MxCuBE : a synchrotron beamline control environment customized for macromolecular crystallography experiments. *Synchrotron Rediation* **1,** 700–707 (2010).
35. Kabsch, W. XDS. *Acta Crystallogr. Sect. D* **D66,** 125–132 (2010).
36. Winn, M. D. *et al.* Overview of the CCP 4 suite and current developments. *Acta Crystallogr. Sect. D* **4449,** 235–242 (2011).
37. Mccoy, A. J. *et al.* Phaser crystallographic software. *Appl. Crystallogr.* 658–674

(2007). doi:10.1107/S0021889807021206

38. Emsley, P. & Cowtan, K. Coot□: model-building tools for molecular graphics. *Acta Crystallogr. Sect. D* 2126–2132 (2004). doi:10.1107/S0907444904019158
39. Adams, P. D. *et al.* PHENIX□: a comprehensive Python-based system for macromolecular structure solution. *Acta Crystallogr. Sect. D* **D66,** 213–221 (2010).
40. Jerabek-willemsen, M., Wienken, C. J., Braun, D., Baaske, P. & Duhr, S. Molecular Interaction Studies Using Microscale Thermophoresis. 342–353 (2011). doi:10.1089/adt.2011.0380
41. Blaha, G. *et al.* Preparation of Functional Ribosomal Complexes and Effect of Buffer Conditions on tRNA Positions Observed by Cryoelectron Microscopy. *RNA Struct. Determ.* **317,** 292–306 (2000).
42. Sharma, M. R. *et al.* PSRP1 Is Not a Ribosomal Protein , but a Ribosome-binding Factor That Is Recycled by the Ribosome-recycling Factor (RRF) and Elongation Factor G (EF-G) * □. *JBC* **285,** 4006–4014 (2010).
43. Zheng, S. Q. *et al.* MotionCor2□: anisotropic correction of beam-induced motion for improved cryo-electron microscopy Automatic tracing of ultra-volumes of neuronal images. *Nat. Methods* **14,** 331–332 (2017).
44. Rohou, A. & Grigorieff, N. CTFFIND4□: Fast and accurate defocus estimation from electron micrographs. *J. Struct. Biol.* **192,** 216–221 (2015).
45. Scheres, S. H. W. RELION□: Implementation of a Bayesian approach to cryo-EM structure determination. *J. Struct. Biol.* **180,** 519–530 (2012).
46. Sohmen, D. *et al.* Structure of the Bacillus subtilis 70S ribosome reveals the basis for species-specific stalling. *Nat. Commun.* **6,** 1–10 (2015).
47. Kucukelbir, A., Sigworth, F. J. & Tagare, H. D. Quantifying the local resolution of cryo-EM density maps. *Nat. Methods* **11,** (2014).
48. Kimanius, D., Forsberg, B. O., Scheres, S. H. W. & Lindahl, E. Accelerated cryo-EM structure determination with parallelisation using GPUs in RELION-2. *Elife* **5,** 1–21 (2016).
49. Steinchen, W. *et al.* Structural and mechanistic divergence of the small (p) ppGpp synthetases RelP and RelQ. *Sci. Rep.* **8,** 1–10 (2018).

Figures and tables

Table 1	**SaRbgA-GDP**	**SaRbgA-GMPPNP**	**SaRbgA-ppGpp**	**SaRbgA-pppGpp**
PDB-ID	6G0Z	6G12	6G14	6G15
Data collection				
Space group	P 21 21 21	P 21 21 21	P 21 21 21	P 21 21 21
Cell dimensions				
a, *b*, *c* (Å)	71.932	71.899	71.781	72.084
	77.812	77.71	74.512	78.467
	124.667	124.36	125.215	125.022
α, β, γ (°)	90.00	90.00	90.00	90.00
	90.00	90.00	90.00	90.00
	90.00	90.00	90.00	90.00
Energy (Å)	0.97625	0.97903	0.97625	0.97625
Resolution (Å)	48.65 - 2.15	62.24 - 1.93	47.93 - 1.80	48.89 - 1.65
	(2.23 - 2.15)	(2.00 - 1.93)	(1.864 - 1.80)	(1.71 - 1.65)
No. unique reflections	38760 (3822)	52769 (5238)	62299 (6048)	85889 (8495)
R_{merge}	0.041 (0.277)	0.056 (0.332)	0.106 (0.555)	0.035 (0.989)
I / **σ**I	8.79 (2.45)	6.36 (2.08)	7.88 (1.74)	24.70 (1.85)
Completeness (%)	99.9 (99.9)	99.2 (99.5)	99.0 (97.5)	100.0 (99.9)
Redundancy	2.0 (2.0)	2.0 (2.0)	4.2 (4.2)	7.4 (7.4)
CC(1/2)	1.00 (0.88)	1.00 (0.54)	1.00 (0.94)	1.00 (0.81)
Refinement				
Resolution (Å)	48.65 - 2.15	62.24 - 1.93	47.93 - 1.80	48.89 - 1.65
R_{work}/ R_{free}	18.2	22.7	21.7	21.8
	21.7	25.6	25.6	24.4
No. atoms	4989	5026	5020	5090
Macromolecule	4636	4636	4541	4611
Ligand	56	64	72	80
Water	297	326	407	399
R.m.s deviations				
Bond lengths (Å)	0.011	0.008	0.009	0.007
Bond angles (°)	1.30	1.12	1.19	1.11
Ramachandran (%)				
Preferred	98	98	99	97
Allowed	1.65	1.65	1	2.82
Outliers	0.35	0.35	0	0.18

*Statistics for the highest-resolution shell are shown in parentheses.

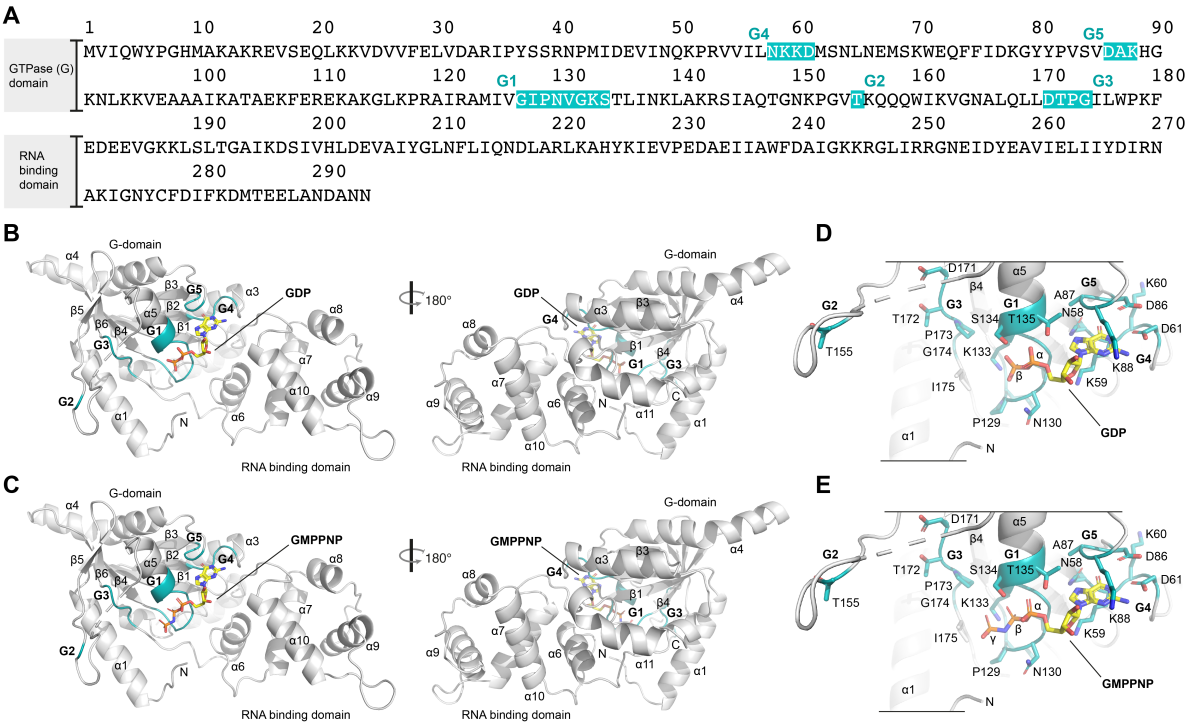

Figure 1: Crystal structures of *S. aureus* RbgA bound to GDP and GTP. A: Amino acid sequence of RbgA illustrating the domain arrangement (N-terminal G-domain and C-terminal RNA binding domain). G-motifs are highlighted in turquoise and labeled according to the identity (G1-G5). **B and C:** Crystal structure of RbgA (grey cartoon representation) in complex with GDP (**B**), respectively GMPPNP (**C**) (yellow stick representation) in two 180° rotated views. Secondary structure elements are labeled according to their identity and N and C indicate the respective termini. The G1-G5 motifs are colored turquoise and are labeled accordingly. **D and E:** Detailed view on the GTPase active sites with the accommodated nucleotide GDP (**D**), respectively GMPPNP (**E**). Coloring as in B. G-motif and adjacent site chains are shown in stick representation and are labeled according to their identity.

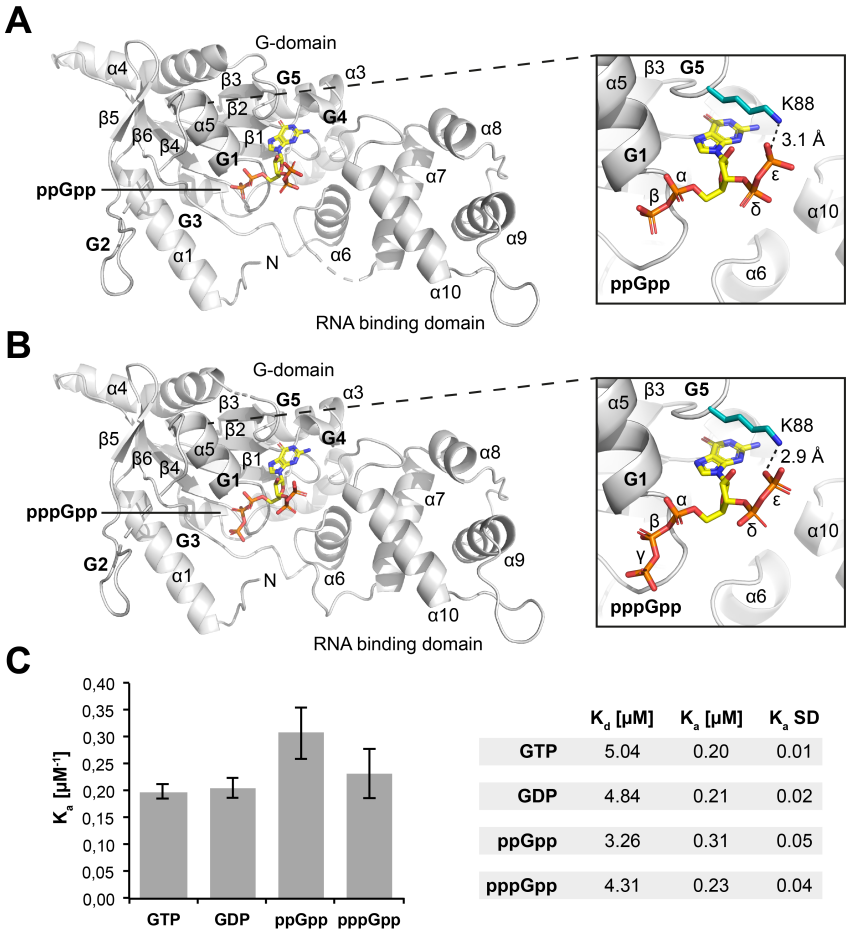

	K_d [µM]	K_a [µM]	K_a SD
GTP	5.04	0.20	0.01
GDP	4.84	0.21	0.02
ppGpp	3.26	0.31	0.05
pppGpp	4.31	0.23	0.04

Figure 2: Crystal structures of *S. aureus* RbgA bound to ppGpp and pppGpp. A and B: Left: Crystal structure of RbgA (grey cartoon representation) in complex with ppGpp (**A**), respectively pppGpp (**B**) (yellow stick representation). Secondary structure elements are labeled according to their identity and N indicates the N-terminus. The G1-G5 motifs are labeled accordingly. Right: Close-up on the GTP binding site. K88 (blue stick representation) of the G5 motif is in close proximity to the ε-phosphate moiety. **C:** Binding and dissociation constants for GTP, GDP, ppGpp or pppGpp and RbgA as determined by MicroScale Thermophoresis (MST). Error bars represent the standard deviation of the calculated K_d or K_a values based on the fitting of the respective experimental data (see supporting information fig. S4).

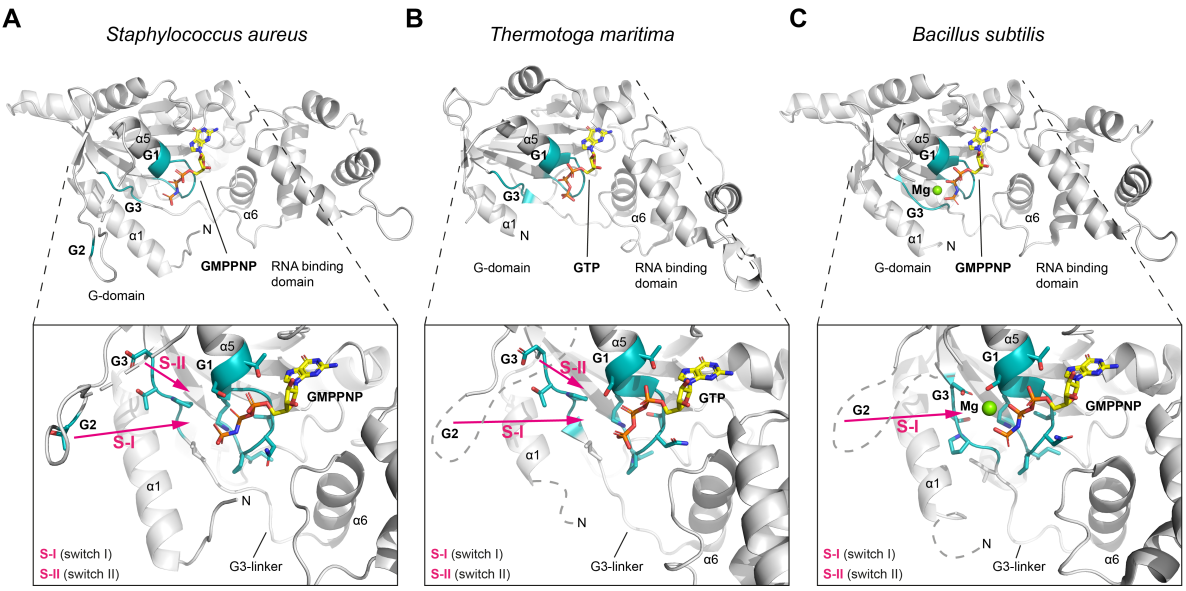

Figure 3: Binding of Mg^{2+} coincides with rearrangement of the G3 motif (switch II). A: Upper panel: Overview of the crystal structure of *S. aureus* RbgA (grey cartoon) in complex with GMPPNP (yellow stick representation). G-motifs that participate in phosphate coordination and hydrolysis are colored in turquoise and labeled according to their identity. Adjacent helices are labeled according to their identity for orientation (compare to fig. 1). Lower panel: Close-up of the GTPase active site. The side chains of the G-motifs G1-G3 are shown in blue stick representation. Magenta arrows emphasize the rearrangements that have to occur to locate the G2-motif (switch I; S-I) and G3-motif (switch II; S-II) in a position compatible GTP hydrolysis. **B:** Crystal structure of *T. maritima* RbgA (PDB-ID: 3CNN [18]). Representations as in subfigure A. **C:** Crystal structure of *B. subtilis* RbgA (PDB-ID: 1PUJ). Representations as in subfigure A and B. In contrast to the structures of *S. aureus* and *T. maritima*, *B. subtilis* RbgA assumes a configuration in which the G3 motif is repositioned to allow for Mg^{2+} (green sphere) coordination.

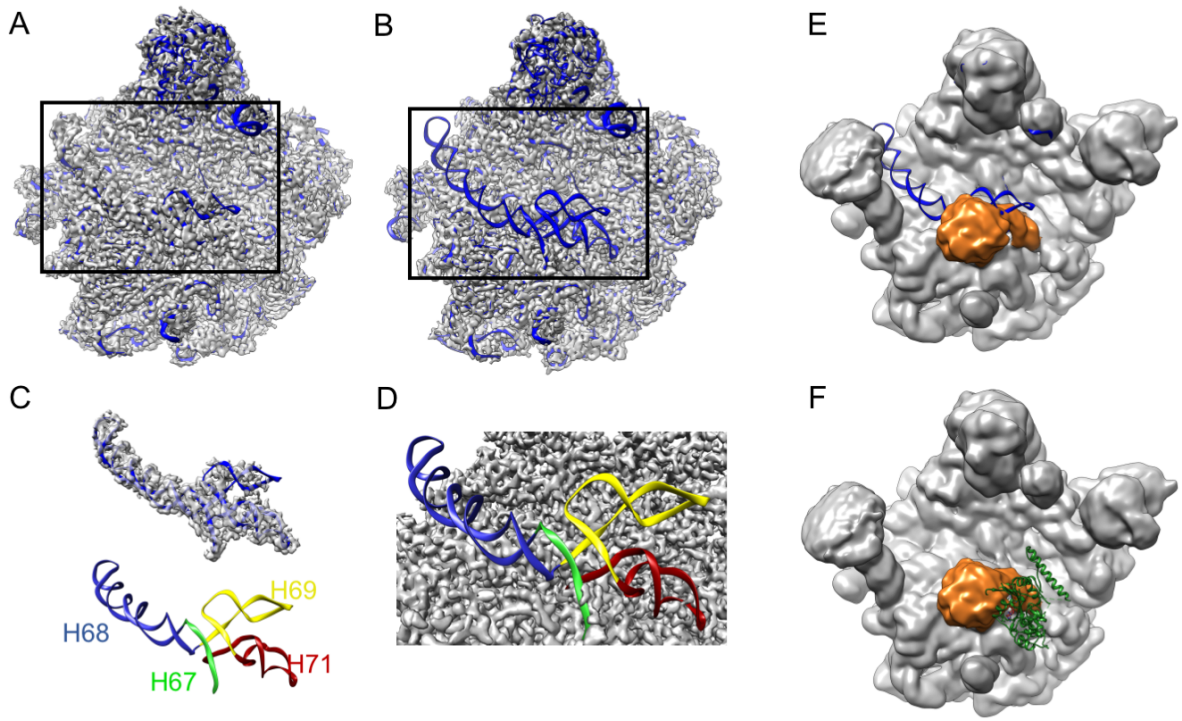

Figure 4: Cryo EM structure of *Bacillus subtilis* RbgA 50S complex. (**A**) Cryo-EM maps of mature 50S, and (**B**) RbgA-50S intermediate with the 50S of PDB-ID 3J9W fitted; the stalks L1 and L7/12 have been edited out for clarity. (**C** and **D**) showing the displaced densities for H67-71 (H67 – green; H68 – blue; H69 – yellow; H71 - red) in the mature 50S and RbgA-50S complex, respectively. (**E** and **F**) Low pass filtered maps of the 50S-RbgA complex, with extra density coloured in orange; (**F**) Lsg1, shown in a green cartoon representation (PDB-ID 5T62 [17]), superimposed in the respective binding site.

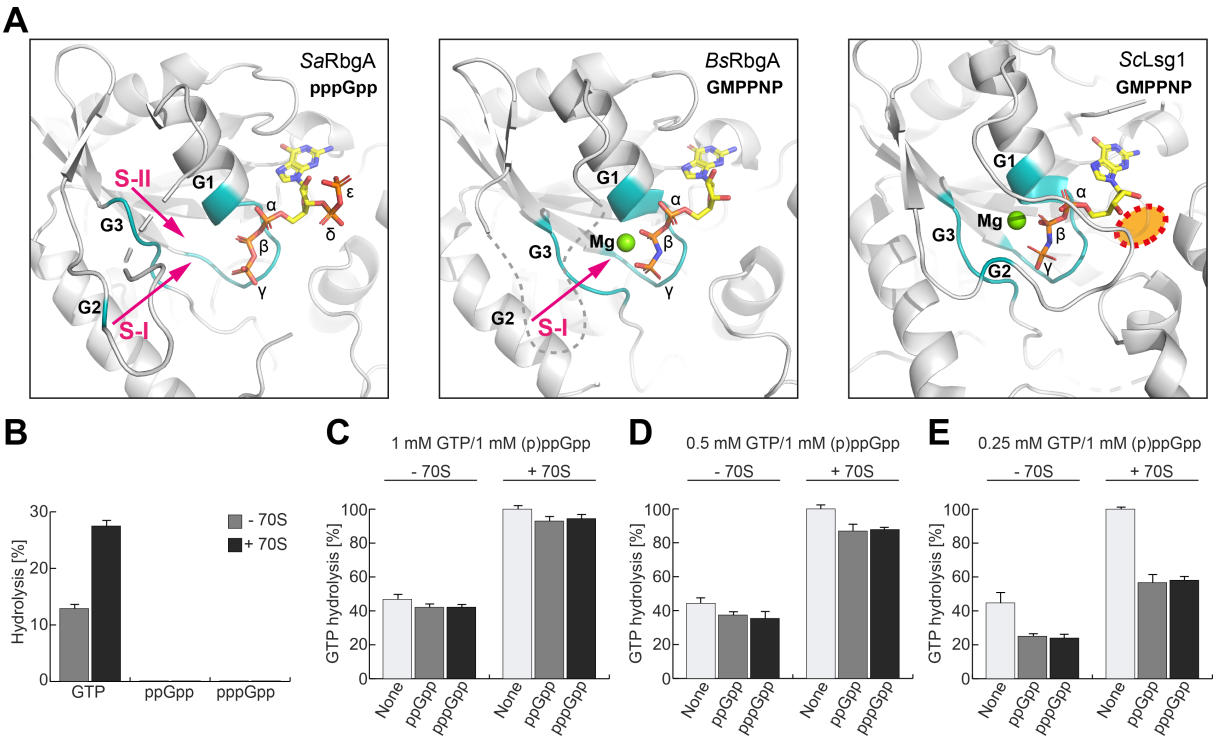

Figure 5: RbgA GTPase inhibition by (p)ppGpp. A: Comparison of the three different GTPase G1-, G2- and G3-motif (turquoise) configurations observed in the crystal structures of *S. aureus* RbgA (left panel; this study), *B. subtilis* RbgA (middle panel; PDB-ID: 1PUJ) and cryo-EM structure of *S. cerevisiae* Lsg1 (right panel; PDB-ID: 5T62 [17]). RbgA/Lsg1 is shown in a grey cartoon representation in a close-up view on the GTPase active site. The associated nucleotides are shown in a yellow stick representation and the coordinated Mg^{2+} ion is shown as a green sphere. Rearrangements of switch I and II required for GTPase activation are indicated by magenta arrows. The δ- and ε-phosphate moiety of (p)ppGpp sterically blocks the association of the G2 motif as suggested by the G-motif configuration observed in the Lsg1 homologue (indicated as orange circle). **B:** GTP and (p)ppGpp hydrolytic activity of *B. subtilis* RbgA in presence (+70S, grey bars) or absence (-70S, black bars) of *B. subtilis* 70S ribosomes. **C, D and E:** GTPase activity of RbgA in presence (+70S) or absence of 70S (-70S) ribosomes and in dependence of the GTP:(p)ppGpp ratio (**C:** 1 mM : 1 mM; **D:** 0.5 mM : 1 mM and **E:** 0.25 mM : 1 mM).

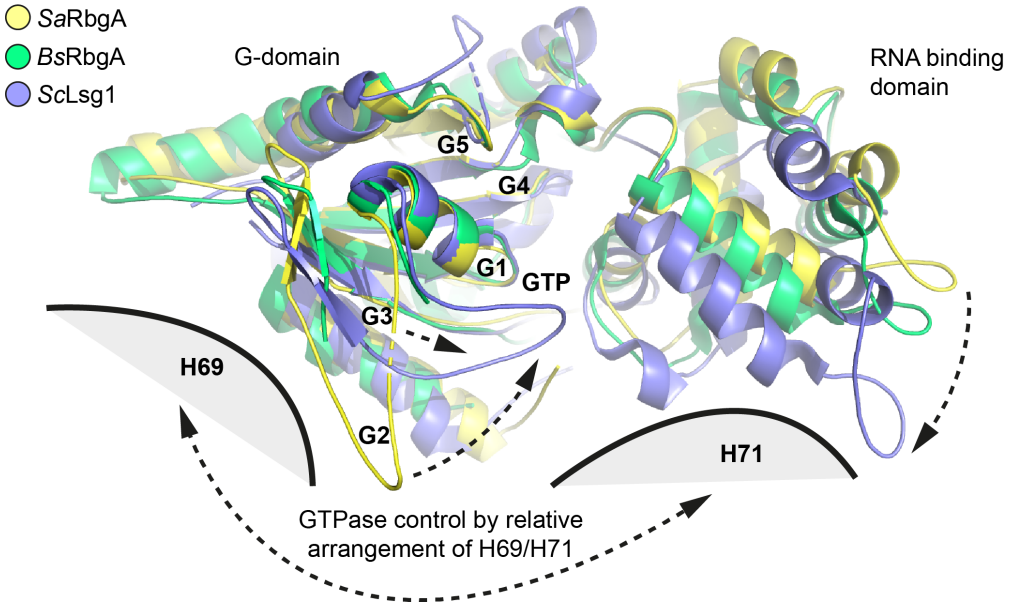

Figure 6: Configuration control of YRG-type GTPase G-motifs by the relative arrangement of H69/H71 of the large subunit. Shown are the crystal structures of *S. aureus* (yellow, this study) and *B. subtilis* (green, PDB-ID: 1PUJ) aligned to the G1-motif of the cryo-EM structure of *S. cerevisiae* Lsg1 (blue, PDB-ID: 5T62 [17]). The relative position of the flexibly connected N-terminal G-domain and C-terminal RNA binding domain of the YRG-type GTPases depends on the configuration of H69/H71. The mature configuration of H69/H71 might eventually signal for LSU completion to allow for GTPase activation by proper positioning of the G-motifs (G1-G5) and subsequent GTPase release.

Supporting information

Structural basis for (p)ppGpp-mediated ribosomal large subunit arrest by RbgA

Patrick Pausch[1,2,*], Maximiliane Wieland[3], Thomas Klaus[1,2], Sven-Andreas Freibert[2,4], Wieland Steinchen[1,2], Daniel N. Wilson[3,*] and Gert Bange[1,2,*]

[1]Department of Chemistry, Philipps-University Marburg, Hans-Meerwein-Strasse, C07, 35043 Marburg, Germany;
[2]Synmikro Center for synthetic Microbiology, Hans-Meerwein-Strasse, 35043 Marburg, Germany;
[3]Institute for Biochemistry and Molecular Biology, University of Hamburg, Hamburg, Germany;
[4]Institute für Cytobiology und Cytopathology, Philipps-University Marburg, Robert-Koch-Strasse 6, 35043 Marburg, Germany

*To whom correspondence should be addressed: Patrick.Pausch@synmikro.uni-marburg.de, Gert.Bange@synmikro.uni-marburg.de, Daniel.Wilson@chemie.uni-hamburg.de

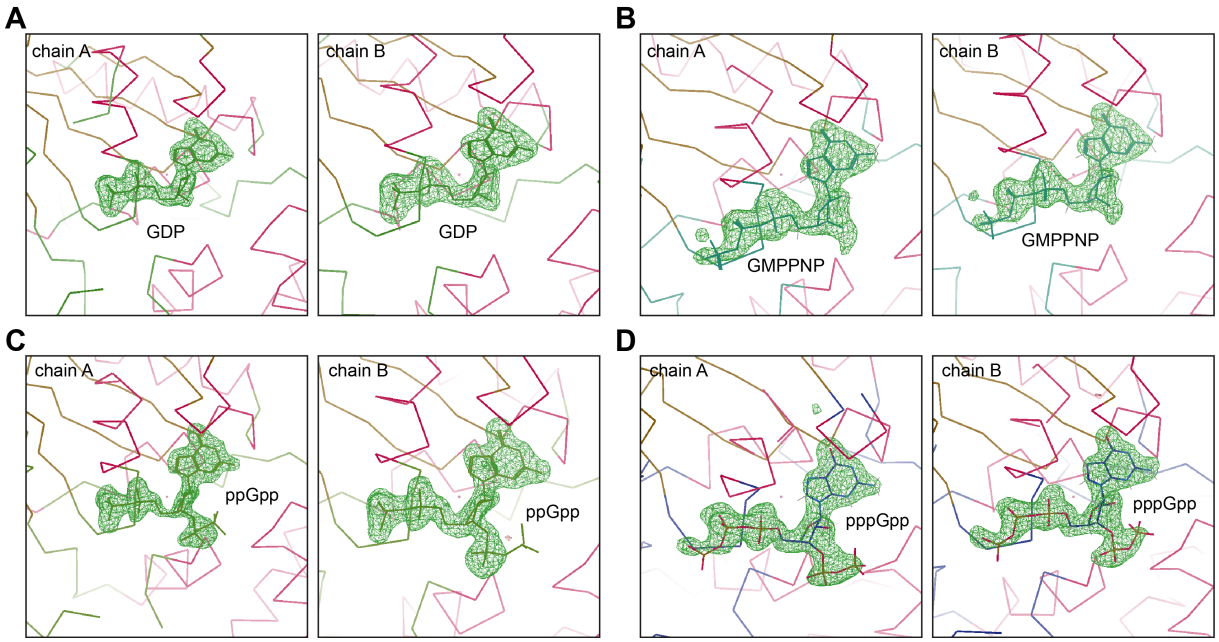

Figure S1: Nucleotide omit maps. RbgA is shown in ribbon representation and the nucleotides are shown in stick representation. Omit difference maps (green: positive density; red: negative density) were calculated from the final models after removing the nucleotide ligands and contoured at 3.6 σ. The respective RbgA chain is indicated in the upper left and the nucleotides are labeled according to their identity. **A**: RbgA-GDP; **B**: RbgA-GMPPNP; **C**: RbgA-ppGpp; **D**: RbgA-pppGpp. The figure was prepared in Coot [1].

Table S1: r.m.s.d.s of RbgA structural alignment

structure	chain	target	chain	r.m.s.d.	# atoms
RbgA-GDP	A	RbgA-GDP	B	0.130	235
RbgA-GMPPNP	A	RbgA-GMPPNP	B	0.139	254
RbgA-GMPPNP	A	RbgA-GDP	A	0.164	259
RbgA-GMPPNP	B	RbgA-GDP	A	0.125	257
RbgA-GMPPNP	A	RbgA-GDP	B	0.123	243
RbgA-GMPPNP	B	RbgA-GDP	B	0.169	239
RbgA-pppGpp	A	RbgA-GMPPNP	A	0.190	255
RbgA-pppGpp	A	RbgA-GMPPNP	B	0.137	250
RbgA-pppGpp	B	RbgA-GMPPNP	A	0.154	274
RbgA-pppGpp	B	RbgA-GMPPNP	B	0.212	264
RbgA-ppGpp	A	RbgA-GDP	A	0.139	234
RbgA-ppGpp	A	RbgA-GDP	B	0.150	228
RbgA-ppGpp	B	RbgA-GDP	A	0.309	262
RbgA-ppGpp	B	RbgA-GDP	B	0.234	261

Structures were aligned in PyMOL (pymol.org)

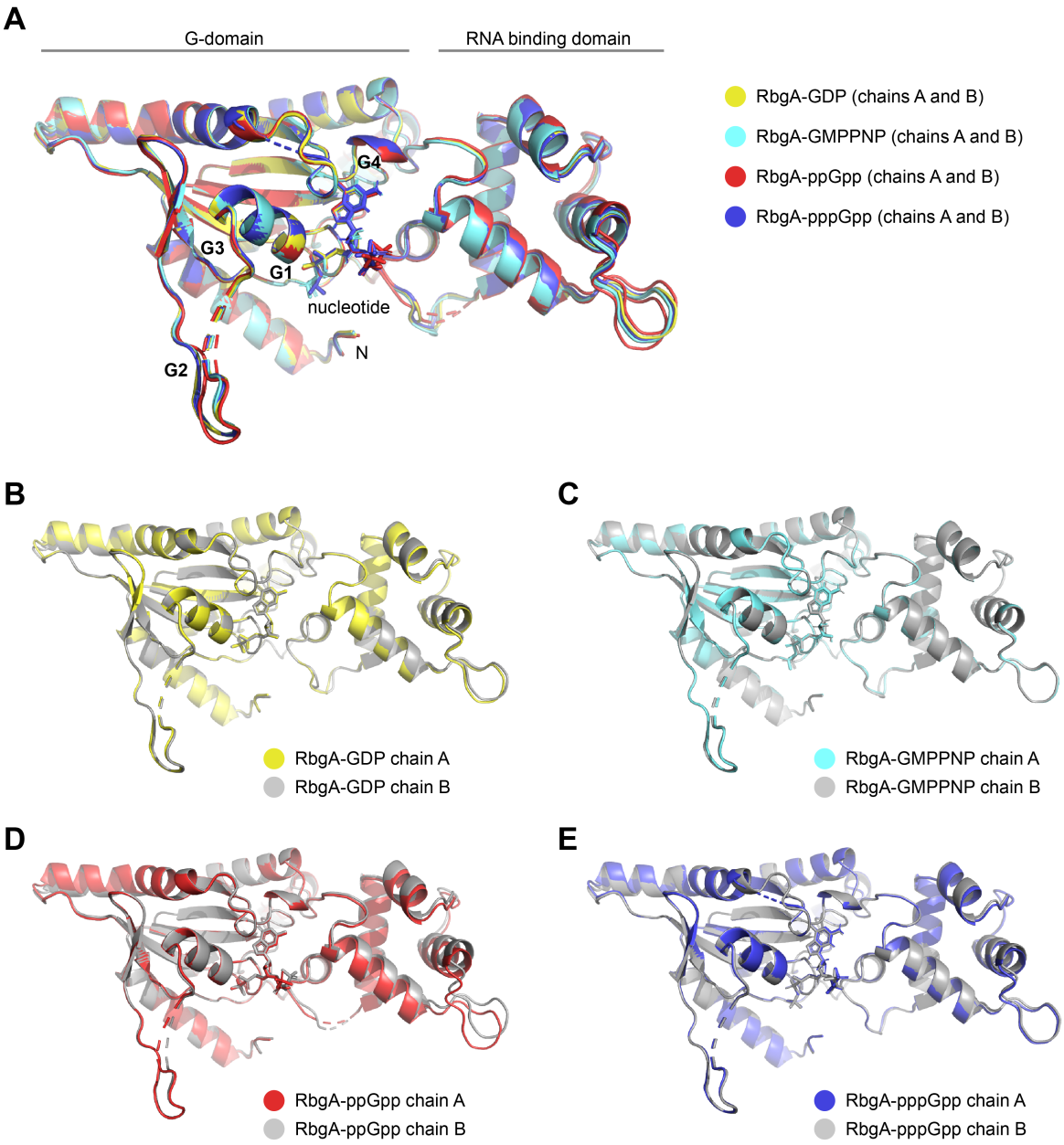

Figure S2: Superimposition of the of *S. aureus* RbgA nucleotide states observed in this study. A: Superimposition of all monomers observed in the crystal structures of RbgA (cartoon) in complex with the nucleotides (stick representation) GDP (yellow), GMPPNP (light blue), ppGpp (red) and pppGpp (dark blue). The G-domain and RNA binding domain of RbgA are indicated and the G-motifs are labeled G1-G5. **B:** Superimposition of chain A and B of RbgA-GDP. **C**: Superimposition of chain A and B of RbgA-GMPPNP. **D:** Superimposition of chain A and B of RbgA-ppGpp. **E:** Superimposition of chain A and B of RbgA-pppGpp.

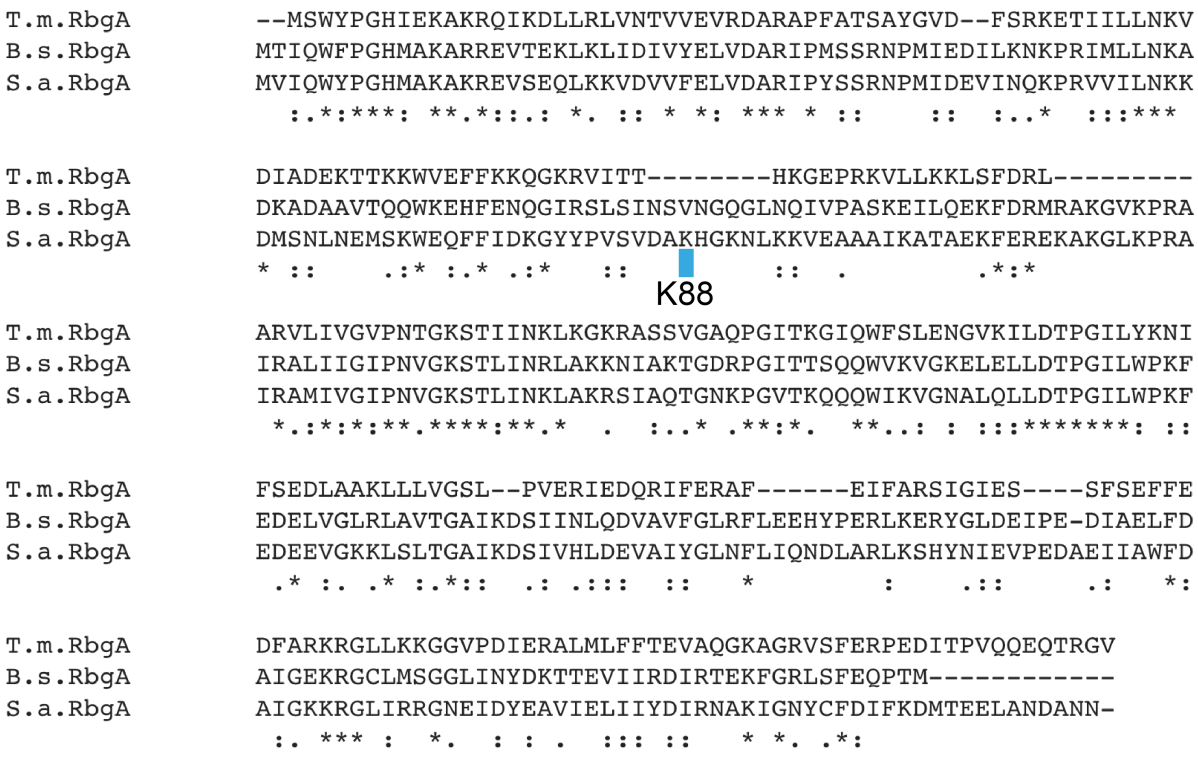

Figure S3: Sequence alignment of RbgA. Shown is the protein sequence alignment of RbgA from *T. maritima*, *B. subtilis* and *S. aureus*, illustrating the non-conserved and alarmone contacting residue lysine 88 (blue label) of *S. aureus* RbgA. The alignment was generated using the MUSCLE online tool (*https://www.ebi.ac.uk /Tools/msa/muscle/*).

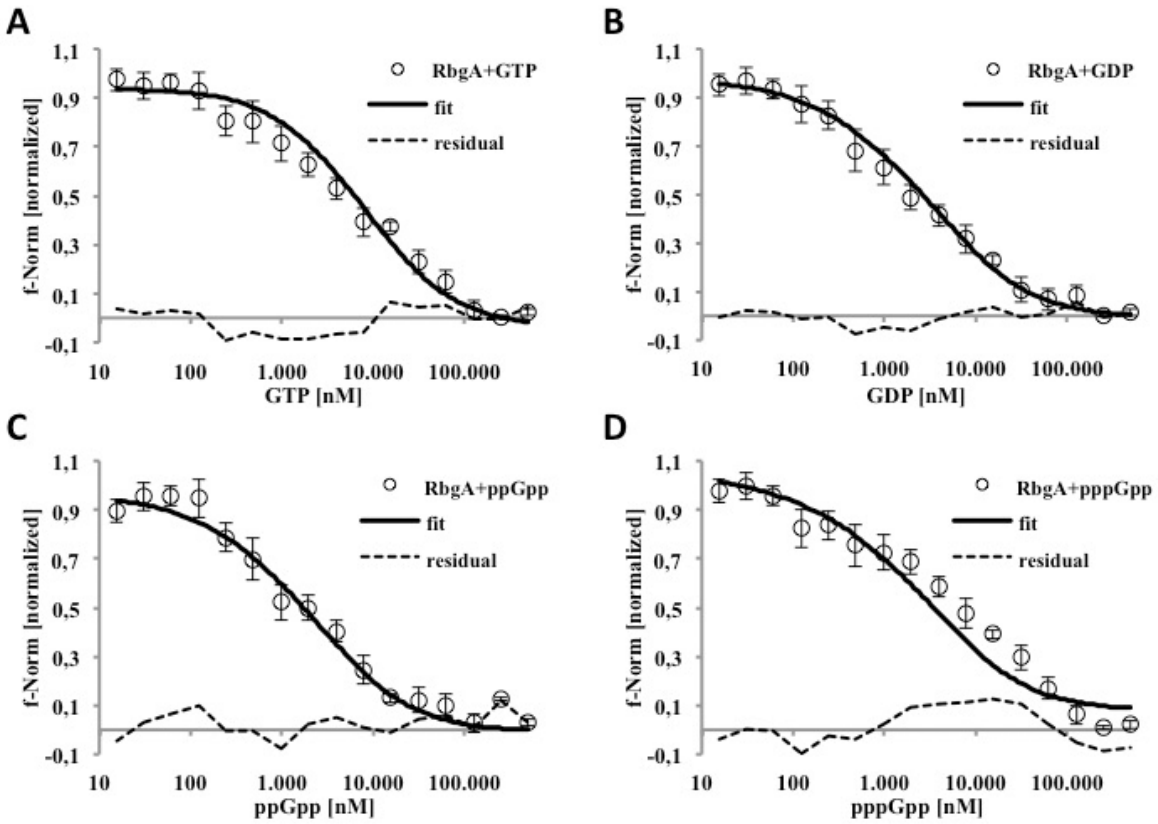

Figure S4: Quantitative determination of the interaction between RbgA and GTP, GDP, ppGpp or pppGpp. RbgA (200 nM) was titrated with increasing amounts of GTP (**A**), GDP (**B**), ppGpp (**C**) and pppGpp (**D**) starting from 0.5 mM. Fitting (solid line) of the experimental data (black circles) was achieved using the Origin8G software. Residuals (dashed line) represent the deviation of the fitting. Error bars of experimental data show the standard deviation (SD) of 9 independent measurements.

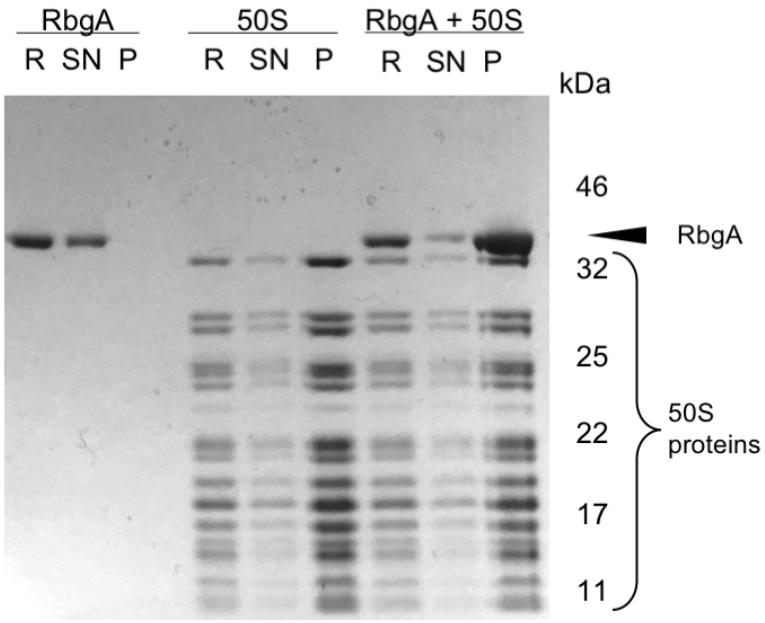

Figure S5: Co-sedimentation assay of RbgA with the mature 50S. Of each sedimentation assay, original reaction (R) before centrifugation and supernatant (SN) and pellet (P) after centrifugation were applied to an SDS-PAGE and stained with Instantblue. RbgA did not pellet without ribosomes, while it can be found in the pellet in the reaction with ribosomes, showing binding to the 50S, as previously reported [2].

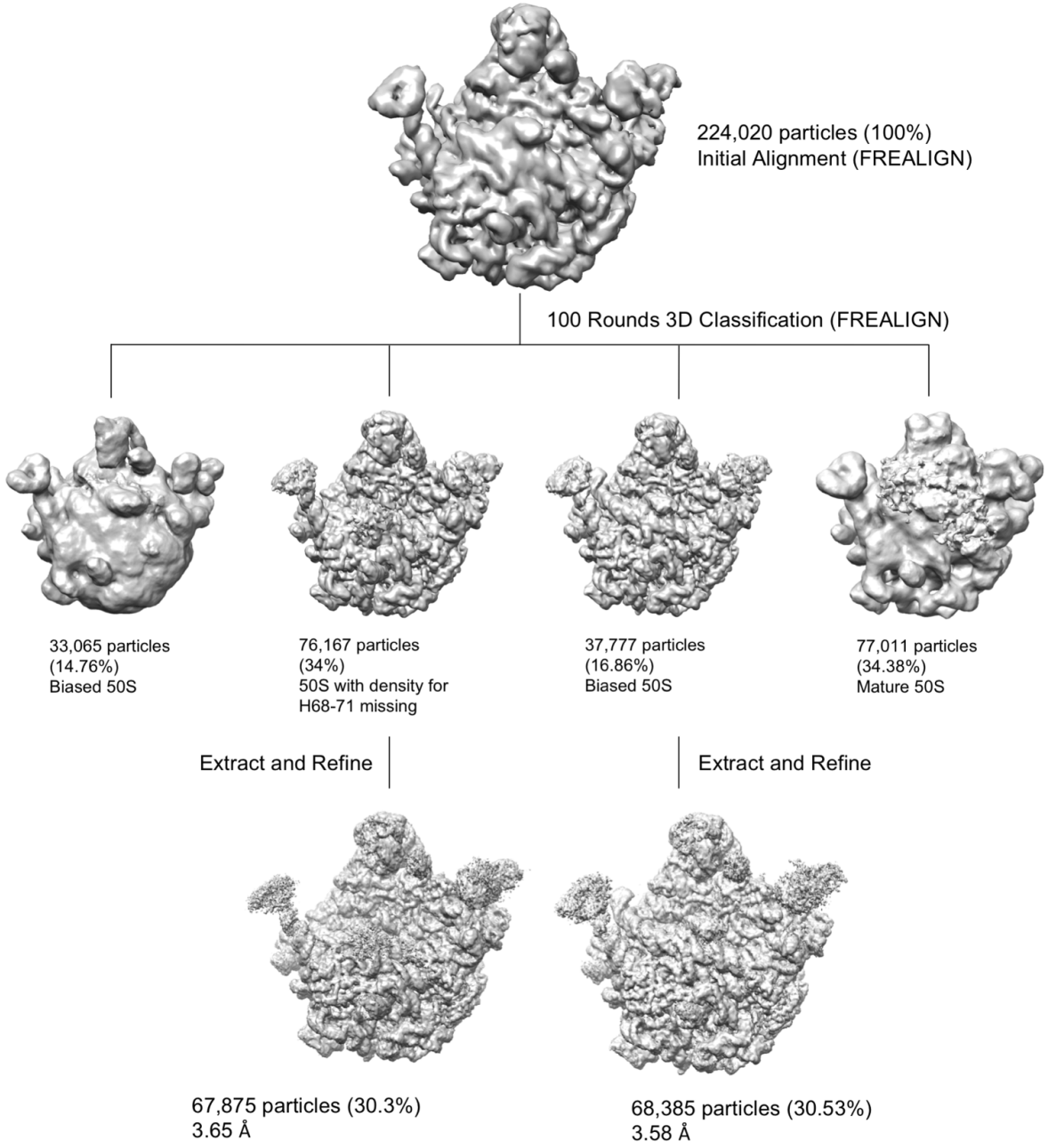

Figure S6: *In Silico* Sorting scheme for the RbgA-50S complex.

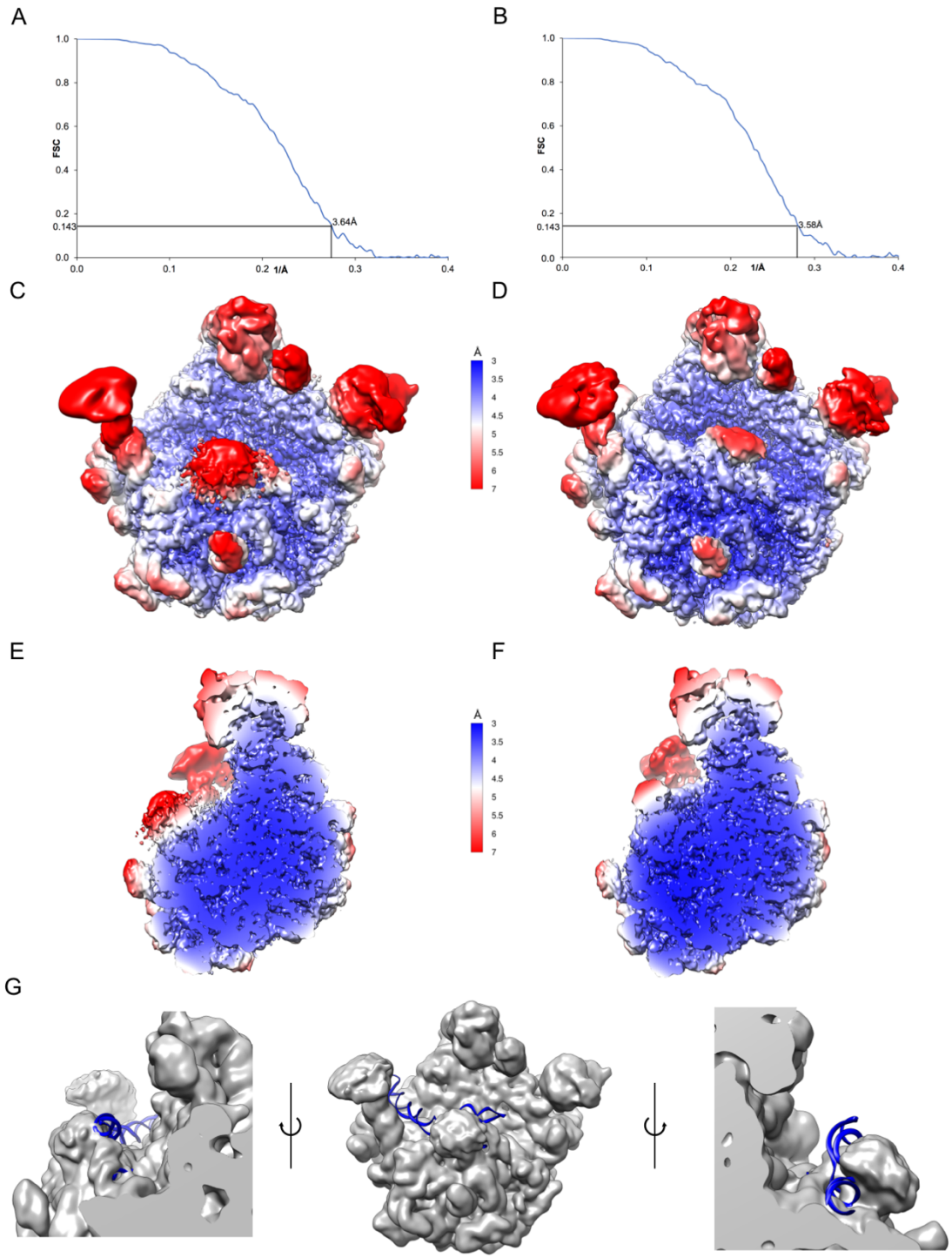

Figure S7: Fourier Shell Correlation (FSC) curves of the $50S_{Int}$ (**A**) and 50S (**B**), the line at FSC = 0.143 indicates average resolution of the volumes. Filtered by local resolution maps coloured according to resolution for the $50S_{Int}$ complex (**C**, **E**) and 50S (**D**, **F**) calculated with RELION. (**G**) Low-pass filtered map for RbgA-50S complex, displaying extra density in proximity to H67.

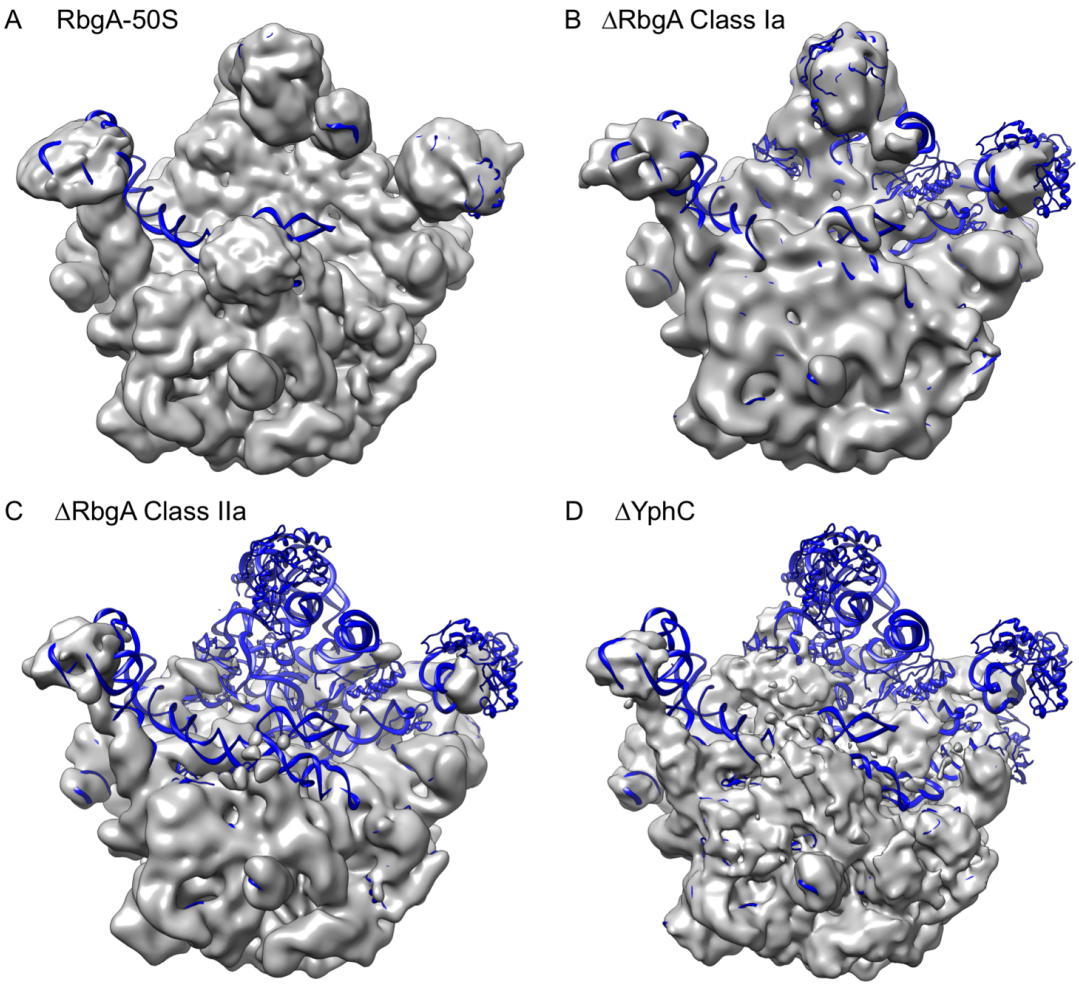

Figure S8: Comparison of 50S-RbgA complex with 45S particles. (**A**) filtered 50S-RbgA complex, showing missing density for H68-71 (**B** and **C**) Class Ia and IIa of RbgA depleted 45S particle [3] showing missing densities for H68-71 and ribosomal Proteins (e.g. L16) (**B**) and displaced H38 and CP (**C**). (**D**) YphC depleted 45S particle [4] showing missing densities for H68-71, ribosomal Proteins as well as the CP.

Supporting references:

1. Emsley, P. & Cowtan, K. Coot□: model-building tools for molecular graphics. *Acta Crystallogr. Sect. D* 2126–2132 (2004).
2. Achila, D., Gulati, M., Jain, N. & Britton, R. A. Biochemical characterization of ribosome assembly gtpase RbgA in Bacillus subtilis. *J. Biol. Chem.* **287,** 8417–8423 (2012).
3. Li, N. *et al.* Cryo-EM structures of the late-stage assembly intermediates of the bacterial 50S ribosomal subunit. **41,** 7073–7083 (2013).
4. Ni, X. *et al.* YphC and YsxC GTPases assist the maturation of the central protuberance , GTPase associated region and functional core of the 50S ribosomal subunit. *Nucleic Acids Res.* **44,** 8442–8455 (2016).

Structural basis for the (p)ppGpp-dependent control of the translation elongation factor EF-Tu

Wieland Steinchen[1,5,6], Mohamad Majkini[1,5], Maximiliane Wieland[2], Anita Dornes[1], Pietro I. Giammarinaro[1], Alexander Lepak[1], Benjamin J. Burnett[3], Scott C. Blanchard[3,4], Daniel N. Wilson[2] and Gert Bange[1,6]

[1]Philipps-University Marburg, Center for Synthetic Microbiology (SYNMIKRO) & Department of Chemistry, Hans-Meerwein-Straße, 35043 Marburg, Germany

[2]Institute for Biochemistry and Molecular Biology, University of Hamburg, Germany.

[3]Weill Cornell Medicine, Department of Physiology and Biophysics, New York, NY 10065

[4]Present address: St. Jude Children's Research Hospital, Department of Structural Biology, MS 312, Room D1007D, 262 Danny Thomas Place, Memphis, TN, USA

[5]These authors contributed equally to this work.

[6]Correspondence:

wieland.steinchen@synmikro.uni-marburg.de

gert.bange@synmikro.uni-marburg.de

ABSTRACT

Bacteria have to continuously adapt to their environment and cope with stress conditions. The second messengers ppGpp and pppGpp (also: (p)ppGpp) regulate a variety of cellular processes including protein biosynthesis. Here we show that (p)ppGpp can inhibit translation through binding to the elongation factor GTPase EF-Tu, which delivers amino-acylated tRNA (aa-tRNA) to the A-site of the translating ribosome. Our structural analysis shows that (p)ppGpp locks the elongation factor into the 'inactive' GDP-bound conformation unable to accommodate aa-tRNAs. Moreover, binding of the alarmone leads to a disordering of the switch I region of EF-Tu, which further restricts the functionality of the EF-Tu GTPase and might affect EF-Tu's phosphorylation state. The guanosine exchange factor EF-Ts removes ppGpp from EF-Tu, which might be important to 'reset' EF-Tu once stress conditions fade away. Our study further shows that EF-Tu acts as hydrolase converting pppGpp into ppGpp thus partaking in metabolism of (p)ppGpp. Taken together, these findings provides a mechanistic framework that helps explain how (p)ppGpp controls protein biosynthesis at the level of translation elongation via EF-Tu.

INTRODUCTION

Protein biosynthesis by ribosomes, translation, is central to all living organisms. The process of translation is divided into the steps of initiation, elongation and termination, where elongation represents the synthesis phase in which amino acids are added to the nascent polypeptide. Elongation critically relies on the delivery of cognate transfer RNA (tRNA) charged with a specific amino acid (aa-tRNA) to a ribosome programmed with a messenger RNA (mRNA). The delivery of aa-tRNAs to the ribosomal A-site is achieved by the elongation factor GTPase EF-Tu, which in its GTP-bound state forms a ternary complex with the aa-tRNA. Upon recognition of cognate codon-anticodon interactions at the ribosomal A-site, the GTPase activity of EF-Tu is stimulated, which ultimately leads to the dissociation of EF-Tu and accommodation of the aa-tRNA into the ribosome followed by peptide bond formation. The elongation factor EF-Ts serves as a guanosine exchange factor (GEF) for EF-Tu, which promotes the GDP to GTP exchange (1) and ternary complex formation (2).

EF-Tu consists of the N-terminal Ras-like GTPase domain (domain I), which is followed by the two β-barrel domains II and III involved in the interaction with aa-tRNA (3). Like in many other G-proteins, domain I contains the characteristic G-protein elements G1 to G5 required for guanosine nucleotide binding and magnesium ion coordination (4). The G2 and G3 elements are part of the switch regions I and II, respectively. Switch I and switch II (in *Escherichia coli* EF-Tu amino acids 40-62 and 83-100, respectively) undergo large conformational rearrangements during ternary complex formation and aa-tRNA selection on the ribosome, which depend on the presence of the magnesium ion and the γ-phosphate of GTP (5, 6). Thus, GTP binding to EF-Tu induces large conformational rearrangements of domains II and III relative to domain I, enforced by the nucleotide-specific configurations of both switch regions (7, 8). The GTP-dependent movement of switches I and II causes domain III to pack against switch II, opening a cleft between domains I and II into to which the acceptor end of the aa-tRNA binds. Domain III provides the binding site for the T stem of tRNA (3).

Protein biosynthesis is inhibited during conditions of amino acid limitation. In bacteria, the response to amino acid limitation is mediated, in part, by the production of the nutritional alarmones ppGpp and pppGpp (collectively: (p)ppGpp or alarmones) (9, 10). Synthesis of (p)ppGpp is carried out by enzymes of the RelA/SpoT homology (RSH) family (11), which bind to ribosomes along with deacylated tRNA within the A-site to catalyze the transfer of pyrophosphate (β- and γ-phosphates) from ATP to the ribose 3'-OH of GDP or GTP to synthesize ppGpp or pppGpp, respectively. The (p)ppGpp alarmones affect a plethora of cellular processes rendering the cellular metabolism more robust to amino acid starvation (10, 12, 13). ppGpp can inhibit translation (14) by binding IF2 (15, 16), EF-G (14, 15) and EF-Tu (14, 17). While, there exists a concrete structural understanding of how ppGpp inhibits IF2 (16) the molecular basis of how (p)ppGpp affects EF-Tu has yet to be revealed.

To fill this knowledge gap, we examined the molecular mechanism underlying the (p)ppGpp-dependent control of EF-Tu. Our study shows that ppGpp and pppGpp interact with EF-Tu with similar affinities as their counterparts GDP and GTP, respectively. We determined the crystal structure of EF-Tu bound to ppGpp/Mg^{2+} showing that the alarmone 'locks' the elongation factor in an 'inactive' conformation consistent with GDP-bound structures and furthermore provokes repulsion of the switch I region due to its 3'-pyrophosphate moiety. Our biochemical analysis reveals that ppGpp disables the binding of EF-Tu to aa-tRNAs and that ppGpp can be discharged from EF-Tu by the nucleotide exchange factor EF-Ts. These

findings collectively suggest that (p)ppGpp inhibits translation by reducing ternary complex concentrations in the cell, which may enhance the nutrient limitation-induced stress response by further increasing RelA-mediated alarmone synthesis.

RESULTS

(p)ppGpp competitively inhibits GTP and GDP binding to EF-Tu. Already 30 years ago, it was suggested that (p)ppGpp can inhibit the elongation factor EF-Tu (14). To recapitulate these early findings based on ppGpp purified from *E. coli* 'magic spot', we re-analyzed the effect with enzymatically synthesized and purified ppGpp and pppGpp (18) on *E. coli* translation *in vitro* using enhanced green fluorescent protein (eGFP) as a reporter. These experiments show that the both alarmones, ppGpp and pppGpp, inhibit translation in a dose-dependent manner (**Fig. 1A**).

Next, we wanted to determine the binding affinity between (p)ppGpp and EF-Tu. The elongation factor was recombinantly produced in *E. coli* and initially purified by a two-step protocol consisting of a Ni-ion affinity followed by size-exclusion chromatography. However, most EF-Tu purified in this fashion was in a GDP-bound state, likely owing to its strong interaction with the nucleotide. We, therefore, purified EF-Tu in the absence of Mg^{2+}, and additionally added EDTA, to strip-off residual Mg^{2+} and nucleotide from EF-Tu (19, 20) (**Fig. S1**). With nucleotide-free EF-Tu in hand, we next probed the binding of a fluorescently labeled GTP (i.e. Mant-GTP) to EF-Tu, which yielded a dissociation constant (K_d) of 1.6 ± 0.4 μM (**Fig. 1B**). The binding of alarmones was probed indirectly through competition with Mant-GTP binding to EF-Tu. Hereby ppGpp displayed a similar inhibitory constant (K_i) value as GDP (i.e. 0.5 ± 1.2 μM and 0.4 ± 1.3 μM, respectively), while the K_i value for pppGpp was closer to GTP (i.e. 1.8 ± 1.2 μM and 1.4 ± 1.1 μM, respectively; **Figs. 1C** and **D**). Hence, the K_i values for the 5'-diphosphate nucleotides GDP and ppGpp are approximately 3- to 4-fold lower than for the 5'-triphosphates GTP and pppGpp, indicative of higher affinity binding to EF-Tu.

In order to clarify of whether the (p)ppGpp is specific to EF-Tu from the Gram-negative model bacterium *E. coli*, or if such findings also extend to other bacteria, we analyzed (p)ppGpp interactions with EF-Tu from the Gram-positive model organism *Bacillus subtilis*. Here, similar values as described above for *E. coli* EF-Tu were observed, suggesting that the (p)ppGpp-dependent regulation of EF-Tu is a conserved feature among evolutionarily divergent bacterial species (**Fig. S2**).

Crystal structure of EF-Tu bound to ppGpp/Mg. To gain insights into the molecular basis of (p)ppGpp-mediated inhibition of EF-Tu, we determined the crystal structure of *E. coli* EF-Tu in the presence of pppGpp to a resolution of 2.0 Å (**Table S1**). The majority of EF-Tu could be built with the exception of amino acid residues 40-60 containing the switch I region (**Fig. 2A**). The structure showed the typical appearance of EF-Tu with its N-terminal GTPase domain (domain I) followed by the two β-barrel domains II and III (**Fig. 2A**). The relative arrangement of the domains I-III to each other was highly reminiscent to the GDP-bound state of EF-Tu with a root mean square deviation (r.m.s.d.) of 0.474 Å over 2011 atoms (**Fig. 2B**; **Fig. S3**). Moreover, the conformation of our EF-Tu structure clearly differed from those previously observed in presence of the GTP analog, GMPPNP (**Fig. 2C**; **Fig. S3**). Inspection of the active site revealed an electron density that could be unambiguously assigned to, and refined with, ppGpp and a single magnesium ion (Mg^{2+}) (**Fig. S4**).

The binding of ppGpp to EF-Tu is achieved in the same manner as for GDP (**Fig. 2D** and ref. (21)). The guanine base is sandwiched between the side chains of K136 and L175. K136 furthermore interacts with its ε-amino group with O1 of the ribose. Hydrogen-bonding interactions with the guanine base of ppGpp are established between N135 and nitrogen 7, D138 and the 6'-oxo group and S173 and the nitrogen 1 and the 2'-amino group of the base, respectively. The α- and β- phosphate moieties at the 5' end of the ribose are coordinated mainly through the backbone amides of D21, G23, K24, T25 and T26 and additionally through the side chains of K24 and T25 (**Fig. 2D**). Four water molecules along with the hydroxyl group of T25 and the β-phosphate of ppGpp coordinate the magnesium ion. The δ- and ε- phosphate moieties of ppGpp are not further coordinated and point away from the active site towards the switch I region (**Fig. 2D**).

The disordered conformation of the switch I region in our ppGpp-bound EF-Tu structure (**Fig. 2E**) is in contrast to its conformation in the GDP-bound state of EF-Tu in which the switch I region forms a short α-helical segment followed by an anti-parallel β–ribbon (**Fig. 2F**). Superposition of the ppGpp- and GDP-bound structures shows that the positions of the δ- and ε- phosphate moieties of ppGpp and the switch I region are incompatible, mainly through electrostatic clashes of the pyrophosphate with the switch I residues F46 and D50 (**Fig. 2F**). The same residues would also provoke clashes with ppGpp in the aa-tRNA-bound closed conformation of EF-Tu (**Fig. 2G**). We thus conclude that (p)ppGpp inhibits the function of EF-Tu by interfering with the conformational rearrangements of the switch I region of the elongation factor.

(p)ppGpp inhibits EF-Tu ternary complex formation. The structure and conformational rearrangements of switch I are crucial for the nucleotide-dependent traversing of EF-Tu between its 'open', GDP-bound and 'closed', GTP-bound conformations, the latter one being able to interact with aa-tRNA (3). These observations suggested to us that (p)ppGpp should destabilize the EF-Tu•GTP•aa-tRNA ternary complex. To test this hypothesis, we initially performed electrophoretic mobility shift assay (EMSA) experiments. In this assay, the binding of Lys-tRNA^{Lys} to EF-Tu in presence of GTP is evidenced by an altered migration behavior of the tRNA compared to the absence of GTP (**Fig. 3A**). Addition of ppGpp or pppGpp with increasing concentrations (ratios of 1:5, 1:1 and 5:1 (p)ppGpp to GTP) diminished the observed difference in band migration, indicating a disruption of the EF-Tu•GTP•Lys-tRNA^{Lys} ternary complex (**Fig. 3A**). To further probe this assessment, we performed an ensemble fluorescence investigation in which ppGpp was added to pre-formed ternary complex (**Fig. 3B**). In the absence of EF-Ts we observed approximately 50% dissociation of ternary complex when ppGpp was added (100 μM; 10,000-fold excess over GTP). Remaining ternary complex was efficiently dissociated by addition of GDP (100 μM). In presence of EF-Ts, the observed rate of ternary complex turnover was markedly enhanced while the overall extent of ternary complex dissociation was unchanged. These finding are consistent with both dissociation processes taking place via nucleotide exchange on the intact ternary complex (2, 22). Taken together, these findings show that alarmones destabilize aa-tRNA binding to EF-Tu, and as such prohibit productive transfer of aa-tRNAs to a translating ribosome.

EF-Tu is able to hydrolyze pppGpp into ppGpp. While we crystallized EF-Tu in the presence of pppGpp, we observed ppGpp in the determined structure. This observation could be explained by non-enzymatic pppGpp hydrolysis or contaminating ppGpp in our pppGpp preparation, upon which the higher affine ppGpp would preferentially bind to EF-Tu instead of pppGpp (**Figs. 1C** and **D**). However, it could also indicate the ability of EF-Tu to actively

remove the γ-phosphate moiety of pppGpp in order to generate ppGpp. Consistent with the latter model, we found that the incubation EF-Tu with pppGpp degraded pppGpp into ppGpp in a dose-dependent manner by removal of the 5' γ-phosphate (**Fig. 4**) suggesting that EF-Tu functions as a pppGpp hydrolase.

Removal of (p)ppGpp by EF-Ts. During the normal cycle of EF-Tu its GTPase activity is stimulated in codon-dependent manner by the translating ribosome, ultimately triggering aa-tRNA accommodation and release of EF-Tu•GDP from the ribosome. Recycling of EF-Tu from the GDP-bound state is facilitated by EF-Ts, a GEF that binds EF-Tu to facilitate GDP release and GTP binding, followed by EF-Ts dissociation (1, 19). To probe whether EF-Ts would similarly act as a GEF on EF-Tu•(p)ppGpp, we performed pull-down experiments where we pre-incubated EF-Tu with an excess of nucleotides and, after incubation with or without EF-Ts followed by removal of unbound (or released) nucleotides by extensive washing, analyzed EF-Tu's nucleotide content by HPLC. In the absence of EF-Ts, EF-Tu retained an approximately equimolar amount of GDP, ppGpp and pppGpp nucleotides while addition of EF-Ts resulted in the loss of nucleotide coordination by EF-Tu (**Fig. 5A**). We also probed EF-Ts-dependent nucleotide coordination by EF-Tu with size-exclusion chromatography again evidencing that EF-Ts weakens the interaction of (p)ppGpp with EF-Tu resulting in release of the nucleotides (**Fig. 5B**). These data suggest that EF-Ts is able to remove (p)ppGpp from the EF-Tu•(p)ppGpp complex.

DISCUSSION

When microorganisms encounter amino acid limitation, productive protein biosynthesis is hindered because less aminoacylated tRNAs are available for translation. The stringent factor RelA (aka Rel) binds to uncharged tRNAs (23, 24) and its (p)ppGpp synthetic activity is massively stimulated when the tRNA/RelA complex binds to the A-site of ribosome lacking cognate aa-tRNAs (25-28) (**Fig. 6**, I). By this mechanism, the intracellular concentrations of (p)ppGpp can rise up to 1 mM (10). Inhibition of translation through ppGpp via the translational GTPase EF-Tu had been identified early on (14, 17). However, the precise molecular mechanism by which (p)ppGpp acted on EF-Tu was unclear.

Our structural analysis now shows that ppGpp and pppGpp interact with EF-Tu in the same way (and with similar affinities) as their counterparts GDP and GTP, respectively. Thus, ppGpp and pppGpp are competitive inhibitors of GTP-binding to EF-Tu in the context of the cell. Our structure of EF-Tu bound to ppGpp shows that the protein adopts a conformation highly similar to the EF-Tu•GDP complex, which is unable to interact with aa-tRNA (**Fig. 6**, II).

Additionally, the δ- and ε-phosphate moieties ppGpp enforces a disordering of the switch I region because of steric clashing. This observation adds another mechanistic level to the ppGpp-dependent inhibition of aa-tRNA binding to EF-Tu, because the switch I region needs to undergo a distinct and GTP-dependent conformational change in order to allow binding of acceptor end of the aa-tRNA into a cleft formed between domains I and II. Thus, our study explains how (p)ppGpp inhibits EF-Tu by hindering the formation of the EF-Tu•GTP•aa-tRNA ternary complex (**Fig. 6**, II).

Our study also showed that EF-Ts is able to remove (p)ppGpp from EF-Tu, which is likely to be important to 'reset' the elongation factor once stringent response conditions fade, and contribute to the steady-state equilibrium between GDP, GTP and (p)ppGpp during 'relaxed' conditions, where the basal level of (p)ppGpp is approximately 10 to 20 μM (**Fig. 6**, III).

To our surprise, we also found that EF-Tu contains a hydrolase activity, which can remove the γ-phosphate moiety from pppGpp in order to generate ppGpp (**Fig. 6**, IV). So far, only the *E. coli* GppA protein was thought to contain such a functionality (29). This finding could suggest that EF-Tu and some other GTPases might also contribute to the conversion of pppGpp to ppGpp inside cells. In contrast to EF-Tu, however, the GTPase RbgA from *B. subtilis*, which is involved in the biogenesis of 50S ribosomal subunits, does not hydrolyze pppGpp (30) and thus further studies are required to elaborate on this idea.

We further noticed that the disordering of the switch I region by ppGpp could have further consequences on EF-Tu. Specifically, regulation of EF-Tu is known to occur through several phosphorylation sites (31-33) including a highly conserved threonine within the switch I region (e.g. T61 (*E. coli*), T63 (*B. subtilis*) or T64 (*Mycobacterium tuberculosis*)). As noted by Talavera et al., however, T61 (*E. coli* EF-Tu) is 'hidden' within the nucleotide-binding pocket in both the GDP- and GTP-bound states (34), making it not intuitively clear how a kinase could gain access to this non–surface-exposed residue (**Fig. 6**, V). Through the (p)ppGpp-induced disordering of the switch I, however, this threonine would readily become surface-exposed (**Fig. S5**) and thus more amenable to phosphorylation. This mechanism would provide an elegant way of coupling the stress-dependent cellular (p)ppGpp pool with the phosphorylation state of EF-Tu to enable an overall inhibition of bacterial protein synthesis at e.g. the onset of (endo-)spore formation (35) or dormancy (36).

MATERIALS & METHODS

Cloning and mutagenesis. *E. coli* EF-Tu and EF-Ts were amplified from *E. coli* K-12 MG1655 and *B. subtilis* EF-Tu from *B. subtilis* strain 3610 genomic DNA by polymerase chain reaction (PCR) with the primers listed in **Table S2** using Phusion High-Fidelity DNA polymerase (NEB) according to the manufacturer's manual. The resulting PCR fragments were introduced into pET24d (*E. coli* and *B. subtilis* EF-Tu) or pET16b (*E. coli* EF-Ts) vectors (Novagen) and encoded hexahistidine-tags in frame with their DNA sequences (**Table S2**).

Protein Production and Purification. Proteins were overproduced in *E. coli* BL21 (DE3) (NEB) carrying the respective plasmids. Cells were grown in lysogeny broth (LB)-medium supplemented with 50 µg/ml kanamycin or 100 µg/ml and 12.5 g/l D(+)-lactose-monohydrate for 20 h at 30 °C and harvested by centrifugation (3,500 x *g*, 20 min, 4 °C). For purification of *E. coli* EF-Tu, the cells were resuspended in lysis buffer (20 mM of HEPES-Na pH 8.0, 20 mM KCl, 250 mM NaCl and 40 mM imidazole) and lysed by French Press (SLM Aminco) at 1,000 psi pressure. After centrifugation of the lysate (47,850 x *g*, 20 min, 4 °C), the supernatant was loaded on a 5-ml HisTrap column (GE Healthcare) equilibrated with 10 column volumes (CV) lysis buffer. After washing with 10 CV of lysis buffer, EF-Tu was eluted with 5 CV elution buffer (lysis buffer containing 500 mM imidazole). 50 mM EDTA-Na pH 8.0 were added to the eluate and incubated for 30 minutes at 4 °C. EF-Tu was concentrated (Amicon Ultracel-10K (Millipore)) and applied to size-exclusion chromatography (SEC) on a HiLoad 26/600 Superdex 200 pg column (GE Healthcare) equilibrated with SEC buffer (20 mM of HEPES-Na, pH 7.5, 20 mM KCl and 200 mM NaCl). Fractions containing nucleotide-free EF-Tu as estimated by HPLC (see below) were pooled, concentrated (Amicon Ultracel-10K (Millipore)), deep-frozen in liquid nitrogen and stored at -80 °C. Protein concentration was determined by a spectrophotometer (NanoDrop Lite, Thermo Scientific). *E. coli* EF-Ts was purified by similar procedure but no EDTA added to the protein. *B. subtilis* EF-Tu was

purified by the same procedure as *E. coli* EF-Tu but all buffers contained 500 mM NaCl and 5% (v/v) glycerol.

Preparation of ppGpp and pppGpp. (p)ppGpp was produced as described previously with the (p)ppGpp synthetase RelQ from *B. subtilis* (18).

***In vitro* translation assays.** The synthesis of enhanced green fluorescent protein (eGFP) was assayed with a coupled transcription/translation system (RTS 100 *E. coli* HY Kit, Biotechrabbit). Reactions of 50 µl contained 12 µl *E. coli* lysate, 10 µl reaction mix, 12 µl amino acid solution, 1 µl of methionine, 5 µl reconstitution buffer and 1 µg of the control vector containing *eGFP*. ppGpp or pppGpp were added with final concentrations of 10, 100 or 1,000 µM. The reaction was allowed to proceed for 4 h at 30 °C and afterwards kept at 4 °C for 24 h for full maturation of eGFP. eGFP production was determined by fluorescence measurement ($\lambda_{Ex}/\lambda_{Em}$ = 395/509 nm) with a spectramax M4 multi-mode microplate reader (Molecular Devices).

Inhibitory constants of (p)ppGpp binding to EF-Tu. Inhibitory constants were determined by fluorescence spectroscopy carried out with a FP-6300 Spectrofluorometer (Jasco) with the following settings: excitation 355 ± 2.5 nm, emission 450 ± 10 nm, response time 0.5 s, sensitivity med and data pitch of 0.5 s. Spectra were evaluated with Spectra Manager for Windows 1.05.03 [Build 1]. Further data analysis was done in GraphPad Prism version 6.04 for Windows (GraphPad Software, San Diego, California, USA). The dissociation constant (K_d) of Mant-GTP was determined by titrating 1 µM Mant-GTP in SEC buffer (supplemented with 20 mM $MgCl_2$) with 0.5 µM EF-Tu per injection and calculated with the equation $\Delta Fluorescence = B_{max} * [EF\text{-}Tu] / (K_d + [EF\text{-}Tu])$. Inhibitory constants ($K_i$) for GDP, GTP, ppGpp and pppGpp were obtained by titrating a mixture of 1 µM Mant-GTP and 5 µM EF-Tu in SEC buffer (supplemented with 20 mM $MgCl_2$) with GDP, GTP, ppGpp or pppGpp and calculated with the 'One site - inhibitory constant' model using equations Fluorescence=Bottom + (Top-Bottom)/(1+10^(log[Nucleotide]-logEC50)) and logEC50=log(10^logK_i*(1+1000/1600)).

Crystallization and structure determination. Prior crystallization, 1 mM *E. coli* EF-Tu was supplemented with 10 mM pppGpp and 10 mM $MgCl_2$ and incubated for 30 minutes at room temperature. Crystallization was carried out at room temperature by sitting drop vapor diffusion method in SWISSCI MRC 2-well plates (Jena Bioscience) with a reservoir volume of 50 µl. Screens were set up by mixing 0.5 µl of protein solution with the same volume of crystallization solution. Crystals of ppGpp/Mg-bound *E. coli* EF-Tu were obtained after 2 days from 0.1 M HEPES pH 7, 0.1 M $MgCl_2$, and 15% (w/v) PEG4000. For crystals harvest, 0.5 µl of a cryo-protecting solution containing mother liquor supplemented with 20% (v/v) glycerol was added to the drop, crystals looped and flash-frozen in liquid nitrogen. Diffraction data of crystals were collected at the European Synchrotron Radiation Facility (ESRF) Grenoble, France, at beamline ID29 under laminar nitrogen flow at 100K (Oxford Cryostream 700 Series) with a DECTRIS PILATUS 6M F detector at 1.07234 Å. Data were processed with XDS (37) and CCP4-implemented AIMLESS (38). The structure was determined with the CCP4-implemented program PHASER (39) using GDP-bound *E. coli* EF-Tu (PDB: 1EFC (21)) as a search model for molecular replacement. The structure was manually built in Coot (40) and refined with REFMAC5 (41). Figures were prepared with PyMOL (www.pymol.org).

Determination of EF-Tu nucleotide content and activity. The nucleotide content of EF-Tu was determined high-performance liquid chromatography (HPLC). 200 µM of EF-Tu were denaturated by adding two volume parts chloroform followed by 15 s vigorous mixing, 15 s heat treatment at 95 °C and flash-freezing in liquid nitrogen. This mixture was centrifuged

(17,300 x *g*, 30 min, 4 °C) and while thawing the aqueous phase removed. The sample was diluted 1:5 with double-distilled water and analyzed for its nucleotide contents by HPLC on an Agilent 1260 Infinity system equipped with Metrosep A Supp 5 - 150/4.0 column. Nucleotides were eluted isocratically with a flow rate of 0.7 ml/min of 100 mM $(NH_4)_2CO_3$ at pH 9.25 and detected at 260 nm wavelength in agreement with standards.

Determination of EF-Tu activity towards pppGpp. Hydrolysis of pppGpp by *E. coli* EF-Tu was probed by incubating 1/2.5/5/10/25 µM EF-Tu together with 1 mM pppGpp for 1/6/30/90/150 min at 37 °C in SEC buffer supplemented with 20 mM $MgCl_2$. Reactions were stopped and analyzed as described above. Non-enzymatic hydrolysis of pppGpp was determined from reactions carried out without EF-Tu. All measurements were performed in triplicates.

Determination of ternary complex formation by fluorescence spectroscopy. Labeled EF-Tu was constructed and purified using the expression system described for native EF-Tu with the modification of a C-terminal acyl-carrier protein recognition epitope (CT-AcpS), as previously described (22). Briefly, labeling was achieved by incubating purified EF-Tu (CT-AcpS) with a 10-fold excess of CoA-linked Cy5Q and a 5-fold excess of AcpS phosphopantetheinyl transferase enzyme in buffer A (50 mM HEPES pH 7.5, 10 mM $Mg(OAc)_2$) for 2 h. Wild-type *E. coli* $tRNA^{Phe}$ was expressed and purified from strain MRE600 as described previously (42). $tRNA^{Phe}$ was site-specifically labeled with Cy3B via the naturally occurring modified nucleotide acp3U at position 47, and purified by hydrophobic interaction chromatography (HIC) on a Phenyl-5PW column (TOSOH) by applying a shallow gradient from buffer C (10 mM $NH_4(OAc)$ pH 5.8, 1.7 M $(NH4)_2SO_4$) to buffer D (10 mM $NH_4(OAc)$ pH 5.8, 10% (v/v) methanol) over 20 column volumes. $tRNA^{Phe}$ was aminoacylated by adding a 0.1x molar ratio of tRNA synthetase and a 1,000-fold excess of phenylalanine in a volume of 10 µL in buffer E (50 mM Tris-HCl pH 8, 20 mM KCl, 100 mM NH_4Cl, 1 mM DTT, 2.5 mM ATP, 0.5 mM EDTA, 10 mM $MgCl_2$) and incubating at 37 °C for 20 min. The extent of aminoacylation was verified by analytical HIC. GDP and GTP were purchased from Sigma and further purified on a Tricorn Mono Q 5/50 GL ion exchange column as previously described (2).

Fluorescence measurements were performed using a Photon Technology International fluorescence spectrometer with a 532 nm long-pass emission filter (LP03-532RS-25 RazorEdge by Semrock). Reactions were analyzed in buffer F (100 mM HEPES pH 7, 20 mM KCl, 100 mM NH_4Cl, 1 mM DTT, 0.5 mM EDTA, 2.5 mM $MgCl_2$) in a 3 mL quartz cuvette with constant mixing at room temperature while exciting at 532 nm and monitoring the emission at 565 nm. Ternary complex was pre-formed *in situ* by manually adding 400 nM Cy5Q-labeled EF-Tu, or Cy5Q-labeled EF-Tu in a 1:1 complex with EF-Ts, to a reaction containing 5 nM Cy3B-labeled Phe-$tRNA^{Phe}$ and 10 µM GTP in buffer F at room temperature with constant mixing.

Determination of ternary complex formation by electrophoretic mobility shift assay. Ternary complex was preformed by mixing 100 µM EF-Tu, 250 µM GTP and 5 µM Lys-$tRNA^{Lys}$ in SEC buffer supplemented with 20 mM $MgCl_2$. (p)ppGpp was added with final concentrations of 50 µM, 250 µM or 1 mM. Reactions were incubated at room temperature for 10 min and directly subjected to gel electrophoresis employing 10% polyacrylamide (19:1) gel and TB buffer (90 mM Tris-Borate, pH 8.3), both supplemented with 1 mM $MgCl_2$. Gels were stained for 15 min with GelRed Nucleic Acid Stain (Biotium) and imaged using UV light of 312 nm wavelength.

Nucleotide removal from EF-Tu by EF-Ts. In pull-down experiments, EF-Tu (100 µM) was incubated in SEC buffer supplemented with 1 mM $MgCl_2$ with nucleotides (1 mM) in absence or presence of EF-Ts (100 µM) for 5 min at room temperature. Subsequently, 100 µl of Ni-NTA beads (Macherey Nagel) were added, transferred into spin columns and washed five times with 500 µl SEC buffer + 40 mM imidazole before elution with SEC buffer + 500 mM imidazole. EF-Tu was dentaturated with chloroform and its nucleotide content analyzed as described above. In analytical SEC experiments, EF-Tu (100 µM) was incubated in SEC buffer supplemented with 1 mM $MgCl_2$ with nucleotides (200 µM) in absence or presence of EF-Ts (100 µM) for 5 min at room temperature and 1 ml of this mixture applied to SEC on a Superdex 200 Increase 10/300 GL column (GE Healthcare) equilibrated with SEC buffer supplemented with 1 mM $MgCl_2$.

DATA AVAILABILITY

Atomic coordinates and structure factors for ppGpp-bound *E. coli* EF-Tu were deposited in the Protein Data Bank (PDB) under accession code 6Z0N.

ACKNOWLEDGEMENTS

We thank the European Synchrotron Radiation Facility (ESRF), Grenoble, France for support during data collection. D.N.W. and G.B. thank the SPP1879 priority program of the Deutsche Forschungsgemeinschaft (DFG) and M.M. the HessenFonds for financial support. We thank Sven-Andreas Freibert for introduction to the fluorescence spectrometer. We thank Hani Zaher (Washington University in St. Louis) for supplying Lys-$tRNA^{Lys}$.

The authors declare no financial conflict of interest.

FIGURES

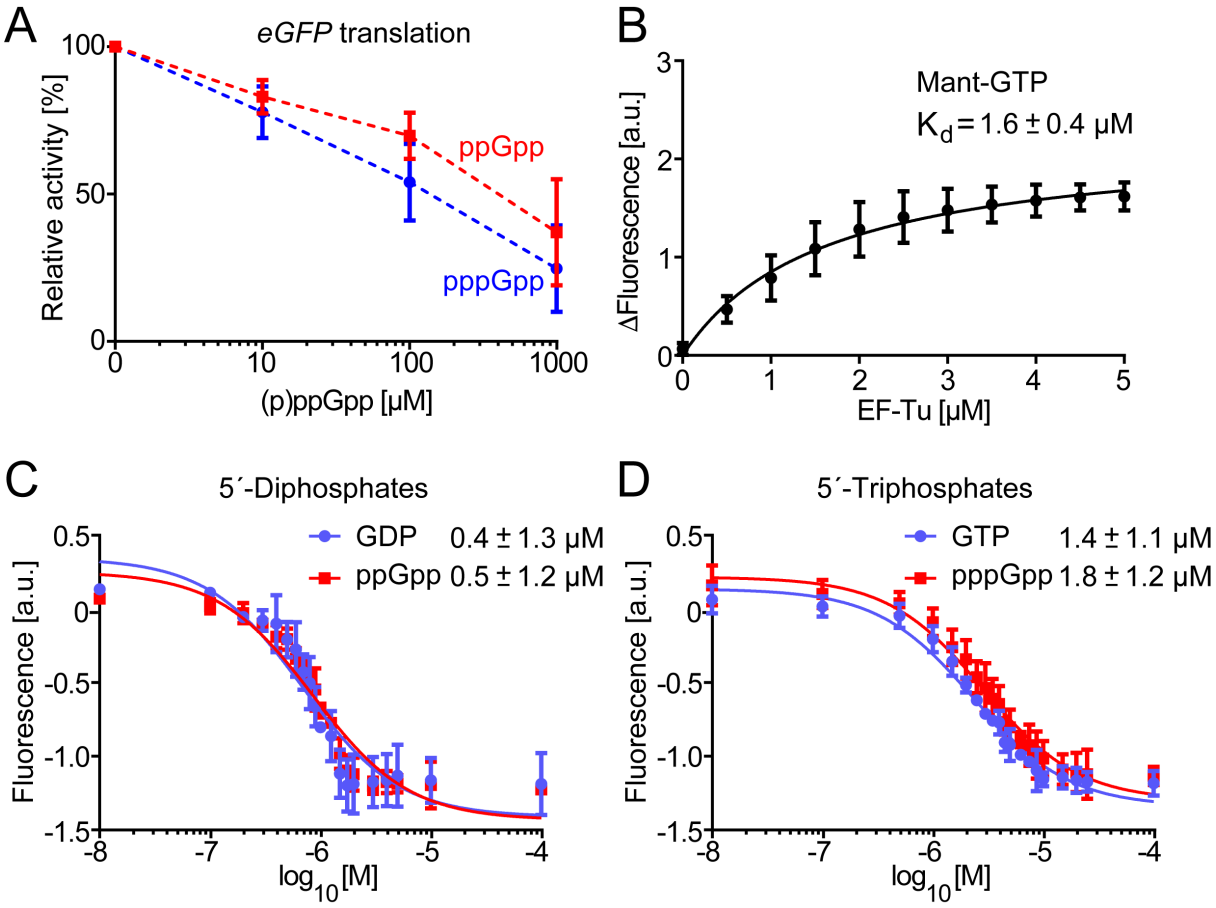

Fig. 1. Binding of (p)ppGpp to EF-Tu. **A.** Inhibition of translation i*n vitro* by ppGpp and pppGpp. Translation activity was determined by quantifying the amount of eGFP. Activity in absence of (p)ppGpp was set to 100%. **B.** Binding of Mant-GTP to EF-Tu. 1 µM of Mant-GTP was titrated with EF-Tu and the change in Mant-GTP fluorescence quantified. Data represent mean ± SD of n=6 technical replicates. **C-D.** Competition of unlabeled GDP and ppGpp (**C**) and GTP and pppGpp (**D**) for binding to Mant-GTP/EF-Tu. A mixture of 1 µM Mant-GTP and 5 µM EF-Tu was titrated with unlabeled nucleotides. Data represent mean ± SD of n=2 technical replicates.

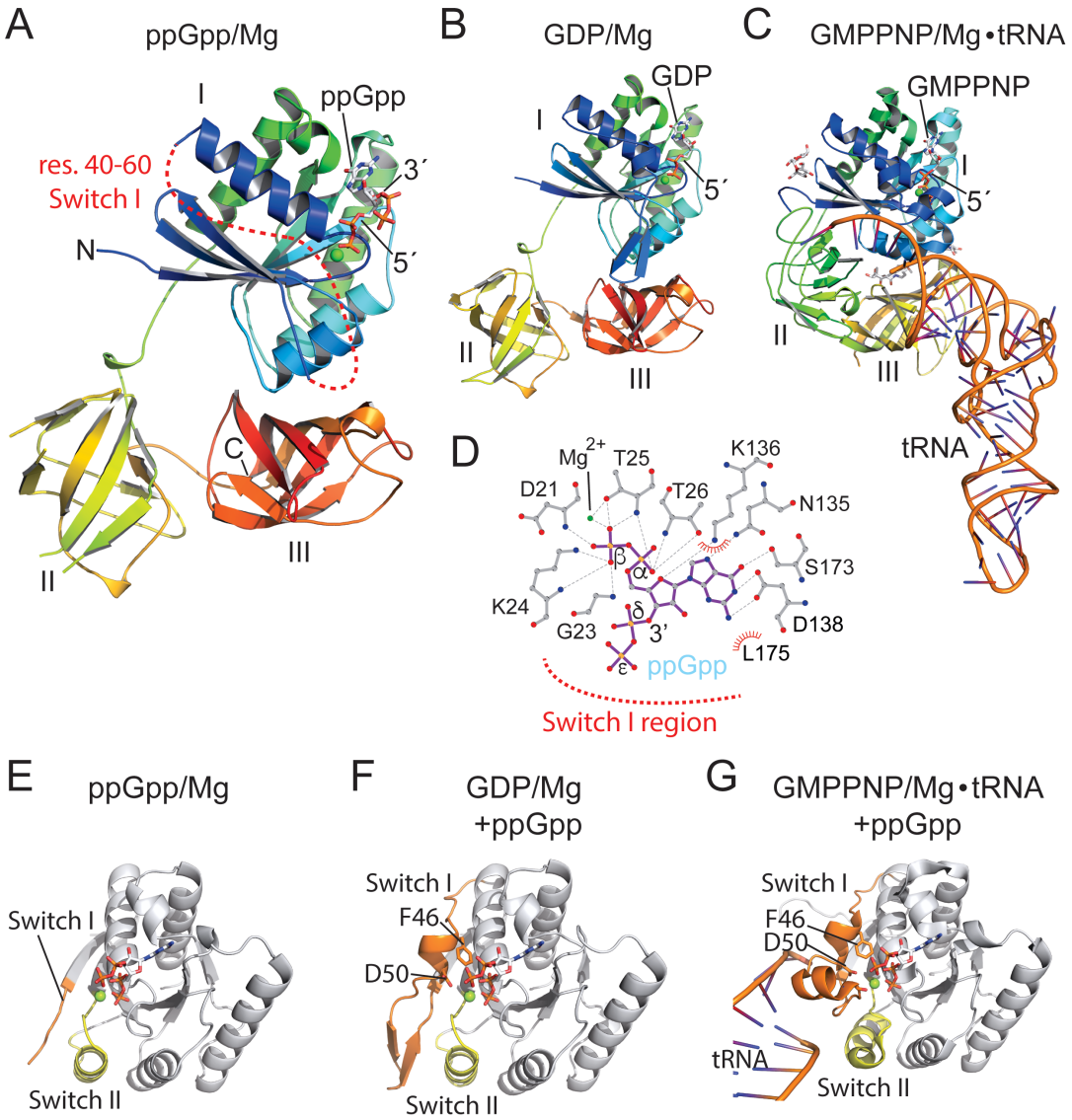

Fig. 2. Crystal structure of ppGpp/Mg^{2+}-bound EF-Tu. **A-C.** Cartoon representation of the crystal structures of EF-Tu in complex with ppGpp/Mg (**A**), GDP/Mg (**B**, PDB: 1EFC (21)) and GMPPNP/Mg, Phe-$tRNA^{Phe}$ and kirromycin (**C**, PDB: 1OB2). All structures are rainbow-colored from their N- to C-termini. Roman numbers denote the domains I-III of EF-Tu. The nucleotides are shown in sticks and the magnesium ions as green spheres. A red dashed line indicates the amino acids 40-60 of ppGpp/Mg-bound EF-Tu (**A**) too flexible to be modeled. **D.** Coordination of ppGpp/Mg by EF-Tu. Atoms are colored in grey (carbon), orange (phosphor), blue (nitrogen) and red (oxygen). Hydrogen-bonding interactions are indicated by black dotted lines. **E-G.** Cartoon representation of the GTPase domains of EF-Tu in complex with ppGpp/Mg (**E**), GDP/Mg (**F**, PDB: 1EFC (21)) and GMPPNP/Mg, Phe-$tRNA^{Phe}$ and kirromycin (**G**, PDB: 1OB2). The switch I and switch II regions are colored in orange and yellow, respectively. The ligand ppGpp was placed into all structures based on superpositions with ppGpp/Mg-bound EF-Tu (see also **Fig. S3**).

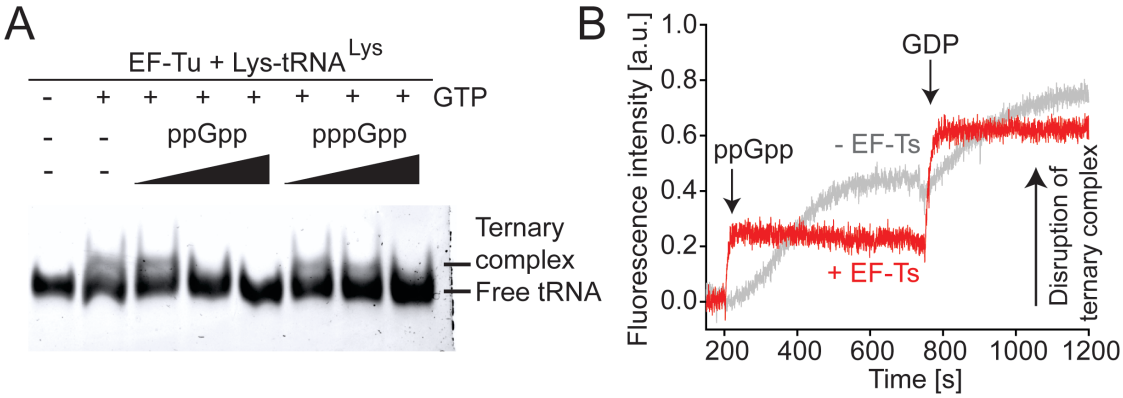

Fig. 3. (p)ppGpp interferes with ternary complexes. A. Inhibition of EF-Tu•GTP•Lys-tRNA^{Lys} ternary complex formation by (p)ppGpp in electrophoretic mobility shift assay. **B.** ppGpp-mediated dissociation of EF-Tu•GTP•Phe-tRNA^{Phe} ternary complexes pre-formed with Cy5Q-labeled EF-Tu in absence (grey) or presence (red) of EF-Ts. Arrows denote the addition of ppGpp (at 200 sec) and GDP (at 750 sec), both with 100 µM final concentration equaling 10,000-fold excess over GTP.

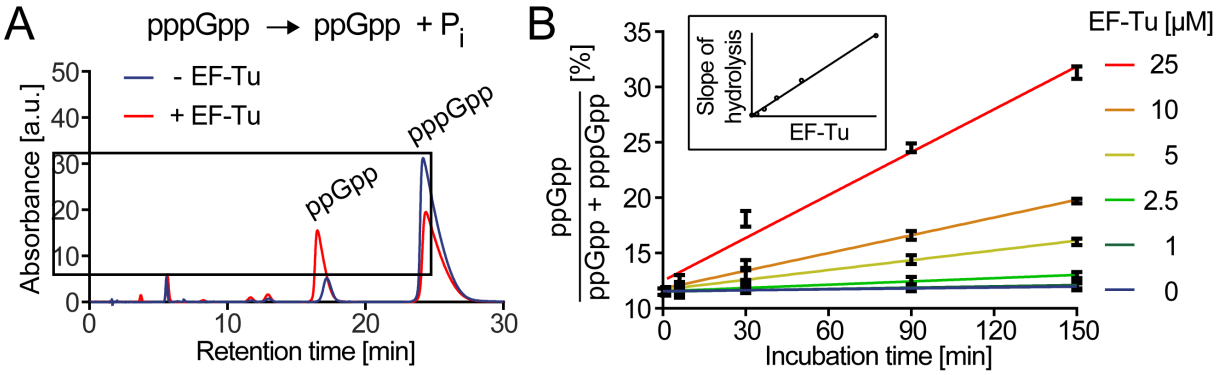

Fig. 4. EF-Tu degrades pppGpp to ppGpp. A. Representative chromatograms depicting the ability of EF-Tu to degrade pppGpp into ppGpp through removal of the 5' γ-phosphate. **B.** Variable concentrations of EF-Tu were incubated with pppGpp and the amount of ppGpp and pppGpp quantified by HPLC. Data represent mean ± SD of n=3 technical replicates. The inset depicts the slope of the linear regressions versus the concentration of EF-Tu.

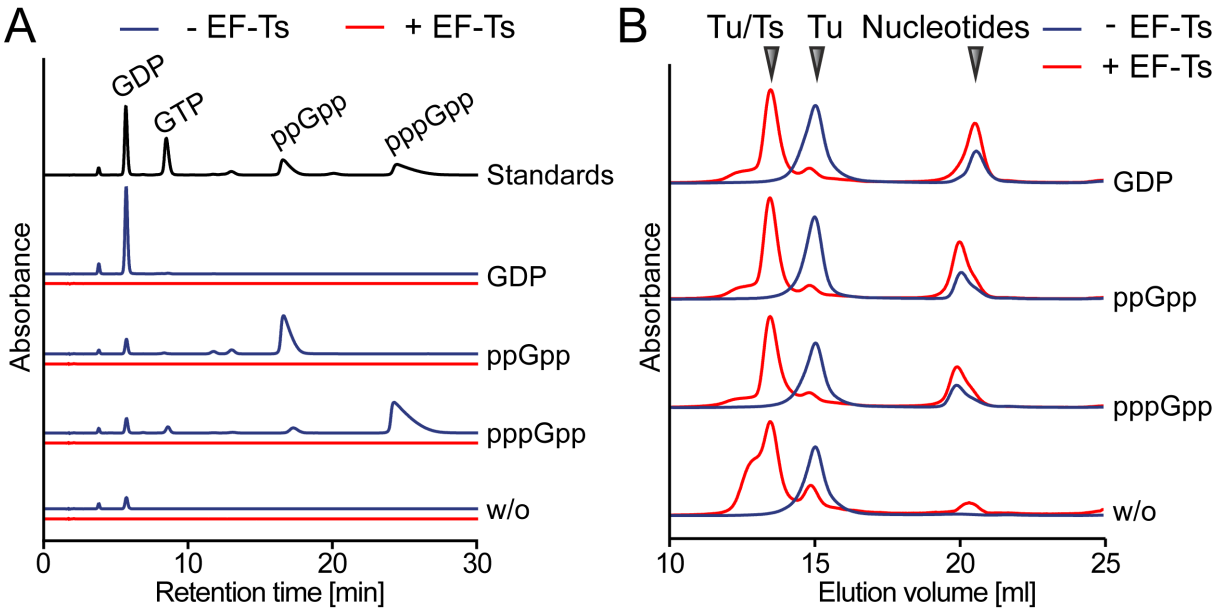

Fig. 5. Removal of (p)ppGpp from EF-Tu by EF-Ts. A. EF-Tu (100 µM) was pre-incubated with nucleotides (1 mM) as indicated either in absence (blue) or presence (red) of EF-Ts (100 µM). Nucleotides bound to EF-Tu were determined by HPLC. **B.** EF-Tu (100 µM) was pre-incubated with nucleotides (200 µM) as indicated either in absence (blue) or presence (red) of EF-Ts (100 µM) and subjected to size-exclusion chromatography. EF-Ts-dependent increase in peak size of free nucleotides indicates nucleotide removal by EF-Ts.

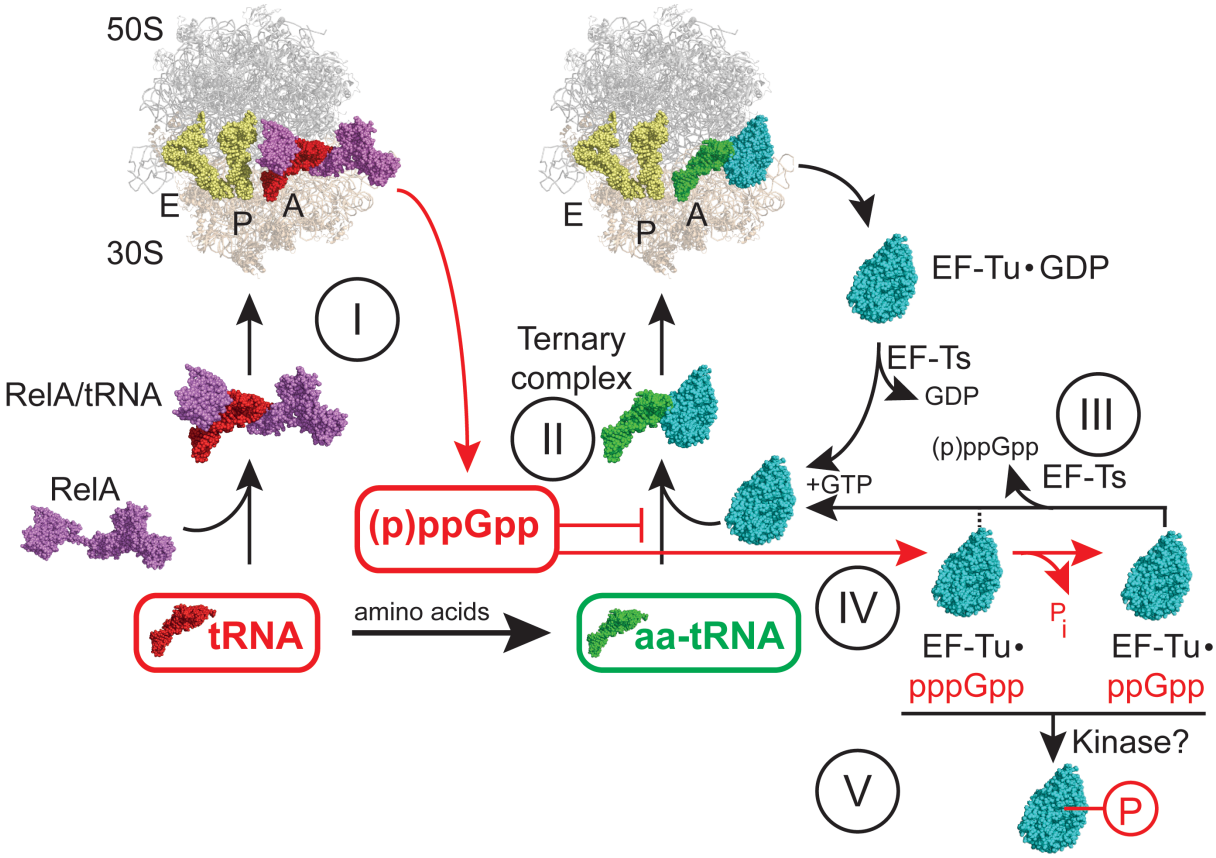

Fig. 6. Framework of (p)ppGpp and EF-Tu. RelA (purple) and EF-Tu (turquoise) interact with uncharged tRNA (red) and aa-tRNA (green), respectively. Both complexes can bind to the A-site of translating ribosomes. The alarmones (p)ppGpp are produced when tRNA/RelA binds to ribosome, and can inhibit formation of the EF-Tu•GTP•aa-tRNA ternary complex through competitive binding into the GTP-binding site of EF-Tu. EF-Tu is able to degrade pppGpp into ppGpp, both of which can be released by EF-Ts. The tRNAs at the P- and E-sites of the ribosome are in yellow. The large (50S) and small (30S) ribosomal units are in grey and ochre, respectively. Further descriptions are given in the discussion.

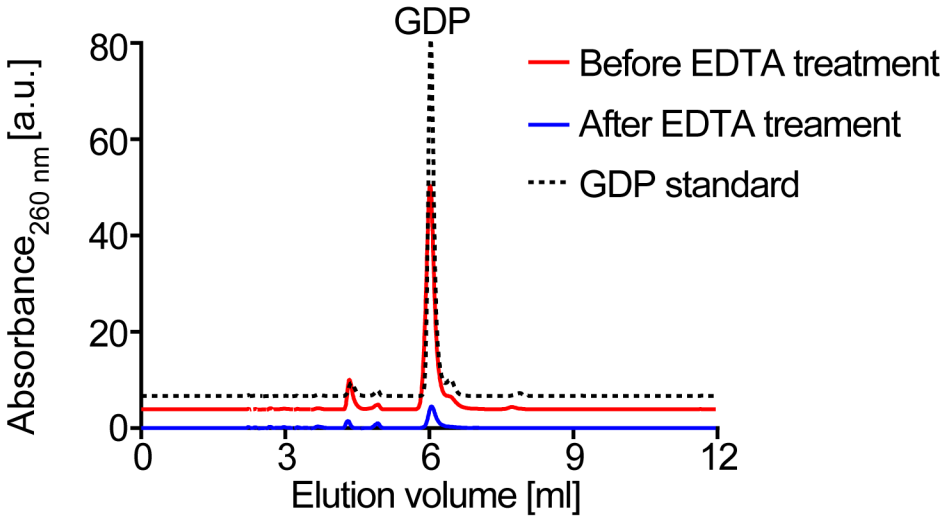

Fig. S1. Removal of GDP during purification of EF-Tu. UV traces of EF-Tu before (red) and after treatment with EDTA (blue). GDP (black) was used as a standard.

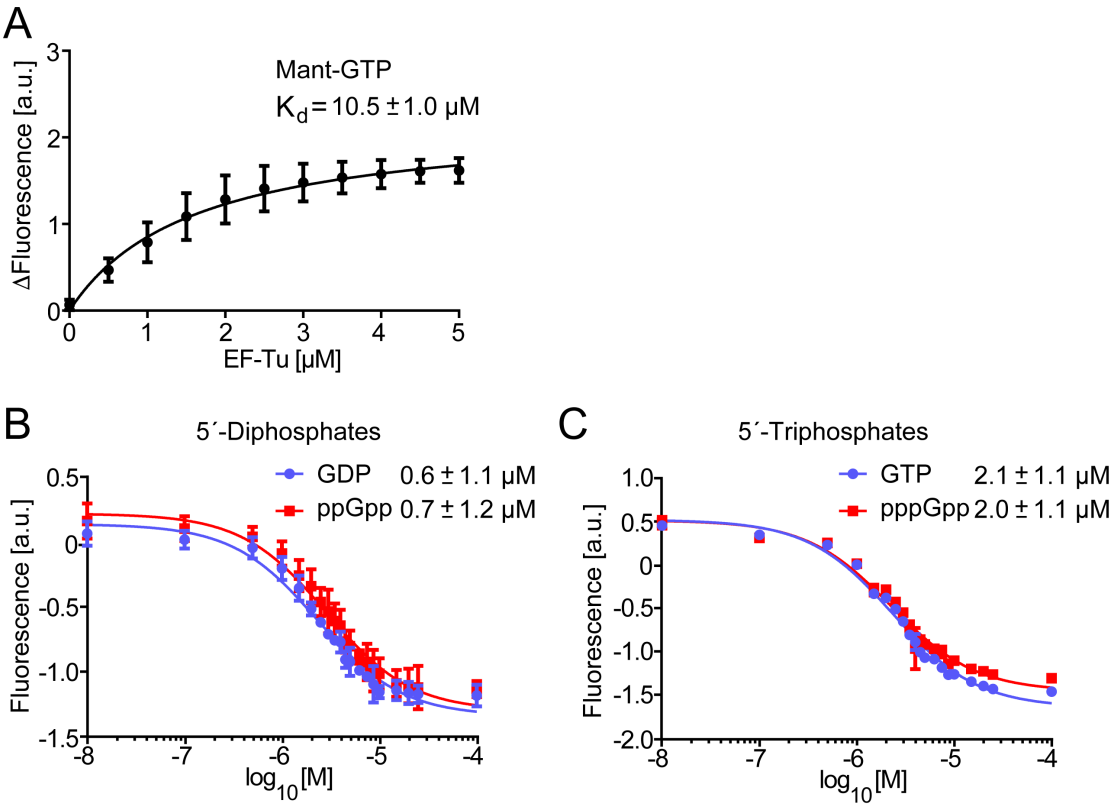

Fig. S2. Binding of (p)ppGpp to *B. subtilis* EF-Tu. A. Binding of Mant-GTP to *B. subtilis* EF-Tu. 1 µM of Mant-GTP was titrated with EF-Tu and the change in Mant-GTP fluorescence quantified. Data represent mean ± SD of n=6 technical replicates. **B-C.** Competition of unlabeled GDP and ppGpp (**B**) and GTP and pppGpp (**C**) for binding to Mant-GTP/EF-Tu. A mixture of 1 µM Mant-GTP and 5 µM EF-Tu was titrated with unlabeled nucleotides. Data represent mean ± SD of n=2 technical replicates.

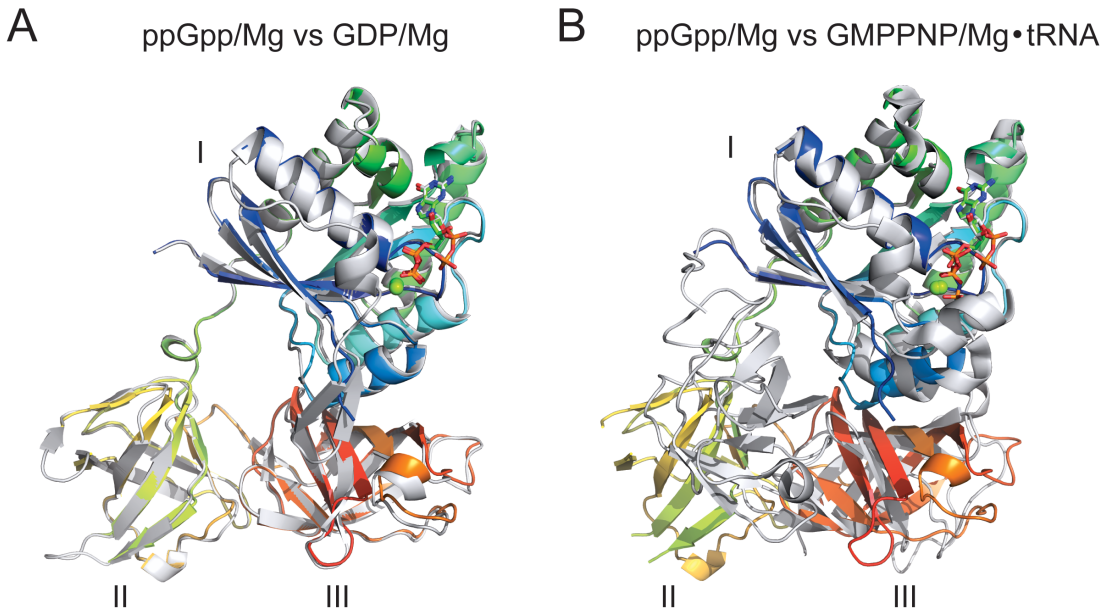

Fig. S3. Superimposition of ppGpp/Mg-bound EF-Tu colored in rainbow from N- to C-terminus with GDP/Mg-bound EF-Tu (**A**, PDB: 1EFC (Song, Parsons et al. 1999)) and EF-Tu bound to GMPPNP/Mg•Phe-tRNA^{Phe} and kirromycin (**B**, PDB: 1OB2). Roman numbers denote the domains I-III of EF-Tu.

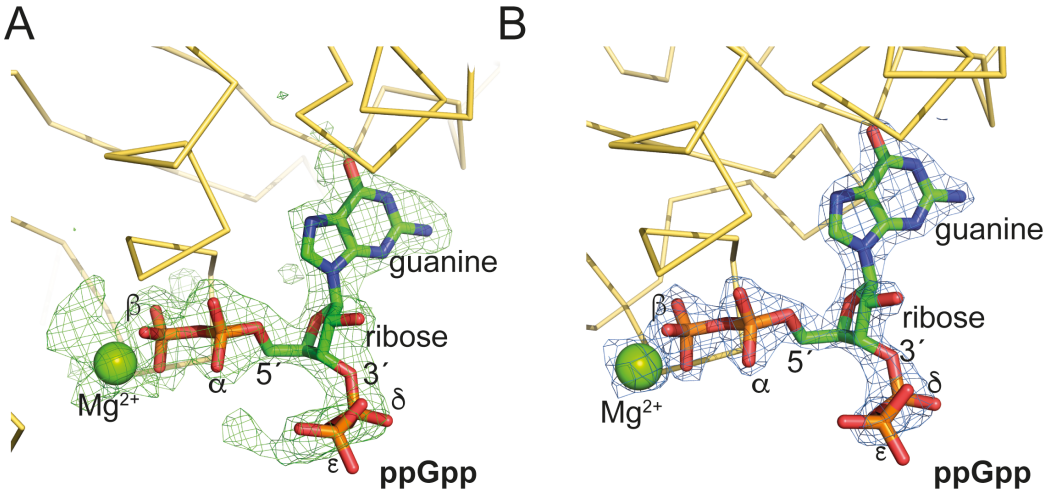

Fig. S4. Electron density for ppGpp/Mg. A. The unbiased F_{obs}–F_{calc} difference electron density of AMPCPP contoured at 2.5 σ is shown as green mesh. Note: The ppGpp molecule (sticks) and magnesium (green sphere) were not present during refinement and are placed only for reasons of illustration. **B.** The $2F_{obs}$–F_{calc} electron density of ppGpp (sticks) and magnesium (green sphere) after final refinement is contoured at 2.5 σ and shown as blue mesh. Yellow ribbons indicate the backbone of EF-Tu. Figures were generated with PyMOL.

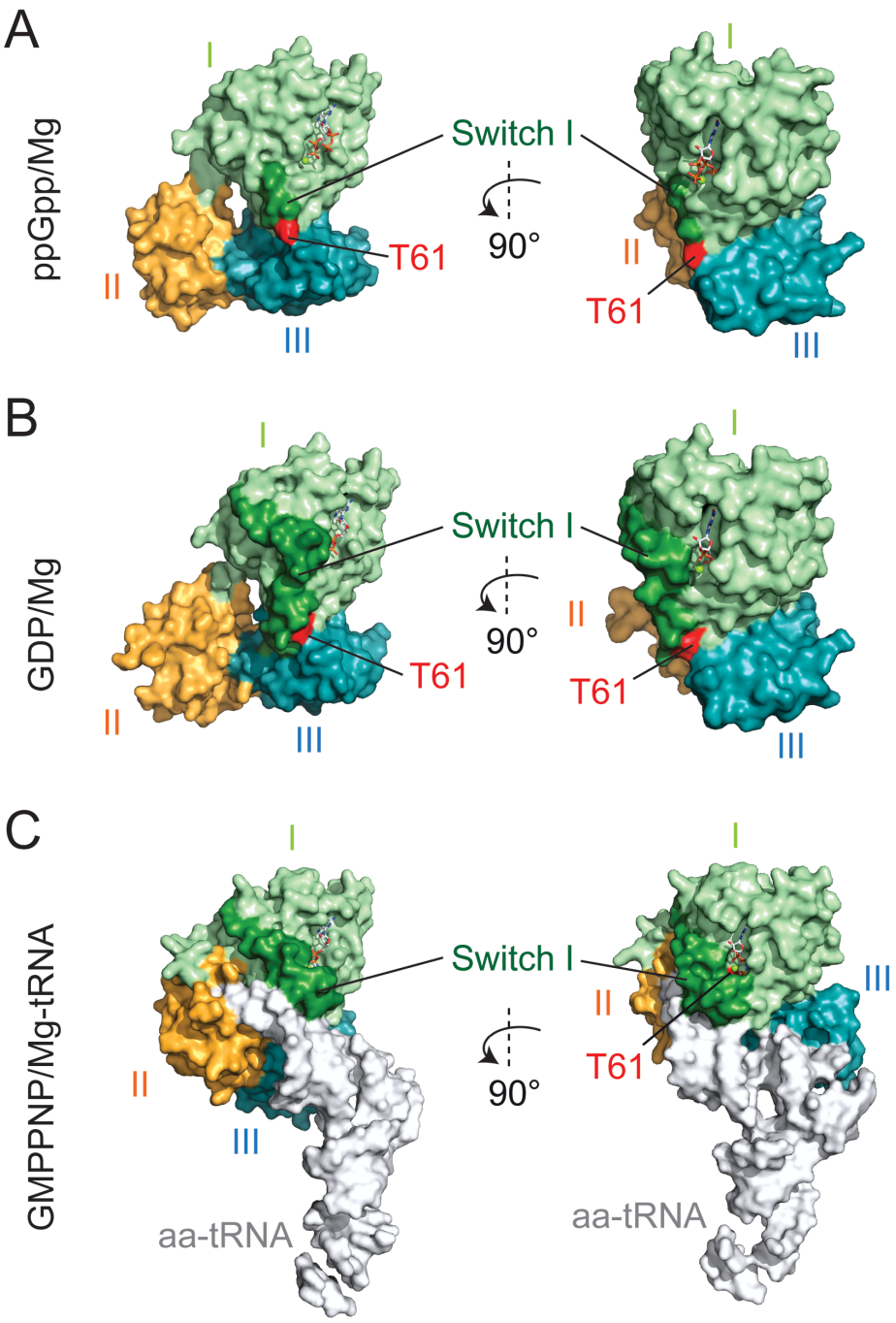

Fig. S5. Accessibility of threonine 61 in different conformational states of EF-Tu. A-C. The crystal structure of *E. coli* EF-Tu in presence of ppGpp (**A**, this study), GDP (**B**, PDB: 1EFC (Song, Parsons et al. 1999)) GMPPNP/Mg/Phe-tRNA^{Phe} (**C**, PDB: 1OB2) is shown in surface representation. Roman numbers denote the domains I-III of EF-Tu colored in pale green (I, residues 1-205), orange (II, residues 206-300), teal (III, residues 300-393). The switch I region, threonine 61 and the tRNA are colored in forest, red and white, respectively.

Table S1. Crystallographic data collection and refinement statistics.

	***E. coli* EF-Tu ppGpp/Mg**
Data collection	
Space group	$P4_32_12$
Cell dimensions	
a, *b*, *c* (Å)	68.991, 68.991, 158.853
a, b, g (°)	90, 90, 90
Wavelength (Å)	1.07234
Resolution (Å)	48.83 - 2.0 (2.052 - 2.0)
R_{merge}	0.1633 (1.733)
$I / \sigma I$	13.17 (1.48)
Completeness (%)	99.99 (100.00)
Redundancy	25.1 (26.0)
CC1/2	0.998 (0.742)
Refinement	
Resolution (Å)	48.83 - 2.0
No. reflections	25416 (1926)
R_{work} / R_{free}	0.2053/0.2624
No. atoms	2981
Protein	2835
Ligand/ion	37
Water	109
B-factors	37.74
Protein	37.84
Ligand/ion	32.92
Water	37.41
R.m.s. deviations	
Bond lengths (Å)	0.007
Bond angles (°)	1.64

*Values in parentheses are for highest-resolution shell.

Table S2. Oligonucleotides.

Primer	Sequence	Purpose
*Ec*EF-Tu_NcoI_F	TTAACCATGGGCTCTAAAGAAAAATTTGAACGTACAAAACCGCACG	Cloning of C-terminal His_6-tagged *E. coli* EF-Tu into pET24d
*Ec*EF-Tu_XhoI_6H_R	TTAACTCGAGTTAGTGGTGATGGTGATGATGGCCCAGAACTTTAGCAACAACGCC	
*Ec*EF-Ts_NdeI_F	TTAACATATGGCTGAAATTACCGCATC	Cloning of N-terminal His_6-tagged *E. coli* EF-Ts into pET16b
*Ec*EF-Ts_BamHI_R	TTAAGGATCCTTAAGACTGCTTGGACATC	
*Bs*EF-Tu_PciI_6H_F	TTAAACATGTCACATCACCATCACCATCACGCTAAAGAAAAATTCGACCGTTCCAAATC	Cloning of N-terminal His_6-tagged *B. subtilis* EF-Tu into pET24d
*Bs*EF-Tu_XhoI_R	TTAACTCGAGTTACTCAGTGATTGTAGAAACAACG	

REFERENCES

1. Gromadski KB, Wieden HJ, & Rodnina MV (2002) Kinetic mechanism of elongation factor Ts-catalyzed nucleotide exchange in elongation factor Tu. *Biochemistry* 41(1):162-169.
2. Burnett BJ*, et al.* (2013) Elongation factor Ts directly facilitates the formation and disassembly of the Escherichia coli elongation factor Tu.GTP.aminoacyl-tRNA ternary complex. *The Journal of biological chemistry* 288(19):13917-13928.
3. Nissen P*, et al.* (1995) Crystal structure of the ternary complex of Phe-tRNAPhe, EF-Tu, and a GTP analog. *Science* 270(5241):1464-1472.
4. Sprang SR (1997) G protein mechanisms: insights from structural analysis. *Annu Rev Biochem* 66:639-678.
5. Knudsen C, Wieden HJ, & Rodnina MV (2001) The importance of structural transitions of the switch II region for the functions of elongation factor Tu on the ribosome. *J Biol Chem* 276(25):22183-22190.
6. Abel K, Yoder MD, Hilgenfeld R, & Jurnak F (1996) An alpha to beta conformational switch in EF-Tu. *Structure* 4(10):1153-1159.
7. Kavaliauskas D, Nissen P, & Knudsen CR (2012) The busiest of all ribosomal assistants: elongation factor Tu. *Biochemistry* 51(13):2642-2651.
8. Louie A & Jurnak F (1985) Kinetic studies of Escherichia coli elongation factor Tu-guanosine 5'-triphosphate-aminoacyl-tRNA complexes. *Biochemistry* 24(23):6433-6439.
9. Steinchen W & Bange G (2016) The magic dance of the alarmones (p)ppGpp. *Molecular microbiology* 101(4):531-544.
10. Hauryliuk V, Atkinson GC, Murakami KS, Tenson T, & Gerdes K (2015) Recent functional insights into the role of (p)ppGpp in bacterial physiology. *Nature reviews. Microbiology* 13(5):298-309.
11. Atkinson GC, Tenson T, & Hauryliuk V (2011) The RelA/SpoT homolog (RSH) superfamily: distribution and functional evolution of ppGpp synthetases and hydrolases across the tree of life. *PloS one* 6(8):e23479.
12. Dalebroux ZD & Swanson MS (2012) ppGpp: magic beyond RNA polymerase. *Nature reviews. Microbiology* 10(3):203-212.
13. Potrykus K & Cashel M (2008) (p)ppGpp: still magical? *Annual review of microbiology* 62:35-51.
14. Rojas AM, Ehrenberg M, Andersson SG, & Kurland CG (1984) ppGpp inhibition of elongation factors Tu, G and Ts during polypeptide synthesis. *Molecular & general genetics : MGG* 197(1):36-45.
15. Mitkevich VA*, et al.* (2010) Thermodynamic characterization of ppGpp binding to EF-G or IF2 and of initiator tRNA binding to free IF2 in the presence of GDP, GTP, or ppGpp. *Journal of molecular biology* 402(5):838-846.
16. Milon P*, et al.* (2006) The nucleotide-binding site of bacterial translation initiation factor 2 (IF2) as a metabolic sensor. *Proceedings of the National Academy of Sciences of the United States of America* 103(38):13962-13967.
17. Miller DL, Cashel M, & Weissbach H (1973) The interaction of guanosine 5'-diphosphate, 2' (3')-diphosphate with the bacterial elongation factor Tu. *Archives of biochemistry and biophysics* 154(2):675-682.
18. Steinchen W*, et al.* (2015) Catalytic mechanism and allosteric regulation of an oligomeric (p)ppGpp synthetase by an alarmone. *Proceedings of the National Academy of Sciences of the United States of America* 112(43):13348-13353.
19. Wieden HJ, Gromadski K, Rodnin D, & Rodnina MV (2002) Mechanism of elongation factor (EF)-Ts-catalyzed nucleotide exchange in EF-Tu. Contribution

of contacts at the guanine base. *The Journal of biological chemistry* 277(8):6032-6036.
20. Dahl LD, Wieden HJ, Rodnina MV, & Knudsen CR (2006) The importance of P-loop and domain movements in EF-Tu for guanine nucleotide exchange. *The Journal of biological chemistry* 281(30):21139-21146.
21. Song H, Parsons MR, Rowsell S, Leonard G, & Phillips SE (1999) Crystal structure of intact elongation factor EF-Tu from Escherichia coli in GDP conformation at 2.05 A resolution. *Journal of molecular biology* 285(3):1245-1256.
22. Burnett BJ*, et al.* (2014) Direct evidence of an elongation factor-Tu/Ts.GTP.Aminoacyl-tRNA quaternary complex. *The Journal of biological chemistry* 289(34):23917-23927.
23. Kushwaha GS, Bange G, & Bhavesh NS (2019) Interaction studies on bacterial stringent response protein RelA with uncharged tRNA provide evidence for its prerequisite complex for ribosome binding. *Curr Genet*.
24. Winther KS, Roghanian M, & Gerdes K (2018) Activation of the Stringent Response by Loading of RelA-tRNA Complexes at the Ribosomal A-Site. *Mol Cell* 70(1):95-105 e104.
25. Wendrich TM, Blaha G, Wilson DN, Marahiel MA, & Nierhaus KH (2002) Dissection of the mechanism for the stringent factor RelA. *Molecular cell* 10(4):779-788.
26. Arenz S*, et al.* (2016) The stringent factor RelA adopts an open conformation on the ribosome to stimulate ppGpp synthesis. *Nucleic acids research* 44(13):6471-6481.
27. Loveland AB*, et al.* (2016) Ribosome*RelA structures reveal the mechanism of stringent response activation. *Elife* 5.
28. Brown A, Fernandez IS, Gordiyenko Y, & Ramakrishnan V (2016) Ribosome-dependent activation of stringent control. *Nature* 534(7606):277-280.
29. Kristensen O, Laurberg M, Liljas A, Kastrup JS, & Gajhede M (2004) Structural characterization of the stringent response related exopolyphosphatase/guanosine pentaphosphate phosphohydrolase protein family. *Biochemistry* 43(28):8894-8900.
30. Pausch P*, et al.* (2018) Structural basis for (p)ppGpp-mediated inhibition of the GTPase RbgA. *The Journal of biological chemistry* 293(51):19699-19709.
31. Lippmann C*, et al.* (1993) Prokaryotic elongation factor Tu is phosphorylated in vivo. *The Journal of biological chemistry* 268(1):601-607.
32. Macek B*, et al.* (2007) The serine/threonine/tyrosine phosphoproteome of the model bacterium Bacillus subtilis. *Molecular & cellular proteomics : MCP* 6(4):697-707.
33. Macek B*, et al.* (2008) Phosphoproteome analysis of E. coli reveals evolutionary conservation of bacterial Ser/Thr/Tyr phosphorylation. *Molecular & cellular proteomics : MCP* 7(2):299-307.
34. Talavera A*, et al.* (2018) Phosphorylation decelerates conformational dynamics in bacterial translation elongation factors. *Science advances* 4(3):eaap9714.
35. Pereira SF, Gonzalez RL, Jr., & Dworkin J (2015) Protein synthesis during cellular quiescence is inhibited by phosphorylation of a translational elongation factor. *Proc Natl Acad Sci U S A* 112(25):E3274-3281.
36. Sajid A*, et al.* (2011) Interaction of Mycobacterium tuberculosis elongation factor Tu with GTP is regulated by phosphorylation. *Journal of bacteriology* 193(19):5347-5358.

37. Kabsch W (2010) Xds. *Acta crystallographica. Section D, Biological crystallography* 66(Pt 2):125-132.
38. Evans PR & Murshudov GN (2013) How good are my data and what is the resolution? *Acta crystallographica. Section D, Biological crystallography* 69(Pt 7):1204-1214.
39. McCoy AJ*, et al.* (2007) Phaser crystallographic software. *Journal of applied crystallography* 40(Pt 4):658-674.
40. Emsley P & Cowtan K (2004) Coot: model-building tools for molecular graphics. *Acta crystallographica. Section D, Biological crystallography* 60(Pt 12 Pt 1):2126-2132.
41. Murshudov GN, Vagin AA, & Dodson EJ (1997) Refinement of macromolecular structures by the maximum-likelihood method. *Acta crystallographica. Section D, Biological crystallography* 53(Pt 3):240-255.
42. Dunkle JA*, et al.* (2011) Structures of the bacterial ribosome in classical and hybrid states of tRNA binding. *Science* 332(6032):981-984.

nature chemical biology

ARTICLES

https://doi.org/10.1038/s41589-020-0578-x

Check for updates

Tetracenomycin X inhibits translation by binding within the ribosomal exit tunnel

Ilya A. Osterman[1,2,11]✉, Maximiliane Wieland[3,11], Tinashe P. Maviza[1,11], Kseniya A. Lashkevich[2], Dmitrii A. Lukianov[1], Ekaterina S. Komarova[1,2], Yuliya V. Zakalyukina[4], Robert Buschauer[5], Dmitrii I. Shiriaev[2], Semen A. Leyn[6,7], Jaime E. Zlamal[6], Mikhail V. Biryukov[4], Dmitry A. Skvortsov[2], Vadim N. Tashlitsky[2], Vladimir I. Polshakov[8], Jingdong Cheng[5], Yury S. Polikanov[9], Alexey A. Bogdanov[2], Andrei L. Osterman[6], Sergey E. Dmitriev[2], Roland Beckmann[5], Olga A. Dontsova[1,2,10], Daniel N. Wilson[3]✉ and Petr V. Sergiev[1,2]✉

The increase in multi-drug resistant pathogenic bacteria is making our current arsenal of clinically used antibiotics obsolete, highlighting the urgent need for new lead compounds with distinct target binding sites to avoid cross-resistance. Here we report that the aromatic polyketide antibiotic tetracenomycin (TcmX) is a potent inhibitor of protein synthesis, and does not induce DNA damage as previously thought. Despite the structural similarity to the well-known translation inhibitor tetracycline, we show that TcmX does not interact with the small ribosomal subunit, but rather binds to the large subunit, within the polypeptide exit tunnel. This previously unappreciated binding site is located adjacent to the macrolide-binding site, where TcmX stacks on the noncanonical basepair formed by U1782 and U2586 of the 23S ribosomal RNA. Although the binding site is distinct from the macrolide antibiotics, our results indicate that like macrolides, TcmX allows translation of short oligopeptides before further translation is blocked.

Aromatic polyketides represent a large and diverse family of natural products synthesized by the nonribosomal type II polyketide synthases[1]. Well-characterized aromatic polyketides include tetracycline (Tet) and the anthracycline doxorubicin (Dox), which despite their structural similarity (Fig. 1a,b) have completely distinct modes of action. Tet binds to the small subunit of the ribosome and inhibits protein synthesis by interfering with the delivery of aminoacyl-transfer RNAs to the A-site[2]. By contrast, Dox intercalates with DNA and thereby inhibits DNA replication and RNA transcription by interfering with topoisomerase II function[3]. While tetracyclines are an important source of clinically used antibiotics[2], anthracyclines, such as Dox, display cytotoxic activity and represent one of the most effective anticancer treatments ever developed[3–5]. Thus, characterization of new aromatic polyketides may result in the discovery of new lead compounds for the development of improved antimicrobial and anticancer agents.

In this context, one of the lesser-characterized families of aromatic polyketides is the tetracenomycins (Tcms). Tcm members contain a tetracyclic naphthacenequinone chromophore (Fig. 1c) and thus have structural similarity to the tetracycline and anthracycline families (Fig. 1a,b). The founding member of the Tcm family is tetracenomycin C (TcmC), which was originally isolated from the soil-actinomycete *Streptomyces glaucescens* and shown to have antimicrobial activity against a variety of *Actinomyces* and *Streptomyces* species[6]. A 12a-*O*-methyl ester of TcmC, termed TcmX, is also produced by *Nocardia mediterranei*[7] and has also been recently identified from the marine-derived actinomycete *Saccharothrix* sp. 10-10 (refs. [8,9]). In addition, *Streptomyces olivaceus* produces Elloramycin, an anthracycline antibiotic closely related to Tcm, but bearing an additional L-rhamnose attached to the tetracyclic chromophore[10].

While tetracenomycins generally display moderate antibacterial activity against some Gram-positive bacteria, these compounds are reported to have some cytotoxic activity against various human cell lines[8–12]. The mechanism of action of tetracenomycins has not been determined, but is assumed to be analogous to the anthracycline Dox[10,11,13]. This assumption is based primarily on the observation that the tetracyclic chromophore of Tcm is flat, resembling Dox, and is therefore optimal for intercalating between the basepairs of DNA. By contrast, the tetracyclic chromophore of Tet is not planar, preventing DNA intercalation. We note also that the original paper reporting the discovery of TcmC demonstrated that TcmC does not inhibit in vitro synthesis of poly(U)-dependent poly(Phe)[6], which may have reinforced the notion that tetracenomycins are not translation inhibitors.

Here we show that tetracenomycins, such as TcmX, do not induce DNA damage as observed for Dox, but rather bind to the ribosome and inhibit protein synthesis. However, unlike the structurally similar compound tetracycline, TcmX does not

[1]Center of Life Sciences, Skolkovo Institute of Science and Technology, Skolkovo, Russia. [2]Department of Chemistry, Faculty of Bioengineering and Bioinformatics and Belozersky Institute of Physico-Chemical Biology, Lomonosov Moscow State University, Moscow, Russia. [3]Institute for Biochemistry and Molecular Biology, University of Hamburg, Hamburg, Germany. [4]Department of Soil Science and Department of Biology, Lomonosov Moscow State University, Moscow, Russia. [5]Gene Center, Department of Biochemistry, University of Munich, Munich, Germany. [6]Infectious and Inflammatory Disease Center, Sanford Burnham Prebys Medical Discovery Institute, La Jolla, CA, USA. [7]A.A. Kharkevich Institute for Information Transmission Problems, Russian Academy of Sciences, Moscow, Russia. [8]Center for Magnetic Tomography and Spectroscopy, Faculty of Fundamental Medicine, Lomonosov Moscow State University, Moscow, Russia. [9]Department of Biological Sciences, University of Illinois at Chicago, Chicago, IL, USA. [10]Shemyakin-Ovchinnikov Institute of Bioorganic Chemistry, Russian Academy of Sciences, Moscow, Russia. [11]These authors contributed equally: Ilya A. Osterman, Maximiliane Wieland, Tinashe P. Maviza. ✉e-mail: i.osterman@skoltech.ru; Daniel.Wilson@chemie.uni-hamburg.de; petya@genebee.msu.su

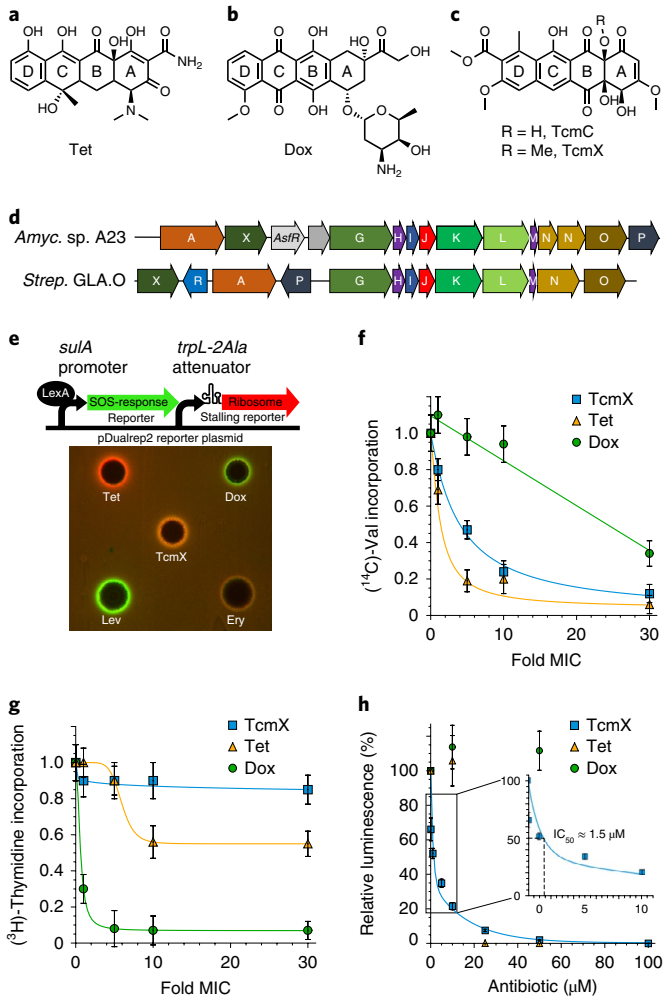

Fig. 1 | TcmX inhibits protein synthesis and not DNA metabolism. **a**–**c**, Chemical structures of Tet (**a**), Dox (**b**) and TcmC and TcmX (**c**). **d**, Chromosomal arrangement of the tetracenomycin biosynthesis gene cluster in *Amycolatopsis* sp. A23 and *S. glaucescens* GLA.O (see also Supplementary Tables 2–4). Orthologous genes are shown with matching colors and letters. **e**, The induction of a two-color dual-reporter system sensitive to inhibitors of ribosome progression or of DNA replication. Spots of Tet (0.5 μg), Dox (2 μg), erythromycin (Ery, 2 μg), levofloxacin (Lev, 0.05 μg) and TcmX (2 μg) were placed on the surface of an agar plate containing *E. coli* Δ*tolC* cells transformed with the pDualrep2 plasmid. Induction of the expression of Katushka2S (red) is triggered by translation inhibitors, whereas RFP expression (green) is induced on DNA damage. **f**, Relative inhibition of protein synthesis with [^{14}C]-valine incorporation used for detection protein synthesis. TcmX, Dox and Tet were added in accordance with their MIC (1–30-fold MIC; MIC, TcmX 2 μg ml^{-1}, Dox 1.3 μg ml^{-1} and Tet 0.3 μg ml^{-1}). **g**, Relative inhibition of DNA metabolism by TcmX, Dox or Tet determined by macromolecular synthesis inhibition via [^{3}H]-thymidine incorporation (with concentrations the same as in **f**). **h**, Protein synthesis inhibition with increasing concentrations of TcmX (blue), Tet (yellow) and Dox (green) using an in vitro cell-free translation system. In **f**–**h**, the error bars represent the s.e.m. for three independent experiments.

bind to the small ribosomal subunit, but rather to the large subunit. Cryo-electron microscopy (cryo-EM) structures reveal that TcmX binds to a unique site inside the polypeptide exit tunnel of both bacterial (*Escherichia coli*) and mammalian (human) ribosomes. In this binding site, TcmX appears to inhibit translation by preventing the prolongation of the nascent polypeptide chain, analogous to the macrolide class of antibiotics. Our biochemical and structural insights into TcmX interaction with the ribosome pave the way for the development of tetracenomycins as antibacterial and/or anticancer agents.

Results

Identification of TcmX from *Amycolatopsis* sp. A23. In an ongoing high-throughput screen of synthetic and natural products[14], we have identified the presence of a translation inhibitor in the culture media of the unclassified *Amycolatopsis* sp. A23. The active compound was purified and analyzed using ultraviolet (UV) and mass spectrometry, as well as nuclear magnetic resonance (NMR) spectroscopy (Supplementary Notes 1–3). The UV spectrum, molecular weight (486 Da) (Supplementary Note 1) and NMR data (Supplementary Notes 2 and 3 and Supplementary Table 1) indicate that the active compound is identical to TcmX. To validate that TcmX is indeed produced by the *Amycolatopsis* sp. A23, we sequenced the complete genome and identified the presence of the gene cluster for TcmX biosynthesis, which is similar to the previously identified TcmC cluster present in the genome of *S. glaucescens*[15] (Fig. 1d). Bioinformatic analysis indicates that similar gene clusters are found in *S. caatingaensis*, *A. rifamycinica* and *A. balhimycina* strains (Supplementary Table 2), suggesting that these species also produce a Tcm compound. Our bioinformatic analysis also identified a second smaller paralogous gene cluster in *Amycolatopsis* sp. A23, which we also identify in *S. glaucescens* GLA.O as well as a number of other *Streptomyces* and *Amycolatopsis* species that do not contain the Tcm gene cluster (Supplementary Tables 2–4). Collectively, our biochemical and bioinformatic findings suggest that the active compound produced by *Amycolatopsis* sp. A23 is TcmX.

TcmX inhibits protein synthesis and not DNA metabolism. Because tetracenomycins are assumed to intercalate with DNA and interfere with DNA metabolism[10,11,13], as described for the anthracyclines such as Dox[3], we were surprised to identify TcmX in a high-throughput screen designed to specifically detect protein synthesis inhibitors. To reassess the mode of action of TcmX, we employed an in vivo dual-reporter assay that is designed to distinguish between compounds that inhibit translation and/or induce DNA damage[14,16] (Fig. 1e). The basis for the reporter is that compounds inhibiting translation induce ribosome stalling within a modified tryptophan operon leader sequence (*trpL-2Ala*), which in turn induces expression of the downstream Katushka2S (far-red fluorescent) protein, shown in red. By contrast, compounds that induce DNA damage evoke the SOS response and derepress the LexA-repressed *sulA* promoter, thereby leading to the expression of red fluorescent protein (RFP) (shown in green pseudo-color). TcmX, along with the known translation inhibitors Tet and the macrolide erythromycin (Ery) as well as the DNA replication inhibitors Dox and levofloxacin (Lev) were spotted onto agar plates where the growth and fluorescence of the *E. coli* strain JW5503Δ*tolC* strain bearing the pDualrep2 reporter plasmid were monitored (Fig. 1e). Unlike Dox and Lev, but similar to Tet and Ery, TcmX led to the appearance of red fluorescence induced by expression of Katushka2S and not of the pseudo-green fluorescence due to RFP expression (Fig. 1e), thus indicating that TcmX indeed inhibits protein synthesis and does not induce DNA damage. To substantiate the results from the dual-reporter assay, we also monitored the incorporation of radiolabeled [^{14}C]-valine into proteins as well as [^{3}H]-thymidine incorporation into DNA during growth of the *E. coli*, in the presence of increasing concentrations of TcmX, Tet or Dox (Fig. 1f,g). The results demonstrated that at concentrations tenfold higher than the minimal inhibitory concentration (MIC), both TcmX and Tet led to a dramatic (80%) reduction in protein synthesis, whereas at the same fold-concentration Dox had little effect (Fig. 1f). By contrast, Dox was an excellent inhibitor of DNA synthesis,

yielding near complete inhibition of [^{3}H]-thymidine incorporation into DNA at fivefold MIC, whereas TcmX had little to no effect on [^{3}H]-thymidine incorporation, even at 30-fold MIC (Fig. 1g). We observed an inhibitory effect (50%) of Tet on thymidine incorporation but only at 10× MIC, which is likely to be indirect and due to alteration of membrane integrity as previously reported[17]. We think it is unlikely that Tet directly effects DNA replication by DNA intercalation since we observe no SOS response in our reporter system with Tet (Fig. 1e). To directly assess the ability of TcmX to inhibit protein synthesis, we also employed an in vitro cell-free translation system to investigate the influence of increasing concentrations of TcmX on the expression of firefly luciferase (Fluc) by monitoring Fluc luminescence (Fig. 1h). Consistent with our in vivo results, we found that TcmX (and Tet) was an efficient inhibitor of protein synthesis, blocking production of Fluc with a half-maximal inhibitory concentration (IC_{50}) of 1.5 µM, whereas Dox had no effect, even at 40 µM (Fig. 1h). Collectively, our results suggest that TcmX, like Tet, is a potent inhibitor of protein synthesis, and unlike Dox, does not intercalate with DNA to induce DNA damage, as previously assumed[10,11,13]. Superimposing TcmX onto the Dox-DNA complex structure[18] on the basis of the tetracyclic chromophores reveals severe clashes with the methoxy groups of ring A of TcmX with the DNA base (Extended Data Fig. 1a–c), consistent with our findings that TcmX does not intercalate with DNA. Based on the structural similarity of TcmX with other tetracenomycins, such as TcmC and elloramycins, we would expect that generally tetracenomycins cannot intercalate with DNA.

Ribosomal mutations conferring TcmX resistance. To ascertain whether TcmX inhibits translation by targeting the ribosome, we employed an *E. coli* SQ110DTC strain to select for TcmX resistance mutations. Unlike wild-type *E. coli* strains that contain seven rRNA operons, the *E. coli* SQ110DTC strain contains only a single rRNA operon (*rrlE*), thus making selection of antibiotic resistance via rRNA mutations much easier[19]. Additionally, the DTC (delta TolC/Δ*tolC*) strain lacks the outer membrane component TolC of efflux pumps that allows lower antibiotic (TcmX) concentrations to be used during the selection procedure, as evident from the 32-fold decrease (>64 to 2 µg ml^{-1}) in MIC for TcmX (Table 1). The selection procedure yielded several strains exhibiting MICs that were 8–16-fold higher than the wild-type strain (Table 1). The MIC increase of these strains was specific for TcmX since no increase in MIC was observed for Ery in comparison with the wild-type strain (Table 1). Sequencing of the entire rRNA operon of the TcmX resistant strains revealed single nucleotide substitutions U2586A, U2586G or U2609G in the 23S rRNA (Table 1). To validate that these nucleotide positions were responsible for the TcmX resistance phenotype, we generated all three possible base substitutions at these positions in the *rrnB* operon located on plasmid pAM552. The plasmids were then introduced into the SQ171DTC strain lacking all seven rRNA operons, so that the plasmid-borne mutated *rrnB* operons served as the sole source of ribosomes following loss of the wild-type rRNA containing pCSacB plasmid. As expected, the presence of U2586G, U2586A or U2609G mutations in the *rrnB* operon led to an 8–16-fold increase in MIC (Table 1), consistent with the spontaneously selected strains. In addition, we could demonstrate that the U2586C mutation also resulted in an eightfold MIC increase (Table 1). Although increased resistance was also observed for the U2609A and U2609C substitutions, the MIC fold-increases were less dramatic (2–4-fold). As controls, A2058G and A2059G substitutions conferred high level Ery resistance (>64-fold), as shown previously[20], but had no effect on the TcmX MIC (Table 1). On the basis of these results, we conclude that TcmX interacts with the large ribosomal subunit, which is distinct from the binding site of the related antibiotic Tet on the small subunit. Superimposing TcmX onto the Tet-70S complexes[2,21] on the basis of the tetracyclic chromophores (Extended Data Fig. 1d,e) supports our finding that TcmX cannot bind similarly to Tet since TcmX would fail to establish a number of interactions that Tet forms with the 16S rRNA (Extended Data Fig. 2) and would additionally result in clashes between TcmX and nucleotides (G1054, U1196 and G1197) of the 16S rRNA (Extended Data Fig. 1e,f).

Table 1 | TcmX MICs in different strains and rRNA resistance mutants

E. coli strain	MIC TcmX µg ml^{-1}	MIC Ery µg ml^{-1}
BW25113	>64	>64
BW25113 Δ*tolC*	2	2
SQ110DTC WT	1	2
SQ110DTC U2586G	16	2
SQ110DTC U2586A	16	2
SQ110DTC U2609G	8	2
SQ171DTC WT	1	2
SQ171DTC U2586G[a]	16	2
SQ171DTC U2586A[a]	16	2
SQ171DTC U2586C[a]	8	2
SQ171DTC U1782C[b]	16	2
SQ171DTC U2609G[a]	8	2
SQ171DTC U2609A[a]	4	2
SQ171DTC U2609C[a]	2	2
SQ171DTC A2059G[a]	1	>64
SQ171DTC A2058G[a]	1	>64
SQ171DTC U1782C/U2586C[b]	4	2

[a]Plasmid with mutated rRNA operon on the basis of pLK35. [b]Plasmid with mutated rRNA operon on the basis of pAM552.

TcmX binds to the *E. coli* large ribosomal subunit. To determine the binding site of TcmX on the bacterial ribosome, we incubated TcmX with *E. coli* 70S ribosomes (Eco70S) and analyzed the resulting complex using cryo-EM. After sorting and refinement (Extended Data Fig. 3a), the final cryo-EM map of the TcmX-Eco70S complex had an average resolution of 2.9 Å (Extended Data Fig. 3b), with local resolutions extending toward 2.75 Å inside the core of the large subunit (Extended Data Fig. 3c,d and Supplementary Table 5). Examination of the cryo-EM map revealed a single additional density present within the polypeptide exit tunnel of the large subunit (Fig. 2a) consistent with the chemical structure of TcmX (Extended Data Fig. 3e–g). Within the binding site, the planar rings C and D of the tetracyclic chromophore of TcmX stack on the bases of 23S rRNA nucleotides U1782 and U2586, which form a noncanonical U–U basepair with each other (Fig. 2b and Extended Data Fig. 2). Due to space restrictions, we predict that the U2586A and U2586G substitutions would break the basepair (Extended Data Fig. 4) and result in nonplanar conformations that would prevent TcmX binding, consistent with the TcmX resistance observed by these mutations (Table 1). Nevertheless, we cannot exclude that the mutated bases can shift to accommodate base-pairing and that TcmX binding is therefore destabilized for another reason. We note that both the U2586C and U1782C substitutions also led to high level (8–16-fold MIC increase) TcmX resistance (Table 1). Since a shift in one of the bases is necessary to maintain nonisosteric C–U or U–C basepairs, we expect that these mutations also result in nonplanar conformations that prevent TcmX binding. By contrast, we observed that U2609G/A/C mutations confer moderate levels of TcmX resistance

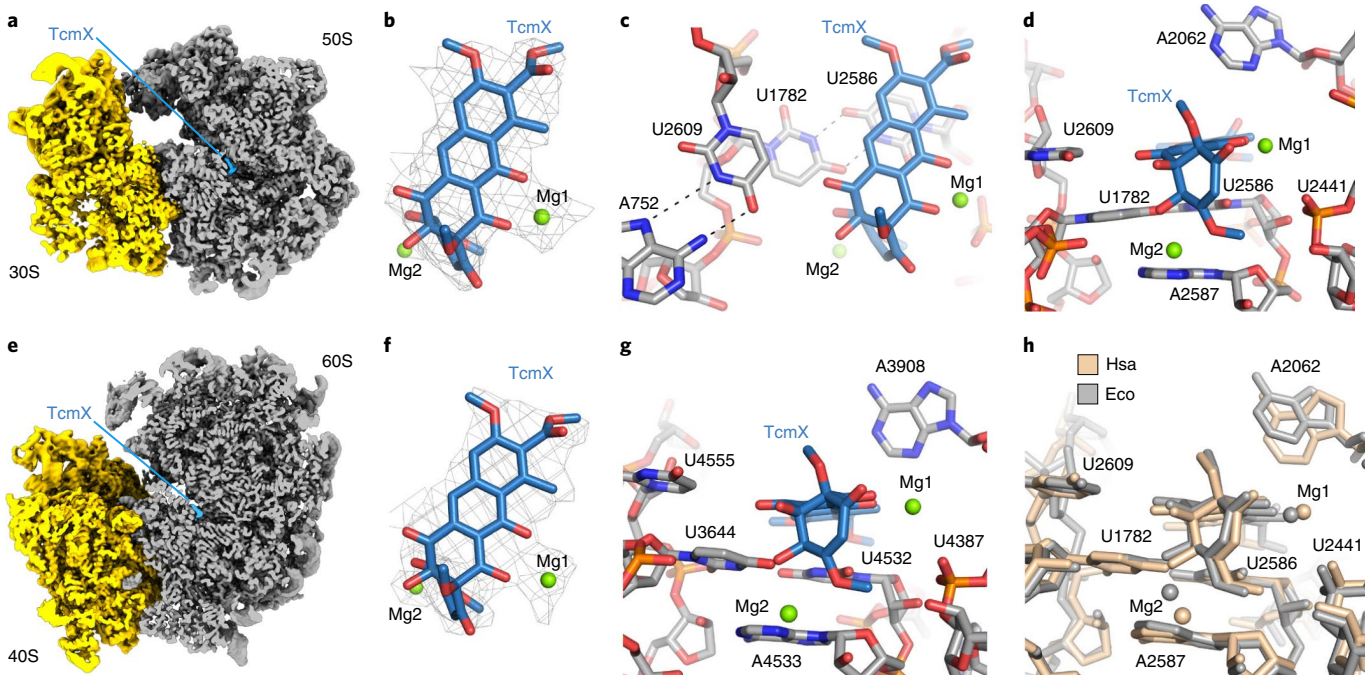

Fig. 2 | Binding site of TcmX on the bacterial and human ribosomes. a, Transverse section of the cryo-EM map of the 70S ribosome (30S, yellow; 50S, gray) showing the TcmX (blue) binding site within the large subunit. **b**, Electron density for TcmX with putative Mg ions (green). **c**,**d**, TcmX interactions on the *E. coli* ribosome. **e**, Transverse section of the cryo-EM map of the human 80S ribosome (40S, yellow; 60S, gray) with TcmX (blue). **f**, Electron density for TcmX, Mg1 and Mg2 on the human 80S ribosome. **g**, Interaction of TcmX with the human 80S ribosome. **h**, Comparison of TcmX binding site on *E. coli* (Eco, gray) and *H. sapiens* (Hsa, wheat) aligned on the basis of the large subunit rRNA nucleotides, *E. coli* numbering is used.

(Table 1), despite the fact that TcmX does not interact with U2609 (Fig. 2c,d). Since U2609 basepairs with A752 (Fig. 2c), one possible explanation for TcmX resistance in these cases is that the U2609 mutations disrupt base-pairing with A752 (Extended Data Fig. 4), which could in turn lead to a conformation that encroach on the TcmX binding site. Aside from the stacking interactions, most of the other TcmX-ribosome contacts are mediated via two ions, which we assume are magnesium (Mg) ions based on the presence and similarity of coordinated Mg ions in the tetracycline-ribosome structure[21,22]. Mg1 and Mg2 coordinate interaction of TcmX with the phosphate-oxygen backbone of U2441, and the ribose and nucleobase of A2587, respectively (Fig. 2b–d and Extended Data Fig. 2). Although A2062 comes into close proximity of TcmX, the density for this base is poorly resolved (Extended Data Fig. 3g), suggesting that it does not establish a stable interaction. Since the only difference between TcmX and TcmC is the 12a-*O*-methyl group (Fig. 1c), which does not establish interactions with the ribosome (Extended Data Fig. 2), we predict that TcmC would bind in an identical fashion to the ribosome as TcmX. Similarly, molecular modeling suggests that the elloramycins can also be accommodated at the TcmX binding site, despite the presence of the 2,3,4-tri-*O*-methyl-L-rhamnose moiety, which is absent in TcmX (Extended Data Fig. 1g,h).

Conservation of the TcmX binding site on the ribosome. Since the stacking interaction between TcmX and the U1782–U2586 basepair within the 23S rRNA appears to be a chief determinant for TcmX binding, we investigated the extent to which these two nucleotides are conserved across different organisms. Based on available data from the comparative RNA web (CRW) site[23], 37% of bacteria (236 sequences) contain a U–U basepair at the equivalent position, similar to that of *E. coli*. In addition to *E. coli*, this includes *Streptomyces* species that are reported to be susceptible to tetracenomycins[6,8], as well as many clinically important pathogens, such as *Neisseria gonorrhoeae*, *Pseudomonas aeruginosa*, *Vibrio cholerae* and *Yersinia pestis* (Extended Data Fig. 4k). Most (63%) bacteria contain the C–C basepair at the equivalent position, which is observed, for example, in the crystal structures of *Thermus thermophilus* 70S ribosomes[21]. Since our initial attempts to determine the crystal structure of TcmX in complex with the *T. thermophilus* 70S ribosome failed, this led us to wonder whether the C–C basepair confers resistance to TcmX. To investigate this, we generated a U1782C–U2586C disubstituted *rrnB* SQ171DTC strain and analyzed the MIC in the presence of TcmX and Ery. As expected, the double mutation did not influence the MIC for Ery, whereas a fourfold increase in MIC was observed for TcmX (Table 1). This finding suggests that the ribosomes from bacteria containing C–C basepair at the equivalent position to the *E. coli* U1782–U2586 basepair are naturally more resistant to TcmX than bacteria containing the U–U basepair. The CRW site[23] also revealed that in contrast to bacteria, this U–U basepair appears to be universally conserved in eukaryotic ribosomes (135 sequences), suggesting that TcmX may also bind analogously to human 80S ribosome, which may be the cause of the observed cytotoxicity[8–12].

TcmX binds to the large subunit of the human ribosome. To determine the binding site of TcmX on the human ribosome, we incubated TcmX with *H. sapiens* 80S ribosomes and analyzed the resulting complex using cryo-EM. After sorting and refinement (Extended Data Fig. 5a), the final cryo-EM map of the TcmX-Hsa80S complex had an average resolution of 2.8 Å (Extended Data Fig. 5b), with local resolutions extending toward 2.5 Å within the core of the large subunit (Extended Data Fig. 5c,d). Examination of the cryo-EM map revealed a single additional density for TcmX located within the polypeptide exit tunnel of the large subunit (Fig. 2e,f and Extended Data Fig. 5d) at the equivalent site observed in the TcmX-Eco70S ribosome structure (Extended Data Fig. 5e,f). On the human 80S ribosome, TcmX stacks on nucleotides U3644

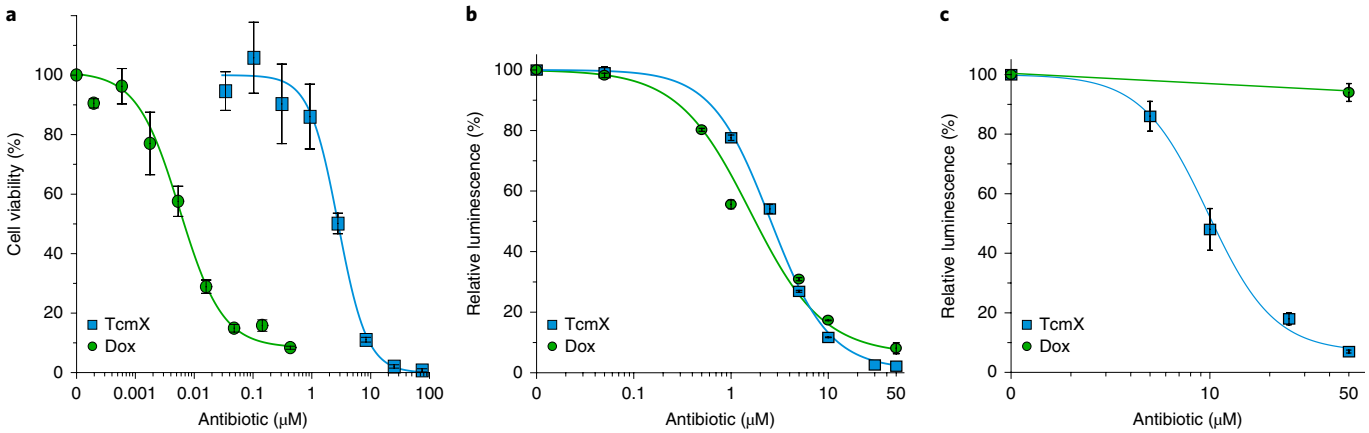

Fig. 3 | Cytotoxicity and inhibition of eukaryotic translation by TcmX. a, Cell viability of HEK293T cells in presence of increasing concentrations of doxorubicin (Dox, green) or tetracenomycin X (TcmX, blue). Dox exhibits cytotoxic effect at extremely low concentrations with a CC_{50} < 10 nM, while the effect of TcmX becomes apparent at much higher concentrations with a CC_{50} of 2 μM. **b**, In vivo translation of Fluc messenger RNA in HEK293T cells in presence of increasing concentrations of TcmX (blue) and Dox (green). TcmX IC_{50} = 2.5 μM; Dox IC_{50} = 1.5 μM. **c**, In vitro translation of Fluc mRNA in HEK293T whole-cell lysate in the presence of increasing concentrations of TcmX (blue) and Dox (green). TcmX IC_{50} = 10 μM; Dox IC_{50} > 50 μM. In all experiments, the error bars represent the s.e.m. for three independent experiments.

(EcU1782) and U4532 (EcU2586), which also form a noncanonical U–U basepair (Fig. 2g), analogous to that observed in the TcmX-Eco70S structure. A similar network of interactions via two coordinated (putative) Mg ions is observed between TcmX and 28S rRNA nucleotides U4387 (EcU2441) and A4533 (EcA2587), respectively. A3908 (EcA2062) is better resolved in the TcmX-Hsa80S structure, where the N3 appears to contribute to the coordination of Mg1 (Fig. 2g and Extended Data Fig. 5d). Overall, the binding site and interactions of TcmX on the *E. coli* 70S and *H. sapiens* 80S ribosome are very similar with a root mean square deviation (r.m.s.d.) of <1 Å. We note that the binding site of TcmX on the human 80S ribosome is in close proximity to one of the putative binding sites of Tet analogs on the large subunit (Extended Data Fig. 5e,f), as determined by crosslinking[24], although we note that none of the cross-linked nucleotides are directly involved in establishing interactions with TcmX (Extended Data Fig. 5e,f).

TcmX inhibits translation on the human ribosome. Since the cryo-EM structure of the TcmX-80S complex used human ribosomes from human embryonic kidney 293T (HEK293T) cells, we were first interested in assessing whether TcmX also displays cytotoxicity against these cells, as reported for other human cell lines, such as HepG2, MCF-7 and K562 (refs. [8–12]). As seen in Fig. 3a, increasing concentrations of TcmX led to a complete loss in HEK293T cell viability, with a calculated cytotoxicity concentration that inhibits 50% viability (CC_{50}) of 2.5 μM, similar to that (5.4–10.9 μM) reported previously against the other human cell lines[8–12]. By comparison, Dox exhibited a much higher cytotoxic activity against HEK293T cells, with an CC_{50} of 0.006 μM (6 nM), which was more than two orders of magnitude lower than for TcmX. Having established that TcmX exhibits cytotoxicity against HEK293T cells, we were interested in assessing whether TcmX can inhibit translation in vivo (Fig. 3b) and in vitro (Fig. 3c). To test the inhibition of translation in vivo, we transfected HEK293T cells with a Fluc reporter construct and monitored Fluc luminescence[25] in the presence of increasing concentrations of TcmX, as well as the control Dox (Fig. 3b). TcmX inhibited Fluc luminescence with an IC_{50} of 2.5 μM (Fig. 3b), comparable with the CC_{50} observed for cytotoxicity, which was also 2.5 μM (Fig. 3a). The identical CC_{50} and IC_{50} values suggested to us that the cytotoxicity caused by TcmX on HEK293T cells is probably due to a direct inhibition of translation. By contrast, Dox inhibited Fluc luminescence with an IC_{50} (of 1.5 μM), which was 250-fold higher than the CC_{50} observed for cytotoxicity (Fig. 3a) and thus likely reflects an indirect effect of Dox on translation, presumably via inhibition of DNA replication and transcription in cells. To confirm that TcmX can directly inhibit translation on human 80S ribosomes, we prepared whole-cell extracts from cultured HEK293T cells and monitored in vitro translation of Fluc[26] in the presence of increasing concentrations of TcmX (Fig. 3c). Using this in vitro translation system, TcmX exhibited a dose-dependent inhibition of Fluc translation with an IC_{50} of 10 μM, which is in a similar range to that observed for cytotoxicity and in vivo translation inhibition. Nevertheless, we cannot completely exclude the possibility that TcmX also has another target within the mammalian cell, which could account for the slight differences in IC_{50} values in vitro and in vivo. Unlike TcmX, Dox did not inhibit in vitro translation of Fluc, even at the highest concentration (50 μM) tested (Fig. 3c).

TcmX inhibits translation elongation. To ascertain the mechanism of action of TcmX during translation, we performed toeprinting assays to monitor the position of the ribosome on the *trpL-2Ala* mRNA using reverse transcription (Fig. 4a). The reactions were performed in the absence of antibiotics as well as presence of TcmX and control antibiotics Ery, Tet and thiostrepton (Ths). As expected, multiple bands were observed in the absence of antibiotic, corresponding to translating ribosomes spread over the entire open reading frame (ORF). By contrast, the addition of Ths led to a loss of the bands within the ORF and the appearance of a strong band corresponding to ribosomes that initiated on the AUG start codon, but could not progress into the elongation phase, as observed previously[22,27]. Similarly, in the presence of Tet, most ribosomes also became trapped at the start codon; however, some translation of the downstream ORF was evident. By contrast, in the presence of Ery, the majority of ribosomes translated the first seven codons of the mRNA, but then became stuck with the seventh (Leu, L) codon located in the P-site and the eighth codon (Lys, K) in the A-site. This is consistent with mode of inhibition of macrolides, such as Ery, to permit synthesis of short oligopeptides, but to prevent further prolongation of the nascent polypeptide chain by occluding the ribosomal tunnel[28]. The toeprinting results in the presence of TcmX resemble closely those observed for Ery, suggesting that TcmX has a similar mechanism of action, allowing synthesis of short oligopeptides before preventing further translation elongation. We also

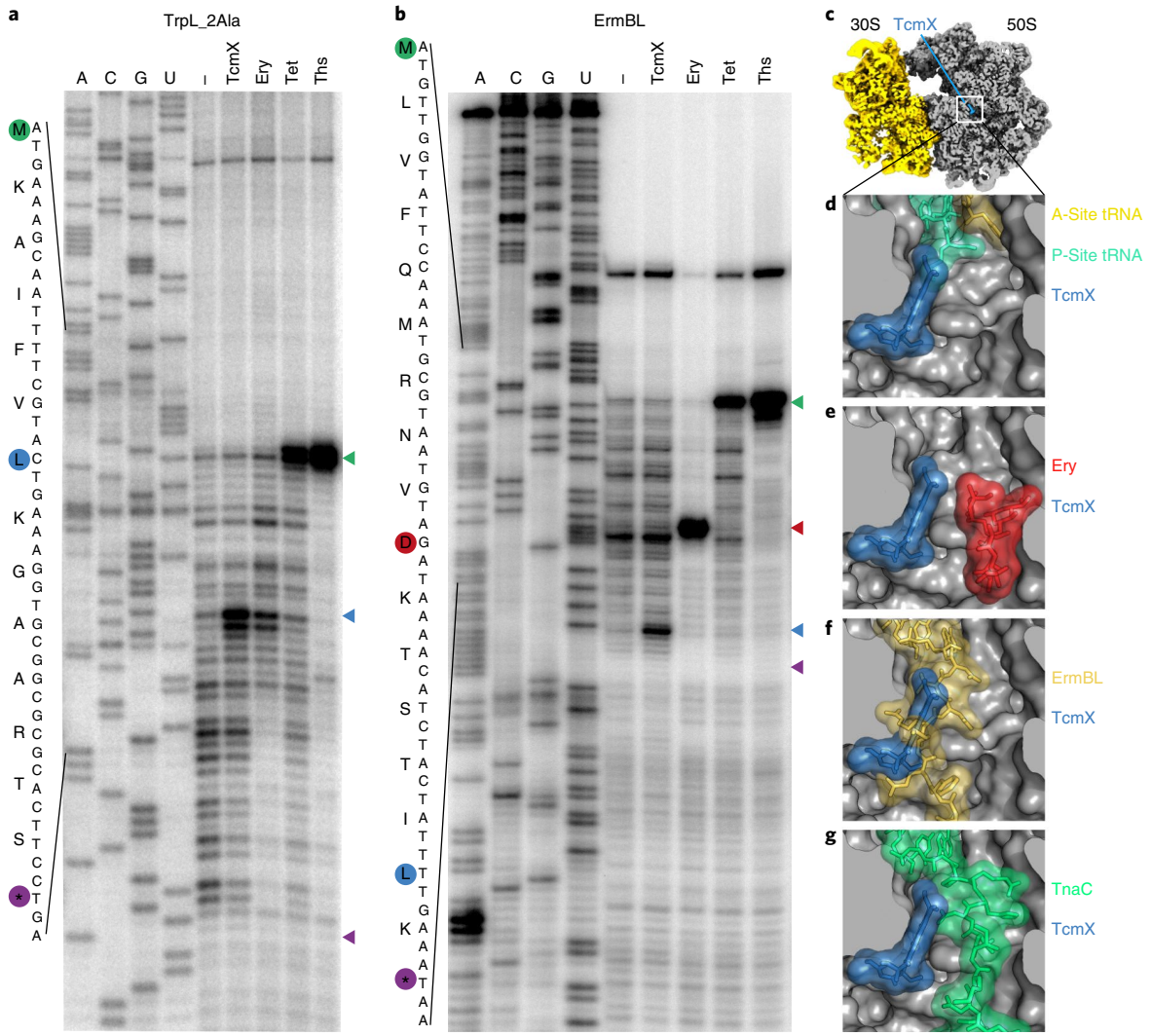

Fig. 4 | TcmX inhibits translation elongation in a template-dependent fashion. a,**b**, Toeprinting assay of TrpL-2Ala (**a**) and ErmBL template (**b**) in the presence or absence (–) of TcmX and control antibiotics erythromycin (Ery), tetracycline (Tet) and thiostrepton (Ths). Ths and Tet inhibit initiation (green arrow), while TcmX and Ery lead to stalling during elongation, at the seventh codon for TrpL_2Ala in **a** or the tenth and 16th codons, respectively, for the ErmBL template in **b**. The no antibiotic control translates to the stop codon at the end (purple arrow). Codons in P site are marked by color circles; note that owing to the large size of the ribosome, the reverse transcriptase stops are at nucleotide +16 relative to the codon located in the P site. **c**–**g**, Transverse section of the cryo-EM map of the TcmX-Eco70S showing the TcmX binding site in the exit tunnel (**c**), with zooms (**d**–**g**) showing the relative location of TcmX (blue) compared to A-site Phe-tRNA (yellow) (**d**) and P site fMet-tRNA (green) (PDB 1VY4)[33], erythromycin (red, PDB 5JTE) (**e**)[30], ErmBL nascent chain (gold, PDB 5JTE) (**f**)[30] and TnaC nascent peptide chain (green, PDB 4UY8) (**g**)[34]. Experiments were repeated twice independently with similar results.

performed toeprinting using another template, namely, the ErmBL mRNA (Fig. 4b). As observed previously, Ery induced translational arrest of ErmBL with the tenth (Asp, D) codon located in the P site[29,30]. While TcmX also induced translational arrest of the ErmBL template, ribosome stalling was not observed at the tenth codon, but rather with the 16th (Leu, L) codon (Fig. 4b). This suggests that analogous to macrolides, the translational arrest mediated by TcmX is also nascent polypeptide chain-dependent, but that TcmX exhibits a different sequence-specificity compared with macrolides such as erythromycin. Our finding that TcmX does not inhibit translation initiation, but rather blocks an early elongation step (Fig. 4a,b), analogous to the mechanism of action of macrolides such as Ery[28], is consistent with the binding position of TcmX (Fig. 4c). TcmX does not overlap with A- or P-site tRNA (Fig. 4d), but is instead located deeper within the exit tunnel, analogous to Ery (Fig. 4e), where it could interfere with the prolongation of nascent polypeptide chains (Fig. 4f). Although TcmX binds on the opposite side of the tunnel with respect to Ery, we note that the extent of tunnel blockage is not complete and that the remaining space may also allow some translation of nascent chains in the presence of the drug (Fig. 4g).

Discussion

The antimicrobial and cytotoxic activity of tetracenomycins has been assumed to result from the ability of this family of compounds to intercalate with DNA and thereby induce DNA damage[10,11,13]. This assumption was also reinforced by the similarity of tetracenomycins with Dox (Fig. 1a), as well as the report that tetracenomycins do not inhibit in vitro poly(U)-dependent poly(Phe) synthesis[6]. Here we challenge these assumptions by showing that (1) TcmX does not evoke the SOS response due to DNA damage, as observed for Dox (Fig. 1e) and (2) TcmX, unlike Dox, does not inhibit thymine incorporation into DNA in living cells (Fig. 1g), but rather (3) TcmX, like Tet, inhibits valine incorporation into proteins (Fig. 1f) and (4) TcmX, like Tet[21], inhibits in vitro cell-free protein synthesis

in bacteria (Fig. 1h) as well as in human lysates (Fig. 3c). Moreover, we demonstrate that in bacteria the ribosome and protein synthesis are the physiological target for TcmX by showing that single point mutations within the 23S rRNA confer TcmX resistance (Table 1).

The tetracyclic chromophore of TcmX stacks on the noncanonical basepair formed between U2586 and U1782. We note that the producers of tetracenomycins, such as *S. glaucescens* and *Amycolatopsis* sp. A23 also contain a U–U basepair (Extended Data Fig. 4), suggesting that their ribosomes should be susceptible to the antibiotics they produce. In these organisms, resistance is instead conferred by the presence of an inducible *tcmA* gene, which encodes the TcmA metabolite transporter responsible for pumping TcmC out of the cell[31]. Consistent with the conservation of the U–U basepair in all eukaryotes, we could demonstrate using cryo-EM that TcmX binds to the same site within the exit tunnel (Fig. 2e–h) and inhibits translation on human 80S ribosomes in vivo and in vitro (Fig. 3b,c). Thus, we suggest that inhibition of protein synthesis, rather than intercalation with DNA, is a likely reason for the observed cytotoxicity of tetracenomycins observed here for HEK293T cells (Fig. 3a) and reported against other human cell lines[8–12].

Compared to the macrolide antibiotics, such as Ery, the TcmX binding site is on the opposite surface of the ribosomal tunnel (Fig. 4d). The distinct binding sites of TcmX and Ery is consistent with our findings that the A2058G mutation within the 23S rRNA confers erythromycin but not TcmX resistance, whereas mutations in U2586 or U1782 that confer TcmX resistance, do not confer Ery resistance (Table 1). The lack of cross-resistance to TcmX by A2058G is important since mutation or modification (methylation) of A2058 represents one of the main determinants for clinical resistance to macrolides, lincosamides and streptogramin B (MLS_B) antibiotics[32]. Nevertheless, the mechanism of action of TcmX appears to resemble that of macrolides to stall translation in a nascent polypeptide-dependent manner[28]; however, the sequence-specificity of stalling for TcmX appears to be distinct. Thus, it will be interesting in the future to analyze in a translatome-wide manner to see whether there is also a sequence-specificity of the inhibition of TcmX and if so, how this specificity compares with the sequence motifs identified for macrolide antibiotics[28].

Collectively, our findings that the binding mode and mechanism of action of TcmX, as well as the lack of cross-resistance with other antibiotics, is likely to be conserved for most, if not all, tetracenomycins, making members of this family potentially attractive lead compounds for future development of new antimicrobial agents.

Online content

Any Nature Research reporting summaries, source data, extended data, supplementary information, acknowledgements, peer review information; details of author contributions and competing interests; and statements of data and code availability are available at https://doi.org/10.1038/s41589-020-0578-x.

Received: 20 January 2020; Accepted: 28 May 2020;
Published online: 29 June 2020

References

1. Zhang, Z., Pan, H. X. & Tang, G. L. New insights into bacterial type II polyketide biosynthesis. *F1000 Res.* **6**, 172 (2017).
2. Wilson, D. N. Ribosome-targeting antibiotics and mechanisms of bacterial resistance. *Nat. Rev. Microbiol.* **12**, 35–48 (2014).
3. Agudelo, D., Bourassa, P., Berube, G. & Tajmir-Riahi, H. A. Review on the binding of anticancer drug doxorubicin with DNA and tRNA: structural models and antitumor activity. *J. Photochem. Photobiol. B.* **158**, 274–279 (2016).
4. Agudelo, D., Bourassa, P., Berube, G. & Tajmir-Riahi, H. A. Intercalation of antitumor drug doxorubicin and its analogue by DNA duplex: structural features and biological implications. *Int. J. Biol. Macromol.* **66**, 144–150 (2014).
5. Agudelo, D., Berube, G. & Tajmir-Riahi, H. A. An overview on the delivery of antitumor drug doxorubicin by carrier proteins. *Int. J. Biol. Macromol.* **88**, 354–360 (2016).
6. Weber, W., Zahner, H., Siebers, J., Schroder, K. & Zeeck, A. Metabolic products of microorganisms. 175. Tetracenomycin C (author's translation). *Arch. Microbiol.* **121**, 111–116 (1979).
7. Anderson, M. G., Khoo, C. L. & Rickards, R. W. Oxidation processes in the biosynthesis of the tetracenomycin and elloramycin antibiotics. *J. Antibiot.* **42**, 640–643 (1989).
8. Liu, B. et al. Identification of tetracenomycin X from a marine-derived *Saccharothrix* sp. guided by genes sequence analysis. *Acta Pharm. Sinica* **49**, 230–236 (2014).
9. Gan, M. et al. Saccharothrixones A-D, tetracenomycin-type polyketides from the marine-derived actinomycete saccharothrix sp. 10-10. *J. Nat. Prod.* **78**, 2260–2265 (2015).
10. Drautz, H., Reuschenbach, P., Zahner, H., Rohr, J. & Zeeck, A. Metabolic products of microorganisms. 225. Elloramycin, a new anthracycline-like antibiotic from *Streptomyces olivaceus*. Isolation, characterization, structure and biological properties. *J. Antibiot.* **38**, 1291–1301 (1985).
11. Rohr, J. & Zeeck, A. Structure-activity relationships of elloramycin and tetracenomycin C. *J. Antibiot.* **43**, 1169–1178 (1990).
12. Adinarayana, G. et al. Cytotoxic compounds from the marine actinobacterium. *Bioorg. Khim* **32**, 328–334 (2006).
13. Egert, E., Noltemeyer, M., Siebers, J., Rohr, J. & Zeeck, A. The structure of tetracenomycin C. *J. Antibiot.* **45**, 1190–1192 (1992).
14. Komarova Andreyanova, E. S. et al. 2-Guanidino-quinazolines as a novel class of translation inhibitors. *Biochimie* **133**, 45–55 (2017).
15. Ortseifen, V., Kalinowski, J., Puhler, A. & Ruckert, C. The complete genome sequence of the actinobacterium *Streptomyces glaucescens* GLA.O (DSM 40922) carrying gene clusters for the biosynthesis of tetracenomycin C, 5′-hydroxy streptomycin, and acarbose. *J. Biotechnol.* **262**, 84–88 (2017).
16. Osterman, I. A. et al. Sorting out antibiotics' mechanisms of action: a double fluorescent protein reporter for high-throughput screening of ribosome and DNA biosynthesis inhibitors. *Antimicrob. Agents Chemother.* **60**, 7481–7489 (2016).
17. Pato, M. L. Tetracycline inhibits propagation of deoxyribonucleic acid replication and alters membrane properties. *Antimicrob. Agents Chemother.* **11**, 318–323 (1977).
18. Frederick, C. A. et al. Structural comparison of anticancer drug-DNA complexes: adriamycin and daunomycin. *Biochemistry* **29**, 2538–2549 (1990).
19. Orelle, C. et al. Tools for characterizing bacterial protein synthesis inhibitors. *Antimicrob. Agents Chemother.* **57**, 5994–6004 (2013).
20. Vester, B. & Douthwaite, S. Macrolide resistance conferred by base substitutions in 23S rRNA. *Antimicrob. Agents Chemother.* **45**, 1–12 (2001).
21. Jenner, L. et al. Structural basis for potent inhibitory activity of the antibiotic tigecycline during protein synthesis. *Proc. Natl Acad. Sci. USA* **110**, 3812–3816 (2013).
22. Polikanov, Y. S. et al. Distinct tRNA accommodation intermediates observed on the ribosome with the antibiotics hygromycinA and A201A. *Mol. Cell* **58**, 832–844 (2015).
23. Cannone, J. J. et al. The comparative RNA web (CRW) site: an online database of comparative sequence and structure information for ribosomal, intron, and other RNAs. *BMC Bioinf.* **3**, 2 (2002).
24. Mortison, J. D. et al. Tetracyclines modify translation by targeting key human rRNA substructures. *Cell Chem. Biol.* **25**, 1506–1518 e1513 (2018).
25. Akulich, K. A. et al. Four translation initiation pathways employed by the leaderless mRNA in eukaryotes. *Sci. Rep.* **6**, 37905 (2016).
26. Terenin, I. M., Andreev, D. E., Dmitriev, S. E. & Shatsky, I. N. A novel mechanism of eukaryotic translation initiation that is neither m7G-cap-, nor IRES-dependent. *Nucleic Acids Res.* **41**, 1807–1816 (2013).
27. Metelev, M. et al. Klebsazolicin inhibits 70S ribosome by obstructing the peptide exit tunnel. *Nat. Chem. Biol.* **13**, 1129–1136 (2017).
28. Vazquez-Laslop, N. & Mankin, A. S. How macrolide antibiotics work. *Trends Biochem. Sci.* **43**, 668–684 (2018).
29. Arenz, S. et al. Molecular basis for erythromycin-dependent ribosome stalling during translation of the ErmBL leader peptide. *Nat. Commun.* **5**, 3501 (2014).
30. Arenz, S. et al. A combined cryo-EM and molecular dynamics approach reveals the mechanism of ErmBL-mediated translation arrest. *Nat. Commun.* **7**, 12026 (2016).
31. Guilfoile, P. G. & Hutchinson, C. R. Sequence and transcriptional analysis of the *Streptomyces glaucescens* temAR tetracenomycin C resistance and repressor gene loci. *J. Bact.* **174**, 3651–3658 (1992).
32. Leclercq, R. Mechanisms of resistance to macrolides and lincosamides: nature of the resistance elements and their clinical implications. *Clin. Infect. Dis.* **34**, 482–492 (2002).
33. Polikanov, Y. S., Steitz, T. A. & Innis, C. A. A proton wire to couple aminoacyl-tRNA accommodation and peptide-bond formation on the ribosome. *Nat. Struct. Mol. Biol.* **21**, 787–793 (2014).
34. Bischoff, L., Berninghausen, O. & Beckmann, R. Molecular basis for the ribosome functioning as an L-tryptophan sensor. *Cell Rep.* **9**, 469–475 (2014).

Methods

Genome sequencing and data analysis. Library Preparation Nanopore long-read sequencing: DNA samples were prepared for long-read Oxford Nanopore Technologies sequencing using the Nanopore Rapid Barcoding genomic DNA Sequencing kit SQK-RBK004 Oxford Nanopore Technologies according to the manufacturer's protocol and sequenced in-house using MinION and flow cell FLO-MIN106. Illumina short read sequencing: DNA samples were prepared for sequencing using NEBNext Ultra II FS DNA Library Prep Kit for Illumina modules E7810L and E7595L (New England BioLabs (NEB)) following the manufacturer's protocol for use with inputs ≥100 ng with modifications to eliminate PCR-amplification steps. IDT for Illumina TruSeq DNA UD Indexes 20022370 (Integrated DNA Technologies) were used in place of NEBNext adaptors. The USER addition and incubation were skipped for this reason, and the volume was replaced instead with water to reach the necessary sample volume for size selection steps. Library size selection and clean up were performed using AMPure XP beads (Beckman Coulter) following the NEB protocol. Prepared libraries were quantified using NEBNext Library Quant Kit for Illumina E7630L (NEB) and pooled with volumes adjusted to normalize concentrations. Library size and quality were analyzed with the 2100 Bioanalyzer Instrument (Agilent). Pooled DNA libraries were sequenced by Novogene Co., Ltd. Hybrid assembly: adapter sequences in Illumina paired reads were cut with trimmomatic v.0.36 (ref. [35]). Nanopore basecalling and demultiplexing was performed by Albacore v.2.3.4 available from ONT community web site (community.nanoporetech.com). To obtain more coverage with long reads we performed secondary demultiplexing of unclassified reads with Porechop v.0.2.4 (https://github.com/rrwick/Porechop). Adapter sequences were cut with the same program. Hybrid assembly was performed with MaSuRCA v.3.2.8 (ref. [36]). Assembly quality was assessed with Quast v.5.0.2 (ref. [37]). Phylogeny construction: the phylogeny of *Amycolatopsis* species was built using 16S–23S rRNA concatenate. Genomes for the analysis were downloaded from the PATRIC database[38]. Sequences of rRNAs were extracted using barrnap v.0.9 (https://github.com/tseemann/barrnap) and aligned with MAFFT[39]. Assembly results: achieved assembly of total length 10,560,374 nucleotides has six contigs with a mean coverage of 58×, N50 of 3,441,384 with largest contig of 4,455,037-nt length. The genome of *Amycolatopsis* sp. A23 was fully annotated using the RAST automated annotation pipeline[40]. The TcmX cluster was analyzed in detailed using a subsystems-based comparative genomic approach implemented in SEED[41].

Detection of the translation inhibitors with pDualrep2 reporter. Reporter strain JW5503 Δ*tolC* (BW25113) pDualrep2 was used as previously described[42]. Tested antibiotic solutions (Spots of Tet (0.5 µg), Dox (2 µg), erythromycin (Ery, 2 µg)), levofloxacin (Lev, 0.05 µg) and TcmX (2 µg)) were applied to an agar plate that already contained a lawn of the reporter strain. After being incubated overnight at 37 °C, the plate was scanned by ChemiDoc (Bio-Rad) in the modes 'Cy3-blot' for RFP and 'Cy5-blot' for Katushka2S.

TcmX purification and structure determination. *Amycolatopsis* sp. A23 strain was grown in 50 ml of Org79 medium[42] for 2 d at 28 °C, and 5 ml of the preculture was used to inoculate seven flasks containing 150 ml of Org79 medium. The cultures were then incubated at 28 °C for 21 d without shaking. Then 1 l was used for gravity-force reverse-phase chromatography on LPS500H sorbent (polyvinylbenzene, pore size 50–1,000 Å) with elution by 10, 25, 50 and 75% acetonitrile solutions. The pDualrep2 reporter system was used to analyze the activity in the fractions[14]. The fraction eluted by 50% acetonitrile demonstrated the highest inhibitory activity and induced Katushka2S expression, indicating presence of protein synthesis inhibitor. This fraction was subjected to further purification by means of high-performance liquid chromatography (HPLC) (Agilent 1260, isocratic elution 42% of MeCN, 0.05% TFA) using a Phenomenex HPLC column (Luna 5 µm C18 (2) 100 Å), collected fraction were again analyzed by means pDualrep2 reporter and individual peak with antibacterial activity was collected and lyophilized. As a result, 11 mg of yellow powder was obtained. The chemical structure of the active compound was revealed by combination of mass spectrometry and NMR analysis.

Determination of the chemical structure of TcmX. NMR spectra of tetracenomycin X were recorded on a Bruker AVANCE spectrometer operating at a proton frequency of 600 MHz, at 298 K in DMSO-d_6. Concentration of the sample was ~100 µM. NMR spectra were processed and analyzed similarly as before[42]. UV and mass spectra were made by means of ultra-efficient liquid chromatography/mass spectrometry on a Waters Acquity ultra-HPLC–tandem mass spectrometry liquid chromatography system (Waters) supplied with TQD (ESI, MS1 mode) and PDA detectors, using an analytical column Acquity UPLC BEH C18 (50 × 2.1 mm², 1.7 µm) by gradient elution 5–100% MeCN (3 min) in the presence 20 mM formic acid (35 °C, 0.5 ml min^{-1}, injection vol. 2 µl). The structure of the isolated compound was established using the mass-spectroscopy data (molecular weight, 486; Supplementary Note 1) and information from NMR spectra. ^{1}H spectrum recorded in DMSO-d6 (Supplementary Notes 2 and 3) contains 12 singlets, including five signals of methyl groups (with chemical shifts in the range between 2.7 and 4.0 ppm), four C–H signals (4.7–8.8 ppm) and three broader signals from exchangeable protons (O–H). This scant information derived from the 1H spectrum is substantially extended by the use of ^{13}C data (Supplementary Note 3). The two-dimensional ^{13}C-^{1}H HMBC spectrum shows correlations between ^{1}H signals and more than twenty ^{13}C resonances (Supplementary Note 3) and allows to suggest a topology of the studied compound. The suggested topology was found to be identical to the topology of TcmX. Comparison of the measured ^{1}H and ^{13}C chemical shifts and NMR parameters published for TcmX[8] shows high level of identity (Supplementary Table 1) and proves the structure of the isolated compound. The low field shift of the signal of O–H (ref. [11]) (13.8 ppm) indicates the formation of a strong intramolecular hydrogen bond.

Determination of MIC and in vivo testing of TcmX. MIC values were determined by monitoring growth in 96-well plates of *E. coli* cultures exposed to TcmX serial dilutions. Specifically, overnight *E. coli* cultures were diluted in 96-well plates to an OD_{600} of 0.01 in LB medium. The wells were then supplemented with antibiotic at concentrations of 64, 32, 16, 8, 4, 2, 1 and 0.5 µg ml^{-1}. After antibiotic addition, the plates were incubated, with shaking (200 r.p.m.) overnight at 37 °C and cell growth was assessed by scanning each well with a VictorX5 reader. For protein synthesis inhibition experiments, JW5503 Δ*tolC* was grown in M9 media, supplemented with all amino acids (40 mg l^{-1} each), except valine, until the optical density (OD of 600 nm) reached 0.2. TcmX, Dox and Tet (30×, 10×, 5×, 1× MIC, MIC: TcmX 2 µg ml^{-1}, Dox 1.3 µg ml^{-1} and Tet 0.3 µg ml^{-1}) were added to 200 µl of cell culture and incubated for 5 min at 37 °C before adding of 0.5 µCi of L-[^{14}C]-valine (Perkin Elmer), cells were incubated for a further 5 min at 37 °C, centrifuged and suspended in urea-containing protein loading dye. The reaction products were analyzed by SDS–PAGE followed by autoradiography, results were quantified with the Image Lab software (Bio-Rad). For DNA synthesis inhibition experiments, JW5503 Δ*tolC* was grown in M9 media, supplemented with all amino acids (40 mg l^{-1} each) overnight, until the optical density ($OD_{600\,nm}$) reached 0.4. TcmX, Dox and Tet (30×, 10×, 5×, 1× MIC) were added to 1,000 µl of cell culture and incubated for 5 min at 37 °C before addition of 1 µl 500 µM (2.2 µCi per nmol) of [^{3}H]-thymidine (Perkin Elmer), cells were incubated for 15 mins more at 37 °C with shaking at 200 r.p.m., centrifuged, washed in 100 µl of 0.9% NaCl, centrifuged and suspended in 7 M Urea 10% SDS buffer and analyzed by a scintillation counter (Perkin Elmer).

Selection of TcmX resistance mutants. The single *rrnE* allele, Δ*tolC E. coli* strain SQ110DTC[19] was grown overnight in LB medium supplemented with 50 µg ml^{-1} of kanamycin, then cells were plated on LB agar plates containing 50 µg ml^{-1} kanamycin and different concentrations of TcmX (from 1–10 µg ml^{-1}). Several colonies appeared on plates with 2.5 and 5 µg ml^{-1} after 24 h of incubation, which were cultivated and the MIC of TcmX was determined. Ribosomal DNA was PCR amplified from five colonies and sequenced with the set oligonucleotides as described previously[27].

Testing TcmX resistance mutations. Plasmids pAM552 and pLK35 with 1,782, 2,058, 2,059, 2,586 and 2,609 mutations in rRNA operon were kindly provided by A. Mankin (Chicago, USA), double mutant 1782/2586 was made in this work, by site-directed mutagenesis of 2586C mutant plasmid with following oligonucleotides:

1782C_F CAAAAACACAGCACTGTGC; 1782C_R ATAAACAGTTG CAGCCAGC.

SQ171Δ*tolC* (SQ171DTC) strain was transformed by mutant plasmids, and the cells were then cured of the wild-type plasmid pCSacB by plating onto an LB agar plates supplemented with 50 µg ml^{-1} ampicillin and 5% sucrose[43]. MIC values of the engineered mutants were tested by serial dilutions as described before.

Cryo-EM maps of *E. coli* and *H. sapiens* TcmX-ribosome complexes. For the human 80S-TcmX sample, HEK293T cells were collected by scraping from seven culture dishes (15 cm) at a confluency of ~50%. The cells were lysed by incubation for 30 min on ice in buffer containing 20 mM HEPES 7.4, 100 mM KOAc, 10 mM $Mg(OAc)_2$, 100 mM sucrose, 1 mM DTT, 0.5% NP-40 substitute and Complete protease inhibitor (Sigma Aldrich). The lysate was layered on top of a sucrose density gradient (10–50% sucrose in 20 mM HEPES 7.4, 100 mM KOAc, 10 mM $Mg(OAc)_2$, 1 mM DTT) and centrifuged at 125,755*g* for 3 h at 4 °C in an SW40 rotor (Beckman Coulter). The gradient was fractionated from top to bottom using a Gradient Master (BioComp). The 80S fraction was collected and centrifuged 356,000*g* for 1 h at 4 °C in a TLA120.2 rotor (Beckman Coulter). The pelleted ribosomes were resuspended in buffer containing 20 mM HEPES 7.4, 100 mM KOAc, 10 mM $MgOAc_2$ and 1 mM DTT. For the *E. coli* 70S-TcmX sample, *E. coli* 70S ribosomes were prepared from *E. coli* BW25112 Δ*yfiA* strain, as previously described[44].

To prepare complexes of TcmX bound to the *E. coli* (TcmX-Eco70S complex) or *H. sapiens* (TcmX-Hsa80S complex), 50 and 100 µM of TcmX was incubated with 4 OD A_{260}/ml 70S or 80S ribosomes, respectively. Subsequently, 3.5 µl of the TcmX-ribosome complexes were applied to 2 nm precoated Quantifoil R3/3 holey carbon supported grids and vitrified using a Vitrobot Mark IV (FEI company). Data collection was performed on a Titan Krios operated at 300 kV, equipped with a Falcon II direct electron detector. Data were collected at a nominal magnification of ×75,000, resulting in a pixel size of 1.084 Å, over a defocus range of −0.5 to

−3.5 µm. Ten frames (dose per frame of 2.5 e^{-} Å^{-2}) were aligned using MotionCor2 (ref. [45]). Power spectra, defocus values, astigmatism and estimation of micrograph resolution were determined using CTFFIND4.1.10 (ref. [46]).

For the TcmX-Eco70S complex, 6,495 micrographs were initially collected. After applying a resolution cut-off of 3.5 Å as well as removal of bad micrographs during manual inspection, the remaining 4,941 micrographs were used for particle picking using Gautomatch (http://www.mrc-lmb.cam.ac.uk/kzhang/). The resulting 818,287 particles were then extracted using RELION 3.0 (ref. [47]) and subjected to two-dimensional classification. The selected two-dimensional classes contained a total of 548,675 particles, which were used for initial alignment and three-dimensional classification, which were performed using three times decimated data. After 300 rounds of sorting into eight classes, one well-resolved 70S class with 161,915 was extracted for further high-resolution refinement. Contrast transfer function (CTF) and beam tilt refinement with subsequent Bayesian polishing was performed[47] and improved the resolution from 3.9 to 2.86 Å. The resolution was estimated using the gold standard criterion (Fourier shell correlation of 0.143)[48,49]. The refined maps were corrected using the modulation transfer function of the detector and sharpened by applying an automatically determined negative *B* factor using RELION 3.0 (ref. [47]). Local Resolution and maps filtered according to local resolution were computed using SPHIRE[50]. A sorting scheme and a visualization of the local-resolution distribution is provided in Extended Data Fig. 3.

For the TcmX-Hsa80S complex, 7,672 micrographs remained after visual inspection and were used for particle picking using Gautomatch (http://www.mrc-lmb.cam.ac.uk/kzhang/). This resulted in 836,588 initial particles, of which 461,131 were used for further processing after two-dimensional classification using RELION 3.0 (ref. [47]). Three-dimensional classification yielded four classes of 80S ribosomes. One low-resolution class was discarded and the remaining well-resolved classes, which differed in eEF2 occupation and 40S subunit conformation were joined (302,737 particles) and refined to 3.7 Å. There was no extra density visible at the canonical tetracycline binding site on the 40S subunit. CTF-refinement, focused refinement with a mask on the 60S subunit and postprocessing in RELION 3.0 resulted in a resolution of 2.76 Å (Fourier shell correlation, 0.143). The final density map was filtered according to local resolution as determined by RELION 3.0, applying a *B* factor of −100 Å^2. A sorting scheme and a visualization of the local-resolution distribution is provided in Extended Data Fig. 5.

Molecular modeling of the *E. coli* and *H. sapiens* TcmX-ribosome complexes. The molecular model for the TcmX-Eco70S complex was based on a previous cryo-EM structure of the *E. coli* 70S ribosome (Protein Data Bank (PDB) 6H4N)[44]. The molecular model for the TcmX-Hsa60S complex was based on previous cryo-EM structure of the *H. sapiens* 80S ribosome (PDB 6EK0)[51]. The rRNA domains and ribosomal proteins were rigid-body fitted into the respective cryo-EM maps using Chimera[52]. An atomic model for TcmX was generated from the chemical structure (PubChem CID 129395) using the PRODRG software[53]. Restraints for TcmX were generated using PHENIX eLBOW[54]. The molecular models were manually adjusted and refined using Coot[55]. The complete atomic model of the respective complexes were subsequently refined into the locally filtered maps using phenix.real_space_refine with secondary structure restraints calculated by PHENIX 1.16 (ref. [56]). The statistics of the refined models were obtained using MolProbity[57] and are presented in Supplementary Table 5 for the TcmX-Eco70S and TcmX-Hsa80S complexes, respectively.

MTT assay. Cytotoxicity was measured using the MTT by Mosman[58] in HEK293T cell line. Then 2,500 cells per well were seeded in a 96-well plate in DMEM/F12 media. The cells were growth for 18 h. The next day, the antibiotic of interest in 10% DMSO was added. Cells were incubated with compounds for 48 or 72 h. Each experiment was done in triplicate. After incubation, MTT was added up to 0.5 mg ml^{-1} to the media and cells were incubated for an additional 2 h. Then the media was changed to DMSO and solution was measured spectrophotometrically at 565 nm (VictorX5, Perkin Elmer). The cytotoxicity concentration that inhibits 50% viability (CC_{50}) of the tested compounds was calculated from the dose-response dependencies with GraphPad Prism software (GraphPad Software, Inc.).

Mammalian cell growth and mRNA transfection. For experiments in mammalian systems, capped and polyadenylated mRNAs were prepared essentially as described previously[25]. In short, a T7 promoter-containing, 50A-tailed PCR products were obtained from the plasmid pActin-Fluc, purified by agarose gel electrophoresis, and used as a template for in vitro transcription. RNA synthesis was performed using the RiboMAX kit (Promega), followed by capping by Vaccinia Capping System (NEB). The transcripts were purified by LiCl precipitation and checked for integrity by denaturing urea PAGE.

For mRNA transfection, HEK293T cells were grown in DMEM (Gibco) supplemented with 10% FBS (HyClone) in the presence of penicillin and streptomycin (Paneco) in a humidified 5% CO_2 atmosphere at 37 °C. One day before transfection, cells were transferred into the white FB/HB 96-well plates (Grenier no. 655074) in 75 µl medium per well. Next day, cell culture at ~70% confluency was supplemented with antibiotic or solvent, as indicated, and immediately after that transfected with the reporter mRNA. For this, 30 ng of mRNA in 20 µl Gibco Opti-MEM (per one well) were mixed with a solution of 0.06 µl of Unifectin-56 (Unifect Group) in 3 µl Opti-MEM (per well), incubated for 15 min, then supplied with 0.4 µl 100 mM D-luciferin (Promega) per well and then 23 µl of the mixture were added to cells in the plate. During these steps, all manipulations were performed as described in the regular fleeting mRNA transfection technique protocol[25], providing a rapid and nonstressful transfection procedure. Real-time luminescence measurements were carried out overnight in the CLARIOstar plate reader (BMG Labtech) equipped with Atmospheric Control Unit to maintain 5% CO_2, at 37 °C (light integration time, 5 s). Light intensities at the time point 4 h after transfection were taken as luciferase activity values. All the experiments were repeated at least three times (including ones with different cell passages), the mean value ± s.d. were calculated.

Mammalian cell-free systems and in vitro translation assays. For in vitro translation, the whole-cell extract prepared from cultured HEK293T cell was used[26]. Translation reactions were performed in a total volume of 10 µl, which contained 5.5 µl of the HEK293T extract, 1× Translation Buffer (20 mM Hepes-KOH pH 7.6, 1 mM DTT, 0.5 mM spermidine-HCl, 0.8 mM $Mg(OAc)_2$, 8 mM creatine phosphate, 1 mM ATP, 0.2 mM GTP, 120 mM KOAc and 25 µM of each amino acid), 2 U of RiboLock RNase inhibitor (Thermo Scientific), 0.5 mM D-luciferin (Promega), 1 µl of either antibiotic solution or solvent (water or 10% DMSO), as indicated and 100 ng mRNA (the latter was added as 1 µl water solution after the reaction mixture supplemented with antibiotic was pre-incubated for 5 min at 30 °C). After mRNA addition, the mixtures were transferred into the pre-heated white FB/NB 384-well plate (Grenier no. 781904), covered by a PCR plate seal and incubated in the CLARIOstar plate reader (BMG Labtech) at 30 °C with continuous measurement of the luciferase activity, essentially as described[25,59]. Light intensities at 30 min were taken as luciferase activity values.

In vitro translation and toeprinting analysis. In vitro translation reactions were made in PURExpress system (NEB), each reaction in 5 µl, supplied with 200 ng of Fluc mRNA and 0.1 mM of D-luciferin. Chemiluminescence was detected by VictorX5 multi-reader. Toeprinting was done according to the described protocol[19] using tryptophan operon leader mRNA obtained by T7 transcription from the linear DNA template. DNA template was obtained by amplification of TrpL-2Ala peptide sequence from pDualrep2 plasmid with primers F:
TGTAATACGACTCACTATAGGGAATTTTTCTGTATAATAGCCGCGGA-AGTTCACGTAAAAAGGGTATCGACAATGAAA
R: GCGTTAAGGCTATGTACGGGTATCTGATTGCTTTACG and GCGTT AAGGCTATGTAC was used for reverse transcription. The ErmBL template was generated by PCR with two partially self-complimented oligonucleotides F: TAATACGACTCACTATAGGGAGTTTTATAAGGAGGAAAAAATATGTT GGTATTCCAAATGCGTAATGTAGATAAAACATCTAC R:
GGTTATAATGAATTTTGCTTATTAACGATAGAATTCTATCACTTTTTT TATTATTATTATTTCAAAATAGTAGATGTTTTATCTACAT as a template and F: TAATACGACTCACTATAGGG R: GGTTATAATGAATTTTGCTTATTAAC as a pair for PCR. GGTTATAATGAATTTTGCTTATTAAC was used for reverse transcription. The concentration of all drugs in toeprint was 50 µM and 1% DMSO for no antibiotic sample.

Figure preparation. Figures showing cryo-EM densities were created using ChimeraX[60]. Figures showing atomic models with or without electron densities, and in silico RNA mutagenesis were generated using PyMol (PyMol Molecular Graphics System, v.2.4.a, Schrödinger). For large subunit rRNA alignment presentation, primary alignments of rRNAs from the CRW Site[23] were shortened to the desired regions, using CLC Workbench (CLC bio). For alignment figure generation, Jalview v.2.11 was used. Plots displaying Fluc inhibition and incorporation assays were generated using QtiPlot (http://soft.proindependent.com/qtiplot.html). Figures were assembled using Adobe Illustrator.

Reporting Summary. Further information on research design is available in the Nature Research Reporting Summary linked to this article.

Data availability

The cryo-EM and associated molecular models for the TcmX-Eco70S and TcmX-Hsa80S ribosome complexes are available from the EMDB (EMD-10705 and EMD-10709) and PDB (ID 6Y69 and PDB 6Y6X), respectively. The complete genome sequence of *Amycolatopsis* sp. A23 has been deposited in the European Nucleotide Archive with the accession number GCA_902497555.1. Source data are provided with this paper.

References

35. Bolger, A. M., Lohse, M. & Usadel, B. Trimmomatic: a flexible trimmer for Illumina sequence data. *Bioinformatics* **30**, 2114–2120 (2014).
36. Zimin, A. V. et al. Hybrid assembly of the large and highly repetitive genome of *Aegilops tauschii*, a progenitor of bread wheat, with the MaSuRCA mega-reads algorithm. *Genome Res* **27**, 787–792 (2017).

37. Gurevich, A., Saveliev, V., Vyahhi, N. & Tesler, G. QUAST: quality assessment tool for genome assemblies. *Bioinformatics* **29**, 1072–1075 (2013).
38. Wattam, A. R. et al. Improvements to PATRIC, the all-bacterial bioinformatics database and analysis resource center. *Nucleic Acids Res.* **45**, D535–D542 (2017).
39. Katoh, K. & Standley, D. M. MAFFT multiple sequence alignment software version 7: improvements in performance and usability. *Mol. Biol. Evol.* **30**, 772–780 (2013).
40. Aziz, R. K. et al. The RAST Server: rapid annotations using subsystems technology. *BMC Genomics* **9**, 75 (2008).
41. Overbeek, R. et al. The subsystems approach to genome annotation and its use in the project to annotate 1000 genomes. *Nucleic Acids Res.* **33**, 5691–5702 (2005).
42. Zakalyukina, Y. V. et al. Nybomycin-producing Streptomyces isolated from carpenter ant *Camponotus vagus*. *Biochimie* **160**, 93–99 (2019).
43. Zaporojets, D., French, S. & Squires, C. L. Products transcribed from rearranged RRN genes of *Escherichia coli* can assemble to form functional ribosomes. *J. Bacteriol.* **185**, 6921–6927 (2003).
44. Beckert, B. et al. Structure of a hibernating 100S ribosome reveals an inactive conformation of the ribosomal protein S1. *Nat. Microbiol* **3**, 1115–1121 (2018).
45. Zheng, S. Q. et al. MotionCor2: anisotropic correction of beam-induced motion for improved cryo-electron microscopy. *Nat. Methods* **14**, 331–332 (2017).
46. Rohou, A. & Grigorieff, N. CTFFIND4: fast and accurate defocus estimation from electron micrographs. *J. Struct. Biol.* **192**, 216–221 (2015).
47. Zivanov, J. et al. New tools for automated high-resolution cryo-EM structure determination in RELION-3. *eLife* **7**, e42166 (2018).
48. Rosenthal, P. B. & Henderson, R. Optimal determination of particle orientation, absolute hand, and contrast loss in single-particle electron cryomicroscopy. *J. Mol. Biol.* **333**, 721–745 (2003).
49. Chen, S. et al. High-resolution noise substitution to measure overfitting and validate resolution in 3D structure determination by single particle electron cryomicroscopy. *Ultramicroscopy* **135**, 24–35 (2013).
50. Moriya, T. et al. High-resolution single particle analysis from electron cryo-microscopy images using SPHIRE. *J. Vis. Exp.* **16**, 55448 (2017).
51. Natchiar, S. K., Myasnikov, A. G., Kratzat, H., Hazemann, I. & Klaholz, B. P. Visualization of chemical modifications in the human 80S ribosome structure. *Nature* **551**, 472–477 (2017).
52. Pettersen, E. F. et al. UCSF Chimera: a visualization system for exploratory research and analysis. *J. Comput. Chem.* **25**, 1605–1612 (2004).
53. Schuttelkopf, A. W. & van Aalten, D. M. PRODRG: a tool for high-throughput crystallography of protein-ligand complexes. *Acta Crystallogr. D.* **60**, 1355–1363 (2004).
54. Moriarty, N. W., Grosse-Kunstleve, R. W. & Adams, P. D. electronic Ligand Builder and Optimization Workbench (eLBOW): a tool for ligand coordinate and restraint generation. *Acta Crystallogr. D.* **65**, 1074–1080 (2009).
55. Emsley, P. & Cowtan, K. Coot: model-building tools for molecular graphics. *Acta Crystallogr. D.* **60**, 2126–2132 (2004).
56. Adams, P. D. et al. PHENIX: a comprehensive Python-based system for macromolecular structure solution. *Acta Crystallogr. D.* **66**, 213–221 (2010).
57. Chen, V. B. et al. MolProbity: all-atom structure validation for macromolecular crystallography. *Acta Crystallogr. D.* **66**, 12–21 (2010).
58. Mosmann, T. Rapid colorimetric assay for cellular growth and survival: application to proliferation and cytotoxicity assays. *J. Immunol. Methods* **65**, 55–63 (1983).
59. Prokhorova, I. V. et al. Amicoumacin A induces cancer cell death by targeting the eukaryotic ribosome. *Sci. Rep.* **6**, 27720 (2016).
60. Goddard, T. D. et al. UCSF ChimeraX: meeting modern challenges in visualization and analysis. *Protein Sci.* **27**, 14–25 (2018).

Acknowledgements

We thank A. Mankin (University of Illinois at Chicago, Chicago, Illinois) for providing pAM552 and pLK35 plasmids carrying various mutations. We are grateful to O. Saveliev for the expert technical assistance in NMR measurements. This work was supported by Russian Science Foundation grant no. 18-44-04005 (to I.A.O., used for microbiological, biochemical and structural study of TcmX action), 19-14-00115 (to V.I.P., used for NMR studies) and the Deutsche Forschungsgemeinschaft grant no. WI3285/6-1 (to D.N.W.), the Russian Foundation for Basic Research grant no. 19-34-51021 (to I.A.O., used for the expression, purification and structure determination of TcmX) and the Moscow State University development program PNR 5.13 (O.A.D.). The work of A.L.O., S.A.L and J.E.Z. on genome analysis and comparative genomics was supported by the Laboratory Funding Initiative at Sanford Burnham Prebys Medical Discovery Institute (to A.L.O.).

Author contributions

I.A.O., D.A.L., D.I.S., T.P.M., Y.V.Z., V.N.T. and M.V.B. isolated and purified TcmX. I.A.O., V.N.T. and V.I.P. determined structure of TcmX. I.A.O., T.P.M., E.S.K., D.A.L., D.I.S. and D.A.S. evaluated bioactivity. K.A.L. and S.E.D. analyzed inhibitory activity of TcmX in mammals. I.A.O. and E.S.K. selected resistant mutants. M.W., R. Buschauer and J.C. determined cryo-EM structures of the TcmX-Eco70S and TcmX-Hsa80S ribosome complexes, respectively. S.A.L., J.E.Z. and A.L.O. sequenced and analyzed genome of *Amycolatopsis* sp. A23. I.A.O., P.V.S. A.A.B. and O.A.D. designed biochemistry and genetic experiments. Y.S.P. designed and performed X-ray crystallography experiments. All authors, including R. Beckmann, interpreted the results. I.A.O., P.V.S. and D.N.W. wrote the manuscript.

Competing interests

The authors declare no competing interests.

Additional information

Extended data is available for this paper at https://doi.org/10.1038/s41589-020-0578-x.

Supplementary information is available for this paper at https://doi.org/10.1038/s41589-020-0578-x.

Correspondence and requests for materials should be addressed to I.A.O., D.N.W. or P.V.S.

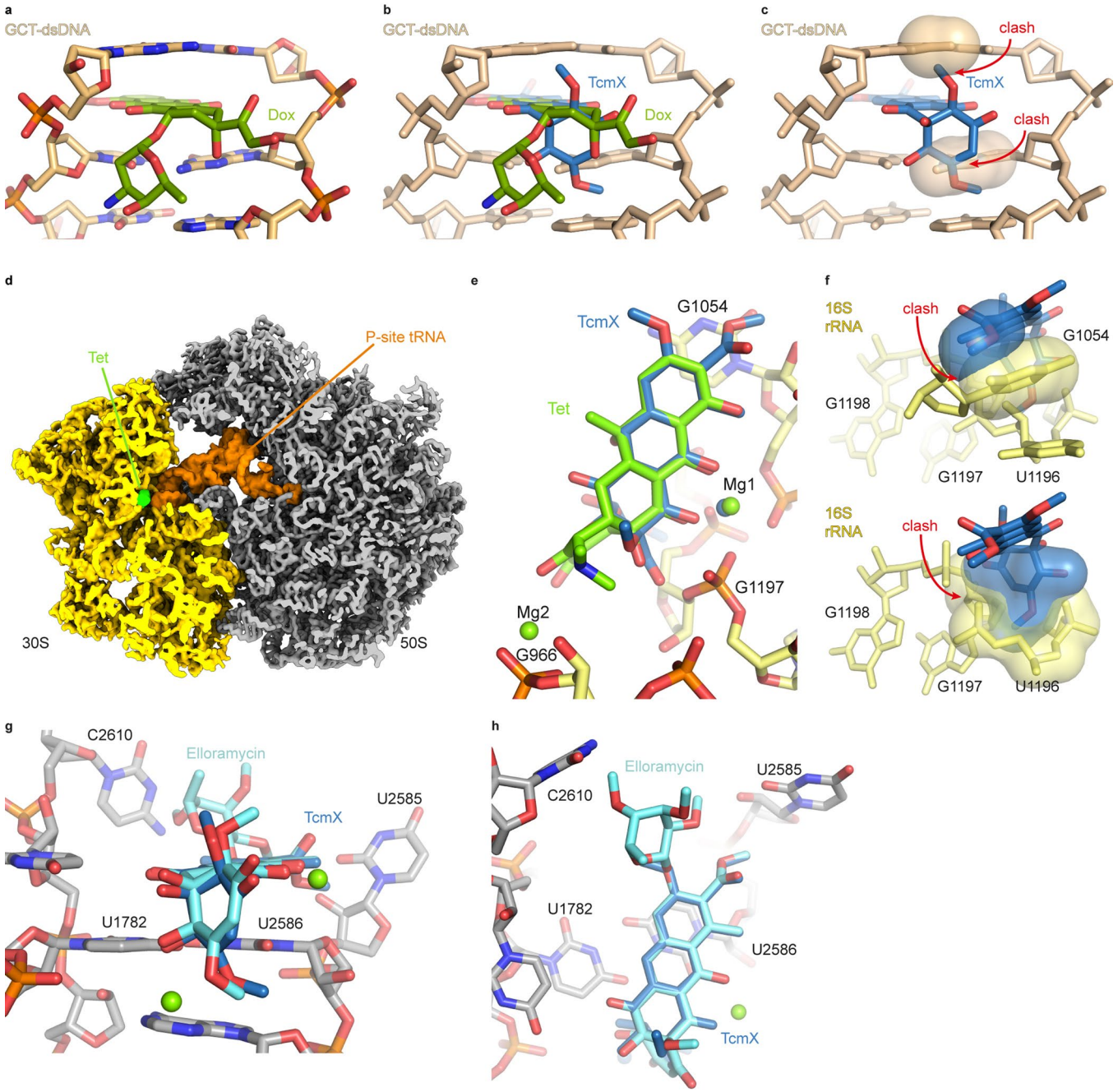

Extended Data Fig. 1 | Modeling of TcmX into DNA and onto the 30S subunit. a, Structure of doxorubicin (Dox, green) intercalating with dsDNA (PDB 1D12). **b**,**c**, Alignment of TcmX (blue) onto Dox (green) based on the planar rings C-D illustrates that the methoxy groups attached to ring A of TcmX would clash with the base⁻pairs and prevent efficient intercalation with DNA. **d**, Transverse section of reconstructed map of *Thermus thermophilus* 70 S (30 S, yellow; 50 S, grey) with the Tet (green) binding site at the decoding site relative to P-site tRNA (orange) (PDB 4V9A)[21]. **e**, Alignment of TcmX (blue) onto Tet (green) (PDB 4V9A)[21] based on rings C and D. **f**, Based on the alignments from (**e**), TcmX clashes with G1054 (top panel) and the backbone of U1196-G1198 (bottom panel). **g**,**h**, Two views showing the tetracyclic antibiotic elloramycin (cyan) aligned onto the TcmX (blue) binding site of the Eco70S based on rings A-D.

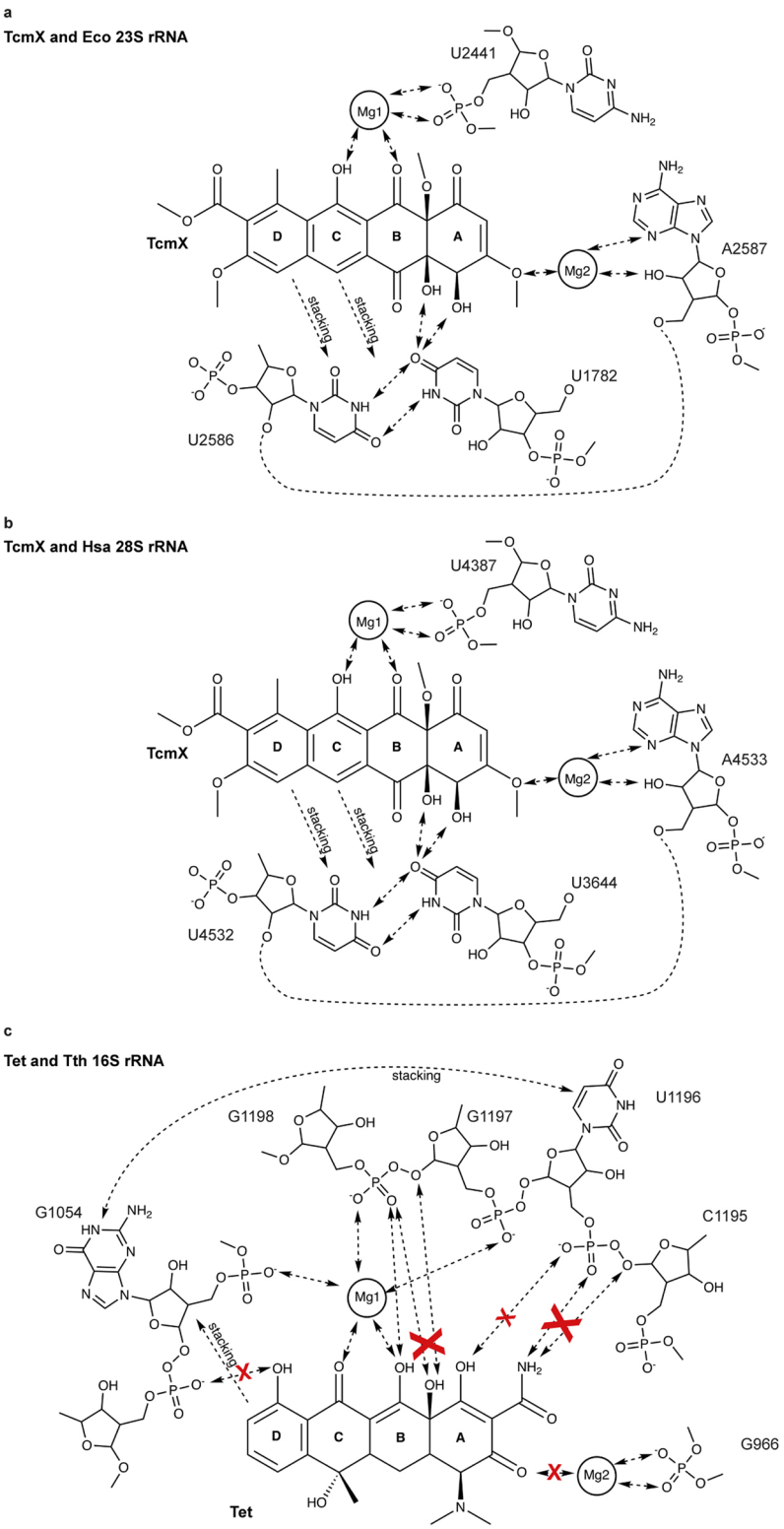

Extended Data Fig. 2 | Interaction schemes of Tetracenomycin X and Tetracycline. a,**b**, Interaction scheme of Tetracenomycin X (TcmX) on the large subunit of the *E. coli* and *H. sapiens* ribosomes, respectively. **c**, Interaction scheme of Tetracycline (Tet) on decoding site of the small subunit of the *T. thermophilus* 70 S ribosome[21], with red crosses marking interactions that TcmX cannot form when docked into the Tet binding site.

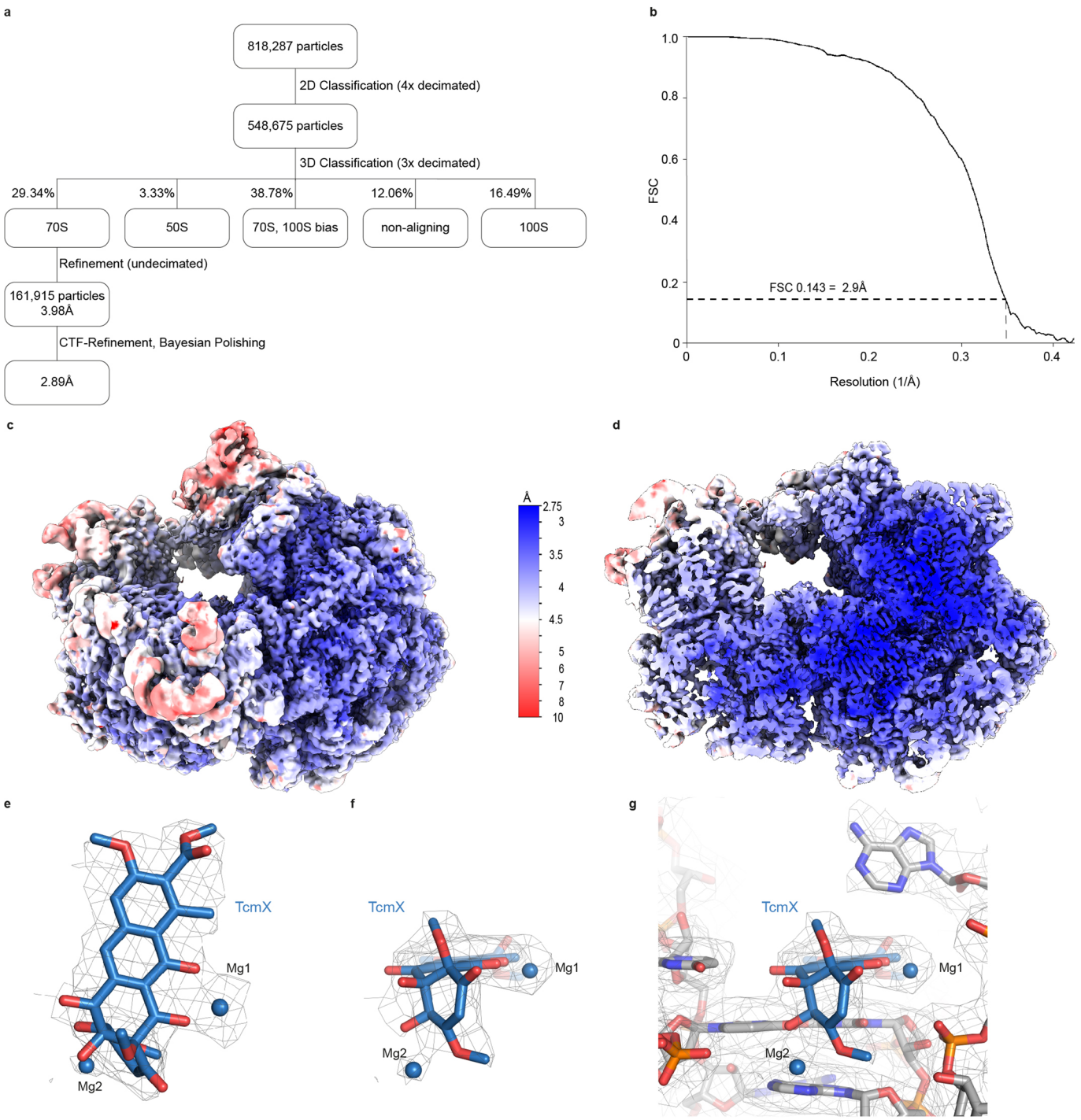

Extended Data Fig. 3 | Cryo-EM structure of the TcmX-Eco70S complex. a, Sorting scheme for cryo-EM data; after initial picking, 818,287 particles were subjected to 2D-Classification, of which 548,675 particles were used for 3D-classification. Particles were sorted into five distinctive classes: non-aligning, 50 S, 100 S, 70 S with 100S-substoichiometric density, and clean 70 S particles. The latter were picked for further refinement (29.34%, 161,915 particles). After CTF-refinement and Bayesian Polishing, a final overall resolution of 2.89 Å was achieved. **b**, Fourier-Shell-Correlation (FSC 0.143) curve of the final reconstruction, with the resolution at FSC = 0.143 indicated with a dashed line. **c**, Overview and (**d**) transverse section of cryo-EM map filtered and coloured according to local resolution. **e**,**f**, Electron density for TcmX with Mg1 and Mg2 and (**g**) the interacting nucleotides of the 23 S rRNA.

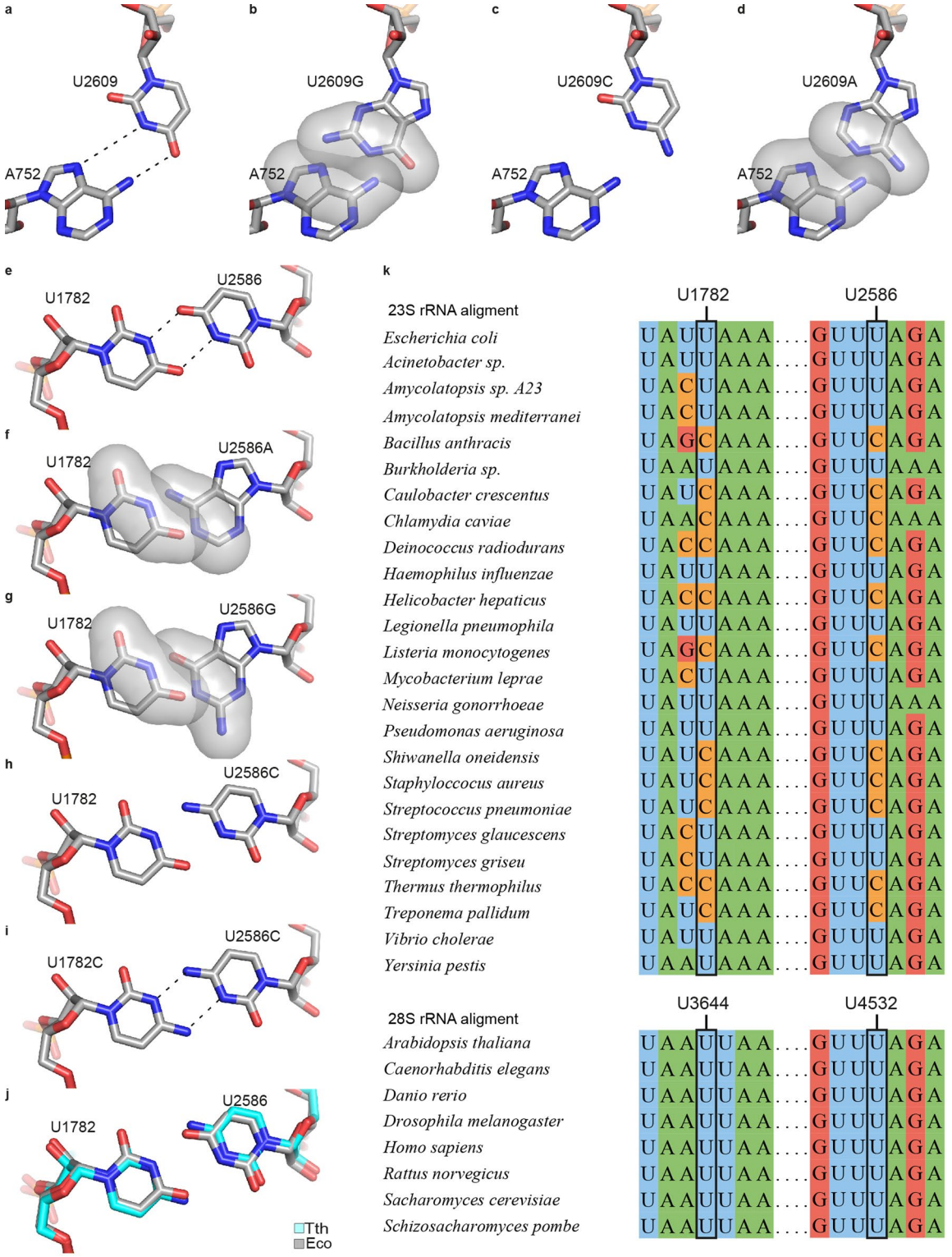

Extended Data Fig. 4 | Conservation of the TcmC binding site. a, In wild-type U2609 basepairs with A752; (**b-d**) *in silico* mutations of TcmX resistant mutations (U2609G, U2609C and U2609A) which can no longer basepair with A752 and due to possible clashing have to adopt a different conformation. **e**, In wild-type U1752 base-pairs with U2586, while in the resistance mutations (**f-i**) the previously base-paired nucleotides will have to adapt a different conformation to avoid clashing, possibly obstructing the TcmX binding site. **j**, In *E. coli* (grey) TcmX stacks upon a U-U basepair U1782-U2586; in *T. thermophilus* (light blue) (PDB 4V9A)[21] it is a C-C base-pair C 1814:C2599. **k**, Bacterial 23 S (above) and eukaryotic 28 S (below) rRNA alignments of select organisms within the vicinity of the U1782 and U2586 (*E. coli* numbering) in eubacteria and U3644 and U4532 (*H. sapiens* numbering).

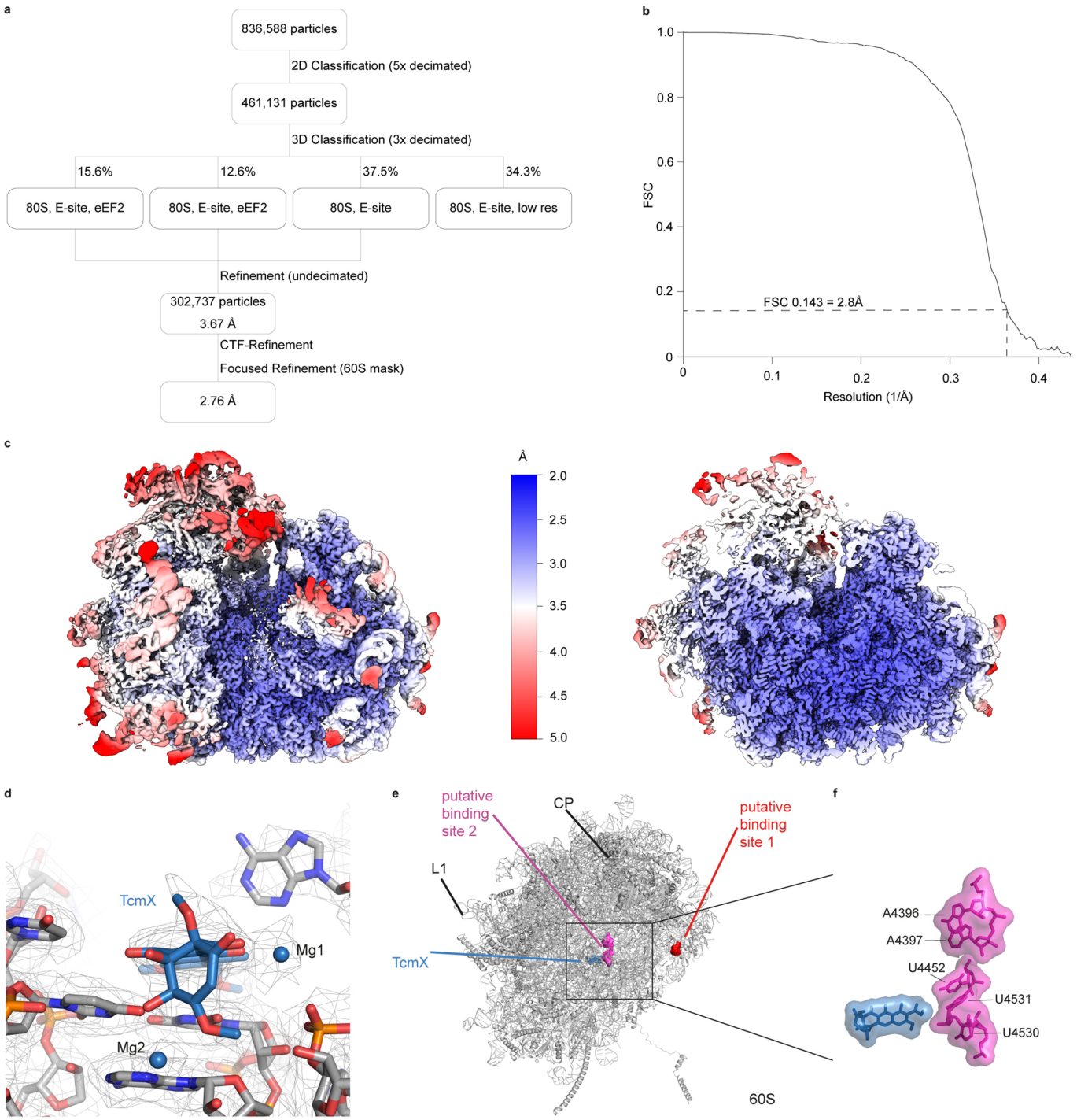

Extended Data Fig. 5 | Processing and analysis of *H. sapiens*-TcmX cryo-EM structure. a, Sorting scheme for cryo-EM data; after Initial picking, 836,588 particles were subjected to 2D-Classification, of which 461,131 particles were used for 3D-classification. Particles were sorted into four classes: low resolution particles, 80 S with E-Site, and two distinct 80 S with E-Site and eEF2. All but low-resolution particles were picked for further refinement (65.7%, 302,737 particles). After CTF-refinement and focused refinement using a 60 S mask, a final overall resolution of 2.76 Å was achieved. **b**, Fourier-Shell-Correlation (FSC 0.143) of the final reconstruction, with the resolution at FSC = 0.143 indicated with a dashed line. **c**, Overview and transverse section of cryo-EM map filtered and coloured according to local resolution. **d**, Electron density (mesh) and molecular model for the TcmX (blue) binding site on the human 80 S ribosome (28 S rRNA nucleotides shown in grey sticks Mg1 and Mg2 as blue spheres). **e**, Overview of the putative Tet-analog binding sites on the Hsa80S ribosome at the terminal loop of H89 (binding site 1, red) and within the exit tunnel (binding site 2, pink)[24] relative to the binding site of TcmX (blue). **f**, Zoom of the relative location of TcmX (blue) to 28 S rRNA nucleotides identified in binding site 2 (magenta).